JOURNAL OF TELECOMMUNICATIONS AND INFORMATION TECHNOLOGY

4/2024

vol. 98

(Contents continued on back cover)

eISSN 1899-8852

Efficient Radio Resource Management in Cell-less Wireless Communication Systems

Israa Zeyad Taha and Ali Othman Al Janaby

Ninevah University, Mosul, Iraq

https://doi.org/10.26636/jtit.2024.4.1678

Abstract — In this paper, the particle swarm optimization (PSO) method with dynamic generation of biasing factors is used to determine the optimal particle size, maximize cell spectral efficiency (CSE) and balance the load in 5G networks. This work studies two distinct interference scenarios: in the first approach, CSE is calculated with varying numbers of users, when different radio services are used by each tier (when several radio access technologies are used), and when interference is received by the consumer only from the same tier base stations (BSs). In the second approach, interference is created when all levels use the same radio services and interference from BSs belonging to the same tier and other tiers is received by the consumer. Simulation results show that the cell-less network performs better than the cellular network in terms of maximizing CSE and balancing the load.

Keywords — 5G, cell-less network, particle swarm optimization, radio resource management

1. Introduction

Several technologies have been employed to control interference in mobile communications [1]. Coordinated multi-point (CoMP) transmission and other techniques have been proposed to cope with ultra-dense network (UDN) constraints, such as ping-pong handover, inter-cell interference, network congestion, and convergence issues. Unfortunately, they were unable to address issues like computing complexity, signal overhead, or practical advantages that fall short of theoretical gains [2].

In heterogeneous networks (HetNet), interference is a challenging issue due to lower signal plus interference-to-noise ratio (SINR). In order for co-channel deployment in HetNet to be effective, extremely efficient interference management is necessary, since low SINR may lower the value of spectral efficiency (SE) [3]. Next generation HetNets must employ new interference management strategies due to the quick development of new technologies, including small cell deployment, enhanced radio access technology and new backbone communications [4].

Base stations (BSs) and radio units (RUs) allocate resources in a sub-optimum manner, due to internal competition for those resources. This competition stems from the design of cellular networks, which has to evolve towards the cell-less architecture in next generation radio access networks (NG-RAN) used in 6G applications [4]. Cell-less networks combine the idea of virtualization, centralization, multi-input multi-output (MIMO), softwarization, and cooperative radio resource management (RRM). A central controller is required to ensure network-wide cooperation. Some attempts have been made to utilize centralized processing for network collaboration purposes, relying on such techniques as cloud/centralized RAN (C-RAN) [2].

By relying on the cell-less concept, a network may meet numerous requirements of 6G use cases, as it will be offering an improved capacity, more effective resource allocation, and enhanced security [4]. Such networks are important for 6G applications in smart cities and industrial automation, as these need high data rates and a simultaneous connection of numerous devices. The networking system's capacity can be significantly increased by controlling interference [4].

Numerous studies have already demonstrated that the cell-less approach may increase the networks' system capacity by collaborating with nearby base stations [5]. Cell-less communication offers dynamic coverage of user equipment (UE) and UE does not have to connect to BS. Therefore, frequent handovers between cells are not required and traffic loads may be dispersed uniformly between several BSs. As UE connects with a group of BS, better energy efficiency and coverage parameters may also be attained [6].

A cell-less network follows the same design as cell-free massive MIMO architecture, with the exception that the user is only served by a subset of the network's BSs. The choice of BSs that serve a given user is based on a user-centric process, where each user has an individual set of cooperating BSs [7]. However, in cell-free massive MIMO, all access points (APs) in the network may be used to serve a given user simultaneously [8].

In wireless communication systems, RRM controls the radio resources, such as power, co-channel interference, time-frequency channels, and other radio transmission parameters [9]. RRM relies on a variety of methods to make the most efficient use of the limited number of radio units. These techniques allow the resources to dynamically modify user access in response to radio environment changes. Hence RRM has a big impact on network performance, densified networks require effective interference management, calling for careful allocation of resource blocks (RBs), APs, and power to ensure satisfactory system performance and user experience metrics [2].

Dynamic partitioning and allocation of radio resources (RR) in the frequency and time domains improves spectrum uti-

lization. Therefore, the system's capacity is improved. Recent studies have shown growing interest in integrating backhaul considerations into resource allocation and interference management solutions for HetNets [10]. RRM is more challenging in hyper dense HetNets environments. Due to the sheer number of devices and the existence of different levels, this environment is impacted by both co-tier and cross-tier interference. Another crucial RRM challenge is to attain peak data rates with effective resource utilization, when spectrum availability is mostly limited. It is the goal of the RRM technique to optimize SE and simultaneously manage interference [11].

The RRM method uses a resource allocation technique consisting in distributing resources to users across various BSs. All available resources of nearby BSs are taken into account when allocating resources to UE. In the cell-less architecture, user association is based on the biasing idea, i.e. the user is not always associated with the closest BS with the highest SINR level. Biasing involves management and optimization techniques used to ensure seamless connectivity and efficient use of network resources in HetNets. Biasing-based user association is essential for balancing the load in cell-less networks.

The aim of this paper is to use a RRM algorithm combined with the cell-less networking technique and the particle swarm optimization (PSO) algorithm in order to greatly enhance system capacity, improve cell spectral efficiency (CSE), and improve load balancing in the network.

The main contributions of this paper are summarized below:

– we propose a cell-less network with an effective RRM technique in order to enhance CSE, reduce interference, and balance the load evenly across all BSs,
– we use the PSO technique to generate the biasing factors in order to determine the optimal particles and calculate CSE for two interference cases in cell-less and cellular networks.

This paper is arranged as follows. Section 2 presents the related works on cell-less techniques. Section 3 explains the proposed cell-less system model and configuration. Section 4 describes the operation of the RRM technology in a cell-less network. In section 5, an explanation is given of the process for creating dynamic biasing factors using PSO. Section 6 presents a simulation of the cell-less model and, finally, Section 7 concludes the paper.

2. Related Works

In [12], the authors described a centralized radio access network (C-RAN) method against the background of time-division duplex (TDD) techniques, empowering a cell-less experience for UE located in the covered areas. UE utilized a certain number of sub-frames from different cells to form a customized cell-less frame, using a flexible method. New queuing models and mathematical analysis methods were identified to optimize low delay and power control targets.

In article [13], the authors developed a dynamic cell-free (or cell-less) network to simplify user signal processing in a network with multiple devices and access points (APs). The architecture divides APs into subgroups, each functioning as a virtual AP with a distributed antenna system (DAS). They introduced an inter-user-interference (IUI)-aware DAS's receive diversity combining strategy and a successive interference cancellation (SIC)-enabled signal to detection approach.

Paper [14] introduces a user-centric cooperation scheme known as Voronoi coordinated multi-point (CoMP), used in a cell-less architecture to mitigate interferences. Users are assigned to small base stations (SBS) clusters, ensuring they are served by the nearest SBS, which maximizes their power while minimizing interference. In [15], a solution to reduce interference in multi-cell domains and optimize inter-cell spectrum utilization using the cell-less technique is proposed. In C-RAN architectures, this approach enhances efficiency by handling data from multiple cells and dynamically manages radio resource allocation.

In [16], the authors introduced a new method of improving energy efficiency in cell-less radio access networks by temporarily switching APs to sleep mode during the interference management phase. this approach uses two-step sleep modes, focusing on load-based conditional criteria and intelligent control over underutilized APs. The system ensures a consistent performance enhancement and efficient power savings during peak traffic hours. Article [17] presents a framework for optimizing the overall throughput of next generation wireless networks (NGWN) that use the multi-carrier cell-less non-orthogonal multiple access (MC-CL-NOMA) architecture. The framework uses scenario data to feed an ensemble metaheuristic technique in order to carry out this task.

In paper [18], the authors presented a multi-architecture coexistence (MACO) network model enabling the deployment of a cell-less architecture with legacy networks to achieve better cost-efficiency, smooth compatibility alignment, and performance enhancement by using the existing architecture for partially deployed cell-less networks, and facilitating network migration towards the ideal entire cell-less RAN. In [19], a new RRM scheme is introduced that combines time and frequency domain schedulers for URLLC and eMBB UE. A UE ranking algorithm is developed to increase scheduling efficiency in large-scale networks with an optimized scheme to reduce delay for URLLC UEs and overcome challenges for eMBB users, ensuring efficient resource utilization in high-density scenarios.

Paper [20] proposes a dynamically changing cell-less wireless network architecture that deals with the high complexity of fully-centralized cell-less architecture in an ultra-dense network (UDN) deployment scenario. It also covers the use of non-orthogonal multiple access (NOMA) to meet the demand for huge wireless connection and applies artificial intelligence (AI)-based techniques to effectively create AP clusters.

Finally, in [21], the authors present the cluster-then-match (CtM) technique that jointly decides on user assignment and point-of-access (PoA) management. Following the human-centric networking paradigm, these determinations take into consideration not only the network's efficiency but also the

level of electromagnetic field exposure that humans experience. Energy use is taken into account as well.

3. System Model and Configuration

PSO is utilized to generate dynamic bias values in HetNets. The proposed system consists of cellular and cell-less networks. We use a downlink 4-tier heterogeneous network with n BSs. Tier 1 stands for conventional macrocells, tier 2 stands for picocells, tier 3 stands for femtocells, and tier 4 stands for RU. Set $N = \{1, 2, 3, \ldots, n\}$ denotes the total number of BSs in this network, where the first element represents the macrocell and other cells (pico, femto, and RU) are represented by the remaining elements. CSE is calculated by using the PSO algorithm, where PSO is used to generate dynamic bias values in HetNets.

RRM application is managed and improved by the cell-less-enabled RAN controller. With system capacity optimization being the main objective, the proposed cell-less networking technique would dynamically adjust to the state of the network [4].

Two different interference cases for the proposed plane in two steps are considered:

1) The first scenario involves calculating CSE with a variable number of users in a situation in which each tier uses a different radio service (it usually occurs when several radio access technologies are used) and where the user receives only interference from BS in the same tier.
2) The second scenario involves calculating CSE with a variable number of users in a situation in which all tiers use the same radio resources and the user experiences interference from the same tier and other tier BSs. The PSO technique is utilized to calculate CSE in the two interference cases, both in cellular and cell-less networks.

A cell-less and a conventional cellular network are shown in Figs. 1–2. A mobile terminal in the cell-less network does not associate with any BSs, but a terminal in the conventional cellular network always associates with one and only one BS. The terminal in this scenario may communicate with one or more BSs in a flexible manner. The results show that the cell-less network outperformed the cellular network as the CSE value improved.

The definitions of the first and second interference cases are as follows:

$$\mathrm{SNIR}_{i,j} = \frac{p_i\, g_{ij}}{\sum l \in A,\ i \neq j\, p_l\, g_{il} + \sigma^2}, \tag{1}$$

$$\mathrm{SNIR}_{i,j} = \frac{p_i\, g_{ij}}{\sum l \in B,\ i \neq j\, p_l\, g_{il} + \sigma^2}, \tag{2}$$

where p_i is the transmitted power of BS j, g_{ij} is the channel gain incorporating path loss and shadowing between user i and BS j, A is the collection of all BSs in the same tier, B is the collection of all BSs in all tiers, σ^2 is the noise power.

The transmission rate is modeled using the truncated Shannon bound (TSB) model, in the following manner:

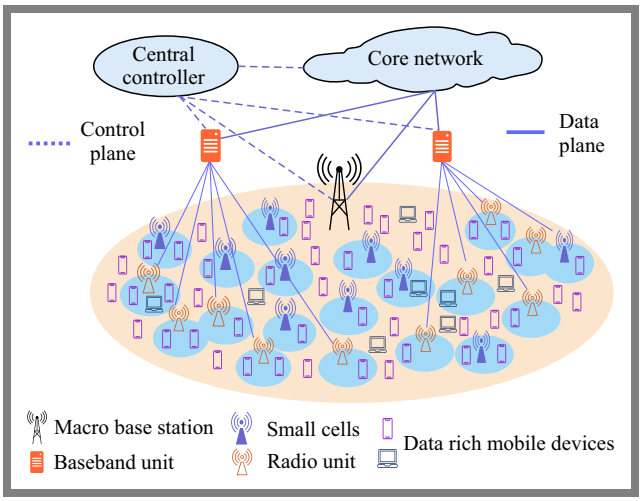

Fig. 1. Cellular network architecture.

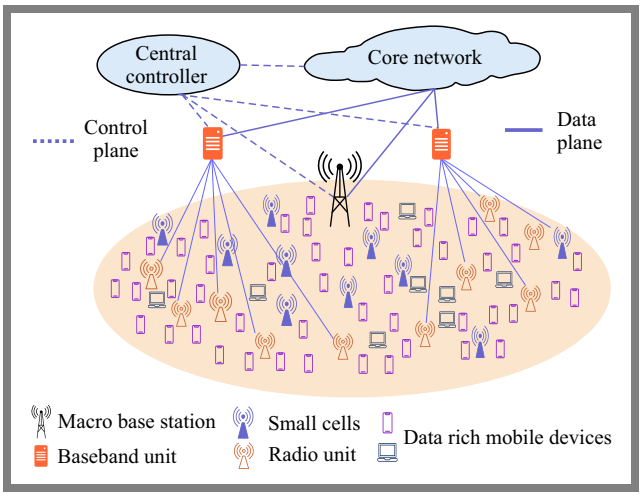

Fig. 2. Cell-less network scheme.

$$T_h = \begin{cases} 0, & \mathrm{SINR} < \mathrm{SINR}_{\min} \\ \alpha \log_2(1 + \mathrm{SINR}), & \mathrm{SINR}_{\min} < \mathrm{SINR} < \mathrm{SINR}_{\max} \\ T_{h_{\max}}, & \mathrm{SINR} > \mathrm{SINR}_{\max} \end{cases} \tag{3}$$

where α is the attenuation factor, $\mathrm{SINR}_{\max}$ is the maximum value of SINR achieving the highest throughput, T_h is the achieved throughput in bps/Hz, $\mathrm{SINR}_{\min}$ is the minimum SINR value that is necessary to guarantee the expected QoS and $T_{h_{\max}}$. As stated in [22], TSB parameters are $\alpha = 0.65$, $\mathrm{SINR}_{\min} = 1.8$ dB, $\mathrm{SINR}_{\max} = 21$ dB, and $T_{h_{\max}} = 4.5$ bps/Hz.

4. RRM Technique with Cell-less Network

Resource allocation is a process that allocates network resources for wireless communication. The distribution of resources across BSs is particularly important in HetNets, where relay nodes are also a component of the network. The distribution of resources is based on the operating band mode and includes access to, as well as direct links between UEs and BSs [11]. Several parameters, mostly controlled at the

BS level, are important for allocating resources. These include the number of users, quantity of available resources, buffer size, and interference. Multiple BSs/RUs are distributed across the network's coverage area. These BSs/RUS are connected via a high-speed backhaul network, allowing them to communicate and coordinate with each other.

A central control unit (CCU) manages the coordination of resources and their allocation to the BSs/RUs. The CCU has a global overview of the network, including its location, channel conditions, and resource requirements of all users. UEs are associated with one or more BSs based on such factors as signal strength, load balancing, and quality of service (QoS). UEs send their channel state information (CSI) and QoS requirements to the BSs/RUs. The CCU uses an advanced algorithm to process CSI and QoS data received from the UEs. These algorithms consider such factors as interference, user priority, channel conditions, and overall network load to optimize resource allocation.

Resources (e.g. time and frequency power) are dynamically allocated to UEs by assigning them to appropriate BSs/RUs. Time and frequency resources are assigned to users based on their demands and QoS requirements. BSs/RUs use such techniques as joint transmission to minimize interference and maximize the data rate. The transmit power of BSs and user devices is adjusted to optimize coverage and reduce interference. This helps maintain a balance between power consumption and signal quality. The network continuously monitors performance and adapts resource allocation as needed. Figure 3 shows a cell-less network with the RRM technique applied.

5. Using PSO for Dynamic Biasing

PSO is one of the sub-fields of artificial intelligence (AI) dedicated to solving optimization problems [23]. PSO algorithms are utilized for discovering the best solution after initializing a set of random particles, by monitoring two extreme values. The particles self-update, yielding the global best particle ($gbest$) and the personal best position ($pbest$).

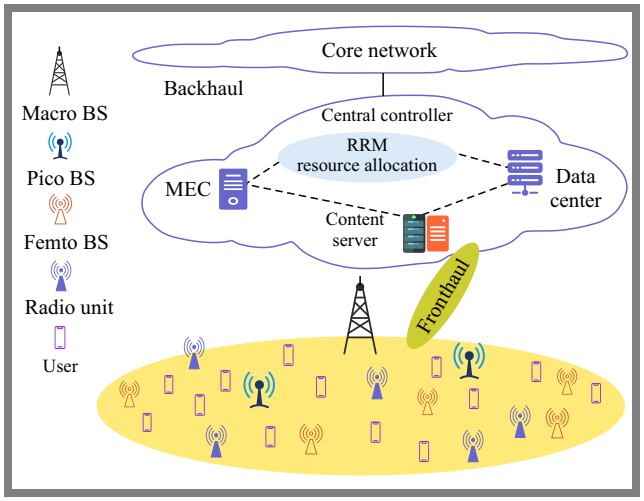

Fig. 3. RRM technique in a cell-less architecture.

All neighbors with extreme values are local extremums. The method employs the whole population but just a subset of them as neighbors [24], [25].

Dynamic biasing is a viable approach allowing to determine the ideal biasing values, as it relies on its strong resilience, quick convergence, and low complexity [26]. Fast convergence speed and a minimal number of controlling parameters are just some of the benefits of utilizing PSO. The main parameters required for PSO are as follows:

1) Swarm size N,
2) Initial position x and initial velocity v,
3) Inertia weight w,
4) The individual and social cognitive c_1 and c_2,
5) Uniformly distributed random numbers r_1 and r_2 in the range $[0, 1]$,
6) Number of iterations T.

In PSO, a swarm of particles randomly generates their initial positions and velocities within predefined bounds. Then, each particle's position and velocity are calculated in a D-dimensional space to find the optimal solution [27]. Each particle i of the swarm has a position and a velocity that can be expressed as follows:

$$V_i = [V_{i1}, V_{i2}, \ldots, V_{iD}], \quad i = 1, 2, \ldots, N, \tag{4}$$

$$X_i = [X_{i1}, X_{i2}, \ldots, X_{iD}], \quad i = 1, 2, \ldots, N. \tag{5}$$

Each particle updates its velocity and position based on the following equations:

$$V_{id}(t+1) = w\, V_{id}(t) + c_1\, r_1 \big(pbest_{id}(t) - X_{id}(t)\big) + c_2\, r_2 \big(gbest_d(t) - X_{id}(t)\big), \tag{6}$$

$$X_{id}(t+1) = X_{id}(t) + V_{id}(t+1). \tag{7}$$

The following is used to compute CSE:

$$\text{System throughput} = \sum_{k=1}^{N} \sum_{j=1}^{M} D_{ki}\, T_{h_{ki}}, \tag{8}$$

$$\text{CSE} = \frac{\text{System throughput}}{N} \times \frac{1}{BW}, \tag{9}$$

$$D_{ki} = \begin{cases} 1, & \text{if a user } i \text{ is connected to } BS_k \\ 0, & \text{if a user } i \text{ is not connected to } BS_k \end{cases},$$

where N is the number of total BSs, m is the number of users, BW is the bandwidth. PSO's task is to find the optimal particle to maximize CSE and to identify procedures for producing dynamic biasing values. A specific algorithm is shown in Fig. 4, illustrating how PSO is applied to find the biasing values to balance the load and maximize CSE.

6. Simulation Results

The results are obtained, in the course of this study, using a Matlab snapshot simulation. We consider a cellular network

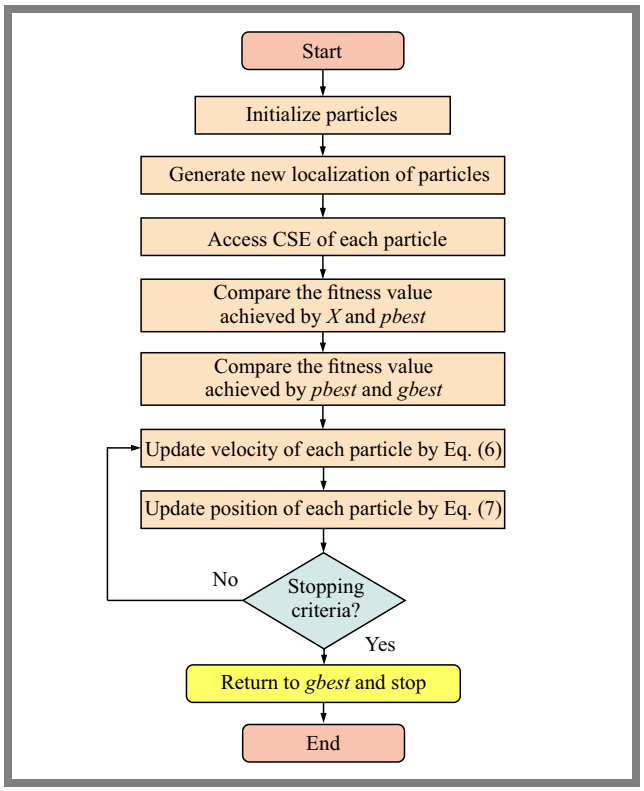

Fig. 4. PSO method used for generating dynamic biasing values.

and a cell-less network, each consisting of 30 BSs (one macro BS, two pico BSs, 17 femto BSs and 10 radio units). The best performance is obtained with a swarm size of 500 particles representing the number of users. The associated path loss model for radio units used in the simulations is retrieved from [28]. The simulation parameters are summarized in Tab. 1, while PSO-related parameters are displayed in Tab. 2.

The cellular and cell-less networks are compared using PSO. CSE is calculated for two interference cases with a bandwidth of 20 MHz and 100 RBs. Figure 5 shows CSE for the two networks with the number of users equaling 500, both in the first and second interference scenario.

Figure 6 explains the CSE value with the number of users equaling 300 for both cases. Figure 7 describes the CSE value in the first and second interference instance, where there are 100 users. In the next step, a comparison between cellular and cell-less networks with a specific number of users in macro, femto and pico BSs as well as in radio units, under two interference scenarios with a bandwidth of 20 MHz is provided. Figure 8 shows how the users are connected to the two networks, with 500 users in the first and second interference case.

Figure 9 shows the total number of users connected to the two networks for 300 UEs and both cases, while Fig. 10 illustrates what happens when the number of users drops to 100 in the initial instance of interference, for both networks and both cases.

Next, PSO is used to compute CSE for two interference scenarios with a bandwidth of 30 MHz and RB equaling 150, in order to compare cellular and cell-less networks.

Tab. 1. Simulation parameters.

Parameter	Value
Bandwidth	20 MHz, 30 MHz
Total number of RBs	100, 150
Tx power of macro BS	46 dBm
Tx power of pico BSs	30 dBm
Tx power of femto BSs	20 dBm
Tx power of RUs	33 dBm
Carrier frequency f_c	4 GHz
Radio unit height	15 m
UE height	1.5 m
Shadowing std. dev.	8 dB (macro), 10 dB (pico), 10 dB (femto)
Macro path loss [29]	$128.1 + 37.6 \log(R)$, R in [km]
Pico path loss [29]	$140.7 + 36.7 \log(R)$, R in [km]
Femto path loss [29]	$127 + 30 \log(R)$, R in [km]
Noise power level	–174 dBm/Hz
Scheduler	Round robin
Traffic model	Full buffer

Tab. 2. PSO parameters.

Parameter	Setting
Swarm size	500, 300, 100
Number of iterations	80
c_1	2
c_2	2
w	0.9–0.4

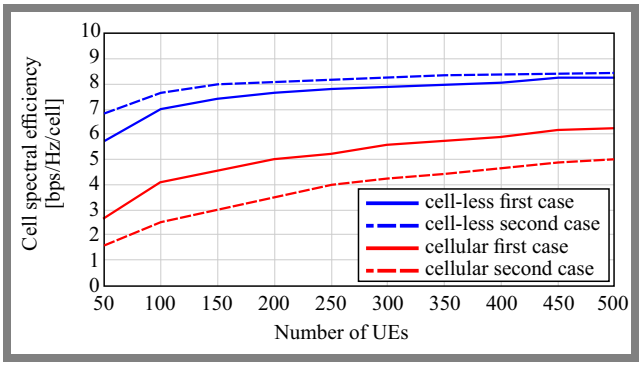

Fig. 5. CSE for different UEs in the first and second interference case.

Figure 11 shows the CSE value for the two networks in the first and second interference instance, when there are 500 users.

Based on all the evaluations conducted, one may conclude that the cell-less networking approach with the proposed

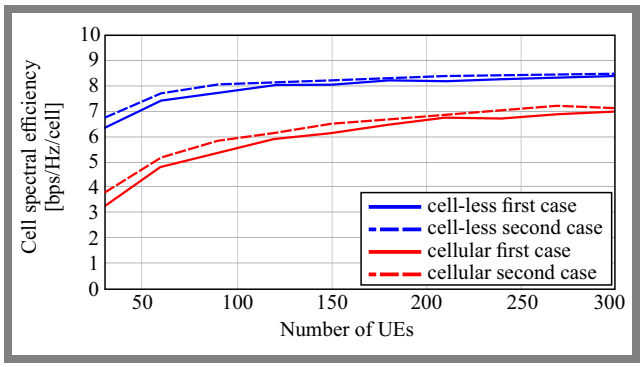

Fig. 6. CSE for different UEs in the first and second interference case.

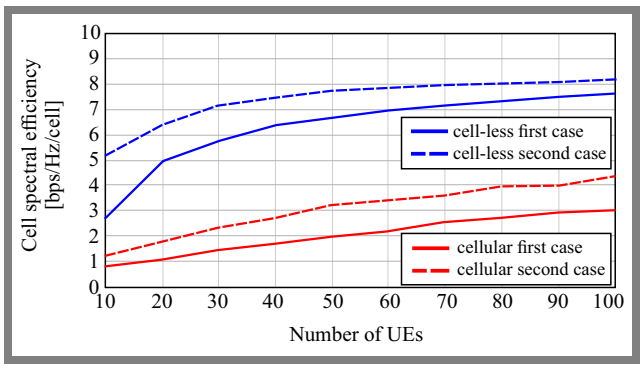

Fig. 7. CSE for different UEs for both interference cases.

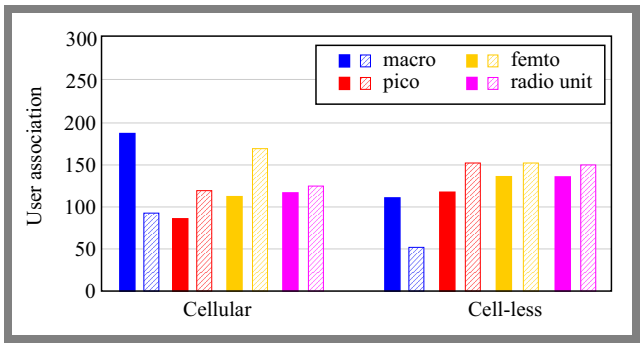

Fig. 8. Number of users linked to every tier in the first and second interference scenario.

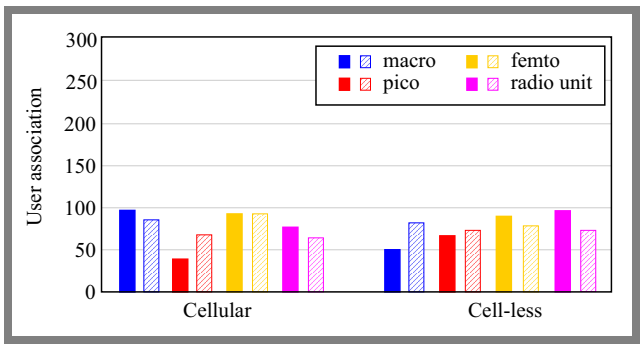

Fig. 9. Number of users linked to every tier in both scenarios.

RRM algorithm is characterized by better CSE performance when compared to cellular networks. This is the result of collaborative scheduling for resources with higher gain will create the more space to allocate resource efficiency in order to achieve higher CSE performance and interference control provided by RRM, the same time utilized to the dynamic bias generated by the PSO in both cellular and cell-less networks to maximizing the CSE. Compared to cellular networks, cell-less networks offer a higher CSE value.

In the second case, where the cellular network uses competitive scheduling to allocate resources to the user, interference is received from all tiers, resulting in severe cross-tier interference between cells that are part of various tiers. Users located at cell edges experience severe interference, which lowers CSE. The CSE value in cell-less networks is higher than in cellular networks.

Figure 6 illustrates that CSE of a cellular network will increase when the number of users drops. Reducing the number of users from 500 to 300 may help minimize network congestion and interference. Less competition for the same bandwidth across users may result in less interference for, thus enabling a more efficient use of the available resources.

In the case of radio resources, less competition results in greater CSE and higher per user data rate, when there are fewer users. The CSE value in cell-less networks remains greater than in cellular networks, even as the number of users decreases.

Figure 7 shows that when the number of users decreases, both cellular and cell-less networks experience a drop in CSE value due to under-utilization of resources. However, cell-less networks maintain higher CSE than cellular networks, because of their ability to dynamically allocate resources, better manage interference, and efficiently utilize the available spectrum, even with fewer users.

Figure 8 shows that users connect to the macro BS more frequently than to other BSs in a cellular network, as there is only one macro BS which transmits at a higher strength than pico BSs, femto BSs, and radio units. Furthermore, users connecting to the macro BS do not encounter interference from other tiers. Users in a cell-less network are dispersed equally throughout all BSs, and radio resource cooperative scheduling is used to share the load between them.

Figure 8 shows also that the number of users connected to the macro BS is lower than in the first interference scenario involving a cellular network, because the macrocell, picocells, femtocells, and RUs share the same frequency for transmission. That is caused by the reduced SINR that a user receives from the microcell, creating an imbalance in the load of the individual BSs. However, in the cell-less network, the load is distributed evenly among all BSs.

Figure 9 illustrates that a cell-less network may still balance the load across all BSs more effectively than a cellular network, even with a drop in number of users from 500 to 300, for two different types of interference, in both networks. High levels of interference from neighboring cells experienced in a cellular network may degrade performance, causing users to connect to more distant cells with lower interference but higher loads, which results in load imbalance.

Figure 10 shows that a cell-less network is still more effective at distributing the load across cells, even when the user count

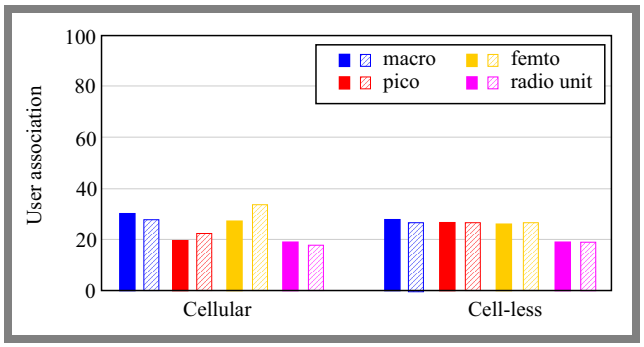

Fig. 10. Number of users linked to every tier in both scenarios.

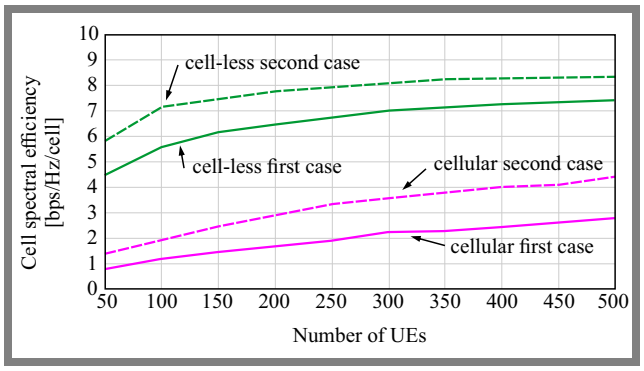

Fig. 11. CSE for different UEs in the first and second interference case

is lowered to 100, but a cellular network still suffers from load imbalance. Figure 11 illustrates a drop in the CSE value observed in the two networks, in line with Eq. (9), since the enormous bandwidth in the cell-less network may result in more significant channel state changes, thus inducing fluctuations which, in turn, cause a drop in CSE and lower signal quality.

The system shows better performance as the user count increases, making better use of the available bandwidth and resources, which may result in higher CSE through optimization. The drop in CSE observed as the bandwidth increases may be the result of a higher number of users in the cellular network competing for the limited capacity, which increases interference. In a cell-less network, the CSE value is larger than in a cellular network.

The results will be different if the PSO algorithm is not used. This is explained in paper [26], where the authors used static biasing and PSO. After comparing the results, it turned out compared that dynamic biasing relying on PSO outperformed static biasing in terms of maximizing CSE and load balancing. Finally, by converting cellular networks to cell-less networks, it will be possible to enhance CSE, decrease interference, reduce network congestion, balance the load across all BSs, and enhance the system's overall performance.

7. Conclusion

In this paper, two distinct interference scenarios were used to compare cell spectral efficiency, for different numbers of users, in cellular and cell-less networks. Particle swarm optimization was applied to determine the optimal particle allowing to maximize CSE and to dynamically generate biasing parameters. 20 MHz and 30 MHz bandwidths were used for CSE calculations in both networks. The benefit of such an approach is that when the bandwidth increases, the number of RBs increase as well, which facilitates CSE value calculations. The result is that when both bandwidths are used, the CSE value increases in the cell-less network.

Simulation-based findings demonstrate that interference management and cooperative RRM scheduling are capable of increasing CSE in cell-less networks, while dynamic biasing is capable of achieving the highest CSE possible and balancing the load between all BSs in cell-less networks.

References

[1] S.A. Ahmed, S.A. Ayoob, and A.O. Al Janaby, "On the Performance of Multi-user Massive MIMO over mm Wave Channels", *2021 7th International Conference on Contemporary Information Technology and Mathematics (ICCITM)*, Mosul, Iraq, 2021 (https://doi.org/10.1109/ICCITM53167.2021.9677730).

[2] S. Pietrzyk *et al.*, "Open Cell-less Network Architecture and Radio Resource Management for Future Wireless Communication Systems", (https://patents.google.com/patent/US20220210794A1), 2023.

[3] A.O. Al Janaby, A. Al-Omary, S.Y. Ameen, and H. Al-Rizzo, "Tracking and Controlling High-speed Vehicles via CQI in LTE-A Systems", *International Journal of Computing and Digital Systems*, vol. 9, no. 6, pp. 1109–1119, 2020 (https://doi.org/10.12785/ijcds/090609).

[4] F. Kooshki *et al.*, "Efficient Radio Resource Management for Future 6G Mobile Networks: A Cell-less Approach", *IEEE Networking Letters*, vol. 5, no. 2, pp. 95–99, 2023 (https://doi.org/10.1109/LNET.2023.3263926).

[5] H.A. Ammar *et al.*, "Downlink Resource Allocation in Multiuser Cell-free MIMO Networks with User-centric Clustering", *IEEE Transactions on Wireless Communications*, vol. 21, no. 3, pp. 1482–1497, 2021 (https://doi.org/10.1109/TWC.2021.3104456).

[6] S. Kim, S. Park, H. Ji, and B. Shim, "AOA-TOA Based Localization for 5G Cell-less Communications", *2017 23rd Asia-Pacific Conference on Communications (APCC)*, Perth, Australia, 2017 (https://doi.org/10.23919/APCC.2017.8304042).

[7] T. Al-shami, "Design of Innovative Access Protocols for Cell-less Architectures", Ph.D. Thesis, University of York, 2020 (https://etheses.whiterose.ac.uk/28469/).

[8] G. Interdonato *et al.*, "Ubiquitous Cell-free Massive MIMO Communications", *EURASIP Journal on Wireless Communications and Networking*, vol. 2019, art. no. 197, 2019 (https://doi.org/10.1186/s13638-019-1507-0).

[9] A.O. Al Janaby, "5G Downlink Throughput Enhancement by Beams Consolidating at Vacant Traffic", *Journal of Communications Software and Systems*, vol. 15, no. 4, pp. 311–316, 2019 (https://doi.org/10.24138/jcomss.v15i4.690).

[10] N. Wang, E. Hossain, and V.K. Bhargava, "Backhauling 5G Small Cells: A Radio Resource Management Perspective", *IEEE Wireless Communications*, vol. 22, no. 5, pp. 41–49, 2015 (https://doi.org/10.1109/MWC.2015.7306536).

[11] T. Akhtar, C. Tselios, and I. Politis, "Radio Resource Management: Approaches and Implementations from 4G to 5G and Beyond", *Wireless Networks*, vol. 27, pp. 693–734, 2021 (https://doi.org/10.1007/s11276-020-02479-w).

[12] V. Sciancalepore *et al.*, "A Service-tailored TDD Cell-less Architecture", *2016 IEEE 27th Annual International Symposium on Personal, Indoor, and Mobile Radio Communications (PIMRC)*, Valencia, Spain, 2020 (https://doi.org/10.1109/PIMRC.2016.7794957).

[13] Y. Al-Eryani, M. Akrout, and E. Hossain, "Multiple Access in Dynamic Cell-free Networks: Outage Performance and Deep Reinforcement Learning-based Design", *arXiv*, 2020 (https://doi.org/10.48550/arXiv.2002.02801).

[14] A. Shen *et al.*, "A Voronoi-based User-centric Cooperation Scheme in Cell-less Architecture", *2021 IEEE Wireless Communications and Networking Conference (WCNC)*, Nanjing, China, 2021 (https://doi.org/10.1109/WCNC49053.2021.9417317).

[15] C. Merlhe and C. Gueguen, "Dynamic Cell-less Radio Access Network Meta-scheduler for High System Capacity Increase", *2020 IEEE 21st International Symposium on "A World of Wireless, Mobile and Multimedia Networks" (WoWMoM)*, Cork, Ireland, 2020 (https://doi.org/10.1109/WoWMoM49955.2020.00031).

[16] F. Kooshki, A.G. Armada, M.M. Mowla, A. Flizikowski, and S. Pietrzyk, "Energy-efficient Sleep Mode Schemes for Cell-less Ran in 5G and Beyond 5G Networks", *IEEE Access*, vol. 11, pp. 1432–1444, 2022 (https://doi.org/10.1109/ACCESS.2022.3233430).

[17] F. de Oliveira Torres *et al.*, "Throughput Maximization for a Multi-carrier Cell-less NOMA Network: A Framework Based on Ensemble Metaheuristics", *IEEE Transactions on Wireless Communications*, vol. 22, no. 1, pp. 348–361, 2022 (https://doi.org/10.1109/TWC.2022.3193328).

[18] F. Kooshki, M.M. Mowla, and A. Flizikowski, "Multi-architecture Coexistence Enabling Network Framework for 5G and Beyond Mobile Systems", *2022 IEEE Conference on Standards for Communications and Networking (CSCN)*, Thessaloniki, Greece, 2022 (https://doi.org/10.1109/CSCN57023.2022.10051097).

[19] F. Kooshki, A.G. Armada, M.M. Mowla, and A. Flizikowski, "Radio Resource Management Scheme for URLLC and eMBB Coexistence in a Cell-less Radio Access Network", *IEEE Access*, vol. 11, pp. 25090–25101, 2023 (https://doi.org/10.1109/ACCESS.2023.3256528).

[20] Y. Al-Eryani and E. Hossain, "A Dynamic Cell-less Architecture for Ultra-dense Wireless Networks", *IEEE ComSoc Technical Committees Newsletter*, 2019 (https://www.comsoc.org/publications/tcn/2019-nov/dynamic-cell-less-architecture-ultra-dense-wireless-networks).

[21] E. Chiaramello *et al.*, "Human-centric Decision-making in Cell-less 6G Networks", *arXiv*, 2024 (https://doi.org/10.48550/arXiv.2402.14344).

[22] T. Jiang, A. Papadogiannis, D. Grace, and A.G. Burr, "EU FP7 BuNGee Project Deliverable 4.1.1 Interim Simulation", European Commission FP7, 2011.

[23] L. Vanneschi and S. Silva, "Particle Swarm Optimization", *Lectures on Intelligent Systems*, pp. 105–111, 2023 (https://doi.org/10.1007/978-3-031-17922-8_4).

[24] T.M. Shami *et al.*, "Particle Swarm Optimization: A Comprehensive Survey", *IEEE Access*, vol. 10, pp. 10031–10061, 2022 (https://doi.org/10.1109/ACCESS.2022.3142859).

[25] S. Wang, F. Zhou, and F. Wang, "Effect of Inertia Weight ω on PSO-SA Algorithm", *International Journal of Online Engineering*, vol. 9, pp. 87–91, 2013 (https://doi.org/10.3991/ijoe.v9iS6.2923).

[26] T.M. Shami, D. Grace, and A. Burr, "User Association in Cell-less 5G Networks Exploiting Particle Swarm Optimization", *14th International Symposium on Wireless Communication Systems (ISWCS)*, 2017.

[27] T.M. Shami *et al.*, "Velocity Pausing Particle Swarm Optimization: A Novel Variant for Global Optimization", *Neural Computing and Applications*, vol. 35, no. 12, pp. 9193–9223, 2023 (https://doi.org/10.1007/s00521-022-08179-0).

[28] ITU, "Guidelines for Evaluation of Radio Interface Technologies for IMT-2020", Report ITU, vol. 2512, 2017 (https://www.itu.int/pub/R-REP-M.2412-2017).

[29] 3GPP, "Evolved Universal Terrestrial Radio Access (E-UTRA); Further Advancements for E-UTRA Physical Layer Aspects (release 9)", 3GPP TR 36.814 Release 9 V9.0.0, 2010 (https://portal.3gpp.org/desktopmodules/Specifications/SpecificationDetails.aspx?specificationId=2493).

Israa Zeyad Taha, B.Sc.
College of Electronics Engineering
https://orcid.org/0009-0003-4449-2836
E-mail: israa.zeyad.eng22@stu.uoninevah.edu.iq
Ninevah University, Mosul, Iraq
https://uoninevah.edu.iq

Ali Othman Al Janaby, Ph.D., Assist. Prof.
College of Electronics Engineering
https://orcid.org/0000-0003-4401-5338
E-mail: ali.mohammed@uoninevah.edu.iq
Ninevah University, Mosul, Iraq
https://uoninevah.edu.iq

Compact All-metal In-line Combline Coaxial Cavity Diplexer

Giacomo Giannetti, Stefano Maddio, and Enrico Boni

University of Florence, Florence, Italy

https://doi.org/10.26636/jtit.2024.4.1783

Abstract — This article describes the design of an all-metal combline coaxial cavity diplexer. The device is based on a Y-shaped star-resonant junction which allows to achieve a compact design by positioning the two channels in an in-line and side-by-side arrangement. The channels share the same geometry and are tuned to resonance using screws. The device was designed using the coupling matrix method. For verification, a combline cavity diplexer was manufactured and tested for E1 Galileo (1559–1591 GHz) and Iridium (1606–1638 GHz) applications with fractional bandwidth equaling 2% for both channels. The order and the return loss of each channel are 5 and 19.4 dB, respectively. The volume is 154.1 × 36 × 27.8 mm^3, corresponding to a normalized volume of 0.810 × 0.189 × 0.146 λ^3. The normalized volume per resonator is as low as 0.0047 λ^3, while isolation is better than 55 dB. The ratio between the unloaded quality factor and the normalized volume per resonator is as high as 19.8 × 10^4 λ^{-3}. The design is very easy to manufacture, since it is all-metal and has a simple geometry.

Keywords — cavity, combline resonators, diplexer, L band

1. Introduction

Microwave diplexers are essential components of RF systems, including cellular base stations and satellite payloads [1]. They are useful in transceiver systems, where the transmitter and receiver signals are close within the frequency spectrum, or when a system operates with two close frequency services. The combline coaxial cavity technology offers low losses and high selectivity and supports high-power signals (hundreds or even thousands of watts). However, this comes at the cost of the occupied volume, which is high, i.e. in the region of tenths of λ^3, compared to microstrip technology [2]–[4]. Therefore, several designs have been introduced to shrink the sizes of cavity filters, either by relying on dual mode operation [5], [6], multi-conductor coaxial cavity resonators [7]–[9] or dielectric resonators [10]–[12].

Combline resonators are an evergreen topic of interest within the microwave community. First papers about combline filters appeared in the 1960s and 1970s [13]–[15] and a comprehensive reference book, which still remains in use, was published in the early 1980s [16]. A deeper understanding of combline filters was obtained in the 1990s and 2000s [17]–[20], when the basics and the fundamentals of combline filters and diplexers were laid down. However, this did not stop research on combline resonators which continued in the following decades and is still conducted nowadays [21]–[23] – all in an effort to ensure better performance and devise tunable devices.

This paper presents a compact all-metal in-line combline coaxial cavity diplexer with enhanced performance. A resonating star junction feeds the two channels. A Y-shaped design is used for the junction, allowing the two channels to be positioned in an in-line arrangement. Since the two channels operate at nearby frequencies, their physical dimensions are the same, and the different resonating frequencies are obtained using tuning screws.

For verification purposes, a diplexer for the E1 Galileo (1559–1591 GHz) and the Iridium (1616–1626.5 GHz) frequency bands was manufactured and tested. The prototype is intended for the LaBarchettaMagica – a showcase, self-navigating vessel built under the VELA project [24]. The simple geometry and the lack of dielectric materials make this cost-effective design easy to manufacture.

2. Design Process

The diplexer model developed is shown in Fig. 1. It is made up of two filters that are joined by a Y-shaped resonating star

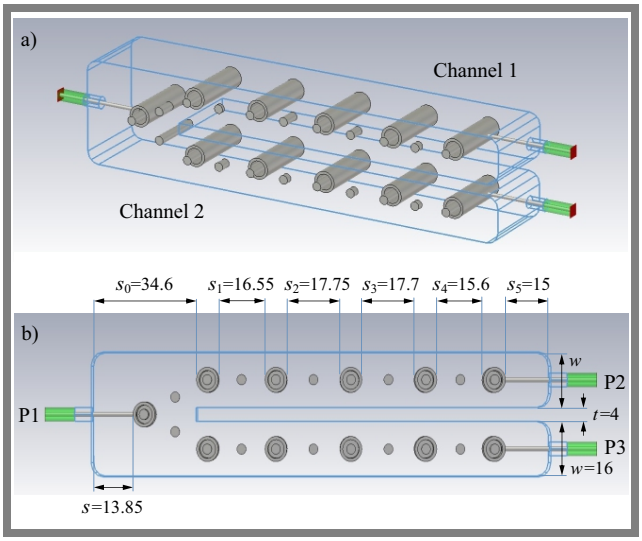

Fig. 1. Model of the diplexer: a) perspective and b) top views. The dimensions (in mm) are: the coaxial inner (outer) diameter is 5.5 and 7.3, the screw diameter is 3, the coaxial cable inner and outer diameters are 1.27 and 4.1, respectively. The heights of the tap points from the bottom of the cavity are 18.75 for P1, 6.75 for P2, and 6.90 for P3, respectively. The radius of the fillets is 4.

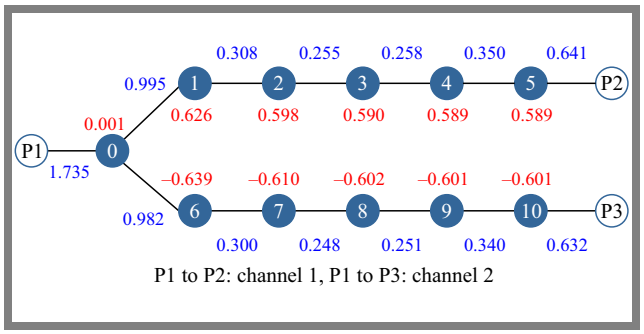

Fig. 2. Topology of the diplexer. The blue circles indicate the resonators, while white circles stand for ports. The numbers in red indicate normalized resonant frequencies $m_{i,i}$, while those in blue indicate normalized coupling coefficients $m_{i,j}$. The white numbers indicate the number of resonators.

junction [25]. The design of a single filter is the same as that described for the filters in [26]–[29]. Then, another filter with the same dimensions is created and aligned with the first one. The separation distance between the two channels is $t = 4$ mm. All coaxial resonators are equal, for ease of manufacture. Their height is $\frac{\lambda}{8}$, with λ being the wavelength at 1.575 GHz. Since the two bandwidths are close, each channel may be tuned to the desired bandwidth [28]. The coupling between adjacent resonators is predominantly of the magnetic type. The input and output couplings are obtained by tapping. To enable the resonators to be tuned to resonance, tuning screws are added above each resonator. To ensure a flexible tuning process, coupling screws are also added midway between the resonators.

The distance between the common resonator and the left-hand side wall is s, while the length of the cavity and its width are s_0 and $2w + t$, respectively (Fig. 1). The star junction is described by s_0 and s parameters, and their values are approximately equal to $2w + t$ and s_5, respectively.

The diplexer has been designed using the coupling matrix method [30]. In view of the above, a return loss (RL) of 19.4 dB is considered, while the passbands of the two channels are 1559–1591 GHz and 1606–1638 GHz, i.e. fractional bandwidth equals 2% for both channels. The number of resonators for each channel is $N = 5$. For the synthesis of the coupling matrix, we rely on the filter toolbox of the CST Studio Suite [31]. The corresponding topology of the diplexer is depicted in Fig. 2, together with the non-zero entries of the synthesized coupling matrix.

The denormalization of the coupling matrix is carried out as in [32], and the values of the resonant frequencies, coupling coefficients, and external quality factors are listed in Tab. 1. Although the desired values for the external quality factors of P2 and P3 are similar, the external quality factor for P1 is significantly lower.

Furthermore, note that the coupling coefficients $k_{0,1}$ and $k_{0,6}$ between the junction resonator and resonators 1 and 6, as shown in Fig. 2, are approximately three or four times greater than the coupling coefficients between the other resonators of the two channels.

Tab. 1. Resonant frequencies (Res. f.), coupling coefficients $k_{i,j}$, and external quality factors Q_E for the proposed design. Res. no. stands for resonator number, as indicated in Fig. 2.

Res. no.	Res. f. [MHz]	$k_{i,j}$		Q_E	
0	1597.98	$k_{0,1}$	0.0492	P1	6.72
1	1573.46	$k_{1,2}$	0.0153	P2	49.23
2	1574.58	$k_{2,3}$	0.0126	P3	50.70
3	1574.87	$k_{3,4}$	0.0128		
4	1574.91	$k_{4,5}$	0.0173		
5	1574.92	$k_{0,6}$	0.0485		
6	1623.43	$k_{6,7}$	0.0148		
7	1622.27	$k_{7,8}$	0.0123		
8	1621.97	$k_{8,9}$	0.0124		
9	1621.93	$k_{9,10}$	0.0168		
10	1621.92				

Note that no cross-coupling is implemented in the proposed diplexer. However, techniques are available to realize in-line cross-couplings [33], [34]. Finally, the dimensions of the coaxial resonators and channel cavities are obtained from the approaches referred to in [35], [36] and are reported in Fig. 1b.

3. Characterization

Figure 3 shows the manufactured diplexer. The cavity is split into two parts, known as the main body and the lid. The lid features a step to prevent radiation leakage and is attached to the main body with 36 M2 screws. The coaxial resonators are manufactured separately and fastened to the bottom of the cavity using screws. The material for the main body, the lid, and the resonators is 6082 aluminum alloy, and no plating is applied. Instead, M3 tuning and coupling screws are made of brass and are fastened to the lid. The input and output ports are realized with SMA connectors. They have a solder cup to connect the wires needed for tapping. The dimensions of the diplexer are 154.1 × 36 × 27.8 mm^3 without the walls, and 162.1 × 44 × 37.8 mm^3 with the walls included.

First, the external couplings are adjusted. In Fig. 4, the measured group delay is shown at the three ports – the resonators at the ports are tuned, while the others are short-circuited, as in [26], [29]. The link between the external quality factor Q_E and the group delay τ_d at the center frequency f_0 is:

$$Q_E = \frac{\pi f_0}{2} \tau_d \,, \tag{1}$$

where no losses are assumed.

The group delays obtained at the center frequencies for the three ports are: 3.1, 20.7, 20.8 ns. These values correspond to the following external quality factors achieved: 7.7, 51.2,

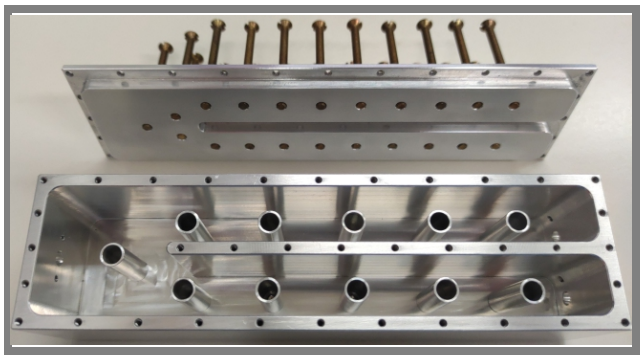

Fig. 3. Manufactured diplexer.

53.0. In Fig. 4, note the wider bandwidth of the group delay of P1, which comprises the bandwidths of both P2 and P3.

Next, the filter is tuned by adjusting the screw penetrations inside the cavity. In Fig. 5, the measured and synthesized magnitude of the scattering parameters is compared. Overall, a good agreement is achieved. In the manual tuning process, the bandwidth of channel 2 has been slightly decreased. However, the Iridium bandwidth is completely contained within the realized bandwidth of channel 2. RL satisfies the specifications requirements and equals at least 19.4 dB in the two bandwidths. A slight deviation for $|S_{21}|$ appears when the frequency is less than 1.559 GHz, due to the manual tuning and the non-ideal frequency characteristics of the coaxial resonators. Note that isolation (ISO) between the channels is as foreseen by the synthesized response, i.e. it is greater than 55 dB at the center frequencies of the channels.

Finally, the measured wideband response of the diplexer is depicted in Fig. 6. For both channels, spurious peaks occur at approximately three times the center frequency of each channel.

In Tab. 2, the performance of this diplexer is compared with other devices sharing the same technology (cavity resonators) described in the literature. To assess compactness, a figure of merit (FoM_1) is introduced. This is equal to the normalized volume per resonator and analogous to the one adopted in [5], [40]. The proposed diplexer is the only one, together with [9], with $\mathrm{FoM}_1 < 0.5 \cdot 10^{-2}\,\lambda^3$. The ISO achieved has one of the highest values, comparable with [5], [37]. Insertion loss (IL) is 1.65 dB for channel 1 and 1.70 dB for channel 2, and corresponds to an unloaded quality factor, averaged over the resonators, of $Q_u \approx 925$. IL is approximately 1 dB higher than that usually characterizing such a class of diplexers, but losses could be reduced either by design changes consisting in varying the shapes of the resonators and the lid, or by technological modifications consisting in plating the interior of the filter with a highly-conductive material.

An additional figure of merit FoM_2, equal to the ratio between Q_u and FoM_1, is introduced. Its value is $19.8 \cdot 10^4\,\lambda^{-3}$, and thus represents the highest value among those reported in Tab. 2. The weight of the prototype is 422 g and is comparable with the mass of analogous diplexers intended for satellite systems, such as the one described in [12], where a weight of 480 g is declared.

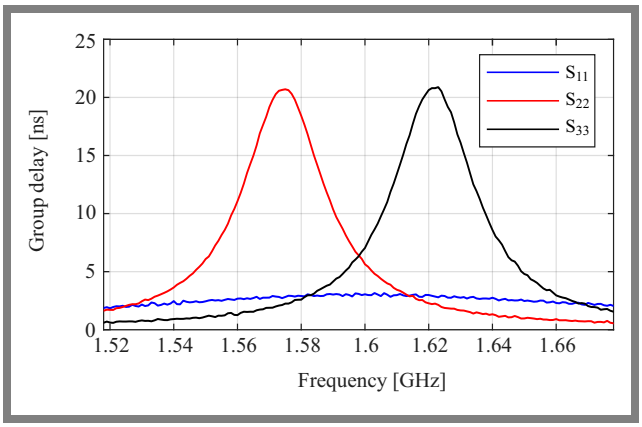

Fig. 4. Group delay measured at the three ports.

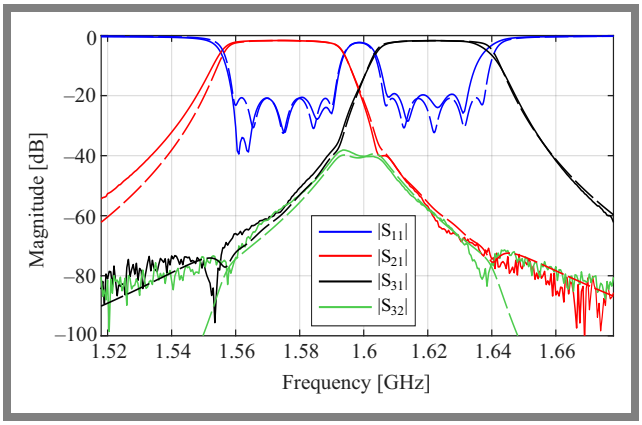

Fig. 5. Comparison between synthesized and measured responses: the former are plotted with dashed lines, the latter with solid ones.

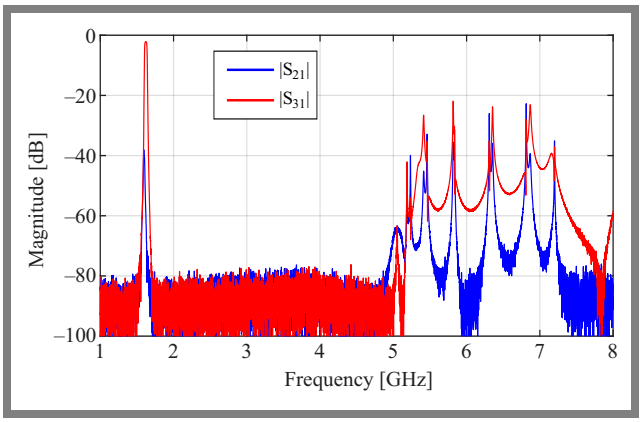

Fig. 6. Measured wideband response in the range 1–8 GHz.

4. Conclusions

The paper presents the design of a combline coaxial all-metal in-line diplexer, where the resonating star junction – a Y-shaped junction – is adopted. The new design is first outlined and then experimentally verified with a diplexer for E1 Galileo and Iridium applications (L band). Both channels have five resonators and are characterized by the same dimensions. The different resonant frequencies are obtained by adjusting screw penetrations.

Tab. 2. Performance comparison of the proposed design and recent examples from the literature.

Ref.	f_1, f_2 [GHz]	CJ	N	FBW [%]	RL	IL	ISO	Vol. $(\cdot 10^2)$	Q_u	FoM_1 $(\cdot 10^2)$	FoM_2 $(\cdot 10^{-4})$
[5]	1 1.8	None	4 4	16 6	>19 >19	0.72 0.55	>50 >50	9.2	–	2.32	–
[6]	4.73 5.03	None	2 2	0.51 0.48	>21 >21	0.7 0.9	>31 >31	2.6	1500	1.28	11.7
[9]	0.77 0.92	RSJ	4 4	22.3 8.7	20 20	0.6 0.6	28 28	0.5	–	0.12	–
[12]	1.54 1.65	TJ	3 3	2.7 3.0	22 16	0.2 0.3	– –	7.0	2000	2.34	8.5
[32]	1.88 1.96	RSJ	10 9	3.7 3.42	22 22	– –	– –	– –	–	– –	–
[37]	1.74 1.87	TJ	8 8	5.63 5.76	22 22	– –	80 80	23.3	–	2.92	–
[38]	2.52 2.67	RSJ	5 5	3.57 3.67	22 22	0.6 0.6	– –	8.9	2000	1.79	11.2
[39]	1.52 1.64	None	2 2	0.85 1.1	14.5 14.0	0.8 0.5	33 33	1.6	–	0.78	–
This paper	1.575 1.621	RSJ	5 5	2.0 2.0	19.4 19.4	1.65 1.70	59.3 57.4	2.3	925	0.47	19.8
Abbreviations: f_1, f_2 – center frequencies, CJ – coupling junction, RSJ – resonating star-junction, TJ – T-junction, FBW – fractional bandwidth, Vol. – volume, $\mathrm{FoM}_1 = \mathrm{Vol.}/N(\lambda^3)$, $\mathrm{FoM}_2 = Q_u/\mathrm{FoM}_1(\lambda^{-3})$, wavelength λ – the one at $\sqrt{f_1 f_2}$											

While proving to offer comparable performance in terms of key indicators, such as RL and ISO, the diplexer proves to be one of the most compact solutions, with a volume of $0.023\,\lambda^3$. In particular, the normalized volume divided by the number of resonators is as low as $0.47 \cdot 10^{-2}\,\lambda^3$, representing one of the lowest values among those reported. Additionally, the ratio between the unloaded quality factor and the normalized volume reaches up to $19.8 \cdot 10^4\,\lambda^{-3}$, making it the highest value available in the literature.

The simple geometry, combined with the Y-shaped junction, the same dimensions for the two channels and an all-metal design make the device easy and cost-effective to manufacture.

Acknowledgments

The authors thank Guglielmo Giannetti from the Ducati Motor Holding and the University of Florence for his invaluable help in manufacturing the prototype.

References

[1] R.J. Cameron and M. Yu, "Design of Manifold-coupled Multiplexers", *IEEE Microwave Magazine*, vol. 8, no. 5, pp. 46–59, 2007 (https://doi.org/10.1109/MMM.2007.904715).

[2] A. Rezaei, L. Noori, and H. Mohammadi, "Design of a Novel Compact Microstrip Diplexer with Low Insertion Loss", *Microwave and Optical Technology Letters*, vol. 59, no. 7, pp. 1672–1676, 2017 (https://doi.org/10.1002/mop.30600).

[3] G. Giannetti and S. Maddio, "Low-loss Compact Diplexer Based on Complementary Spiral Resonators", *Microwave and Optical Technology Letters*, vol. 66, no. 6, art. no. e34202, 2024 (https://doi.org/10.1002/mop.34202).

[4] G. Giannetti, S. Maddio, and S. Selleri, "A Compact Low-loss Single-layer Vialess Diplexer Based on Complementary Microstrip Spiral Resonators for Satellite Communications", *Progress in Electromagnetics Research Letters*, vol. 122, pp. 45–51, 2024 (https://doi.org/10.2528/PIERL24061104).

[5] Y. Xie, F.-C. Chen, Q.-X. Chu, and Q. Xue, "Dual-band Coaxial Filter and Diplexer Using Stub-loaded Resonators", *IEEE Transactions on Microwave Theory and Techniques*, vol. 68, no. 7, pp. 2691–2700, 2020 (https://doi.org/10.1109/TMTT.2020.2987558).

[6] A. Widaa and M. Höft, "Very Compact Diplexer Based on Dual-mode Dielectric TM-mode Resonators", *IEEE Microwave and Wireless Technology Letters*, vol. 33, no. 4, pp. 387–390, 2023 (https://doi.org/10.1109/LMWT.2022.3228398).

[7] E. Musonda and I.C. Hunter, "Microwave Bandpass Filters Using Re-entrant Resonators", *IEEE Transactions on Microwave Theory and Techniques*, vol. 63, no. 3, pp. 954–964, 2015 (https://doi.org/10.1109/TMTT.2015.2389216).

[8] E. Doumanis, S. Bulja, and D. Kozlov, "Compact Coaxial Filters for BTS Applications", *IEEE Microwave and Wireless Components Letters*, vol. 27, no. 12, pp. 1077–1079, 2017 (https://doi.org/10.1109/LMWC.2017.2757446).

[9] Z. Li, V. Rudakov, V. Sledkov, and V. Zemlyakov, "Compact UHF Diplexer on Multi-conductor Coaxial Cavity Resonators", *2023 Ra-*

diation and Scattering of Electromagnetic Waves (RSEMW), Divnomorskoe, Russian Federation, 2023 (https://doi.org/10.1109/RSEMW58451.2023.10202047).

[10] C. Wang and K.A. Zaki, "Dielectric Resonators and Filters", *IEEE Microwave Magazine*, vol. 8, no. 5, pp. 115–127, 2007 (https://doi.org/10.1109/MMM.2007.903648).

[11] L. Pelliccia, F. Cacciamani, C. Tomassoni, and R. Sorrentino, "Ultra-compact High-performance Filters Based on TM Dual-mode Dielectric-loaded Cavities", *International Journal of Microwave and Wireless Technologies*, vol. 6, no. 2, pp. 151–159, 2013 (https://doi.org/10.1017/S1759078713001001).

[12] L. Pelliccia *et al.*, "Compact On-board L-band Dielectric-loaded Diplexer for High-power Applications", *2019 49th European Microwave Conference*, Paris, France, 2019 (https://doi.org/10.23919/EuMC.2019.8910684).

[13] M. Dishal, "A Simple Design Procedure for Small Percentage Bandwidth Round-rod Interdigital Filters", *IEEE Transactions on Microwave Theory and Techniques*, vol. 13, no. 5, pp. 696–698, 1965 (https://doi.org/10.1109/TMTT.1965.1126066).

[14] R.J. Wenzel, "Synthesis of Combline and Capacitively Loaded Interdigital Bandpass Filters of Arbitrary Bandwidth", *IEEE Transactions on Microwave Theory and Techniques*, vol. 19, no. 8, pp. 678–686, 1971 (https://doi.org/10.1109/TMTT.1971.1127609).

[15] E.G. Cristal, "Tapped-line Coupled Transmission Lines with Applications to Interdigital and Combline Filters", *IEEE Transactions on Microwave Theory and Techniques*, vol. 23, no. 12, pp. 1007–1012, 1975 (https://doi.org/0.1109/TMTT.1975.1128734).

[16] G.L. Matthaei, L. Young, and E.M.T. Jones, *Microwave Filters, Impedance-matching Networks, and Coupling Structures*, Boston: Artech House, 1120 p., 1980 (ISBN: 9780890060995).

[17] H.-W. Yao, K.A. Zaki, A.E. Atia, and R. Hershtig, "Full Wave Modeling of Conducting Posts in Rectangular Waveguides and Its Applications to Slot Coupled Combline Filters", *IEEE Transactions on Microwave Theory and Techniques*, vol. 43, no. 12, pp. 2824–2830, 1995 (https://doi.org/10.1109/22.475641).

[18] J.B. Ness, "A Unified Approach to the Design, Measurement, and Tuning of Coupled-resonator Filters", *IEEE Transactions on Microwave Theory and Techniques*, vol. 46, no. 4, 1998 (https://doi.org/10.1109/22.664135).

[19] J. Thomas, "Cross-coupling in Coaxial Cavity Filters - A Tutorial Overview", *IEEE Transactions on Microwave Theory and Techniques*, vol. 51, pp. 1368–1376, 4 2003 (https://doi.org/10.1109/TMTT.2003.809180).

[20] D. Swanson and G. Macchiarella, "Microwave Filter Design by Synthesis and Optimization", *IEEE Microwave Magazine*, vol. 8, no. 2, pp. 55–69, 2007 (https://doi.org/10.1109/MMW.2007.335529).

[21] J.-X. Xu, L. Yang, Y. Yang, and X.Y. Zhang, "High-Q-factor Tunable Bandpass Filter with Constant Absolute Bandwidth and Wide Tuning Range Based on Coaxial Resonators", *IEEE Transactions on Microwave Theory and Techniques*, vol. 67, no. 10, pp. 4186–4195, 2019 (https://doi.org/10.1109/TMTT.2019.2926251).

[22] J.J. Vague *et al.*, "Inline Combline Filters of Order N with up to N + 1 Transmission Zeros", *IEEE Transactions on Microwave Theory and Techniques*, vol. 69, no. 7, pp. 3287–3297, 2021 (https://doi.org/10.1109/TMTT.2021.3072370).

[23] H. Jamshidi-Zarmehri *et al.*, "Efficient Design Procedure for Combline Bandpass Filters with Advanced Electrical Responses", *IEEE Access*, vol. 11, pp. 52168–52184, 2023 (https://doi.org/10.1109/ACCESS.2023.3278791).

[24] E. Boni, M. Montagni, and L. Pugi, "Project VELA, Upgrades and Simulation Models of the UNIFI Autonomous Sail Drone", *Lectures Notes in Electrical Engineering*, vol. 627, pp. 389–396, 2020 (https://doi.org/10.1007/978-3-030-37277-4_45).

[25] G. Macchiarella and S. Tamiazzo, "Synthesis of Star-junction Multiplexers", *IEEE Transactions on Microwave Theory and Techniques*, vol. 58, no. 12, pp. 3732–3741, 2010 (https://doi.org/10.1109/TMTT.2010.2086570).

[26] E. Boni, G. Giannetti, S. Maddio, and G. Pelosi, "Fast and Efficient Systematic Procedure for and Flexibility on the End Coupling Design in Microwave Filters", *2023 Kleinheubach Conference*, Miltenberg, Germany, 2023 (https://ieeexplore.ieee.org/document/10296826).

[27] E. Boni, G. Giannetti, S. Maddio, and G. Pelosi, "An Equation-based Method for the Design of End Couplings in Combline Microwave Cavity Filters", *2023 IEEE International Symposium on Antennas and Propagation*, Portland, USA, 2023 (https://doi.org/10.1109/USNC-URSI52151.2023.10237496).

[28] E. Boni, G. Giannetti, S. Maddio, and G. Pelosi, "Comparison of Inductive and Capacitive End Couplings in the Design of a Combline Microwave Cavity Filter for the E1 Galileo Band", *Advances in Radio Science*, vol. 22, pp. 1–8, 2024 (https://doi.org/10.5194/ars-22-1-2024).

[29] E. Boni, G. Giannetti, S. Maddio, and G. Pelosi, "Capacitive End-couplings in Combline Microwave Cavity Filters with Probe Parallel to Resonators' Axes: Comparison and Design Guidelines", *2023 Kleinheubach Conference*, Miltenberg, Germany, 2023 (https://ieeexplore.ieee.org/document/10296707).

[30] R.J. Cameron, C.M. Kudsia, and R.R. Mansour, *Microwave Filters for Communication Systems: Fundamentals, Design, and Applications*, John Wiley & Sons, 897 p., 2018 (https://doi.org/10.1002/9781119292371).

[31] Dassault Systemes, "CST Studio Suite", 2023 [Online]. Available: (https://www.3ds.com/products-services/simulia/products/cst-studio-suite/).

[32] G. Macchiarella and S. Tamiazzo, "Novel Approach to the Synthesis of Microwave Diplexers", *IEEE Transactions on Microwave Theory and Techniques*, vol. 54, no. 12, pp. 4281–4290, 2006 (https://doi.org/10.1109/TMTT.2006.885909).

[33] Y. Wang and M. Yu, "True Inline Cross-coupled Coaxial Cavity Filters", *IEEE Transactions on Microwave Theory and Techniques*, vol. 57, no. 12, pp. 2958–2965, 2009 (https://doi.org/10.1109/TMTT.2009.2034221).

[34] M. Höft and F. Yousif, "Orthogonal Coaxial Cavity Filters with Distributed Cross-coupling", *IEEE Microwave and Wireless Components Letters*, vol. 21, no. 10, pp. 519–521, 2011 (https://doi.org/10.1109/LMWC.2011.2165533).

[35] D. Natarajan, "A Practical Design of Lumped, Semi-lumped and Microwave Cavity Filters", *Lecture Notes in Electrical Engineering*, vol. 183, pp. 1–157, 2013 (https://doi.org/10.1007/978-3-642-32861-9_1).

[36] M.S. Anwar and H.R. Dhanyal, "Design of S-band Combline Coaxial Cavity Bandpass Filter", *2018 15th International Bhurban Conference on Applied Sciences and Technology (IBCAST)*, Islamabad, Pakistan, 2018 (https://doi.org/10.1109/IBCAST.2018.8312328).

[37] P. Zhao and K.-L. Wu, "Adaptive Computer-aided Tuning of Coupled-resonator Diplexers with Wire T-junction", *IEEE Transactions on Microwave Theory and Techniques*, vol. 65, no. 10, pp. 3856–3865, 2017 (https://doi.org/10.1109/TMTT.2017.2686852).

[38] P. Zhao and K.-L. Wu, "An Iterative and Analytical Approach to Optimal Synthesis of a Multiplexer with a Star-junction", *IEEE Transactions on Microwave Theory and Techniques*, vol. 62, no. 12, pp. 3362–3369, 2014 (https://doi.org/10.1109/TMTT.2014.2364222).

[39] L. Xu, W. Yu, and J.-X. Chen, "Unbalanced-/Balanced-to-unbalanced Diplexer Based on Dual-mode Dielectric Resonator", *IEEE Access*, vol. 9, pp. 53326–53332, 2021 (https://doi.org/10.1109/ACCESS.2021.3070328).

[40] Y. Xie, F.-C. Chen, and Q.-X. Chu, "Triple-band Bandpass Filter and Triplexer Using Quad-ridge Cavity Resonators", *IEEE Transactions on Microwave Theory and Techniques*, vol. 69, no. 8, pp. 3832–3841, 2021 (https://doi.org/10.1109/TMTT.2021.3082556).

Giacomo Giannetti, M.Sc.
Department of Information Engineering
https://orcid.org/0000-0002-4318-8176
E-mail: giacomo.giannetti@unifi.it
University of Florence, Florence, Italy
https://www.unifi.it/en

Stefano Maddio, Ph.D.
Department of Information Engineering
https://orcid.org/0000-0002-4481-1791
E-mail: stefano.maddio@unifi.it
University of Florence, Florence, Italy
https://www.unifi.it/en

Enrico Boni, Ph.D.
Department of Information Engineering
https://orcid.org/0000-0002-9899-8782
E-mail: enrico.boni@unifi.it
University of Florence, Florence, Italy
https://www.unifi.it/en

Realistic Approach to Description of Signals at Output of A/D Converters

Andrzej Borys

Gdynia Maritime University, Gdynia, Poland

https://doi.org/10.26636/jtit.2024.4.1682

Abstract — It is common knowledge that no signals having the form of a sequence of weighted Dirac deltas, as they are currently modelled so, are present, in reality, at the output of analog-to-digital converters (ADC). No such signals are available in the otherwise large variety of physical signals. This has been illustrated in many works and shown by means of measurements. However, it is highly intriguing that the same papers (with the exception of this article) consider it necessary to model the signals at the output of ADC via sequences of Dirac deltas because only such an approach allows to describe the aliasing effect occurring in the spectra of these signals. But due to this incorrect description such an approach is obviously incomprehensible to everyone. In accepting this, however, it has been overlooked that this does not have to be the case at all. The effect of aliasing in the spectrum of a sampled signal may be explained by modeling this signal as a weighted step function. Moreover, such an approach offers also a quantitatively more accurate result for this spectrum than the one obtained using the current method. All that is illustrated in this paper that focuses on this specific theme.

Keywords — modeling ADC output signals, spectra of sampled signals

1. Introduction

Let us start by listing some facts that do not receive much attention, but are related to modeling and describing analog signals being the output signals of analog-to-digital converters (ADCs). We shall enumerate those facts and provide their brief descriptions.

It is well known that people find it difficult to understand why the time waveforms at the output of ADC have to be modelled using weighted Dirac delta series (weighted Dirac combs) despite the fact that they are considered to be step functions.

Engineers working in various industries relying on digital techniques know that analog-to-digital converters do not generate Dirac deltas. Nevertheless, the descriptions of output waveforms of ADCs are realized through non-physical objects, called Dirac deltas. Furthermore, it shall be noted that the spectrum of a sampled signal in the form of an endless repetition of the same pattern (with or without overlapping) looks rather strange. In particular, the spectra known to engineers, researchers, and students from laboratories, even if they are periodic in nature, extinguish as the frequency increases.

People often assume that when they use the formula that is currently applied, in the literature, to the spectra of sampled signals, they deal with their Fourier transforms. However, this is not true. Such an identification of one with another often leads to misunderstandings and/or overinterpretation.

The above-mentioned ambiguities are discussed in detail in this paper. Their clarification and explanation are very important, as they allow us to correctly understand the analog signal sampling process.

Following numerous conversations and having exchanged opinions with people inventing new digital signal processing algorithms, the author of this paper has the impression that all of the above-mentioned ambiguities are considered irrelevant by his interlocutors who do not attach much attention to them. Such an approach of those researchers may be partly understandable, but only in cases in which they work with signals they understand as functions of a discrete variable, leaving aside the existence of a physical time. Using mathematical terminology, one may say that they then operate in the spaces of discrete functions only.

The trouble is that they continuously switch from their solutions in the form of functions of a discrete variable to functions of a continuous variable, denoting a continuous time t belonging to the set of real numbers, and vice versa. In other words, the researchers move directly with their solutions from the spaces of discrete functions to the spaces of functions of a continuous variable, and vice versa. But this can generate errors and indeed it does. However, these errors are marginalized or ignored.

It seems that this approach should be given a closer look as far as signal processing is concerned, primarily due to the very simple reason that while focusing on this area, we always measure and/or use signals that are functions of a continuous real time variable t, and are not function of an abstract discrete variable. This is also the case when we talk about the so-called discrete time and/or consider the measurement process to be a specific type of sampling of an analog signal.

The so-called discrete time, a concept used in digital signal processing, must then be understood as a set of ordered discrete time instants "immersed" in a continuous real-time axis. It is "embedded in this axis, built into this time context" and should be interpreted as more than merely a set of ordered discrete values [1].

Moreover, as shown in [2] and [3], if we perceive the process of measuring a physical signal to be similar to the sampling of an analog signal and model it as such, then this "sampled" signal must be understood as a function of a continuous real

time variable t, e.g. it must be a step function of variable t or must have a similar form, but cannot be a sequence of the weighted time-shifted Dirac deltas.

Therefore, all the ambiguities listed at the beginning of this section are directly related to proper perception, description, and modeling of the signals that are used in various electronic signal processing devices. Furthermore, because of the relationships just mentioned above, explaining those ambiguities is of vital importance for all people dealing with signal processing. With that taken into consideration, this is exactly one of the main objectives of this paper.

It is also worth noting that since digital-to-analog (D/A) conversions are the reverse of A/D operations, the considerations presented in this paper are also directly applicable to modeling the former [4].

The remainder of this paper is organized as follows. In Sections 2–4, pitfalls related to modeling operations performed with the use of weighted Dirac and Kronecker sequences, as well as taking into account improperly nonidealities of the sampling process, are presented. Sections 5 and 6 are devoted to modeling ADC output waveforms via step functions, and to presenting measurement results confirming the reliability of this model. In Section 7, calculations of the spectra of the aforementioned signals are discussed. The paper ends with some conclusions and remarks in Section 8.

2. Modeling Relying on Dirac Deltas

The process of modeling time waveforms at the output of A/D converters with the use of Dirac deltas is widely assumed to be the only correct approach. It is worth noting that this method is taught to students all over the world, including the USA [5]. In this context, let us mention a couple of very well-known textbooks [6]–[10] that promote this approach.

The method of modeling a sampled signal in the space of a continuous time t with the use of replicated weighted Dirac deltas is illustrated in Fig. 1. This signal is called $x_T(t)$.

Further, in the context of the visualization shown in Fig. 1, it is also worth noting that the upper curve in this figure is nothing else but the so-called Dirac comb shown in Fig. 2 and denoted as $\delta_T(t)$, multiplied by the values of samples of signal $x(t)$ – see the lower curve in Fig. 1.

The Dirac delta is defined in many ways in the literature. One of those definitions uses the notion of a functional. In such a context, one may write:

$$\langle \delta, z \rangle = \int_{-\infty}^{\infty} \delta(\tau)\, z(\tau)\, d\tau = z(0)\ , \tag{1}$$

where δ stands for the Dirac delta (Dirac pulse) and z is a test function, respectively.

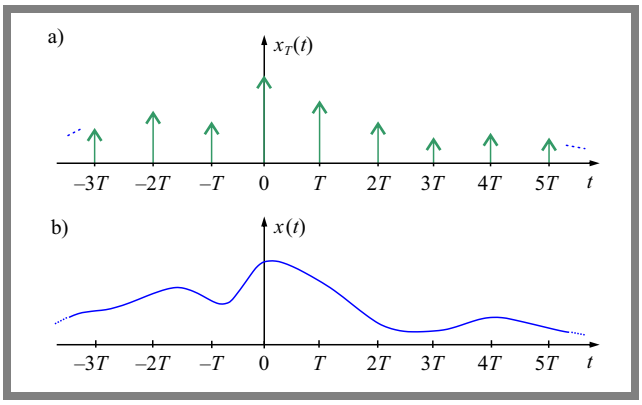

Fig. 1. Example sampled signal a) in the form of a series of weighted Dirac deltas occurring uniformly along the continuous time axis, at intervals T from each other, and its un-sampled version b), where t stands for a continuous time variable [11].

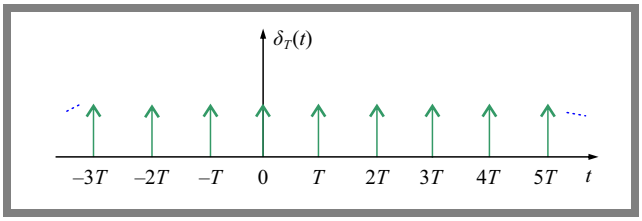

Fig. 2. Visualization of the Dirac comb being a series (sum) of Dirac deltas replicated uniformly along the continuous time axis, at T intervals [11].

Further, note that a shifted Dirac delta multiplied by a constant $x(kT)$ is given by:

$$\begin{aligned}\langle x(kT)\,\delta(\tau - kT), z\rangle &= \int_{-\infty}^{\infty} x(kT)\,\delta(\tau - kT)\, z(\tau)\, d\tau \\ &= x(kT)\, z(kT) = x(kT) \neq \infty\end{aligned}\ , \tag{2}$$

with $z(kT) = 1$. In Eq. (2), T is the sampling period of an analog signal $x(t)$ of a continuous time t, k is an integer, i.e. $k \in \{\ldots, -2, -1, 0, 1, 2, \ldots\}$.

With the context presented above taken into consideration, one needs to note that this non-physical and abstract object referred to as the Dirac delta (a.k.a. Dirac pulse or Dirac distribution), not being a function, is defined – for teaching-related purposes – as follows:

$$\delta(t - kT) = \begin{cases} \infty & \text{for } t = kT \\ 0 & \text{otherwise} \end{cases}\ , \tag{3}$$

as it is a common opinion that engineers are not able to correctly understand a sophisticated theory of distributions originally devised by L. Schwartz and developed further by other researchers.

At this point, let us refer to one example, taken from [12]. According to the research findings presented therein, an integral of the Dirac delta exists and is given by:

$$\int_{-\infty}^{\infty} \delta(t - kT)\, dt = 1\ . \tag{4}$$

In fact, the integrals from Eqs. (1), (2) and (4), with δ understood in the manner given in Eq. (3), do not exist in the Riemann sense or are equal to zero in the Lebesgue sense. Thus, they can only play a role of symbols of certain operations there.

The approach mentioned above, relied upon when teaching engineers, is called "primitive" – see, for instance, the textbook by Hoskins [13]. It is also adopted at the Massachusetts Institute of Technology (MIT) [5].

The fact that they have to deal with (observe) finite values equal to $x(kT)$ (with some tolerance) at the sampling instants kT is undoubtedly shocking to engineers, but according to Fig. 1a, they are to believe that these values of the signal samples amount to $x(kT)\,\delta(\tau - kT)$, respectively, with the same values being, in another interpretation, infinite or undefined simultaneously, This shows that we are dealing with a contradiction here. Therefore, the argumentation presented above is absolutely not understandable to engineers.

The fact that the values of the waveform shown in Fig. 1a for time instants differing from kT are identically equal to zero is another drawback of the model with the Dirac deltas.

Obviously, the above is not true, as the values of the signal samples do not disappear at the outputs of ADCs outside the sampling instances. One may assume that they remain the same (constant) between the successive signal sampling instants.

3. Kronecker Functions in Modeling

The first drawback of the model with the Dirac deltas may be easily removed by simply describing the signal samples at the time sampling instants kT, as we observe (measure) them. Then, we get a model illustrated by the function shown $x_{K,T}(t)$ in Fig. 3. And we notice that we have a weighted comb of the so-called Kronecker functions (Kronecker deltas), weighted by the values of signal samples.

The definition of the Kronecker function is given by:

$$\delta_{k,\frac{t}{T}}(t) = \begin{cases} 1 & \text{if } k = \frac{t}{T} \\ 0 & \text{otherwise} \end{cases}, \tag{5}$$

where k is an integer, while t represents a real number.

The problem with the type of modeling presented in Fig. 3 is the following. The signal shown in this figure does not have a spectrum (understood as its Fourier transform) when Riemann integrals are used in its definition, or is equal to zero when Lebesgue integrals are used.

The remedy in this case may be to adopt a common-sense definition of the spectrum by choosing some relation to the Fourier transform of the related signal, provided that the latter exists, of course.

Additionally, when looking at Fig. 1a and Fig. 3a, it is also worth noting that they are similar. This does not mean, however, that they are the same. Both represent "modulated" combs. In the first case, it is a Dirac comb, while in the other, a Kronecker comb; the latter is visualized in Fig. 4 and

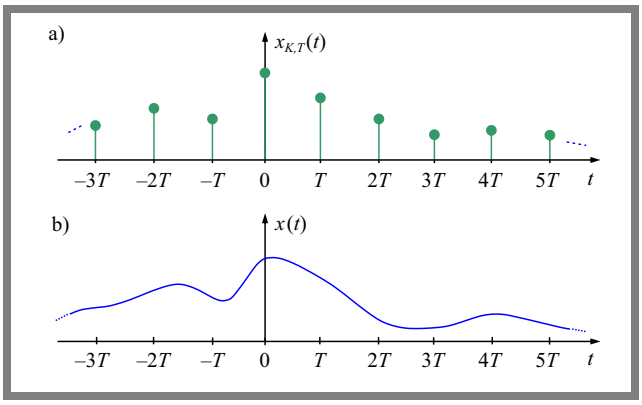

Fig. 3. Example sampled signal a) in form of a series of signal samples occurring uniformly along the continuous time axis, at intervals T, and its un-sampled version b) [14].

denoted as $\delta_{K,T}(t)$. Note that the difference between both scenarios consists in the fact that the former has infinite values at the sampling instants, whereas the latter has finite ones. These finite values equal ones.

Now, returning to the previous statement and proposition (given immediately before Fig. 3), one may say that the relation mentioned there can be (theoretically) of any variety. So, in this case, we are dealing with an ambiguity of the proposed method. Therefore, it cannot be accepted.

By the way, one should note that this is exactly the method used to define the spectrum of a signal at the output of an ADC by using a closely related signal that exploits the Dirac deltas (Fig. 1) in its description, for which there exists a Fourier transform (as mathematicians prove in a distributional sense). It is the signal that is "closely" related with the one shown in Fig. 3a.

In other words, in this spectrum calculation procedure, we take the signal shown in Fig. 1a instead of the one presented in Fig. 3a. For the reason described above, i.e. due to the lack of success in applying the above approach, it was necessary to continue the search for a proper description of the sampled signal, i.e. of the signal occurring at the ADC output. Such a search was undertaken by the author. The results of these efforts are described in the following sections.

4. Proper Description Based on Analyzing the Non-ideal Sampling Process

The most relevant proposals concerning the modeling of non-ideal behavior of the process of sampling an analog

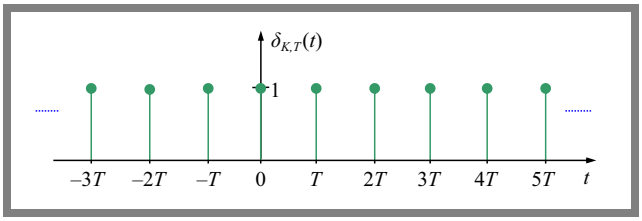

Fig. 4. Visualization of the Kronecker comb – the series (sum) of Kronecker functions, also known as Kronecker deltas, forms the Kronecker comb [14].

signal using ADC are described (among others) in [15]. They consider two non-idealities of the sampling process, namely: the fact that the signal sampling time τ in ADC is finite (1) and the samples obtained are blurred (smeared) (2).

The author of this paper has taken a closer look at the non-idealities mentioned above to check their potential applicability in obtaining such a description of the sampled signal which makes it possible to correctly calculate the spectrum of the actual signal occurring at the ADC output. Detailed results of this search were presented in [14] and [16]. Here, only the resulting conclusions are mentioned.

The inconveniences of modeling a sampled signal using the above-mentioned non-idealities are most apparent when the ideal case is considered. Thus, in the first case, the spectrum of this signal is directly proportional to the sampling time τ. So, when τ moves towards zero, the spectrum also moves towards zero, and for the value of $\tau = 0$, it is equal to zero. Therefore, only one conclusion may be drawn from this fact: this kind of modeling diverges from reality and should be considered useless.

In the case of the other non-ideality mentioned above, its idealization means that the blurring effect of the signal samples is getting smaller and smaller, or that the effective blurring time of the signal samples decreases to zero. Consequently, the blurred signal samples become more and more similar to weighted Dirac impulses. That is, here, in the limiting case, it turns out that we are modeling a signal sampled with a weighted Dirac comb – an approach that was criticized previously.

It is possible to combine both of the non-idealities listed above, i.e. to approach cases 1 and 2 together, assuming that they occur at the same time. This was done in [16] and a rather unexpected result was obtained, according to which this modeling method leads to a description of the sampled signal in the form of a weighted Kronecker comb. This outcome is unsatisfactory as well, due to the reasons given in Section 4.

5. Description of ADC Output Waveforms via Step Functions

A brief analysis of the proposals concerning the modeling the sampled signal, applied in the calculation of the spectrum of the ADC output signal, as presented in Section 4, leads to the conclusion that such a method also does not yield positive results. A closer look reveals that this is due to the fact that in these models, during the periods between taking the sample values, all other signal values are zero (in the ideal variant of a given model), mostly zero or close to zero (in the non-ideal variant of a given model).

It seems to us that in order to provide a correct answer to the problem discussed in this paper, the best way is to refer, in the first instance, to the reality of the sampling process as it is implemented in an A/D converter. This is illustrated schematically in Figs. 5 and 6 which allow us to understand the operation of the converter and the time waveforms, as functions of a continuous time t, that it generates at its output. One can assume that these time waveforms have the form of a slightly disturbed step function presented in Fig. 7. In Fig. 7, $[x_{s,H}(-3T)]_Q$ and $[x_{s,H}(T)]_Q$, where the lower index Q means the amplitude quantization operation, illustrate the quantized values of the sampled signal $x_s(t)$. These values are assigned to the following instants: $-3T$ and T, respectively. Moreover, parameter τ can be identified with the sum of the track part and the beginning of the hold part of an actual output signal at the output of ADC, at the time at which the sampling of a signal takes place [4], [17].

The shape of actual waveforms at the outputs of A/D converters is richer than the step function shown in Fig. 7 and depends upon the architecture and technology a given A/D converter relies upon. This shape is characterized by such parameters as: settling time, acquisition time, aperture, aperture jitter, hold mode settling time, hold mode feedthrough, droop [4]. The values of those parameters may be relevant in signal processing specific applications [19]–[21].

In view of the above, one may say that the problem can be formulated as: how to best model physical reality. And according to this, do the following:

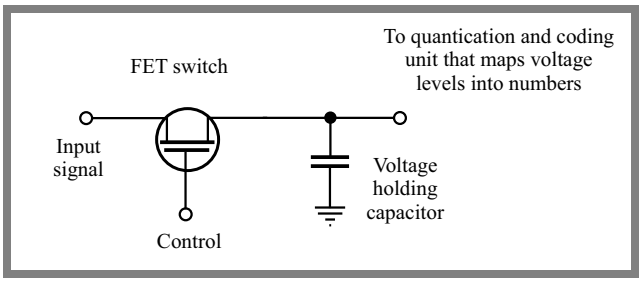

Fig. 5. Illustration of the basic idea behind analog-to-digital conversion with the use of a FET transistor switch connected to a capacitor holding the value of an analog input signal taken at the time of switching [18].

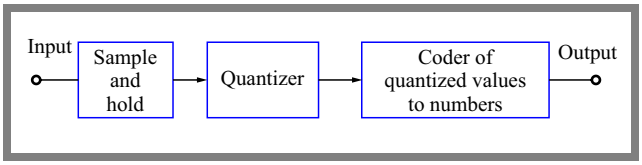

Fig. 6. Block diagram of an A/D converter consisting of three blocks: a sample and hold unit, an amplitude quantization stage, and a mapper (coder) of quantized values to numbers [4].

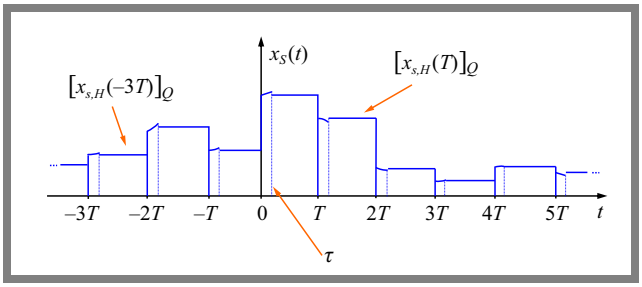

Fig. 7. Time waveform of an example sampled signal $x_s(t)$, related with an un-sampled one $x(t)$ (not shown).

– perform the signal averaging operation on a part of or the entire signal between the successive signal samples, to get a clearer picture,
– treat the difference between the sample value and the averaged value as a constant error over a given sampling period,
– treat, for each time instant, the difference between the value of the output signal of an A/D converter and the sum of the constant error mentioned above and the averaged value as a value of an error (we may refer to it as overall noise) for that time instant in the period between the successive sampling instants,
– realize that the value of the signal sample remains, throughout the entire period, between the successive sampling times, with the overall noise changing around this value.

Note that the application of the above procedure leads to the following analytical description of the time waveform at the ADC output:

$$x_g(t) = x_g(kT) \quad \text{for} \quad kT \leqslant t < (k+1)T \text{ and } k = \left\lfloor \frac{t}{T} \right\rfloor, \quad (6)$$

where the lower index g in $x_g(t)$ stands for "general" as well as for "generic".

In Eq. (6), $x_g(t)$ means $x(kT) + \mathrm{bias}(kT)$ for the subsequent periods. This formula is general in nature because it correctly describes, in a completely general manner, the time waveforms at the output of A/D converters. It is also generic, because it is "ready" – see the $\mathrm{bias}(kT)$ component mentioned above – to take into account different forms of the error function, which will obviously depend upon the architecture and technology used in the implementation of a given ADC [4], [19]–[21]. Interestingly, it may also depend upon the sampling frequency [19]. Furthermore, when assuming that the bias is identically equal to zero, then, obviously, $x_g(kT) \equiv x(kT)$. Note also that this parameter, referred to as bias, is constant in a given time period between the successive sampling instants, but not necessarily in all of these periods.

6. Measurement-based Validation of the Model

The fact that the waveforms at outputs of A/D converters may be considered weighted step functions, i.e. being good approximations of their real-world counterparts, has been noted in various research papers. Here, we place an emphasis on several of them, namely to [18] and [22]–[26].

For the purpose of this paper, in order to demonstrate the validity of the model presented in Section 5 and description of the waveforms at the output of A/D converters, a series of measurements was performed.

The measurements were carried out using the TMS320C5515 eZdsp 16-bit DSP runtime platform, i.e. a development tool for the TMS320C5515 DSP equipped with the AIC3204 codec, containing two 16-bit ADCs. In the course of the measurement campaign, one of the available ADCs was used.

The planned experiments performed with the use of the TMS320C5515 eZdsp development tool were subject to several limitations. Firstly, the number of quantization steps could not be lowered to better illustrate the step-like nature of the waveforms from initial resolution, i.e. 65536 quantization steps. Secondly, the sampling frequency could not be arbitrarily set. Thirdly, it was not possible to connect an oscilloscope to the ADC output in the AIC3204 codec.

With such shortcomings affecting the sampling frequency, the highest value offered in TMS320C5515 eZdsp, i.e. 192 kHz was selected to ensure a sufficiently high resolution on the time axis of the waveform diagrams. Further, signals with very small amplitudes were sampled to ensure transparency and visibility of details on the ordinate axis, i.e. with the changing amplitude of the waveform. Therefore, the amplitude of a signal "passed" through a low number of quantization steps only, at the expense of exposing this signal to a high level of noise, close to the values of its changing amplitude. Finally, as for the oscilloscope, we used a virtual programmable block that can be designed using the TMS320C5515 eZdsp software.

In Figs. 8–9, two series of example signal waveforms at the output of the A/D converter are presented, as recorded for two sinusoidal signals sample: the first with the frequency of 2 kHz and the other with the frequency of 5 kHz.

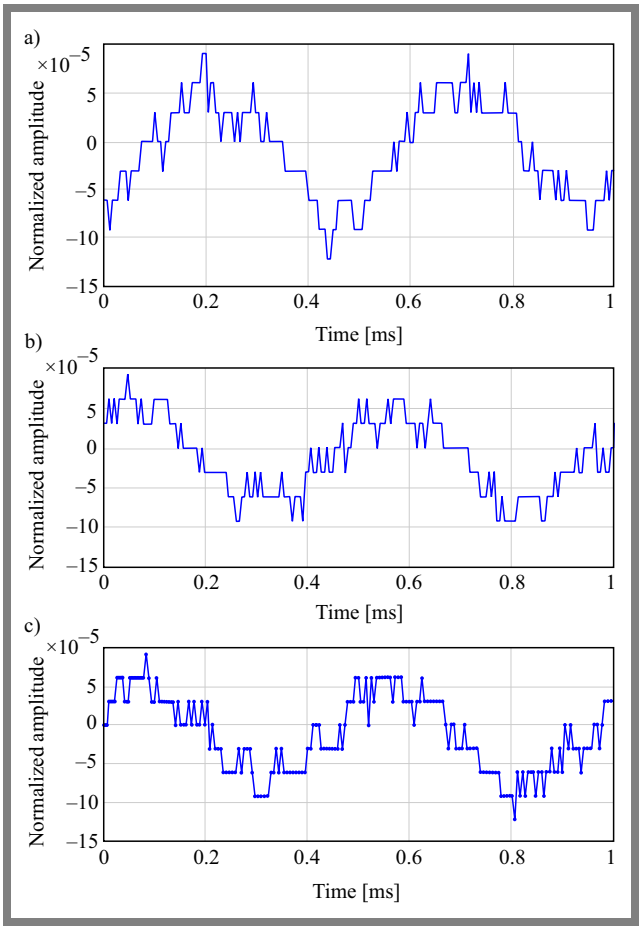

Fig. 8. Waveform recorded for a 2 kHz sinusoidal signal: a) first, b) second, and c) third one, where signal samples are marked by dots.

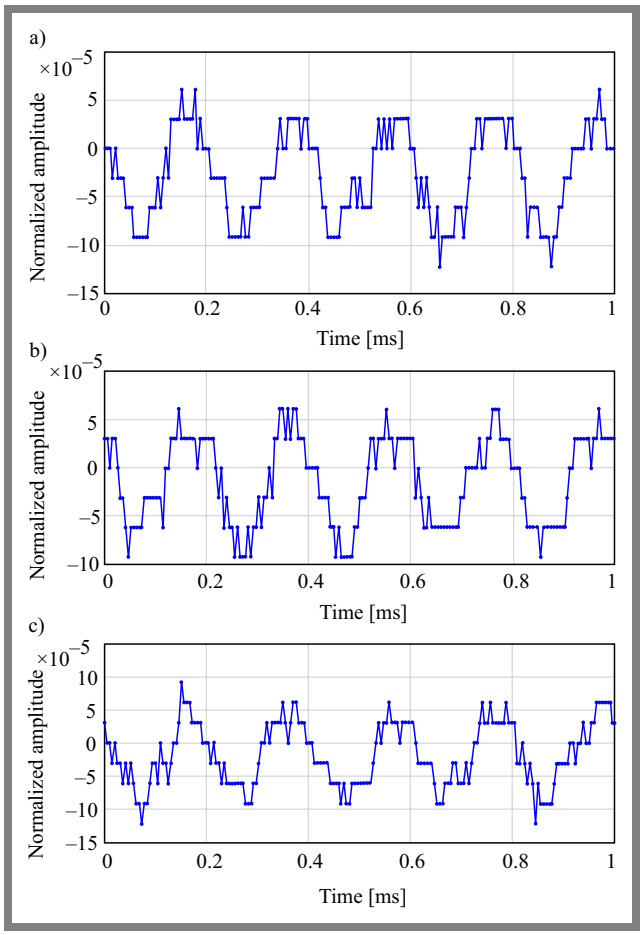

Fig. 9. Recorded waveform for a 5 kHz sinusoidal signal with sample values denoted by dots: a) first, b) second, and c) third instance.

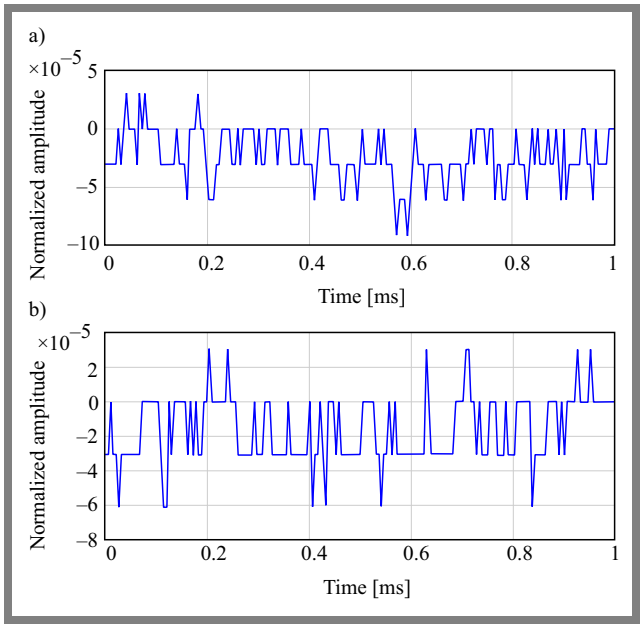

Fig. 10. Example of a noise waveform recorded using the oscilloscope: a) first and b) second instance.

Figures 8–9 show normalized amplitude values presented as quantized levels. Quantization mapping was performed using the Q1.15 format. So, in this case, the range that can be covered extends from –1 to 0.99997, with a resolution of 2^{-15}=0.0000305.

Figures 8–9 show also a non-ideal operation of the virtual oscilloscope used. Its time resolution equals $(192000)^{-1}$ s $\simeq$ 5.2 ns. Therefore, the signal amplitude values for adjacent (i.e. closest to each other) time instants following from this resolution are connected by a straight line. The sloping segments of straight lines, clearly visible at numerous locations, make it difficult to interpret the presented waveforms.

The waveforms presented in Figs. 8–9 show a significant influence of noise that is added to the useful signal and changes the output code of the ADC converter. Figure 10 allows to assess the noise level presenting on ADC output for two examples of a zero-valued signal at the input. One may notice that the level is high and its value is equal to four quantization steps. This is a large value compared to the value of the same measure for the sampled useful signal, which was eight quantization steps (see Figs. 8–9). Such a noise cannot be eliminated by subtraction from the useful signal, because the noise is random and the useful signal is deterministic. The second remark concerns the way in which Figs. 8–9 as well as Fig. 10 illustrate the transition between the quantization levels, using an inclined straight-line segment. It may not be very transparent, but it is not so difficult to imagine that at these locations significant up or down shifts occur for the neighboring time instants.

One may conclude that due to the curves observed in these figures (leaving aside the influence of noise), we are dealing with sinusoidal waveforms in which step functions (with their change values being lower than the amplitudes of the sinusoids themselves) are inscribed. This means that the model description of the sampled signal presented in the previous section and illustrated in Fig. 7 is correct and that its validity has been demonstrated by measurements.

7. Calculation of the Sampled Signal Spectrum

Calculation of the Fourier transform of function $x_g(t)$, i.e. its spectrum which is a step function, does not present any problems, as it is a function for which the Fourier transform (understood in a classical form) exists. In the following calculations, we present the main steps of the process.

Let us start with a basic formula:

$$X_g(f) = \mathcal{F}\big(x_g(t)\big) = \int_{-\infty}^{\infty} x_g(t)\, e^{-j2\pi ft} dt = \\ = \ldots + \int_{-T}^{0} x_g(-T)\, e^{-j2\pi ft} dt + \int_{0}^{T} x_g(0) \qquad (7) \\ \times e^{-j2\pi ft} dt + \int_{T}^{2T} x_g(T)\, e^{-j2\pi ft} dt + \ldots$$

Then, calculation of the integrals in Eq. (7) leads to:

$$\begin{aligned} X_g(f) &= \ldots + \frac{x_g(-T)}{-j2\pi f}\, e^{-j2\pi ft}\,\Big|_{-T}^{0} \\ &+ \frac{x_g(0T)}{-j2\pi f}\, e^{-j2\pi ft}\,\Big|_{0}^{T} + \frac{x_g(T)}{-j2\pi f} \\ &\times\ e^{-j2\pi ft}\,\Big|_{T}^{2T} + \ldots = \frac{j}{2\pi f}\Big\{ \ldots - x_g(-T)\, e^{j2\pi fT} \\ &+\ x_g(-T)\, e^{-j2\pi f(0T)} - x_g(0T)\, e^{-j2\pi f(0T)} \\ &+\ x_g(0T)\, e^{-j2\pi fT} - x_g(T)\, e^{-j2\pi fT} + x_g(T) \\ &\times\ e^{-j2\pi f(2T)} + \ldots \Big\} = \frac{j}{2\pi f}\Big\{ \ldots + \big[x_g(-2T) - x_g(-T)\big] \\ &\times\ e^{j2\pi fT} + \big[x_g(-T) - x_g(0T)\big]\, e^{j2\pi f(0T)} \\ &+\ \big[x_g(0T) - x_g(T)\big]\, e^{-j2\pi fT} + \big[x_g(T) - x_g(2T)\big] \\ &\times\ e^{-j2\pi f(2T)} + \ldots \Big\}\,. \end{aligned} \tag{8}$$

With the use of the definition of DTFT, Eq. (8) can be rewritten as:

$$X_g(f) = \frac{1}{j2\pi f}\Big\{\mathrm{DTFT}\big(x_g(kT)\big) - \mathrm{DTFT}\big(x_g((k-1)T)\big)\Big\} \tag{9}$$

Moreover, we can write:

$$\begin{aligned} \mathrm{DTFT}\big(x_g((k-1)T)\big) &= \sum_{k=-\infty}^{\infty} x_g\big((k-1)T\big) \\ &\times\ e^{-j2\pi fkT} = \sum_{k'=-\infty}^{\infty} x_g(k'T) \\ &\times\ e^{-j2\pi f(k'+1)T} = e^{-j2\pi fT} \\ &\times \sum_{k'=-\infty}^{\infty} x_g(k'T) e^{-j2\pi fk'T} \\ &= \mathrm{DTFT}\big((x_g(kT)\big) e^{-j2\pi fT}. \end{aligned} \tag{10}$$

Further, introducing Eq. (10) into Eq. (9) we get:

$$\begin{aligned} X_g(f) &= \frac{\mathrm{DTFT}\big(x_g(kT)\big)}{j2\pi f}\,(1 - e^{-j2\pi fT}) \\ &= T\cdot \mathrm{DTFT}\big(x_g(kT)\big)\,\frac{e^{j\pi fT} - e^{-j\pi fT}}{j2\pi fT\, e^{j\pi fT}} \\ &= T\cdot \mathrm{DTFT}\big(x_g(kT)\big)\, e^{-j\pi fT}\,\frac{\sin(\pi fT)}{\pi fT} \\ &= T\cdot \mathrm{DTFT}\big(x_g(kT)\big)\ \mathrm{sinc}(\pi fT)\ e^{-j\pi fT}. \end{aligned} \tag{11}$$

The final form may be determined as:

$$X_g(f) = T\cdot \mathrm{DTFT}\big(x_g(kT)\big)\ \mathrm{sinc}(\pi fT)\ e^{-j\pi fT}. \tag{12}$$

Let us consider a special case $\frac{f}{f_s} \ll 1 \rightarrow f \ll f_s$, where $f_s = \frac{1}{T}$. We can then simplify the expression given by Eq. (12) to:

$$X_g(f) \cong T\cdot \mathrm{DTFT}\big(x_g(kT)\big)\ . \tag{13}$$

For $f \gg f_s$, we can write:

$$X_g(f) \cong 0\ . \tag{14}$$

For the frequencies lying between the ranges mentioned above, the full formula given by Eq. (12) must be used.

Note that the above means a low-pass filtering character of the influence of the function $\mathrm{sinc}(\pi fT)$ in changing DTFT to arrive at $X_g(f)$. Finally, we shall draw the reader's attention to another interesting relationship. It is well known that a relationship exists between the DTFT of a discrete time signal and the spectrum of its un-sampled version, say $X(f)$. It has the following form:

$$\mathrm{DTFT} = \frac{1}{T}\sum_{k=-\infty}^{\infty} X(f - kf_s)\ . \tag{15}$$

Using this expression in Eq. (12), we get:

$$X_g(f) = \mathrm{sinc}(\pi fT)\ e^{-j\pi fT} \times \sum_{k=-\infty}^{\infty} X(f - kf_s)\ . \tag{16}$$

In view of the results achieved in this paper, formula (16), rather than the one given in Eq. (15), should be used in any analyses of the aliasing effects in the frequency domain.

8. Conclusions and Remarks

It has been shown in this paper that the description of the signals at the outputs of A/D converters, using the weighted Dirac combs, suffers from two severe drawbacks. The most satisfactory description relies on modeling A/D behavior that fully complies with the realities of the physical sampling process. It uses step functions instead of Dirac deltas.

Finally, a modified formula for calculation of the spectrum of a signal at the output of an A/D converter has been derived, in follow up to [27], better describing the spectrum of the A/D converter output signal through the spectrum of the un-sampled waveform and its aliases.

Acknowledgment

The author of this paper would like to thank his colleague, Andrzej Łuksza, Ph.D. for performing the measurements presented in this paper and for agreeing to their publication.

References

[1] A. Borys, "Some Topological Aspects of Sampling Theorem and Reconstruction Formula", *International Journal of Electronics and Telecommunications*, vol. 66, no. 2, pp. 301–307, 2020 (https://doi.org/10.24425/ijet.2020.131878).

[2] A. Borys, "Measuring Process via Sampling of Signals, and Functions with Attributes", *International Journal of Electronics and Telecommunications*, vol. 66, no. 2, pp. 309–314, 2020 (https://doi.org/10.24425/ijet.2020.131879).

[3] A. Borys, "Further Discussion on Modeling of Measuring Process via Sampling of Signals", *International Journal of Electronics and Telecommunications*, vol. 66, no. 3, pp. 507–513, 2020 (https://doi.org/10.24425/ijet.2020.134006).

[4] R. van de Plassche, *Integrated Analog-To-Digital and Digital-To-Analog Converters,* Berlin: Springer Verlag, 501 p., 1994 (https://doi.org/10.1007/978-1-4615-2748-0).

[5] MIT, OpenCourseWare, "Signal Processing – Continuous and Discrete", [Online]. Available: https://ocw.mit.edu/courses/2-161-signal-processing-continuous-and-discrete-fall-2008/pages/readings/.

[6] J.H. McClellan, R. Schafer, and M. Yoder, *DSP First*, London: Pearson, 2015 (ISBN: 9780136019251).

[7] V.K. Ingle and J.G. Proakis, *Digital Signal Processing Using Matlab*, 3rd ed., Stamford: Cengage Learning, 672 p., 2011 (ISBN: 9781111427375).

[8] R.J. Marks II, *Introduction to Shannon Sampling and Interpolation Theory*, New York: Springer-Verlag, 324 p., 1991 (https://doi.org/10.1007/978-1-4613-9708-3).

[9] R.N. Bracewell, *The Fourier Transform and Its Applications*, 3rd ed., New York: McGraw-Hill, 640 p., 2000 (ISBN: 9780073039381).

[10] R. Brigola, *Fourier-Analysis und Distributionen*: *Eine Einführung mit Anwendungen,* Hamburg: Tredition, 448 p., 2013 (ISBN: 9783847287421) (in German).

[11] A. Borys, "Spectrum Aliasing does not Occur in Case of Ideal Signal Sampling", *International Journal of Electronics and Telecommunications*, vol. 67, no. 1, pp. 71–77, 2021 (https://doi.org/10.24425/ijet.2021.135946).

[12] S.C. Gupta, "Delta Function", *IEEE Transactions on Education*, vol. 7, no. 1, pp. 16–22, 1964 (https://doi.org/10.1109/TE.1964.4321835).

[13] R.F. Hoskins, *Delta Functions: An Introduction to Generalized Functions*, Oxford: Woodhead Publishing, 280 p., 2010 (ISBN: 9781904275398).

[14] A. Borys, "Spectrum Aliasing does Occur only in Case of Non-ideal Signal Sampling", *International Journal of Electronics and Telecommunications*, vol. 67, no. 1, pp. 79–85, 2021 (https://doi.org/10.24425/ijet.2021.135947).

[15] A. Dąbrowski, "Fundamentals of Systems, Signals and Information Theory: Sampling of Signals", Department of Control and Systems Engineering, Technical University of Poznań, Poland, 2008.

[16] A. Borys, "An Unexpected Result on Modelling the Behavior of A/D Converters and the Signals They Produce", *International Journal of Electronics and Telecommunications*, vol. 69, no. 1, pp. 193–198, 2023 (https://doi.org/10.24425/ijet.2023.144350).

[17] A. Borys, "Sampled Signal Description That is Used in Calculation of Spectrum of This Signal Needs Revision", *International Journal of Electronics and Telecommunications*, vol. 69, no. 2, pp. 319–324, 2023 (https://doi.org/10.24425/ijet.2023.144367).

[18] P. Prandoni and M. Vetterli, *Signal Processing for Communications*, Lausanne: EPFL Press, 371 p., 2008 (ISBN: 9781420070460).

[19] N. Ma *et al.*, "Influence of Sampling Frequency on Magneto-optical Imaging under Alternating Magnetic Field Excitation", *IEEE Sensors Journal*, vol. 19, no. 23, pp. 11591–11600, 2019 (https://doi.org/10.1109/JSEN.2019.2937629).

[20] K. Sozański, *Digital Signal Processing in Power Electronics Control Circuits*, London: Springer-Verlag, 285 p., 2013 (ISBN: 9781447152668).

[21] T.S. Low and C. Bi, "Design of A/D Converters with Hierarchic Networks", *IEEE Transactions on Industrial Electronics*, vol. 43, no. 1, pp. 184–191, 1996 (https://doi.org/10.1109/41.481424).

[22] MathWorks, "Switched Capacitor Analog to Digital Converter", [Online]. Available: https://www.mathworks.com/help/sps/ug/switched-capacitor-analog-to-digital-converter.html.

[23] A. Mertins, *Signaltheorie: Grundlagen der Signalbeschreibung, Filterbänke, Wavelets, Zeit-Frequenz-Analyse, Parameter- und Signalschätzung*. Berlin: Springer Verlag, 461 p., 2020 (https://doi.org/10.1007/978-3-658-29648-3) (in German).

[24] U. Zölzer, *Digital Audio Signal Processing*, Chichester: Wiley & Sons, 340 p., 2008 (ISBN: 9780470997857).

[25] C. Marven and G. Ewers, *A Simple Approach to Digital Signal Processing*, Hoboken: Wiley-Interscience, 236 p., 1996 (ISBN: 9780471152439).

[26] SlideServe, "Analog/Digital Conversion", [Online]. Available: https://www.slideserve.com/papaj/analog-digital-conversion-powerpoint-ppt-presentation.

[27] A. Borys, "A New Result on Description of the Spectrum of a Sampled Signal", *International Journal on Marine Navigation and Safety of Sea Transportation*, vol. 18, no. 2, 2024 (https://doi.org/10.12716/1001.18.02.17).

Andrzej Borys, Ph.D.
Faculty of Electrical Engineering
https://orcid.org/0000-0003-1316-4031
E-mail: a.borys@we.umg.edu.pl
Gdynia Maritime University, Gdynia, Poland
https://umg.edu.pl/en/

Non-uniformly Spaced Antenna Arrays with Overlapped Elements Constraint

Noor Mohammed Qassim and Jafar Ramadhan Mohammed

Ninevah University, Mosul, Iraq

https://doi.org/10.26636/jtit.2024.4.1740

Abstract — In the literature, inter-element spacing antenna design methods have been widely discussed and presented as an alternative approach to element excitation amplitude and/or phase control methods that may be relied upon to achieve the required array pattern shapes. However, methods associated with non-uniformly distributed elements suffer from the element overlap problem, where some of the optimized element locations may overlap each other and cause changes in the overall array aperture length. Practically, these element overlaps cannot be implemented, due to the physical antenna element size, without omitting some of them. Consequently, the overall performance of the antenna array is degraded. Further, degradation may occur when considering phased arrays with scanned main beams. In this paper, we first illustrate the effect of the problem of overlapped element locations and then we propose two approaches based on the genetic algorithm to optimize non-uniformly spaced arrays with overlapped element locations, while simultaneously preserving the array's directivity. To solve the problem of overlapping and to determine the physical array element size, the minimum element-spacing constraints are incorporated in a simple way in the proposed approaches. Thus, the time required to perform optimization-related computations is greatly reduced. Simulation results confirm the effectiveness of the two proposed solutions, where the probability of the elements overlapping has been reduced to zero under specific conditions related to the locations of the some of the elements, while the peak sidelobe levels were always kept below –15 dB and directivity was maintained, to the extent possible, at the level of that of standard uniformly spaced arrays.

Keywords — element location overlaps, non-uniformly spaced arrays, phased antenna arrays, sidelobe level minimization

1. Introduction

In the process of synthesizing an antenna array, several design variables which can be efficiently controlled to achieve the desired beam pattern shapes offering low sidelobe level, limited beam width and good directivity need to be taken into consideration. These include the separation distances between the array's elements (or absolute element locations), amplitude weighting and/or phase weighting of the array element excitation vector. The amplitude and/or phase weighting-based design methods with uniformly spaced elements (i.e. fixed element locations) are referred to as electronic approaches, with the array patterns being reshaped electronically, and the element locations remaining fixed and uniform. The unequally spaced array methods are referred to as mechanical approaches, as the array patterns are mechanically reshaped by changing the locations of the specific elements. In the case of automated scanning beam arrays, both mechanical and electronic approaches require controllable phase shifters to achieve wide-angle beam scanning. These phase shifters are separate and independent from those used for element excitation phase weighting control [1].

From the point of view of implementing the designs, the feeding network of the electronic approaches requires fine adjustment of the attenuators/amplifiers used for amplitude excitation weighting. Additionally, accurate phase shifters are required for phase excitation weighting of the array's elements, to reshape the array's pattern in accordance with the requirements [2]. Any errors or deviations from those fine values will cause significant and unavoidable changes in the radiation pattern [3], [4]. Therefore, these electronic approaches are very sensitive, relatively costly and require that advanced RF components be used.

On the other hand, mechanical approaches with uniform amplitude excitation weighting have been widely used due to the need for a simple feeding divider network which can be implemented without any attenuators or amplifiers. Therefore, no sensitivity-related errors can be made [5]. These advantages have recently motivated many researchers from around the world to fully explore the benefits of these types of arrays [6]–[10].

Further, non-uniformly spaced arrays are expected to be more popular in current and future wireless communication systems due to their great array pattern reshaping capability. In order to meet some desirable requirements, several user-defined constraints may be introduced concerning either the array's geometry itself (the number of elements and the spacing between them) its radiation pattern (minimum sidelobe level and limited beamwidth). These constraints mean that the synthesis of such arrays becomes a non-linear problem [11] requiring efficient optimization techniques. Thus, various evolution algorithms, such as the genetic algorithm (GA) [12], [13], differential evolution (DE) [14], particle swarm optimization (PSO) [15] and the whale optimization algorithm (WOA) [16] have been used to solve this non-linear problem.

Other solutions determine an optimal combination of feeding current and inter-element spacing to produce array patterns with the lowest sidelobe level, improved beamwidth, and maximum directivity [17]. Moreover, the thinning process produces non-uniform inter-element spacing and it has been exploited to minimize sidelobe levels [18], [19]. However,

thinned arrays need a very high number of combinations to examine all potential element locations. Thus, non-uniformly spaced arrays obtained with the use of the thinning process are very time consuming to produce [20]. Therefore, determination of inter-element spacing or element locations may provide greater control over the shape of the array's radiation pattern than thinning methods.

Recently, a T-shaped clustered array [21], a circular boundary array [22] and control over the position of selected elements [23] have been also relied upon for sidelobe reduction. Other methods use a redundancy elimination technique to synthesize large-scale planar isophoric sparse arrays in order to achieve low sidelobe levels. In this approach, the theoretical limits for the achievable minimum spacing and aperture are calculated to enable selective retention of non-redundant positional constraints only [24]. In [25], an alternating convex optimization was suggested to synthesize non-uniformly spaced arrays with minimum element spacing constraints.

In this paper, the problem of element location overlap, which is unavoidable when optimizing the absolute element locations using all non-uniformly spaced methods, is addressed. Then, two efficient solutions based on the bounding location limits are suggested to prevent this problem from occurring. Finally, a comprehensive and optimized method for designing non-uniformly spaced arrays with minimum element spacing constraints and improved response time is presented. This problem becomes more significant and may include all or most of the array element locations when imposing more user-defined constraints and steering the main beams towards direction other than the normal referenced direction. Thus, the process of designing such arrays in practice calls for increased attention.

Finally, it is worth mentioning that the problem of overlapping element locations in non-uniformly spaced arrays has not been fully discussed and addressed in the literature and continues remains a truly challenging issue that needs to be resolved.

2. Principles of the Proposed Method

2.1. Formulation of the Element Overlap Problem

Non-uniform spacing between the array's elements may be expressed in terms of inter-element spacing d_n or actual element location with respect to the center of the array x_n. The overall array pattern AP, which is a product of element pattern EP and array factor AF (being equal to inter-element spacing d_n) for N even and symmetrical radiating elements can be written as:

$$\begin{aligned} AP(u) &= EP(u) \times AF(u) \\ &= \sum_{n=1}^{\frac{N}{2}} a_n \cos\left[(n-0.5)k\, d_n(u-u_o)\right], \end{aligned} \tag{1}$$

where $u = \sin(\theta)$, θ is the elevation angle within the range of $0 \leqslant \theta \leqslant \pi$, $EP(u)$ is the element pattern which is equal to one for isotropic radiators, a_n is the complex (amplitude and phase) weighting of the n-th element in the array which is equal to $a_n = 1$ for unit-amplitude weighting, $k = \frac{2\pi}{\lambda}$, and u_o is the steering direction of the main beam.

Equation (1) can be rewritten – in terms of element locations x_n as follows:

$$AP(u) = \sum_{n=1}^{\frac{N}{2}} a_n \cos\left[k\, x_n(u-u_o)\right]. \tag{2}$$

To clearly explain the difference between Eqs. (1) and (2), it is important to determine the bounds concerning both minimum and maximum potential values of both d_n and x_n, as they need to be examined by the optimizer for inter-element spacing $d_n = \Delta(\frac{d}{\lambda})$, $0 \leqslant \Delta \leqslant 1$ and for x_n being $0 \leqslant x_n \leqslant L_{AA}$, where L_{AA} is the length of the array's aperture.

To minimize the peak sidelobe level in the region $FNBW \leqslant |u-u_o| \leqslant 1$ of the array pattern in Eq. (1) or Eq. (2), the following cost function can be used [12]:

$$\text{Cost} = 20\log_{10}\min\left(|AP(u-u_o)|\right), \tag{3}$$

where $FNBW$ is the first null beam width in the array pattern which defines the starting point of the sidelobe region.

Such a cost function minimizes the sidelobes by optimizing either the array element locations x_n or inter-element spacings d_n, according to Eqs. (1) and (2). In both cases, only these two sets of variables, i.e. d_n and x_n, are the design-related parameters that need to be optimized.

In order to keep the beam width and, consequently, the directivity of the optimized non-uniformly spaced array as close as possible to that of the standard uniformly spaced array, the overall array apertures of both of them should be kept the same. Thus, the following location bounds are imposed on the proposed non-uniformly spaced array:

$$\begin{aligned} \frac{d}{2} \leqslant x_n \leqslant L_{UAA} \text{ with } L_{UAA} = x\left(\frac{N}{2}\right), \\ n = 1, 2, \ldots, \frac{N}{2}, \end{aligned} \tag{4}$$

where L_{UAA} is the aperture length of the standard uniformly spaced array.

From this equation, it can be seen that the locations of the first and last elements on the right side of the array center were fixed at $x_1 = \frac{d}{2}$ and $x_{\frac{N}{2}} = L_{UAA}$. Locations of other elements in between can be optimized according to the cost function given in Eq. (3).

The locations of the in-between elements are random. Thus, there is a great chance that an element may be placed over another element or that they may located close to each other. Therefore, physical element size overlaps are unavoidable in these types of arrays.

To illustrate this problem, let us consider an array of $N = 40$ elements that are distributed symmetrically around the array's center. By fixing the location of the first element on each side of the array only, $\frac{N}{2} - 1$ element locations can be optimized according to Eq. (3). The number of controlled element locations is 19 on each side of the array, while the first element was fixed at the original uniformly spaced elements $x_1 = \frac{d}{2}$.

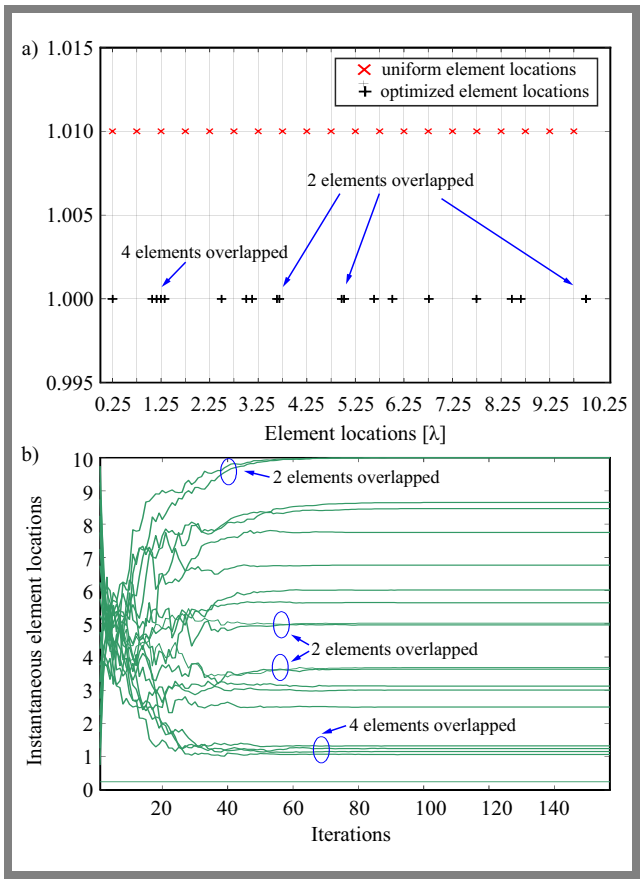

Fig. 1. Array element overlaps: a) element locations and b) instantaneous element locations.

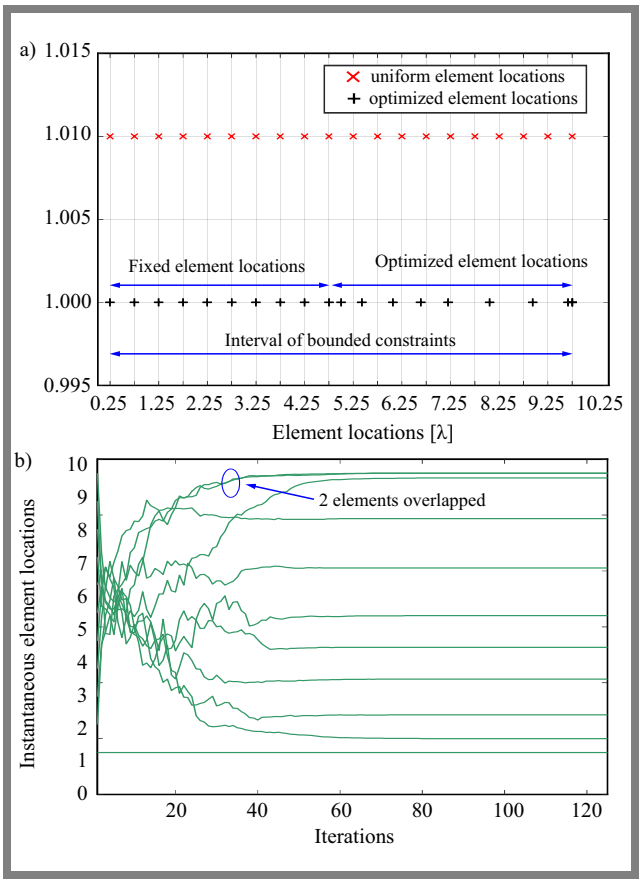

Fig. 2. Partially controlled element location approach: a) element locations and b) instantaneous element locations.

Further, we assumed that the steered direction of the main beam is $u_o = 0.6$ radians in u-space. Figure 1 shows the resultant element locations of the optimized array. The standard array geometry that uses uniformly spaced elements has been also shown for comparison. One may notice that the most of the resultant optimized element locations overlap. Therefore, such a design configuration without overlapped elements is practically impossible.

2.2. Proposed Solutions

In this section, we present two approaches to dealing with the problem of element location overlaps.

The first approach is based on controlling the locations of a number of outer elements instead of all element locations, as shown in Fig. 2. The locations of inner elements remain fixed and match the locations of the original uniformly spaced array elements. By optimizing the locations of outer elements only, we will reduce the probability of overlapping and will mitigate the array's implementation cost. The probability of overlapping is reduced, but the phenomenon cannot be prevented entirely.

This approach also offers a level of directivity that is higher than the one achieved when relying on fully optimized element locations. The only loss is a slight increase in the sidelobe level, when compared to that of the fully optimized element locations. This is mainly due to the lower number of degrees of freedom available.

The second approach is based on enforcing constraints on the location of each element, as shown in Fig. 3. This allows to completely prevent the overlapping of specific elements while simultaneously preserving the array's performance without sacrificing sidelobe level, due to the availability of all degrees of freedom. The applied bound constraints can be written as follows:

$$x_{uniform_n} - \Delta \leqslant x_n \leqslant x_{uniform_n} + \Delta, \; n = 1, 2, \ldots, \frac{N}{2}, \quad (5)$$

where $x_{uniform_n}$ is the location of the n-th element of the standard uniformly spaced array and Δ is the bound constraint for lower and upper intervals which can be specified by the user.

The design steps may be summarized as follows:

1) Define the initial parameters, such as array parameters, population size, and the variable number of element locations.
2) Set the goals or user-defined constraints related to array element locations that can be provided by the designer.
3) Set the optimization parameters, such as parents, mutation, crossover, and the maximum number of iterations. Calculate and sort the cost function values.
4) Perform genetic optimization which includes mirage process, choosing best siblings and mutations.
5) Perform best pattern calculation.

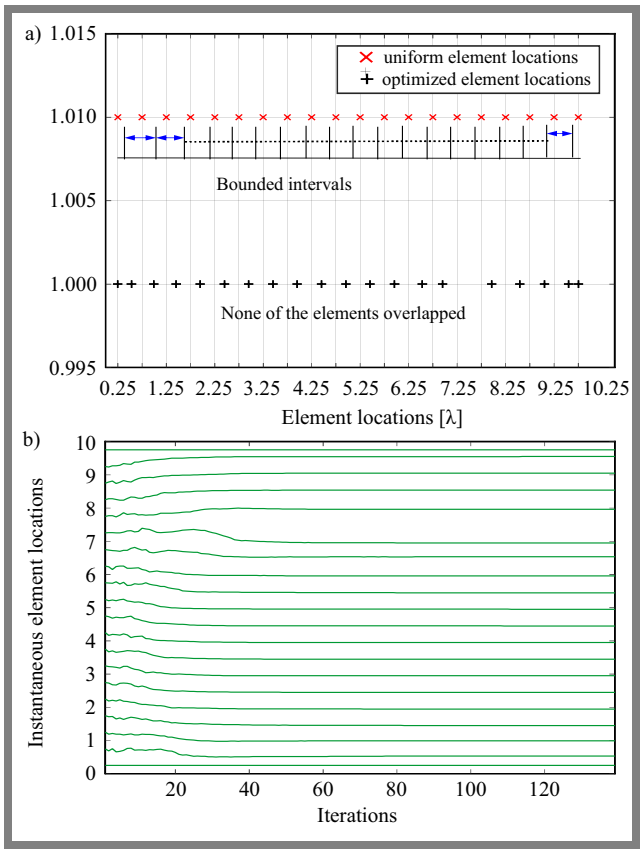

Fig. 3. The bound constraints approach: a) element locations and b) instantaneous element locations.

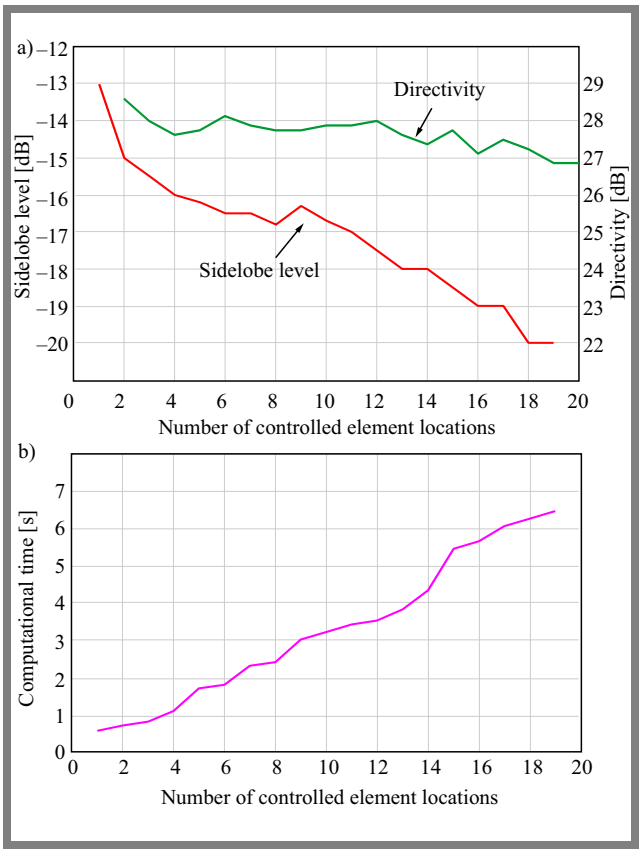

Fig. 4. SLL variation versus number of controlled element locations and directivity variation for unscanned main beam $u_o = 0^\circ$ a) and computational time b).

3. Simulation Results

In all of the considered scenarios, a symmetric phased array of $N = 40$ radiating elements with either fully or partially non-uniformly spaced elements was examined. For the genetic optimization algorithm used, the size of the population is set to 100. The remaining parameters were chosen in the following manner: uniform crossover, selection was tournament, and the mutation rate was 0.2. Finally, the mating pool was chosen to be 4. The main beam has been steered to remain within the range of the elevation plane between $-0.5 \leqslant u_o \leqslant 0.5$.

In the first example, performance in terms of sidelobe level (SLL), directivity (D), and the computational time of the proposed non-uniformly spaced array was studied for various controlling element locations. Figure 4 illustrates SLL and D variations, as well as the required computational time.

Generally, one may notice from these two figures that SLL reduction improves as the number of controlled element locations increases, while the D parameter is slightly degraded and the computational time becomes longer when increasing the number of the controlled element locations.

In the second example, SLL variations with the scan angle of the main beam are illustrated in Fig. 5. Here, three instances of non-uniformly spaced arrays were considered and compared. In the first instance, full control is exercised over all element locations (i.e. all element locations are optimized), while in the second and third instances, half or quarter of element locations are controller, respectively. The main beam has been steered in a range of $-0.5 \leqslant u_o \leqslant 0.5$ in the u-space. Directivity was evaluated using the same procedure.

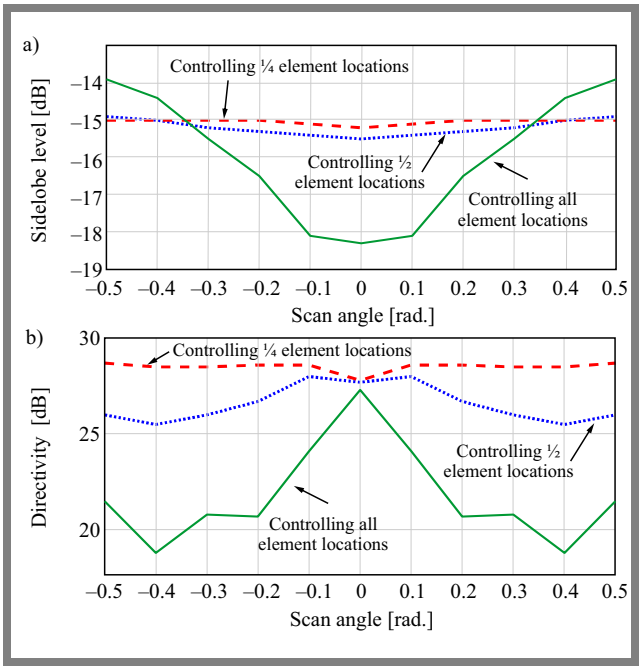

Fig. 5. SLL variation versus scan angle a) and directivity variation for three element location control instances b).

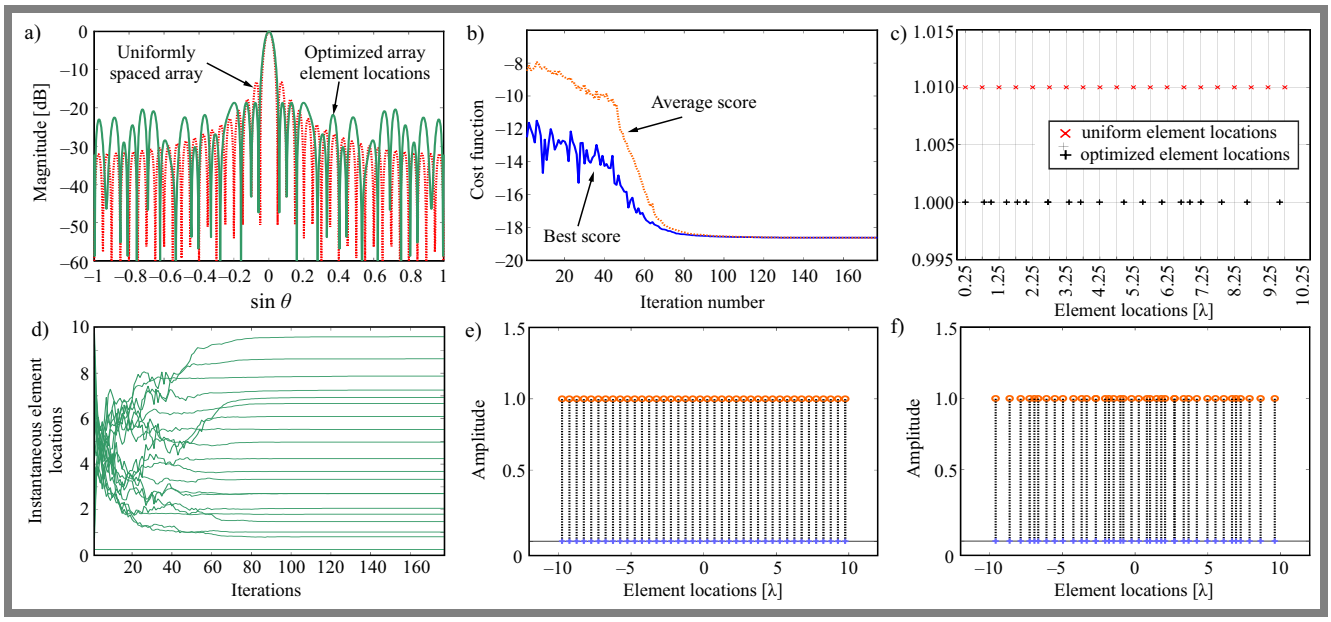

Fig. 6. Results of controlling all element locations: a) radiation patterns, b) cost function variations, c) element locations, d) their instantaneous variations, and e–f) element amplitude weights.

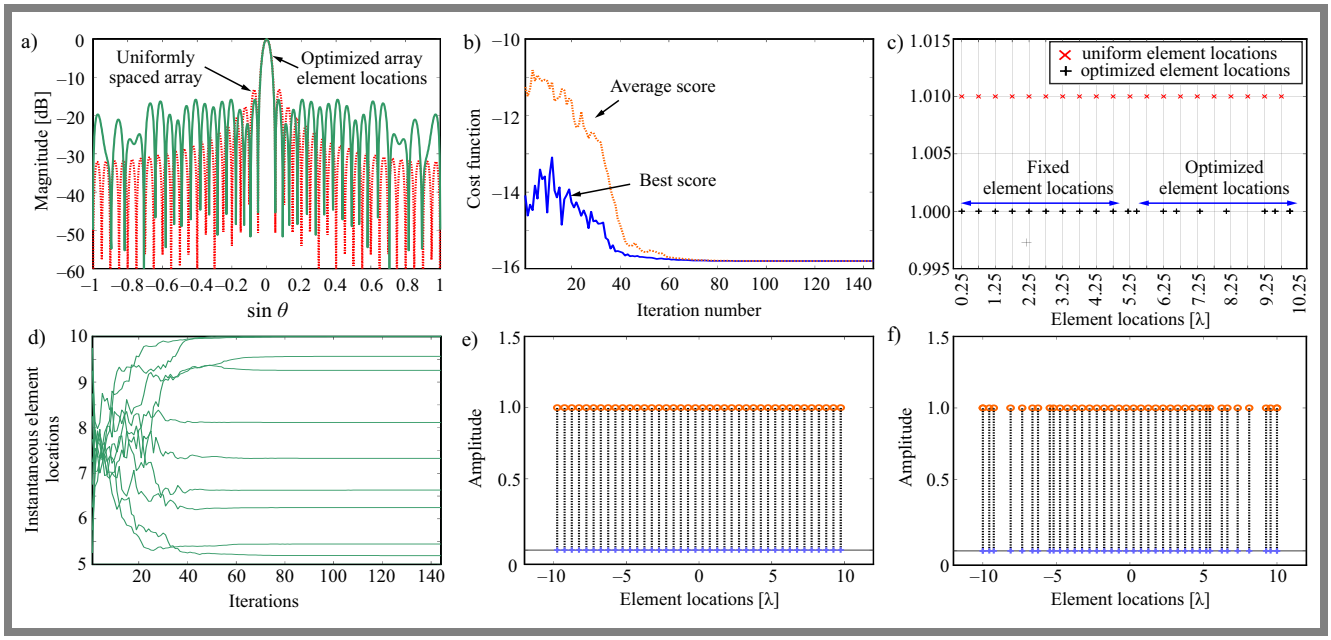

Fig. 7. Results of controlling half element locations: a) radiation patterns, b) cost function variations, c) element locations, d) their instantaneous variations, and e–f) element amplitude weights.

Further, the results of these three instances in which all, half, and a quarter of the element locations are controlled are shown in Figs. 6–8, respectively.

Directivity D, SLL, and computational time T of these three instances were $D = 27.2$ dB, $SLL = -18.6$ dB, $T = 7.875$ s, $D = 27.3$ dB, $SLL = -15.5$ dB, $T = 5.471$ s, $D = 28.0$ dB, $SLL = -15.2$ dB, $T = 2.27$ s, respectively.

The optimized element locations for these three instances were:

- x_{fully}={0.2500 0.8084 1.0179 1.4764 1.8005 2.0588 2.7005 2.7088 3.3348 3.6790 4.2418 4.9666 5.5234 6.0957 6.6634 6.9290 7.2540 7.8689 8.6270 9.5963},
- x_{half}={0.2500 0.7500 1.2500 1.7500 2.2500 2.7500 3.2500 3.7500 4.2500 4.7500 5.0000 5.4614 5.9897 6.5948 7.2056 7.9667 8.9249 9.75 9.750 9.75},
- $x_{quarter}$={0.25 0.75 1.25 1.75 2.25 2.75 3.25 3.75 4.25 4.75 5.25 5.75 6.25 6.75 7.25 8.27 9.129 9.75 9.75 9.75}.

One may see that the performance of a partially controlled element locations approach is better in terms of directivity and computational time than that of the fully controlled element locations approach, except for the peak side lobe level which is slightly higher due to a smaller number of degrees of freedom, as mentioned earlier.

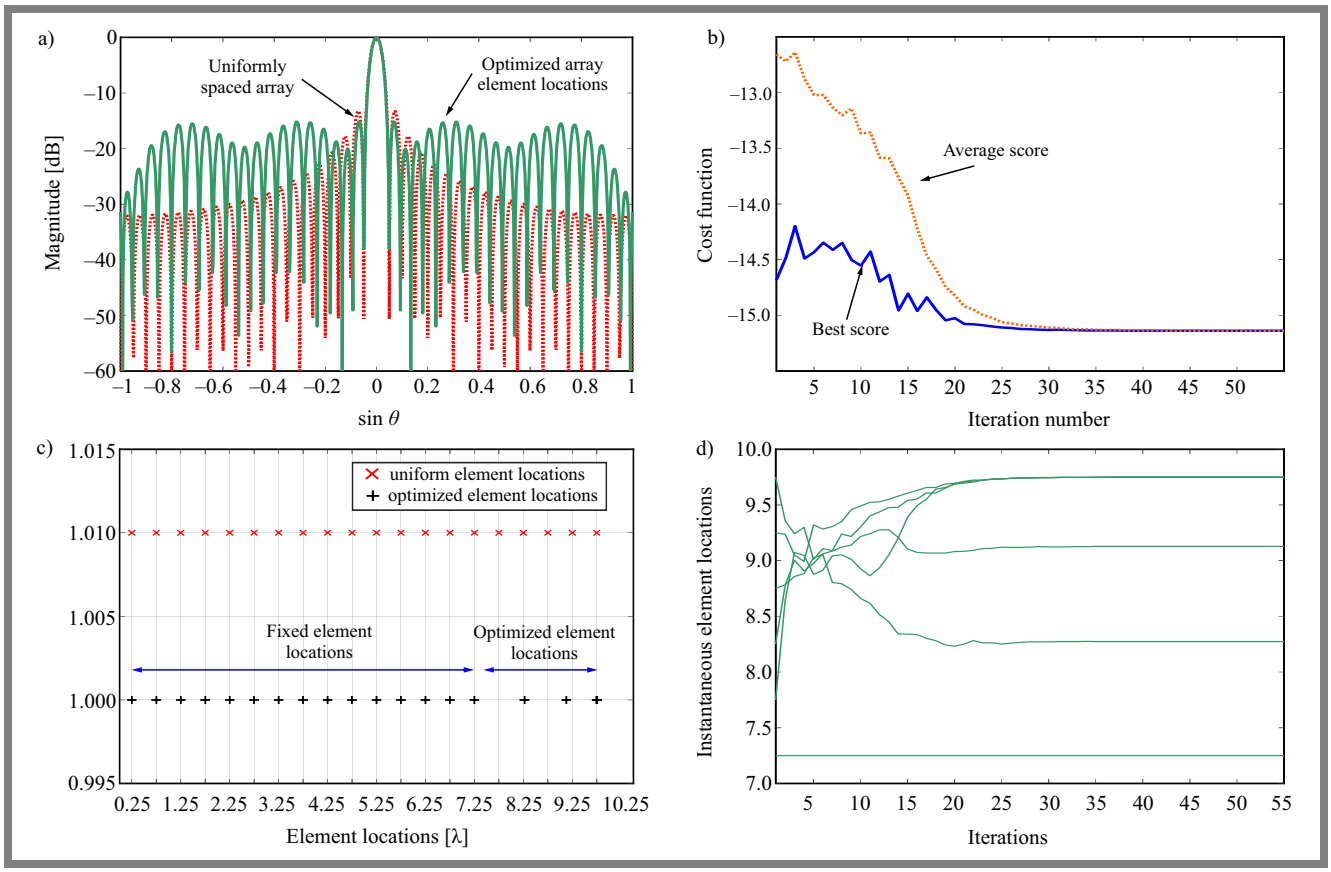

Fig. 8. Results of controlling quarter element locations: a) radiation patterns, b) cost function variations, c) element locations, and d) their instantaneous variations.

More importantly, it can be observed that the element location overlaps still exist, even with the partially controlled element locations approach. This is mainly due to the wide bound constraints used, as shown in Eq. (4), which only preserve the overall array aperture (i.e. beamwidth), with overlaps between optimized element locations not being included.

In the next example, the lower and upper bounded constraints on each controlled element location are considered to prevent overlaps between the array's elements. At first, the proposed approach is applied to the fully controlled element locations method (see Fig. 9), and then to the partially controlled element locations method (see Fig. 10) to assess their performance.

The performance of the fully controlled element locations method with bounded constraints was $D = 27.74$ dB, $SLL = -17.0$ dB, $T = 9.2$ s, and x_n={0.25 0.583 0.9768 1.458 1.952 2.45 2.95 3.45 3.95 4.45 4.95 5.45 5.9679 6.4929 6.95 7.9717 8.5386 9.0496 9.55 9.75}.

For the partially controlled element locations method with bounded constraint, the achieved parameters were: $D = 27.66$ dB, $SLL = -16$ dB, $T = 5.1$ s, and x_n={0.25 0.496 1.25 1.45 2.25 2.4539 3.25 3.00 4.25 4.323 5.25 5.00 6.25 6.674 7.25 7.793 8.25 8.945 9.25 9.983}.

From Figs. 9–10, one may see that element location overlaps have been completely solved and the performance obtained was very acceptable.

4. Conclusions

The results obtained in the simulation have shown that non-uniformly spaced arrays with fully or partially absolute element location controls could offer a considerable improvement in terms of side lobe level reduction and also in terms of beamwidth. An equally narrow beamwidth as that of the standard uniformly spaced array was achieved by maintaining the same array aperture, i.e. by keeping the locations of the first and the last element constant. Consequently, similar directivity was obtained in the optimized array.

It was also observed that in non-uniformly spaced arrays, location overlaps were usually encountered between optimized elements – a phenomenon which is undesirable and may cause performance degradation in the practical applications of such arrays.

Two efficient approaches have been proposed to solve this problem. The first one relies on partially optimized element location controls, while the other one imposes bounded constraints on the location of each element. The principal advantage of using the two approaches proposed above is their short computational time. This feature is very important in the application of null placement for interference suppression. Thus, the proposed approaches can be extended to control the nulls in antenna array patterns by using randomly distributed elements with bounded constraints.

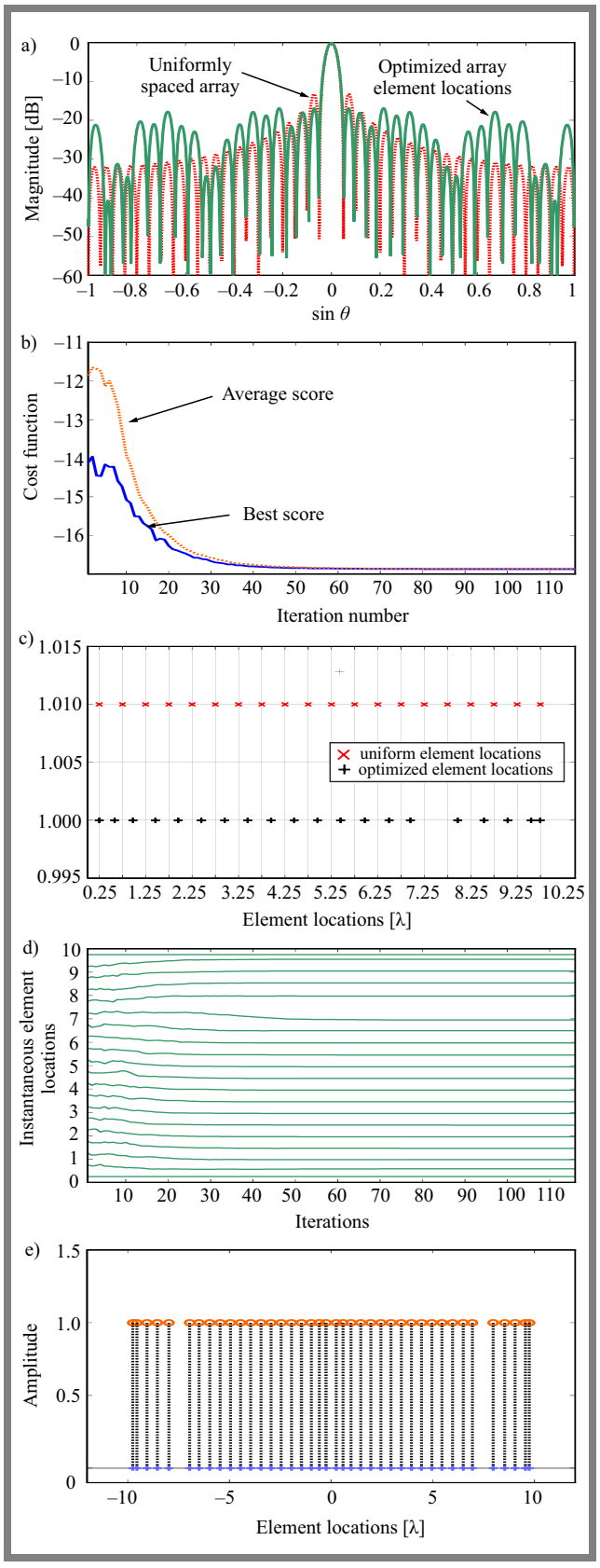

Fig. 9. Results of controlling all element locations with bounded constraints: a) radiation patterns, b) cost function variations, c) element locations, d) their instantaneous variations, and e) amplitude weights.

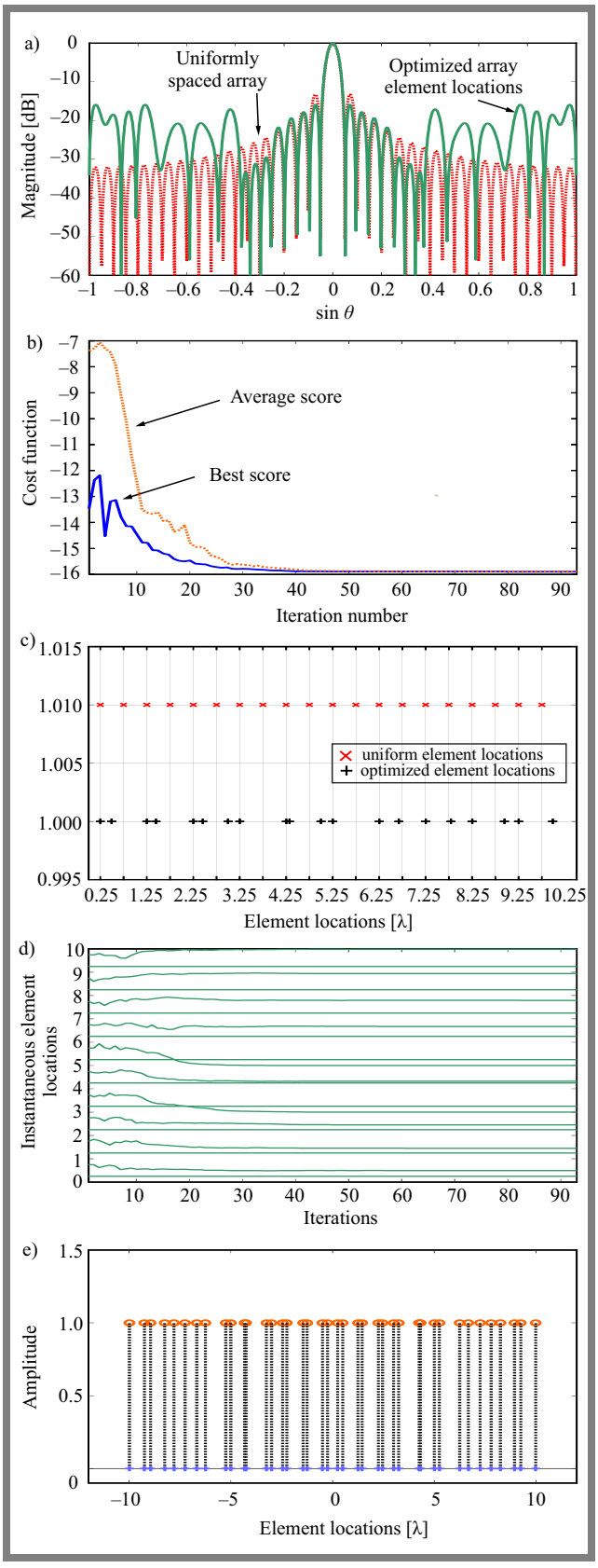

Fig. 10. Results of controlling half element locations with bounded constraints: a) radiation patterns, b) cost function variations, c) element locations, d) their instantaneous variations, and e) amplitude weights.

In contrast to sidelobe reduction, nulls placement requires a much lower number of the degrees of freedom, and these may be appropriately provided, in sufficient quantities, by the presented approaches. This should be the subject of future research work.

References

[1] A.J. Abdulqader, J.R. Mohammed, and R.H. Thaher, "Phase-only Nulling with Limited Number of Controllable Side Elements", *Progress in Electromagnetics Research C*, vol. 99, pp. 167–178, 2020 (https://doi.org/10.2528/PIERC20010203).

[2] J.R. Mohammed, A.J. Abdulqader, and R.H. Thaher, "Array Pattern Recovery under amplitude Excitation Errors Using Clustered Elements", *Progress in Electromagnetics Research M*, vol. 98, pp. 183–192, 2020 (https://doi.org/10.2528/PIERM20101906).

[3] J.R. Mohammed and K.H. Sayidmarie, "Sensitivity of the Adaptive Nulling to Random Errors in Amplitude and Phase Excitations in Array Elements", *Journal of Telecommunication, Electronic and Computer Engineering*, vol. 10, no. 1, pp. 51–56, 2018 (https://jtec.utem.edu.my/jtec/article/view/2023).

[4] M. Takuro and F. Mitoshi, "Reduction of Quantization Error Using Auxiliary Antenna on Array Antenna", *IEICE Communications Express*, vol.7, no.10, pp. 347–351, 2018 (https://doi.org/10.1587/comex.2018XBL0091).

[5] J.R. Mohammed and K.M. Younis, "Null Steering Implementation by Controlling Side-elements Positions", *International Journal of Microwave and Optical Technology*, vol. 16, no. 6, pp. 568–575, 2021.

[6] N. Anselmi, L. Tosi, P. Rocca, and A. Massa, "On the Design of Next Generation Phased Array Antennas - Methods, Architectures, and Trends", *2023 17th European Conference on Antennas and Propagation (EuCAP)*, Florence, Italy, 2023 (https://doi.org/10.23919/EuCAP57121.2023.10133211).

[7] J.R. Mohammed, "An Optimum Side Lobe Reduction Method with Weight Perturbation", *Journal of Computational Electronics*, vol.18, no. 2, pp. 705–711, 2019 (https://doi.org/10.1007/s10825-019-01323-5).

[8] J. Sanchez-Gomez, D.H. Covarrubias, and M.A. Panduro, "A Synthesis of Unequally Spaced Antenna Arrays Using Legendre Functions", *Progress In Electromagnetics Research M*, vol. 7, pp. 57–69, 2009 (https://doi.org/10.2528/PIERM09032305).

[9] J.R. Mohammed and K.H. Sayidmarie, "Synthesizing Asymmetric Side Lobe Pattern with Steered Nulling in Nonuniformly Excited Linear Arrays by Controlling Edge Elements", *International Journal of Antennas and Propagation*, vol. 2017, 2017 (https://doi.org/10.1155/2017/9293031).

[10] J.R. Mohammed, "Phased Array Antenna with Ultra-low Sidelobes", *Electronics Letters*, vol. 49, no. 17, pp. 1055—1056, 2013 (https://doi.org/10.1049/el.2013.1642).

[11] S.K. Goudos *et al.*, "Sparse Linear Array Synthesis with Multiple Constraints Using Differential Evolution with Strategy Adaptation", *IEEE Antennas and Wireless Propagation Letters*, vol. 10, pp. 670–673, 2011 (https://doi.org/10.1109/LAWP.2011.2161256).

[12] J.R. Mohammed, "Obtaining Wide Steered Nulls in Linear Array Patterns by Controlling the Locations of Two Edge Elements", *AEU International Journal of Electronics and Communications*, vol. 101, pp. 145–151, 2019 (https://doi.org/10.1016/j.aeue.2019.02.004).

[13] T.H. Ismail and M.M. Dawoud, "Null Steering in Phased Arrays by Controlling the Element Positions", *IEEE Transactions on Antennas and Propagation*, vol. 39, no. 11, pp. 1561–1566, 1991 (https://doi.org/10.1109/8.102769).

[14] A. Mukherjee, S.K. Mandal, and R. Ghatak, "Synthesis of Non-uniformly Spaced Planar Array Geometry Using Differential Evolution Algorithm", *2016 IEEE Indian Antenna Week (IAW 2016)*, Madurai, India, 2016 (https://doi.org/10.1109/IndianAW.2016.7883599).

[15] D.W. Boeringer and D.H. Werner, "Particle Swarm Optimization versus Genetic Algorithms for Phased Array Synthesis", *IEEE Transactions on Antennas and Propagation*, vol. 52, no. 3, pp. 771–779, 2004 (https://doi.org/10.1109/TAP.2004.825102).

[16] C. Zhang *et al.*, "Synthesis of Broadside Linear Aperiodic Arrays with Sidelobe Suppression and Null Steering Using Whale Optimization Algorithm", *IEEE Antennas and Wireless Propagation Letters*, vol. 17, no. 2, pp. 347–350, 2018 (https://doi.org/10.1109/LAWP.2018.2789919).

[17] G. Toso and P. Angeletti, "Optimal Combined Amplitude-density Synthesis of Aperiodic Arrays", *Proc. of the 5th European Conference on Antennas and Propagation (EUCAP)*, pp. 3044–3047, 2011 (https://ieeexplore.ieee.org/document/5782222).

[18] J.R. Mohammed, "Thinning a Subset of Selected Elements for Null Steering Using Binary Genetic Algorithm", *Progress in Electromagnetics Research M*, vol. 67, pp. 147–157, 2018 (https://doi.org/10.2528/PIERM18021604).

[19] A. Khan and J.S. Roy, "Design of Low Power Thinned Smart Antenna for 6G Sky Connection", *Journal of Telecommunications and Information Technology*, no. 1, pp. 26–33, 2024 (https://doi.org/10.26636/jtit.2024.1.1438).

[20] J.R. Mohammed, "A Method for Thinning Useless Elements in the Planar Antenna Arrays" *Progress In Electromagnetics Research Letters*, vol. 97, pp. 105–113, 2021 (https://doi.org/10.2528/PIERL21022104).

[21] A.J. Abdulqader, J.R. Mohammed, and Y.A. Ali, "A T-shaped Polyomino Subarray Design Method for Controlling Sidelobe Level", *Progress In Electromagnetics Research C*, vol. 126, pp. 243–251, 2022 (https://doi.org/10.2528/pierc22080803).

[22] J.R. Mohammed, "Simplified Rectangular Planar Array with Circular Boundary for Side Lobe Suppression", *Progress In Electromagnetics Research M*, vol. 97, pp. 57–68, 2020 (https://doi.org/10.2528/PIERM20062906).

[23] J. Hejres, "Null Steering in Phased Arrays by Controlling the Positions of Selected Elements", *IEEE Transactions on Antennas and Propagation*, vol. 52, no. 11, pp. 2891–2895, 2004 (https://doi.org/10.1109/TAP.2004.835128).

[24] L. Chen *et al.*, "Synthesis of Large-Scale Planar Isophoric Sparse Arrays Using Iterative Least Squares with Nonredundant Constraints (ILS-NRC)", *IEEE Transactions on Antennas and Propagation*, vol. 72, no. 5, pp. 4232–4245, 2024 (https://doi.org/10.1109/TAP.2024.3375971).

[25] P. You *et al.*, "Synthesis of Unequally Spaced Linear Antenna Arrays with Minimum Element Spacing Constraint by Alternating Convex Optimization", *IEEE Antennas and Wireless Propagation Letters*, vol. 16, pp. 3126–3130, 2017 (https://doi.org/10.1109/LAWP.2017.2764069).

Noor Mohammed Qassim, Student
College of Electronics Engineering
E-mail: noor.22enp29@student.uomosul.edu.iq
Ninevah University, Mosul, Iraq
https://uoninevah.edu.iq

Jafar Ramadhan Mohammed, Ph.D.
College of Electronics Engineering
https://orcid.org/0000-0002-8278-6013
E-mail: jafar.mohammed@uoninevah.edu.iq
Ninevah University, Mosul, Iraq
https://uoninevah.edu.iq

Enhancing Biometric Security with Bimodal Deep Learning and Feature-level Fusion of Facial and Voice Data

Khaled Merit and Mohammed Beladgham

Tahri Mohammed University of Bechar, Bechar, Algeria

https://doi.org/10.26636/jtit.2024.4.1754

Abstract — Recent research in biometric technologies underscores the benefits of multimodal systems that use multiple traits to enhance security by complicating the replication of samples from genuine users. To address this, we present a bimodal deep learning network (BDLN or BNet) that integrates facial and voice modalities. Voice features are extracted using the SincNet architecture, and facial image features are obtained from convolutional layers. Proposed network fuses these feature vectors using either averaging or concatenation methods. A dense connected layer then processes the combined vector to produce a dual-modal vector that encapsulates distinctive user features. This dual-modal vector, processed through a softmax activation function and another dense connected layer, is used for identification. The presented system achieved an identification accuracy of 99% and a low equal error rate (EER) of 0.13% for verification. These results, derived from the VidTimit and BIOMEX-DB datasets, highlight the effectiveness of the proposed bimodal approach in improving biometric security.

Keywords — biometric recognition, deep learning, multimodal systems, SincNet, voice modality

1. Introduction

Recently, there has been considerable growth in the number of applications that require the verification of an individual's identity. This is applicable to digital services provided by public or private entities and various other processes, such as forensic sciences or security tasks. Traditional methods of identity verification include memorizing passwords, relying on physical credentials or electronic devices containing user information. However, these methods pose security risks. For example, people may forget their password, lose their credentials or identification device, have their physical credentials forged, or discover their password through unauthorized means [1].

The scientific study of measuring and analyzing distinctive physical and behavioral traits that enable individual identification is known as biometrics. A biometric system utilizes data extracted from one or more biometric features, such as voice, face recognition, or fingerprints, to authenticate a user's identity. This approach eliminates the need for individuals to memorize information, possess credentials, or carry devices for authentication, as a unique characteristic of their body or behavior is inherent to them and cannot be lost, transferred, or stolen [2].

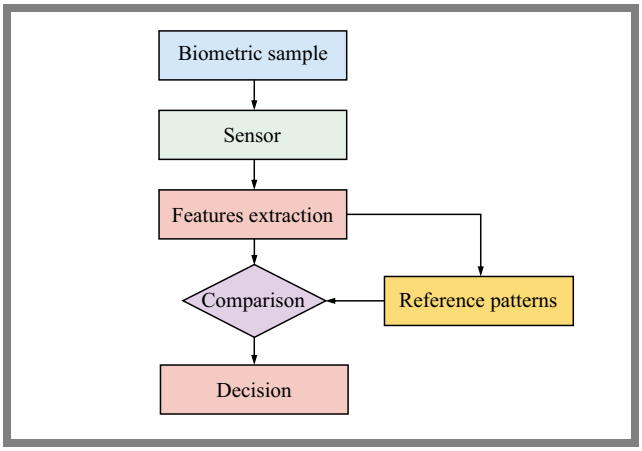

Fig. 1. Block diagram of a biometric system.

A biometric system is made up of several interconnected modules that perform the following steps to authenticate an individual's identity. The sensor acquires and digitizes biometric information, mathematical methods are used to extract discriminatory characteristics, and a set of these characteristics is stored in the biometric system to serve as a reference standard. Each time a user accesses the system, the characteristics extracted from their biometric sample are compared with one or more reference standards to generate a numerical rating, and finally a module uses this rating to decide whether to accept or reject the user's identity [3]. Figure 1 illustrates the modules that make up a biometric system.

Biometric systems are inherently vulnerable to various degrees of deception, either through imitation of physiological or behavioral traits, the use of devices to falsify these traits, or the use of audio or video recordings to deceive the system [4].

To address this issue, the use of multimodal systems is a relevant strategy in the design of biometric systems. By combining various sources of information, such as combining data from multiple traits acquired by sensors, characteristics acquired by different methods, ratings generated by comparing samples of various traits with their respective patterns, or decisions made after processing several traits [5], the security of the system can be significantly strengthened. Thanks to this, the likelihood of erroneously recognizing an impostor

can be significantly reduced. Furthermore, using two or more biometric features to authenticate an identity can further enhance the system safety, making it more challenging for an imposter to validate one's identity falsely.

In addition to using established techniques, this paper presents a novel approach to feature-level fusion by integrating SincNet for voice feature extraction and local binary patterns (LBPs) for face features, optimizing their combination through deep learning techniques. This work introduces and evaluates a biometric neural network, termed BiCNN, designed for identification and verification tasks. The integration of voice and facial modalities is achieved through the combination or averaging of their corresponding feature vectors within the network architecture.

This merging process is optimized during the training phase, where the extracted feature vectors are adjusted according to network parameters. Face images are analyzed using the LBP algorithm, which is invariant to image rotation and lighting changes, while the speech modality employs SincNet, a single-dimensional convolutional layer that extracts frequency characteristics from segmented speech signals.

SincNet offers advantages such as direct audio processing, fewer trainable parameters, and faster convergence. To train and assess the proposed model, we constructed a virtual data set merging BIOMEX-DB and VidTimit datasets, expanding the available biometric data by injecting noise into voice signals and applying transformations to images. This integration and its evaluation under various conditions represent a significant advance over previous studies that often focus on single-modality or simpler fusion techniques.

The voice and facial modalities of the bimodal system were chosen for their ease of acquisition and minimal intrusion into the participants. These modalities allow for simple data manipulation, enabling the implementation of artificial data augmentation schemes to prevent model overfitting. Additionally, it is essential to note that these traits are not mutually dependent, allowing the combination of databases with similar characteristics to increase the amount of available information, as demonstrated in our work, to fill in missing data.

In contrast, the utilization of a deep learning (DL) model for this proposal is justified by its ability to overcome limitations found in machine learning (ML) models. One of such limitations is the requirement for feature extraction, where ML methods require mathematical procedures to extract data characteristics, which may not be compatible with certain types of biometric data or databases, or if the information is altered by noise or transformation [6].

Deep learning models can automatically extract characteristics from input data and adjust their parameters during the training process to improve recognition performance. Furthermore, the multimodal fusion of feature vectors within the network architecture also benefits from this optimization.

This research is presented as follows. Section 2 outlines a comprehensive survey of significant multimodal biometric projects that focus on the integration of feature vectors through neural network models or machine learning. Section 3 provides the essential aspects of BiCNN training. Sections 4 and 5 outline the criteria for assessing network performance and provide the corresponding outcomes. Lastly, Section 6 provides the conclusions and outlook.

2. Related Work

The biometric system requires relevant characteristics from the modalities of voice and face, which continue to be the focus of research through unimodal methods. Machine learning techniques and computational intelligence with deep learning-based approaches are utilized in modern approaches for voice-based biometrics [7], [8]. Additionally, facial trait-based biometrics employs various techniques, such as combining thermal and visual images [9], employing one-shot learning with data augmentation [10], or mapping images to a Euclidean space using convolutional networks [11].

The literature on multimodal biometrics demonstrates different approaches to combining data from multiple biometric features. The selection of these approaches is influenced by the traits being considered and the classification techniques employed. Table 1 provides an overview of significant studies in this field.

3. Development of the Bimodal Biometric System

The bimodal biometric system proposed in this paper comprises a convolutional neural network with two inputs, each corresponding to a distinct biometric feature. Each input is connected to a subnet that independently processes information related to each trait and delivers an attribute vector.

The two vectors are combined (concatenated) to generate a bimodal vector that is refined using a densely connected layer to extract additional significant information and reduce its dimensionality.

The network was trained using the Keras library with an Adam optimizer, a learning rate 0.001, and a step size of 50 epochs. Training involved eight batches of 32 pairs each for training and validation. The convolutional layers for face processing used filters of increasing size (32, 64) and kernel dimensions (3×3, 5×5) with Leaky ReLU activations and batch normalization. Voice processing utilized the SincNet architecture with 120 filters and a kernel size of 251, followed by additional 1D convolutional layers.

The result is a densely connected layer that functions as a SoftMax classifier. The architecture of the suggested BiCNN is listed in the Tab. 2, while Fig. 2 shows the configuration of proposed bimodal network.

3.1. Feature Extraction

An objective of this research is to integrate facial and vocal records at the attribute level to realize the multimodal aspect of the proposed biometric architecture. Recent research suggests

Tab. 1. Review of works on multimodal biometrics.

Ref.	Modalities	Method	Database	Results
[6]	Iris, face, and veins of the fingers	Concatenation of feature vectors extracted by a VGG16 network and fusion of scores	SDUMLA-HMT: 106, IT Delhi and FERET	Identification accuracy: concatenation 99.39%, fusion of scores 100%
[12]	Face and iris	Concatenation of vectors extracted by neural network based on VGG-19 architecture	CASIA-webface: 10576, ND-Iris-0405: 1356, WVU-multi-modal: 2264	Verification: genuine acceptance rate (GAR) 99.67%
[13]	Iris and area peripheral of the eye	Concatenation of extracted weighted vectors neural network with maxout units	CASIA-IrisV4, CASIA-CSIR 2015	Verification: EER 1.88%
[14]	Face, fingerprint, and veins of the fingers	Concatenation of computed Fisher vectors from feature vectors	Self-acquired: 51	Identification accuracy: 50 participants 88.01%, 20 part. 90.01%, 15 part. 93.01%
[15]	Voice and face	Fusion of scores by mixed Gaussian mixture models (GMM), alternative universal models (UBM) and neural network	Self-acquired	Identification accuracy: 95%
[16]	Face and voice	Extraction of characteristics by means of various methods. The fusion of information led toc out at the level of characteristics and at the level of scores	Self-acquired	Verification: EER 0.62%
[17]	Voice and face	The feature vectors of the two modes were used to train a K-classifier nearest neighbors (KNN)	CSUF-SG5: 28	Verification: EER 8.05%
[18]	Face and voice	Fusion of scores generated by the comparison of LBP features and a GMM model by a weighted sum	XJTU: 103	Verification:true positive rate (TPR) 100%, type I error rate 0%, type II error rate 0%
[19]	Fingerprint and face, electro-cardiogram (ECG)	Concatenation of extracted feature vectors by a multi-tasking neural network. They were also made tests with fusion of score by different methods	Virtual database: 58, created from the ECG-ID databases, PTBECG, Faces95, and FVC2006	Identification accuracy: fusion of characteristics 98.97%, rule of the sum 98.95%, product rule 96.55%
[20]	Digital signature and fingerprint	Concatenation of extracted feature vectors by a convolutional network. Concatenation occurs on two points of architecture	Self-acquired: 280	Identification accuracy: early modality fusion (EMF) 99.11%, late modality fusion (LMF) 98.36%
[21]	Voice and face	The fusion was carried out by normalizing and adding of scores of each modality generated by comparison of vectors	MOBIO	Verification: area under the ROC curve 0.98
[22]	Iris and digital fingerprint	Fusion by canonical correlation and principal component analysis (PCA)	SDUMLA-HMT	Identification accuracy 100%, verification EER 0.176%
[23]	Fingerprint, fingervein, palmprint	Multimodal biometric model, U-Net with attention, feature fusion	Union DB1: 400, DB2: 500, DB3: 5500	Identification: EER 0.098%, EER 0.024%, EER 0.117%
[24]	Ear and palm vein	Adaptive 2D Gabor filter, curvature detection, morphological operations, sensor- and feature-level fusion	PUT vein database, custom ear database	Accuracy 97.65%, EER 2.15%
[25]	Online signatures, fingerprints	Empirical modal decomposition (EMD) for signatures, minutiae extraction for fingerprints, score-level fusion	MYCT-100, SVC2004, FVC2004	Best EER 1.69% with min-max normalization

incorporating a module within the network structure that effectively integrates the obtained characteristics from all biometric features [13]. This fusion block generates a singular descriptor that encapsulates an individual's most critical identity information.

LBP face images were processed using a series of two-dimensional convolutional layers. In each layer, the number of filters increased, as did the dimensions of the convolutional mask, in order to capture more detailed information. A "max pooling" process was utilized for feature maps to decrease

Tab. 2. Architecture of BICNN.

Layers	Filters/neurons	Dimensions	Step	Activation function
Face processing layers				
2D convolution	32	3×3	1×1	LReLU
Batch normalization	–	–	–	–
MaxPool 2D	–	2×2	1×1	–
2D convolution	64	5×5	1×1	LReLU
Batch normalization	–	–	–	–
MaxPool 2D	–	2×2	1×1	–
Densely connected	512	–	–	LReLU
Batch normalization	–	–	–	–
Voice processing layers				
SincNet	120	251	–	LReLU
Batch normalization	–	–	–	–
MaxPool 1D	–	5	1×1	–
1D convolution	32	5	1×1	LReLU
Batch normalization	–	–	–	–
MaxPool 1D	–	5	1×1	–
1D convolution	64	5	1×1	LReLU
Batch normalization	–	–	–	–
MaxPool 1D	–	5	1×1	–
Densely connected	512	–	–	LReLU
Batch normalization	–	–	–	–
Fusion and exit				
Averaging/concatenation	–	–	–	–
Densely connected	512	–	–	LReLU
Dropout	0.5	–	–	–
Batch normalization	–	–	–	–
Densely connected	45	–	–	Softmax

their size and eliminate irrelevant information. Ultimately, the final convolutional layer generated maps that were processed by a fully connected layer to produce a fixed-dimensional characteristic vector of 512 points, which contained the discriminatory information of the face image.

Voice signals were processed with the SincNet convolutional layer [26]. This layer is characterized by a bank of bandpass filters that extract frequency characteristics from voice signals. The bandpass filters are defined with sinc functions in the time domain, as illustrated in Eq. (1).

$$g[n, f_1, f_2] = 2\, f_1\, \mathrm{sinc}(2\pi f_2 n) - 2\, f_1\, \mathrm{sinc}(2\pi f_1 n)\,, \qquad (1)$$

where f_1 and f_2 are the high and low cut-off frequencies of the bandpass filters, the values of these frequencies are optimized during the training phase. For our experiments, the cut-off frequencies of the filter bank were initialized in logarithmic form, to obtain the MFCCs [27].

The SincNet layer extracts features, which are subsequently processed using one-dimensional convolutional blocks, culminating in a max pooling operation to eliminate irrelevant information. Lastly, a fully connected layer comprising 512 neurons generates a voice information vector for everyone.

3.2. Bimodal Data Fusion

The combination of face and voice vectors is implemented by concatenation or averaging. A feature combination block was also realized through a weighted average regulated by an optimization variable ρ. This variable is adjusted during the training phase, and its measure indicates which mode contributes more significantly to the individuality of the person. Equation (2) illustrates the weighted average utilized in the bimodal embedding.

$$V_{SF} = \rho\, V_F + (1 - \rho)\, V_S\,, \qquad (2)$$

where V_S and V_F represent the face and speech vectors, correspondingly, and V_{SF} is the resultant multimodal embedding. The initial value of ρ was set to 0.5. Following the fusion step, a densely connected layer is used to reduce the dimensionality of the resulting fusion vector to a fixed size, comprising 512 neurons and featuring a dropout rate of 0.5.

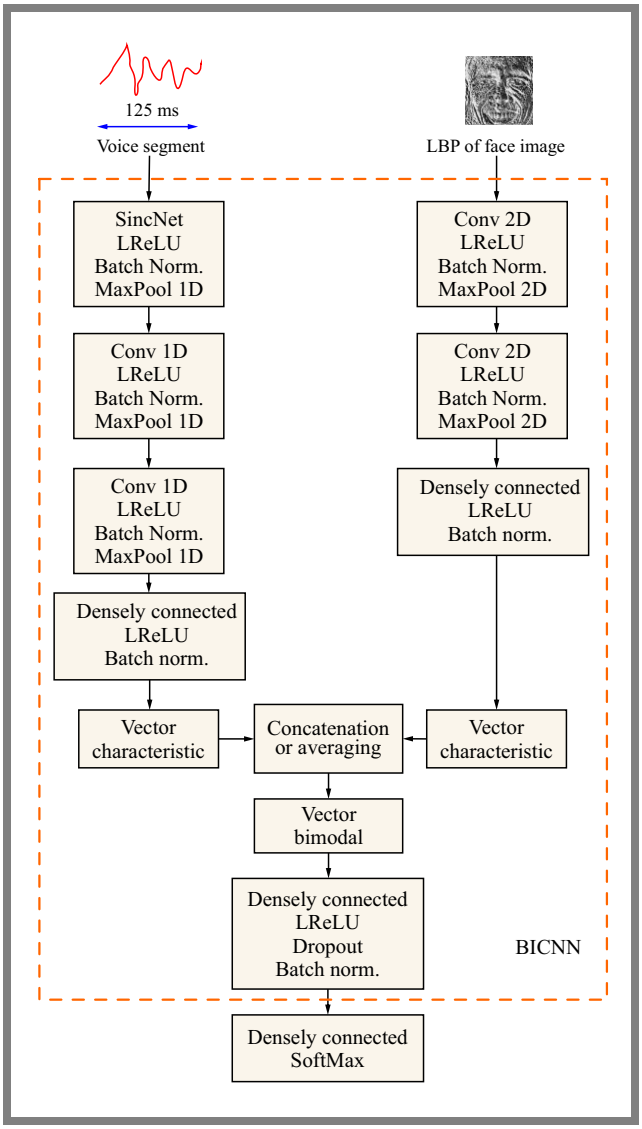

Fig. 2. Schematic diagram of the bimodal convolutional network (BNet).

3.3. Outputs

The final result of BiCNN is a fully connected layer that functions as a SoftMax classifier, incorporating an equal number of neurons as the legitimate user count registered in the biometric system. It is crucial to note that the 512-dimensional vector provided by the penultimate layer contains the features of both voice and face characteristics and will hereafter be referred to as the bimodal vector.

All convolutional layers, apart from the output layer, have batch normalization as a regulator and employ the LReLU activation function according to the findings described in [28]. This research examines the convergence time of a neural network and its recognition performance when utilizing the MNIST database. It evaluates the activation functions of differences between the ReLu and LReLU. The results show that LReLU enables the network to converge more quickly while maintaining performance comparable to that of the ReLu function.

3.4. Pre-processing Data

Several bimodal voice and face biometrics works implemented with different fusion methods are listed in [4]. A part of these works considered relatively small populations for their experiments. This situation occurs because few publicly accessible multimodal databases contain a large population in which all individuals have complete biometric information. Many of the cited authors resorted to generating databases that fit the requirements of their studies. The process of acquiring biometric data requires many resources, so it is sometimes only possible to have large populations. Another alternative is to combine two databases by matching the individuals of each.

3.5. Datasets

To develop our bimodal network, we used voice and face data from the BIOMEX-DB database [29]. However, as some subjects lacked facial data, we opted to supplement this information with a set of images from the VidTimit bimodal database [30].

The BIOMEX-DB database contains information on EEG, voice, and face modalities. It consists of a total of 51 subjects, including 25 women and 26 men. The voice data comprises recordings of English pronunciations of strings of digits, with each subject having 20 audio files, 10 of which correspond to 10-digit string pronunciations, and the remaining ten correspond to 5-digit strings. Face data consists of face videos recorded while participants uttered their strings of digits. The database has a population of 43 people and includes voice and face information. The voice data comprises pronunciations of 10 short English sentences, while the face data consists of images extracted from videos recorded while pronouncing these sentences.

It is crucial to note that 12 BIOMEX-DB subjects do not have face data, which requires the completion of this missing information with face images of 12 VidTimit subjects, as previously mentioned. Consequently, a population of 51 subjects was formed for the study, which was randomly divided into two sets: 45 legitimate users and six impostors.

Although our current study is based on the BIOMEX-DB and VidTimit datasets comprising 51 subjects, future work will involve larger and more diverse datasets such as VoxCeleb and MOBIO to further validate the findings and enhance the generalizability of the results.

3.6. Data Processing and Augmentation

The standardization of voice data was performed to confirm that the signal values were within the range of $-1, \ldots, 1$. Speech signals were processed to remove silences or pauses between pronunciations. To improve speech signals, artificial enhancement was carried out incorporating background noise sampled from the MUSAN database [31] and adjusting the noise level by 0 and 5 dB according to the signal-to-noise ratio.

The face images of all individuals in BIOMEX-DB were extracted from their corresponding videos using the OpenCV

Tab. 3. Experimental setup and training parameters.

Parameters	Value
Training epochs	60
Batch size	32
Learning rate	0.001
Optimizer	Adam
Loss function	CCE

[31] library's face detector to crop the area of interest into a final 128×128 grayscale pixel image. The LBP features with eight neighborhood pixels and a radius of 1 were then extracted from these images. These features are robust to changes in facial posture and variations in image illumination and have been successfully used in conjunction with convolutional networks for face image classification tasks [33]–[35].

The same procedure for detection, face cropping, and extraction of LBP features was employed for the images obtained from VidTimit. Two transformations were carried out using the Imgaug library to increase the number of images [36]. First, the lighting of each image was modified, and second, they were randomly rotated at angles between $-45°, \ldots, 45°$. It is important to note that these transformations were applied to the grayscale images and the LBP operator was applied to the images resulting from the transformations.

3.7. Hyperparameters

The network was implemented using Keras with the Adam optimizer, with a learning rate of 0.001 and was trained over 50 epochs. A batch size of 32 was chosen to optimize learning efficiency while managing computational resources. Table 3 outlines the experimental setup and training parameters.

3.8. Architectural Choices

SincNet was chosen for voice processing because of its unique capability to directly process raw audio signals without extensive processing. This architecture utilizes sinc functions as learnable filters, allowing it to effectively capture important frequency information while reducing the number of trainable parameters. By focusing on the temporal and spectral characteristics of the waveform, SincNet enhances the robustness of feature extraction, leading to improved performance under challenging conditions, such as background noise or varying speaker characteristics. This efficiency is particularly advantageous in scenarios where computational resources are limited or where real-time processing is essential.

For face recognition, local binary patterns (LBP) were selected due to their effectiveness in encoding texture information while being invariant to changes in lighting and facial expressions. LBP operates by thresholding neighborhood pixels and generating a binary code, which allows the creation of a histogram that summarizes the texture features. This method is computationally efficient and has been demonstrated to provide a strong performance in various face classification tasks. By maintaining the integrity of the feature under various conditions, LBP enables the system to achieve higher accuracy in face recognition, especially when dealing with variations in pose, illumination, and occlusion.

The integration of these two architectural choices: SincNet for voice and LBP for face recognition form a robust bimodal biometric system capable of managing the complexities inherent in multimodal data.

3.9. Bimodal Network Training

The data set was partitioned into training, validation (evaluation) and test sets using a 65/05/30 ratio, which provided a distinct validation set for optimizing the model's parameters and enhancing its performance. During the training phase, we used specific neural network architectures along with their configurations and hyperparameters. Important training parameters, such as the learning rate, batch size, number of epochs, and optimizer, were carefully chosen to maximize the efficiency of the training process.

We developed and trained the bimodal network using the Keras library. Training was carried out over 50 epochs, with a learning rate of 0.001 and the Adam optimizer. Categorical cross entropy (CCE) served as the loss function. The models were trained on the training dataset and evaluated on the validation set to keep track of their performance, allowing for any necessary adjustments. Ultimately, the models were evaluated on a separate test set to determine their effectiveness in unseen data.

For training and validation purposes, voice samples of 10–digit string pronunciations and the corresponding face images from the associated videos were utilized. Each training instance required pairs of an image and a voice segment. To promote the generalization of the proposed model, we randomly generated eight batches of 32 pairs for training and eight batches of 16 pairs for validation. This was designed with the understanding that the SincNet convolutional layer can process segments of raw speech signals that last several milliseconds. The BIOMEX-DB videos have a frame rate of 8 frames per second, and each speech segment lasts 125 ms. Additionally, a monitoring mechanism was implemented to track validation accuracy during each epoch, ensuring that only those parameters that maximized this metric were retained.

4. Experimental Evaluation

One of the key objectives of this work is to introduce a novel approach in the field by comparing the performance of proposed BICNN using two methods of feature fusion: concatenation and averaging.

To carry out the evaluation, the pronunciation data of 5-digit strings and the facial images of their corresponding videos were applied.

To assess the bimodal system, we use the biometric data resulting from the artificial increase in the data together with the unmodified samples. This will permit us to assess the performance of the network under diverse conditions for both

modalities. In some of the related works, the authors mention that they also used a data augmentation scheme to train their models, however, their evaluations do not offer information about whether they tested only with their original data or if they included data from the artificially generated set and how they could affect the reconnaissance performance.

For this reason, we present results that demonstrate the effect of artificially generated voice and face samples on identification and verification in a schematic way, assuming that these samples approximate actual operating conditions.

4.1. Identification Evaluation

In the identification task, a user delivers his biometric data to the system, and the latter will provide the identification number or label of the legitimate user registered in the biometric system whose characteristics are more closely resemble those of the user. It's a one-to-many comparison.

In this work, the above procedure is carried out by feeding the output SoftMax classifier with the bimodal vector. The result is a normalized probability distribution from which we can determine the identification number of the legitimate user whose voice and face characteristics resemble more closely those found in the bimodal vector using the argmax function.

The identification experiments were performed in closed set mode, which means that the system assumes that any user is enrolled in it and that its function is to determine their identity and not to verify or validate it. Therefore, data belonging to impostors were not tested, as they do not contribute to correctly evaluating the network's performance. Considering what was described above, the metric for measuring performance was the accuracy defined as:

$$Accuracy = \frac{P_c}{N}, \tag{3}$$

where P_c is the number of times the system successfully predicted a user's identity and N is the total number of tests performed.

4.2. Verification Evaluation

The verification process involves evaluating the biometric features of a user against a set of characteristics stored in the system that correspond to a legitimate user. The outcome of this comparison is the confirmation or denial of the user's identity.

In experimental efforts, we evaluated biometric features by contrasting bimodal vectors. To fashion a legitimate user's pattern, ten pairs of randomly chosen voice and face samples were supplied to the BiCNN, and the pattern was generated by averaging the resulting ten bimodal vectors.

To carry out identity verification, we compared the pattern of a specific legitimate user with a bimodal vector generated by an individual seeking to validate their identity. In this instance, we employed the cosine similarity function to make the comparison, which returns a value that increases as the pattern and sample vector become more similar. Furthermore, we utilized a threshold value to assess cosine similarity and decide to accept or reject the validation of the said identity. The cosine similarity function is:

$$Similarity = \cos(\theta) = \frac{P.M}{\|P\| * \|M\|}, \tag{4}$$

where P is the pattern of a legitimate user and M is the sample vector of a user who wants to verify or validate their identity.

The equal error rate (EER) metric is typically utilized to assess the effectiveness of a biometric system in the verification task. This metric refers to the point at which the number of precisely classified negative examples equals the number of correctly positively categorized examples [37].

Tab. 4. Identification results (in percent) in the precision of the bimodal network with (A – averaging, C – concatenation) of voice and face vectors.

SNR [dB]	No transformations		Transformations			
			Lighting		Rotation	
	A	C	A	C	A	C
Noise free	98.5	99.4	97.6	99.1	84.6	91.5
0	99.0	99.1	98.0	99.1	83.6	89.7
5	99.1	99.2	97.8	99.1	85.1	90.6

5. Results and Commentary

5.1. Identification Outcomes

The results of the identification task are shown in the tab. 4, in each of the evaluation conditions, 1000 tests were performed to calculate the percentage of accuracy.

The results show that accuracy was greater than 97% for most conditions, while conditions involving images with rotation delivered lower values between 83% and 92%.

Concatenation fusion produces better results than averaging. This gap is more significant under conditions that include image rotation. The latter factor indicates that different conditions of a face image affect the accuracy value more than the noise of voice signals. To provide a comprehensive comparison, we evaluated the proposed BDLN against other state-of-the-art multimodal and unimodal techniques such as VGG-19, Fisher vectors, and traditional SVM classifiers across datasets such as CASIA and MOBIO. The results consistently show superior performance in terms of accuracy and EER. Additionally, real-world testing scenarios were simulated by introducing varying levels of noise and transformations.

5.2. Verification Outcomes

The verification task was evaluated by performing 1000 tests with samples from legitimate users and another 1000 with samples from the set of impostors for each condition contemplated in this research. Table 5 illustrates the results in terms of EER delivered by the bimodal biometric system.

Tab. 5. Verification outcomes (in percent) in terms of equal error rate EER for the bimodal distribution network upon vector (A – averaging, C – concatenation).

SNR [dB]	No transformations		Transformations			
			Lighting		Rotation	
	A	C	A	C	A	C
Noise free	0.19	0.60	0.92	0.79	5.65	3.70
0	0.14	0.74	0.91	0.95	4.96	4.21
5	0.13	0.56	1.0	0.70	5.80	3.76

In most cases, the EER values are less than 1%, which is indicative of good verification performance. Similarly, the identification task conditions involving image rotation obtained significantly higher values than the rest. When comparing the EER values of both methods of characteristic fusion, the averages delivered more competent results in this case. Under the conditions in which the images were not transformed, averaged fusion obtained better values. Although the current study focuses on the concatenation and averaging of feature vectors, future work will explore more advanced fusion methods such as principal component analysis (PCA), linear discriminant analysis (LDA), and deep feature fusion (DFF). Preliminary experiments with PCA have already shown potential improvements in verification accuracy.

When analyzing the differences between EER values, it is again seen that the gap is more noticeable when comparing image transformations than between the different SNR values. Therefore, it is possible that also in the verification task, the conditions of the face images have a more significant influence on the results than the noise of the voice samples.

5.3. Comparison of Results

In the last evaluation stage, some unimodal voice and face systems were trained in order to demonstrate better performance delivered by multimodal systems compared to the first ones. The approaches chosen for this comparison are widely used in literature, their structure makes them compatible to be trained with different databases, and facilitates the reproduction of the results of this work. Multimodal approaches may not be implementable with different databases, since feature extraction methods might not be compatible with specific biometric data [20]. In the case of implementations with DL, another factor to consider is that an architecture designed to be trained with a database with specific characteristics may not converge with other databases.

Two unimodal systems were chosen for each biometric feature. The training and evaluation conditions were the same as for BiCNN. The biometric data of BIOMEX-DB and VidTimit were taken, and the same number of legitimate users and impostors were considered.

The face recognition systems considered are a ResNet network with four residual layers [38]. This architecture was chosen since adding more residual layers did not achieve significantly better results. The second face recognition system is based on eigenfaces, we use the definition found in the OpenCV library with the parameters described in [39]. However, the voice recognition systems chosen were the original implementation of the SincNet network [26] and a X-vector-based system as initially described in [40]. In references [41], [42] you can consult the face recognition systems used in this study, and in [43], [44] you can find information on voice recognition systems.

Tab. 6. Comparison of the accuracy results of the identification task.

Biometric system	No transformations	Transformations	
		Lighting	Rotation
BNet (averaged)	99.1%	98%	85.1%
BNet (concatenation)	99.4%	99.1%	91.5%
ResNet CNN	100%	99.6%	93.6%
Eigenfaces (PCA algorithm)	100%	98.76%	85.43%
SNR	Noise free	0 dB	5 dB
BNet (averaged)	98.5%	99%	99.1%
BNet (concatenation)	99.4%	99.1%	99.2%
SincNet (SNC)	100%	88.1%	96.43%
X-vectors (XVEC)	95.21%	83.1%	92.1%

5.4. Identification

Table 6 provides a comparison of the best results of our identification experiments with those obtained with unimodal systems.

In the face identification modality, all modes had an accuracy of more than 97% for untransformed images and with changing illumination. In the rotation condition, the accuracy values significantly decreased. Only the bimodal network with feature concatenation and the ResNet CNN model delivered results of just over 90%. In this analysis, our bimodal model and the ResNet CNN model have similar results.

In terms of speaker identification, it is worth mentioning that the two techniques for merging the bimodal network exhibited outstanding performance, achieving accuracy levels greater than 95% when noiseless voice signals were used. However, when noise was present in the voice signals, the two methods of merging the bimodal network demonstrated significantly higher accuracy values compared to unimodal systems.

This suggests that the proposal for a bimodal system can maintain a high level of identification performance even in the presence of noise. In contrast, other systems experience a noticeable decrease in performance under similar circumstances.

Tab. 7. Comparison of the EER results of the verification task.

Biometric system	No transformations	Transformations	
		Lighting	Rotation
BNet (averaged)	0.13%	0.93%	4.98%
BNet (concatenation)	0.56%	0.72%	3.72%
ResNet CNN	0.55%	1.44%	3.59%
Eigenfaces (PCA algorithm)	2.97%	12.83%	27.78%
SNR	Noise free	0 dB	5 dB
BNet (averaged)	0.21%	0.16%	0.13%
BNet (concatenation)	0.62%	0.76%	0.56%
SincNet (SNC)	1.82%	13.4%	5.56%
X-vectors (XVEC)	1.73%	4.93%	2.38%

5.5. Verification

Table 7 summarizes an evaluation of the effectiveness of the verification task in terms of the equal error rate (EER).

In face verification, the bimodal network with its two fusion methods and the ResNet CNN model delivered results with little difference between their EER values for all image transformations. In the rotation condition, all models showed an increase in EER. This is a situation similar to that seen in identification. Eigenfaces, being a non-neural network-based method, showed the worst performance in all conditions by a significant difference.

In the domain of voice verification, the bimodal network that utilized averaging emerged as the top performer in all three evaluation scenarios, while the concatenation fusion method demonstrated slightly inferior results. Both bimodal networks consistently outperformed the SincNet and X-vector approaches by a significant margin when dealing with speech samples that had noise added to them. These findings suggest that the proposed network demonstrates superior performance in verification tasks when working with speech samples that have noise added to them at these specific SNR values.

Finally, we accumulated all the scores used to evaluate the conditions of each biometric system to generate the corresponding receiver operating characteristic (ROC) curves. Figure 3 shows the ROC curves of all the models evaluated.

The general EER values obtained using the ROC curves are as follows: bimodal network (BNet) averaged 3.28%, bimodal network (BNet) concatenation 2.16%, ResNet CNN 2.37%, eigenfaces 17.84%, SincNet (SNC) 9.32%, and X-vectors (XVEC) 3.52%. These values show that the bimodal proposal in its two variants delivered expected results and, in most cases, superior to the considered unimodal systems. The fusion method by concatenation of vectors showed the best verification performance and this result is consistent with what was obtained in the previous evaluations.

5.6. Comparison with Related Works

Table 8 shows a brief comparison of our results with other relevant work on bimodal voice and face biometrics. We select papers whose number of subjects in their experiments is similar or not much higher than ours. As can be seen, the results are comparable to those presented by other authors who implemented other techniques and used other databases. Furthermore, Fig. 3 presents the ROC curves for our experimental results, offering a visual comparison of performance across different methods and conditions.

Figure 4 compares the percentages of equal error rate (EER) of several studies focusing on the efficiency of biometric or authentication systems. The EER is a critical performance metric that marks the intersection point between the false acceptance rate (FAR) and the false rejection rate (FRR). A lower EER percentage indicates a more accurate and reliable system.

The methodology proposed in the current analysis provides an EER of only 0.13%, compared to 0.56% for a concatenation approach. This represents a significant improvement over other systems, especially in contrast to much higher EERs reported in previous literature, such as 20.59% for [45], 25.70% for [51], and 19.90% for [53]. Even state-of-the-

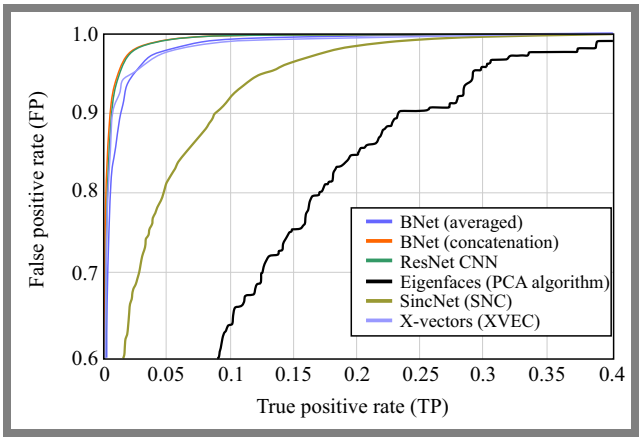

Fig. 3. Comparison of ROC curves.

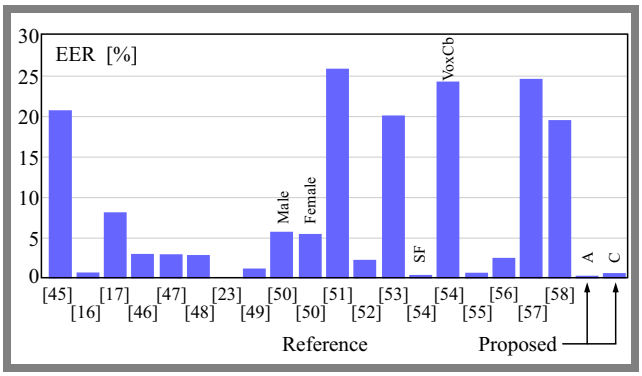

Fig. 4. Comparison of the equal error rate (EER) between different studies.

Tab. 8. The EER score of the proposed model along with the state-of-the-art methods on bimodal voice and face biometrics.

Paper	Classifier	Database	EER
[16]	Various classifiers	Acquired by the authors: 100	0.65%
[17]	KNN	CSUF-SG5: 27	8.04%
[18]	Comparison of LBP and GMM characteristics	XJTU: 102	0%
[45]	Support vector machine (SVM)	CSUF-SG5: 27	20.59%
[46]	FaceNet + dilated residual network (DRN)	SWAN: 88	3.01%
[47]	Logistic regression	NIST SRE19: 47	2.78%
[48]	ResNet	NIST SRE19: 42	2.78%
[49]	CNN with two inputs	Deep lip (virtual database): 150	1.11%
[50]	ResNet-50	VoxCeleb1-Test: 40, MOBIO: 150, AveRobot: 111	5.7% male, 5.4% female, 7.7% male, 9.1% female 30% male, 31.6% female
[51]	Single-branch network (Git)	VoxCeleb1 (VC1): 40	25.7%
[52]	Fusion (JCA) with U-BLSTM and J-BLSTMs	VoxCeleb1	2.214%
[53]	Multi face-voice association learning with keynote speaker diarization (MFV-KSD)	FAME 2024	19.9%
[54]	Universal transformer, vision transformer (ViT), multimodal prototypical network loss	SpeakingFaces (SF), VoxCeleb (VoxCb)	0.27%, 24.1%
[55]	Gammatonegram for voice and VGGFace2 for face	VoxCeleb2	0.62%
[56]	Real additive angular marlin loss, attention-based fusion	SpeakingFaces	2.5%
[57]	Voice-face aligner (VFAligner)	VoxCeleb2	24.40%
[58]	Fuse after align (FAA) framework, multimodal encoder	VoxCeleb	19.3%
Proposed	BNet (two stream-CNN)	BIOMEX-DB, VidTimit: 51	BNet (averaged): 3.28% general, 0.13% best, BNet (concatenation): 2.16% general, 0.56% best

art approaches, such as [16] (0.65%) and [49] (1.11%), fail to match the performance of the proposed method.

Furthermore, [18] achieved an EER of 0.00%, which is notable for its precision but still does not diminish the significance of the low EER values in the proposed solution, especially considering the broader scope and versatility of the system presented in this paper.

6. Conclusion and Future Work

The evaluation results show that the bimodal network with fusion by concatenation obtained better recognition results in most of the conditions considered in both identification and verification.

In the second evaluation stage, where popular unimodal proposals were trained with the same virtual database and were tested under the same conditions as BiCNN, in case of the face modality, the results are very similar to the unimodal network based in ResNet. Despite that, our proposal demonstrated superior performance to the eigenfaces system and the two unimodal voice approaches in most conditions considered.

Our proposal delivers decent EER values and is comparable with the other works in which the amount of population considered experiments is like ours. Although our research demonstrates the technical viability of bimodal biometric systems, it is imperative to address ethical concerns such as privacy, data security, and user consent. Biometric data are inherently sensitive and proper measures must be taken to ensure their protection.

Additionally, to further validate the system's robustness and scalability, we plan to incorporate more diverse datasets that closely mimic real-world conditions. Testing on larger databases such as VoxCeleb and MOBIO will allow us to evaluate the system's performance across varied environments. This will help improve its generalizability and reliability, making it more suitable for practical applications in diverse real-world scenarios.

References

[1] S.A. Abdulrahman and B. Alhayani, "A Comprehensive Survey on the Biometric Systems Based on Physiological and Behavioral Characteristics", *Materials Today: Proceedings*, vol. 80, pp. 2642–2646, 2023 (https://doi.org/10.1016/j.matpr.2021.07.005).

[2] S.K.S. Modak and V.K. Jha, "Multibiometric Fusion Strategy and its Applications: A Review", *Information Fusion*, vol. 49, pp. 174–204, 2019 (https://doi.org/10.1016/j.inffus.2018.11.018).

[3] D. Patel, S. Patel, A.A. Thadeshwar, and R. Chaturvedi, "Multimodal Biometric Systems: A Review", *International Journal of Advanced Research in Computer Science*, vol. 9, no. 2, pp. 361–365, 2018 (https://doi.org/10.26483/ijarcs.v9i2.5742).

[4] H. Mandalapu *et al.*, "Audio-visual Biometric Recognition and Presentation Attack Detection: A Comprehensive Survey", *IEEE Access*, vol. 9, pp. 37431–37455, 2021 (https://doi.org/10.1109/access.2021.3063031).

[5] M. Singh, R. Singh, and A. Ross, "A Comprehensive Overview of Biometric Fusion", *Information Fusion*, vol. 52, pp. 187–205, 2019 (https://doi.org/10.1016/j.inffus.2018.12.003).

[6] N. Alay and H.H. Al-Baity, "Deep Learning Approach for Multimodal Biometric Recognition System Based on Fusion of Iris, Face, and Finger Twenty Traits", *Sensors*, vol. 20, no. 19, art. no. 5523, 2020 (https://doi.org/10.3390/s20195523).

[7] S. Shakil, D. Arora, and T. Zaidi, "Feature Based Classification of Voice Based Biometric Data Through Machine Learning Algorithm", *Materials Today: Proceedings*, vol. 51, pp. 240–247, 2022 (https://doi.org/10.1016/j.matpr.2021.05.261).

[8] N.D. Al-Shakarchy, H.K. Obayes, and Z.N. Abdullah, "Person Identification Based on Voice Biometric Using Deep Neural Network", *International Journal of Information Technology*, vol. 15, no. 2, pp. 789–795, 2023 (https://doi.org/10.1007/s41870-022-01142-1).

[9] N.K. Benamara, E. Zigh, T.B. Stambouli, and M. Keche, "Towards a Robust Thermal-visible Heterogeneous Face Recognition Approach Based on a Generative Cycle Adversarial Network", *International Journal of Interactive Multimedia and Artificial Intelligence*, vol. 7, no. 4, pp. 132–145, 2022 (https://doi.org/10.9781/ijimai.2021.12.003).

[10] D.M. Jiménez-Bravo *et al.*, "Edge Face Recognition System Based on One-shot Augmented Learning", *International Journal of Interactive Multimedia and Artificial Intelligence*, vol. 7, no. 6, pp. 31–44, 2022 (https://doi.org/10.9781/ijimai.2022.09.001).

[11] A. Alcaide *et al.*, "LIPSNN: A Light Intrusion-proving Siamese Neural Network Model for Facial Verification", *International Journal of Interactive Multimedia and Artificial Intelligence*, vol. 7, no. 4, pp. 121–131, 2022 (https://doi.org/10.9781/ijimai.2021.11.003).

[12] V. Talreja, M.C. Valenti, and N.M. Nasrabadi, "Multibiometric Secure System Based on Deep Learning", *2017 IEEE Global Conference on Signal and Information Processing (GlobalSIP)*, Montreal, Canada, 2017 (https://doi.org/10.1109/globalsip.2017.8308652).

[13] Q. Zhang, H. Li, Z. Sun, and T. Tan, "Deep Feature Fusion for Iris and Periocular Biometrics on Mobile Devices", *IEEE Transactions on Information Forensics and Security*, vol. 13, no. 11, pp. 2897–2912, 2018 (https://doi.org/10.1109/tifs.2018.2833033).

[14] Y. Xin *et al.*, "Multimodal Feature-level Fusion for Biometrics Identification System on IoMT Platform", *IEEE Access*, vol. 6, pp. 21418–21426, 2018 (https://doi.org/10.1109/access.2018.2815540).

[15] V.V. Khryashchev, A.I. Topnikov, A.F. Stefanidi, and A.L. Priorov, "Bimodal Person Identification Using Voice Data and Face Images", *Eleventh International Conference on Machine Vision (ICMV 2018)*, Munich, Germany, 2019 (https://doi.org/10.1117/12.2523138).

[16] A. Abozaid, A. Haggag, H. Kasban, and M. Eltokhy, "Multimodal Biometric Scheme for Human Authentication Technique Based on Voice and Face Recognition Fusion", *Multimedia Tools and Applications*, vol. 78, pp. 16345–16361, 2019 (https://doi.org/10.1007/s11042-018-7012-3).

[17] O. Olazabal *et al.*, "Multimodal Biometrics for Enhanced IoT Security", *2019 IEEE 9th Annual Computing and Communication Workshop and Conference (CCWC)*, Las Vegas, USA, 2019 (https://doi.org/10.1109/ccwc.2019.8666599).

[18] X. Zhang *et al.*, "An Efficient Android-based Multimodal Biometric Authentication System with Face and Voice", *IEEE Access*, vol. 8, pp. 102757–102772, 2020 (https://doi.org/10.1109/access.2020.2999115).

[19] E. Al Alkeem *et al.*, "Robust Deep Identification Using ECG and Multimodal Biometrics for Industrial Internet of Things", *Ad Hoc Networks*, vol. 121, art. no. 102581, 2021 (https://doi.org/10.1016/j.adhoc.2021.102581).

[20] M. Leghari *et al.*, "Deep Feature Fusion of Fingerprint and Online Signature for Multimodal Biometrics", *Computers*, vol. 10, no. 2, art. no. 21, 2021 (https://doi.org/10.3390/computers10020021).

[21] C.F.F. Costa-Filho, J.V. Negreiro, and M.G.F. Costa, "Multimodal Biometric System Based on Autoencoders and Learning Vector Quantization", *Brazilian Congress on Biomedical Engineering*, Vitoria, Brazil, 2020 (https://doi.org/10.1007/978-3-030-70601-2_236).

[22] C. Kamlaskar and A. Abhyankar, "Feature Level Fusion Framework for Multimodal Biometric System Based on CCA with SVM Classifier and Cosine Similarity Measure", *Australian Journal of Electrical and Electronics Engineering*, vol. 20, no. 2, pp. 205–218, 2023 (https://doi.org/10.1080/1448837x.2022.2129147).

[23] Z. Zhang, H. Lu, P. Sang, and J. Wang, "MultiBioGM: A Hand Multimodal Biometric Model Combining Texture Prior Knowledge to Enhance Generalization Ability", in: *Biometric Recognition (CCBR 2023)*, pp. 106–115, 2023 (https://doi.org/10.1007/978-981-99-8565-4_11).

[24] V. Gurunathan and R. Sudhakar, "Multimodal Biometric System Using Palm Vein and Ear Images", *Proceeding of International Conference on Computer Visions and Robotics*, pp. 439–451, 2023 (https://doi.org/10.1007/978-981-99-4577-1_36).

[25] T. Hafs, H. Zehir, A. Hafs, and A. Nait-Ali, "Multimodal Biometric System Based on the Fusion in Score of Fingerprint and Online Handwritten Signature", *Applied Computer Systems*, vol. 28, no. 1, pp. 37–49, 2023 (https://doi.org/10.2478/acss-2023-0006).

[26] M. Ravanelli and Y. Bengio, "Speaker Recognition from Raw Waveform with SincNet", *2018 IEEE Spoken Language Technology Workshop (SLT)*, Athens, Greece, 2018 (https://doi.org/10.1109/slt.2018.8639585).

[27] Y. Badr, P. Mukherjee, and S.M. Thumati, "Speech Emotion Recognition using MFCC and Hybrid Neural Networks", *Proceedings of the 13th International Joint Conference on Computational Intelligence*, pp. 366–373, 2021 (https://doi.org/10.5220/0010707400003063).

[28] A.K. Dubey and V. Jain, "Comparative Study of Convolution Neural Network's ReLU and Leaky-ReLU Activation Functions", in: *Applications of Computing, Automation and Wireless Systems in Electrical Engineering*, pp. 873–880, 2019 (https://doi.org/10.1007/978-981-13-6772-4_76).

[29] D.B. Jadhav, G.S. Chavan, V.C. Bagal, and R.R. Manza, "Review on Multimodal Biometric Recognition System Using Machine Learning", *Artificial Intelligence and Applications*, vol. 20, pp. 1–7, 2023 (https://doi.org/10.47852/bonview3202593).

[30] C. Sanderson and B.C. Lovell, "Multi-region Probabilistic Histograms for Robust and Scalable Identity Inference", in: *Advances in Biometrics (Conference Proceedings)*, pp. 199–208, 2009 (https://doi.org/10.1007/978-3-642-01793-3_21).

[31] D. Snyder, D. Povey, and G. Chen, "MUSAN: A Music, Speech, and Noise Corpus", *ArXiv*, 2015 (https://doi.org/10.48550/arxiv.1510.08484).

[32] A. Zelinsky, "Learning OpenCV–Computer Vision with the OpenCV Library", *IEEE Robotics & Automation Magazine*, vol. 16, no. 3, p. 100, 2009 (https://doi.org/10.1109/mra.2009.933612).

[33] M. Wang, Z. Wang, and J. Li, "Deep Convolutional Neural Network Applies to Face Recognition in Small and Medium Databases", *2017 4th International Conference on Systems and Informatics (ICSAI)*, Hangzhou, China, 2017 (https://doi.org/10.1109/icsai.2017.8248499).

[34] P. Ke, M. Cai, H. Wang, and J. Chen, "A Novel Face Recognition Algorithm Based on the Combination of LBP and CNN", *2018 14th IEEE International Conference on Signal Processing (ICSP)*, Beijing, China, 2018 (https://doi.org/10.1109/icsp.2018.8652477).

[35] Q. Xu and N. Zhao, "A Facial Expression Recognition Algorithm Based on CNN and LBP Feature", *2020 IEEE 4th Information Technology, Networking, Electronic and Automation Control Conference (ITNEC)*, Chongqing, China, 2020 (https://doi.org/10.1109/itnec48623.2020.9084763).

[36] A.B. Jung *et al.*, "Imgaug", GitHub: San Francisco, USA, 2020 (https://github.com/aleju/imgaug).

[37] J.-M. Cheng and H.-C. Wang, "A Method of Estimating the Equal Error Rate for Automatic Speaker Verification", *2004 International Symposium on Chinese Spoken Language Processing*, Hong Kong, China, 2004 (https://doi.org/10.1109/CHINSL.2004.1409642).

[38] K. He, X. Zhang, S. Ren, and J. Sun, "Deep Residual Learning for Image Recognition", *IEEE Conference on Computer Vision and Pattern Recognition*, Las Vegas, USA, 2016 (https://doi.org/10.1109/cvpr.2016.90).

[39] I. Aliyu, M.A. Bomoi, and M. Maishanu, "A Comparative Study of Eigenface and Fisherface Algorithms Based on OpenCV and Sci-kit Libraries Implementations", *International Journal of Information Engineering & Electronic Business*, vol. 14, no. 3, pp. 30–40, 2022 (https://doi.org/10.5815/ijieeb.2022.03.04).

[40] D. Snyder *et al.*, "X-vectors: Robust DNN Embeddings for Speaker Recognition", *2018 IEEE International Conference on Acoustics, Speech and Signal Processing (ICASSP)*, Calgary, Canada, 2018 (https://doi.org/10.1109/icassp.2018.8461375).

[41] Y. Kortli, M. Jridi, A. Al Falou, and M. Atri, "Face Recognition Systems: A Survey", *Sensors*, vol. 20, no. 2, art. no. 342, 2020 (https://doi.org/10.3390/s20020342).

[42] A. Verma, A. Goyal, N. Kumar, and H. Tekchandani, "Face Recognition: A Review and Analysis", in: *Computational Intelligence in Data Mining (Conference Proceedings)*, pp. 195–210, 2022 (https://doi.org/10.1007/978-981-16-9447-9_15).

[43] Z. Bai and X. L. Zhang, "Speaker Recognition Based on Deep Learning: An Overview", *Neural Networks*, vol. 140, pp. 65–99, 2021 (https://doi.org/10.1016/j.neunet.2021.03.004).

[44] A.Q. Ohi, M.F. Mridha, M.A. Hamid, and M.M. Monowar, "Deep Speaker Recognition: Process, Progress, and Challenges", *IEEE Access*, vol. 9, pp. 89619–89643, 2021 (https://doi.org/10.1109/access.2021.3090109).

[45] M. Gofman *et al.*, "Multimodal Biometrics via Discriminant Correlation Analysis on Mobile Devices", *International Conference on Security and Management (SAM)*, Las Vegas, USA, 2018.

[46] R. Ramachandra *et al.*, "Smartphone Multimodal Biometric Authentication: Database and Evaluation", *ArXiv*, 2019 (https://doi.org/10.48550/arXiv.1912.02487).

[47] G. Antipov, N. Gengembre, O.L. Blouch, and G.L. Lan, "Automatic Quality Assessment for Audio-visual Verification Systems: The LOVe Submission to NIST SRE Challenge 2019", *ArXiv*, 2020 (https://doi.org/10.48550/arXiv.2008.05889).

[48] S.O. Sadjadi *et al.*, "The 2019 NIST Audio-visual Speaker Recognition Evaluation", *The Speaker and Language Recognition Workshop: Odyssey 2020*, Tokyo, Japan, 2020 (https://doi.org/10.21437/odyssey.2020-37).

[49] M. Liu *et al.*, "Exploring Deep Learning for Joint Audio-visual Lip Biometrics", *ArXiv*, 2021 (https://doi.org/10.48550/arXiv.2104.08510).

[50] G. Fenu and M. Marras, "Demographic Fairness in Multimodal Biometrics: A Comparative Analysis on Audio-visual Speaker Recognition Systems", *Procedia Computer Science*, vol. 198, pp. 249–254, 2022 (https://doi.org/10.1016/j.procs.2021.12.236).

[51] M.S. Saeed *et al.*, "Single-branch Network for Multimodal Training", *2023 IEEE International Conference on Acoustics, Speech and Signal Processing (ICASSP)*, Rhodes Island, Greece, 2023 (https://doi.org/10.1109/ICASSP49357.2023.10097207).

[52] G.P. Rajasekhar and J. Alam, "Audio-visual Speaker Verification via Joint Cross-attention", *International Conference on Speech and Computer*, Dharwad, India, 2023 (https://doi.org/10.1007/978-3-031-48312-7_2).

[53] R. Tao *et al.*, "Multi-stage Face-voice Association Learning with Keynote Speaker Diarization", *ArXiv*, 2024 (https://doi.org/10.48550/arXiv.2407.17902).

[54] M. Abdrakhmanova *et al.*, "One Model to Rule Them All: A Universal Transformer for Biometric Matching", *IEEE Access*, vol. 12, pp. 96729–96739, 2024 (https://doi.org/10.1109/ACCESS.2024.3426602).

[55] A. Farhadipour, M. Chapariniya, T. Vukovic, and V. Dellwo, "Comparative Analysis of Modality Fusion Approaches for Audio-visual Person Identification and Verification", *ArXiv*, 2024 (https://doi.org/10.48550/arXiv.2409.00562).

[56] C. Wang, H. Zhu, and L. Xu, "Research on the Improvement of the Target Speaker Recognition System Based on Dual-Modal Fusion", *2024 5th International Conference on Computer Vision, Image and Deep Learning (CVIDL)*, Zhuhai, China, 2024 (https://doi.org/10.1109/cvidl62147.2024.10603613).

[57] Y. Jiang *et al.*, "Target Speech Diarization with Multimodal Prompts", *ArXiv*, 2024 (https://doi.org/10.48550/arXiv.2406.07198).

[58] C. Peng, L. He, and D. Su, "Fuse after Align: Improving Face-voice Association Learning via Multimodal Encoder", *ArXiv*, 2024 (https://doi.org/10.48550/arXiv.2404.09509).

Khaled Merit, Ph.D.
Laboratory of TIT, Department of Electrical Engineering
https://orcid.org/0000-0002-7762-1898
E-mail: merit.khaled@univ-bechar.dz
Tahri Mohammed University of Bechar, Bechar, Algeria
https://www.univ-bechar.dz

Mohammed Beladgham, Ph.D., Full Professor
Laboratory of TIT, Department of Electrical Engineering
https://orcid.org/0000-0002-2371-6859
E-mail: beladgham.mohammed@univ-bechar.dz
Tahri Mohammed University of Bechar, Bechar, Algeria
https://www.univ-bechar.dz

Tree Quantum Key Agreement Protocol for Secure Multiparty Communication

Rima Djellab[1], Youssouf Achouri[2], Malak Emziane[3], and Lyamine Guezouli[3]

[1]*LAMIE Laboratory, University of Batna 2, Batna, Algeria,*
[2]*LASTIC Laboratory, University of Batna 2, Batna, Algeria,*
[3]*LEREESI Laboratory, HNS-RE2SD, Batna, Algeria*

https://doi.org/10.26636/jtit.2024.4.1711

Abstract — The paper introduces a tree multiparty quantum key agreement protocol for secure communication between multiple participants, specifically tailored for tree topologies. Based on the BB84 protocol, the proposed solution employs hierarchical tree structures and XOR operations to facilitate efficient and secure key generation. Key elements are exchanged among participants in an equitable manner, ensuring that each participant contributes equally to the generation of the shared key. The protocol demonstrates robust security, effectively defending against both external and internal attacks, and achieves a quantum efficiency of ½(*N*–1), where *N* is the number of participants. Additionally, the protocol is readily implementable with current quantum technologies, utilizing single-photon transmission to facilitate secure key distribution.

Keywords — BB84 protocol, quantum efficiency, quantum key agreement, tree topology

1. Introduction

Cryptography protocols are essential for establishing secure communication channels. Key distribution is a vital process for creating these mechanisms, as it enables the exchange of secret data between remote parties over an insecure channel. Although most key distribution protocols utilize asymmetric algorithms [1], their security is tied to the difficulty of solving specific mathematical problems, ensuring computational security within traditional computing environments. Nevertheless, the fact that computational capabilities of potential eavesdroppers increase due to technological progress could render these protocols ineffective.

Asymmetric algorithms, such as RSA or ECC [2] rely on the mathematical difficulty of such problems as factorizing large prime numbers or solving discrete logarithms. The security of these protocols is predicated on computational infeasibility, meaning they are secure as long as solving the underlying mathematical problem remains computationally too time-consuming.

However, with the advent of quantum computing, the efficacy of these traditional protocols tends to be insufficient, as quantum computers – leveraging principles of quantum mechanics – promise to solve these complex problems in polynomial time.

BB84 [3] is a protocol that is commonly used in the field of quantum key distribution, as it facilitates the generation of a completely secure key at the end of exchanges. This key may be subsequently employed in a one-time pad (OTP) protocol to secure the communication channels.

One significant advancement in this field is the multiparty quantum key agreement (MQKA) protocol which extends the benefits of quantum key distribution to multiple parties. MQKA allows a group of participants to establish a shared secret key, ensuring that all parties are equally involved in the key generation process [4]. This is particularly useful in scenarios where collaboration among multiple entities is required. By leveraging entanglement and quantum communication channels, MQKA protocols provide robust security guarantees and are resilient to quantum attacks, ensuring integrity and confidentiality of data.

With that borne in mind, we propose a tree MQKA (T-MQKA) protocol tailored to facilitate key agreement within a tree-organized group. By leveraging the proven security of quantum principles, T-MQKA aims to fortify communication channels, ensuring their resilience against emerging threats posed by quantum computing advancements. The rest of this paper is organized as follows. A brief overview of classic and quantum key management approaches is presented in Section 2, with preliminaries and related work following in Sections 3 and 4, respectively. In Section 5, the proposed protocol is presented. A comparative analysis of our T-MQKA protocol benchmarking it against solutions belonging to a similar category (tree topology), with an emphasis placed on their quantum efficiency, is given in Sections 6–7. In Section 8, a security analysis is provided and, finally, conclusions are drawn in Section 9.

2. Classic Versus Quantum Key Management

In classic contexts, key management protocols fall into three main categories: centralized, decentralized, and distributed [5]. In centralized protocols, a central entity oversees key management and distribution within the group. Decentralized protocols distribute this responsibility among multiple entities, mitigating issues such as bottlenecks. This catego-

ry further distinguishes between time-oriented decentralized protocols, where key changes occur at set intervals, and dynamic-oriented protocols, where key adjustments accommodate member departures or arrivals to maintain confidentiality.

The last category, distributed or also called by agreement, entails all members contributing to key elaboration, with the key being a product of collective calculations, rather than a predetermined result. Typically, Diffie-Hellman-based, the security of such protocols is contingent on the adversary's computational capabilities.

Quantum cryptography emerges as a cornerstone application of quantum informatics, with various protocols developed for the needs of this specific field, including quantum key distribution (QKD) and quantum key agreement (QKA). When implemented correctly, QKD offers unconditional security. The BB84 protocol stands out as a prominent QKD example, aiming to resolve the classic key establishment problem by generating a symmetric key between two parties.

In contrast to classic methods, the security of quantum cryptography protocols, including QKD, is not contingent on the adversary's computational capabilities, but rather on quantum principles, enabling to detect intrusions during the key elaboration stage. Through QKD, multiple participants can securely share secret and random keys.

It is worth noting the distinction between QKD and QKA. In QKD, one entity generates the key distributed to other participants, while in QKA, none of the participants possess the key initially. Instead, it is collectively generated through communication and calculations, ensuring that no subset of participants can determine the key independently.

Since the pioneering work performed by Zhou *et al.* [6], numerous quantum key agreement protocols have been proposed, including two-party and multi-party variants (MQKA protocols). This study focuses specifically on multi-party protocols, categorized based on transmission structures into complete (CGT-MQKA), circle (CT-MQKA), and tree (TT-MQKA) configurations (Fig. 1).

In the complete-graph category, every participant shares their secret sequence with all other participants. Within the circle category, one participant transmits the sequence to the next participant, who then processes it and subsequently passes it on to the subsequent participant, continuing until the sequence returns to the original sender. The tree category involves a root participant disseminating information to other participants organized in a hierarchical tree structure.

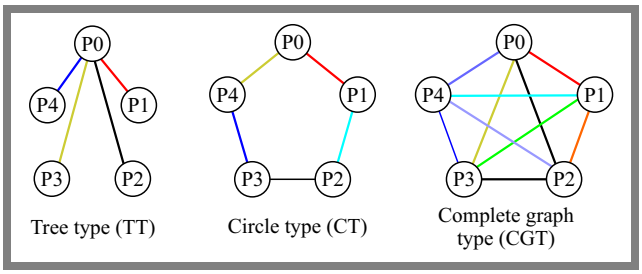

Fig. 1. Classification of quantum key agreement protocols [7].

3. Preliminaries

3.1. Superposition

In quantum computing, the fundamental unit of information infrastructure is represented as a qubit. The polarization state of a photon serves as the pivotal characteristic defining the value held by the qubit. From the physical perspective, the qubit may be represented by elementary entities, such as photons. In the context of quantum computing, the qubit plays the role of a data unit, analogous to the classical bit. Notably, a single qubit possesses the capacity to concurrently store two values of information (1 and 0). In a Dirac notation, the qubit is symbolized as follows:

$$|\psi\rangle = \alpha|0\rangle + \beta|1\rangle \ , \tag{1}$$

where:

$$|0\rangle = \begin{pmatrix} 1 \\ 0 \end{pmatrix} \quad \text{and} \quad |1\rangle = \begin{pmatrix} 0 \\ 1 \end{pmatrix} \ . \tag{2}$$

In Eq. (1) α, β are complex numbers, where:

$$|\alpha|^2 + |\beta|^2 = 1 \ . \tag{3}$$

α represents the probability amplitude to have $|0\rangle$ and β is the probability amplitude to have $|1\rangle$ after the measurement.

3.2. Non-cloning Theorem

The qubit, in accordance with the principle of superposition, can concurrently embody two distinct values. Upon measurement, one of these values is arbitrarily discarded, giving way to the manifestation of the other. This inherent property renders replication of a quantum state unattainable, as any attempt to perform a measurement inevitably alters the state, thereby modifying the value held by the qubit. A fundamental tenet underpinning quantum cryptography is encapsulated in the non-cloning theorem.

3.3. Heisenberg Uncertainty Principle

A quantum state comprises a confluence of diverse parameters, such as the position and velocity of a photon. According to Heisenberg's principle, attempting to measure one of these parameters inherently disrupts the other. This principle fortifies the rationale behind the non-cloning theorem, as obtaining a complete description of a quantum state is imperative for replication. Conversely, any measurement inherently perturbs certain characteristics, precluding the precise duplication of the quantum state without possessing its comprehensive description.

These foundational principles afford security to communications shared between entities, often denoted as Alice and Bob, without susceptibility to eavesdropping. Any attempt by a third-party listener to intercept the communication inevitably distorts its value, creating a discrepancy discernible to Alice and Bob through a post-transmission examination of

error rates. This mechanism enables the detection of eavesdropping attempts, as alterations to the message's value are indicative of unauthorized intrusion. It is important to note that while quantum cryptography facilitates secure communication, the inherently random nature of the messages precludes the transmission of predetermined information. Nevertheless, the random string generated through quantum processes may serve as an ideal key in the implementation of the one-time pad (OTP) cryptographic protocol.

4. Related Works

In contrast to key distribution, the key agreement process involves the creation of a key through exchanges between two or more participants, in a manner analogous to the Diffie-Hellman protocol. Each participant contributes a part of the key, yet none can individually ascertain the key in its entirety. Such a concept was introduced by Zhou *et al.* in [6]. The paper presents the first proposal of a quantum key agreement protocol, leveraging quantum teleportation to generate shared keys. However, subsequent analysis revealed its susceptibility to insider attacks [8].

In [9], a key agreement protocol based on BB84 was introduced. Nevertheless, this protocol relied on quantum memory, the utilization of which remains prohibitively costly. Sun *et al.* [10] proposed enhancements to the multiparty quantum key agreement, introducing two additional unitary operations to improve protocol efficiency within the circle-based category. Another protocol predicated on entanglement swapping was proposed, and it utilized Bell states as quantum resources and Bell measurements as primary operations [11]. Furthermore, an alternative multi-party quantum key agreement protocol based on two entangled qubits was proposed, albeit it was applicable solely to three parties [12].

In article [13], leveraging a tree structure, the authors proposed a multiparty quantum key agreement protocol grounded in Greenberger-Horne-Zeilinger (GHZ) states. Subsequently, Ye *et al.* [14] and Sun *et al.* [15] developed two-party and three-party quantum key agreement protocols, respectively, based on unitary operations and four-qubit cluster states or an entangled six-qubit state.

In [16], the authors proposed a quantum key agreement protocol based on BB84. Differing from prior endeavors [8], this protocol ensures computational security against internal attacks through the utilization of hash functions, while preserving unconditional security against eavesdropping. It is intended for key agreement between two participants.

Table 1 summarizes the different protocols, referencing the best known solutions described in the literature.

To the best of our knowledge, there is no proposal for a key agreement protocol that may be used within a tree-organized group, founded on BB84 and employing XOR operation. This deficiency underscores our motivation to present protocols grounded in BB84, not only due to their well-established security but also their XOR-based efficiency, with simplicity and low execution cost being their additional advantages.

5. Proposed Protocol

The objective of the proposed tree-MQKA (T-MQKA) protocol is to address the issue of key generation and distribution in a hierarchically structured group relying on a tree configuration. The concept is based on the BB84 quantum key distribution protocol the security of which has been demonstrated in [17]. The initial phase of the protocol entails the execution of BB84 between the root node and each node within the group. Subsequent to the completion of the BB84 process, each node shares a confidential and secure string with the root node. Each of these strings is divided into two parts:

– seed (designated as S), which is employed in the generation of the final group key,

– part K, which serves as an intermediate key during the distribution of parts.

Upon completion of the initial stage, the root node proceeds with the party distribution phase. Subsequently, each node within the group will receive the S parts of the other nodes which have been XOR-ed. The resulting message is then encrypted with its K part and transmitted from the root. The aforementioned procedure is repeated for each remaining node in the group until all the nodes have obtained the S parts of the other nodes. Once a node has received the encrypted message containing the combination of S parts, it can decrypt the message and then add its own part, thereby obtaining the final group key.

5.1. Algorithm Description

For clarity, an algorithmic description of procedure is provided below.

Step 1 is the first phase, where the group is initialized and the root node is selected from among the nodes in the group, as shown in Algorithm 1.

Algorithm 1 Initialization of participants and the central node

1: Let N be the number of participants
2: Let $P[1], P[2], \ldots, P[N]$ be the set of participants
3: Let C be the central node selected from the participants

In step 2, each participant executes the BB84 protocol, thereby maintaining a chain that is shared with the root node (Algorithm 2). The security and confidentiality of the chain are guaranteed by the inherent security of BB84.

Algorithm 2 Execution of the BB84 protocol

1: **for** each participant $P[i]$ from the set of participants, where i ranges from 1 to N **do**
2: **if** $P[i] \neq C$ **then**
3: $P[i]$ executes the BB84 protocol with the central node C.
4: Store the resulting key as $K[i]$.
5: **end if**
6: **end for**

Tab. 1. Summary of existing quantum key agreement protocols.

Protocol name	Purpose	Key features	Reference
Quantum key agreement via teleportation	QKA	Utilizes quantum teleportation; susceptible to insider attacks	[6], [8]
BB84-based quantum key agreement	QKA	Relies on quantum memory; costly	[9], [16]
Enhanced multiparty quantum key agreement	MQKA	Introduces two additional unitary operations	[10]
Entanglement swapping-based multiparty QKA	MQKA	Uses Bell states and Bell measurements	[11]
Two qubits entanglement-based three-party QKA	3-party QKA	Applicable solely to three parties	[12]
GHZ states-based multiparty QKA	MQKA	Leverages a tree structure and GHZ states	[13]
Unitary operations-based two-party QKA	2-party QKA	Uses unitary operations and four-qubit cluster states	[14]
Unitary operations-based three-party QKA	3-party QKA	Utilizes an entangled six-qubit state	[15]
BB84-based two-party QKA with hashes	2-party QKA	Ensures computational security against internal attacks; hash functions	[8], [16]

Finally, in step 3, the chain is divided into two parts, the first of which is employed in the key agreement process, while the other is utilized as an intermediate key in the key distribution process. The final phase of the protocol entails the distribution of the key seeds and the construction of the final key through the assembly of all the key seeds. The chain obtained in the second phase is split into two parts: the first part is used in the key agreement process, while the other is used as an intermediate key in the key distribution process. The missing seeds S_i are transmitted to each node by sending an encrypted message containing them. Encryption is performed with the k part that it shares with the root – see Algorithm 3.

Algorithm 3 Key agreement and key distribution

$Xor\_result = 0$
for each participant $P[i]$ in the set of participants **do**
    split $K[i]$ into $S_{C,P[i]}$ and $K_{C,P[i]}$
end for
for each participant $P[j]$ where $j \neq i$ **do**
    $Xor\_result = Xor\_result \oplus S_{C,P[j]}$
    $Xor\_result = Xor\_result \oplus K_{C,P[i]}$
    ▷ Central node encrypts the result
    $C \rightarrow P[i] : Xor\_result$
    ▷ Central node sends encrypted result to $P[i]$
    $Xor\_result = Xor\_result \oplus K_{C,P[i]}$
    ▷ $P[i]$ decrypts Xor_result
    $Xor\_result = Xor\_result \oplus S_{C,P[i]}$
    ▷ $P[i]$ adds its seed and retrieves the final key
end for

Consider an example with a group of 4 nodes, a root node and 3 other nodes, as illustrated in Fig. 2, with the notation provided in Tab. 2. The center node A, acting as the initiator, shares the generated seeds of each participant with the remaining members through an XOR operation. Subsequently, the root node encrypts the XOR output using a shared key with each participant. Upon receiving the encrypted seeds, each participant (B, C, and D) decrypts the data and incorporates its own seed to derive the final key. This iterative process is carried out for all the members. At the end, every participant will have obtained the final key.

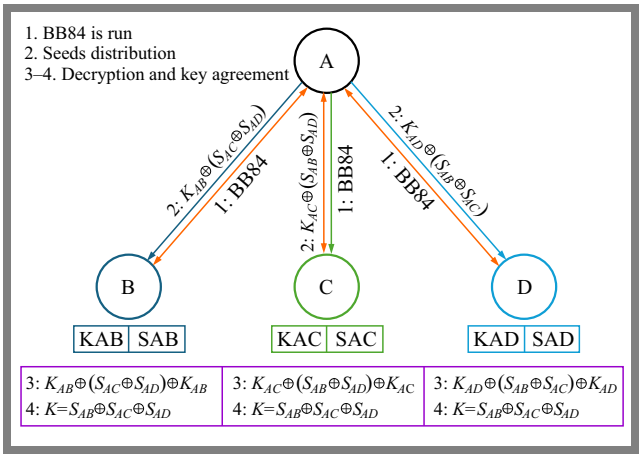

Fig. 2. New T-MQKA based on BB84.

Tab. 2. Notations of the example of proposed protocol.

Notation	Description
A, B, C, D	Participants (nodes)
K_{AB}, K_{AC}, K_{AD}	Encoding keys of participants B, C, and D
S_{AB}, S_{AC}, S_{AD}	Seeds part shared between A and respectively B, C, and D
$A \rightarrow B$:	A sends to B
$\oplus$	Bitwise XOR (exclusive OR)

The step-by-step equations shown in Algorithm 4 illustrate the communication process between A, B, C, and D, respectively, aiming to determine final key.

Algorithm 4 Key agreement and key distribution

1: A $\rightarrow$ B : $(S_{AC} \oplus S_{AD}) \oplus K_{AB}$
▷ A sends $(S_{AC} \oplus S_{AD})$ encrypted by K_{AB}
2: B does $[(S_{AC} \oplus S_{AD}) \oplus K_{AB}] \oplus K_{AB} \oplus S_{AB}$
▷ B decrypts and adds its seed S_{AB} and gets the final key
3: A $\rightarrow$ C : $(S_{AB} \oplus S_{AD}) \oplus K_{AC}$
▷ A sends $(S_{AB} \oplus S_{AD})$ encrypted by K_{AC}
4: C does $[(S_{AB} \oplus S_{AD}) \oplus K_{AC}] \oplus K_{AC} \oplus S_{AC}$
▷ C decrypts and adds its seed S_{AC} and gets the final key
5: A $\rightarrow$ D : $(S_{AB} \oplus S_{AC}) \oplus K_{A,D}$
▷ A sends $(S_{AB} \oplus S_{AC})$ encrypted by K_{AD}
6: D does $[(S_{AB} \oplus S_{AC}) \oplus K_{AD}] \oplus K_{AD} \oplus S_{AD}$
▷ D decrypts and adds its seed S_{AD} and gets the final key

5.2. Protocol Properties

Tree topology is selected based on the fact that it is more resilient to collusive attacks, as it needs fewer qubits for the all-to-all transmission of quantum states. Consequently, it reduces the need for quantum resources. It is worth noting another advantage here: if a device operating within a tree topology fails, the failure does not necessarily affect the entire communication network, making it more reliable.

The proposed solution exhibits the following characteristics:

- Implementation of the XOR operation in the protocols lowers computational complexity.
- The BB84 protocol is used, relying on a single-photon scenario, making the proposed solution compliant with current technology.
- Security is based on the proven capabilities of BB84 [17], [18] which employed probabilistic model checking techniques with the PRISM model checker. The resultant key derived from BB84 is safeguarded by the principles of quantum physics, automatically detecting any eavesdropping attempts during its generation phase. Similarly, the seed, being both secure and random, remains undisclosed until execution of the BB84 protocol.
- There is no need to preload any of the secret or random seeds, as they are secured by quantum rules.
- Generation of the group's common key takes place through secure exchanges between all participants, with each of them contributing their seed to formulate the final key, and such an approach allows to keep it unknown to any participants beforehand.
- Participants are prevented from recovering the shares of other participants, is realized by XOR operations.
- Thanks to optimization of the message exchange process, the solution requires only $2\ (N-1)$ messages.
- The participating nodes contribute equally to the generation of the final key. Each node adds its seed to the collective construction of the group key.

6. Security Analysis

The concept of agreeing upon a quantum key presents distinct challenges compared to key distribution, as it necessitates active involvement of all participants in the key generation process. Unlike key distribution, where a single participant prepares and disseminates the key to others, quantum key agreement demands that no participant possesses or is capable of predicting the key beforehand. It requires each participant to contribute equally to the key generation process, ensuring that the resulting key remains unpredictable to any subset of participants.

The proposed tree quantum key agreement protocol (T-MQKA) upholds this fundamental principle by ensuring that participants lack prior knowledge of the key. Instead, each participant contributes a seed to the key generation process, relying on a secure exchange facilitated by keys generated via the BB84 protocol. This quantum-based methodology guarantees the complete security of the exchanged keys, thereby preserving the integrity and fairness of the key generation process in the quantum key agreement phase.

6.1. Immunity to Internal Attacks

Internal attacks can be initiated by malicious participants within the network. These attacks are divided into two main categories: attacks undertaken by a single participant and massive attacks involving multiple participants.

A single malicious participant may attempt to deduce the group key using their own key $K_{C,P[i]}$ and the messages received from the root node. The resilience of T-MQKA to such attacks is ensured through the following mechanisms:

- Key division. Each BB84 key generated by the root node is divided into two parts: S and $K_{C,P[i]}$. The S part is used to generate the group key, while the $K_{C,P[i]}$ part is used for encrypting and decrypting S. This division adds a layer of complexity, as a single participant would need to know multiple S and $K_{C,P[i]}$ values to deduce the group key.
- XOR operations. The m' messages sent from the root node to each participant are formed by XOR-ing multiple S values with the participant's $K_{C,P[i]}$. For example, $m' = S_{i+1} \oplus S_{i+2} \oplus S_n \oplus (K_{C,P[i]})$. The receiving participant can then compute the group key by XOR-ing m' with its $K_{C,P[i]}$. This XOR operation ensures that knowing a single $K_{C,P[i]}$ value without the corresponding S values provides no useful information.

Therefore, it is mathematically challenging for a single participant to reconstruct the group key without possessing the knowledge of other S and K values, which makes the protocol resistant to single-participant attacks.

In a collusive attack, multiple participants might collude to share their information to determine the group key. Despite this, T-MQKA remains secure due to the following reasons:

- Multiple XOR-ed values. Each m' message sent to a participant includes XOR operations with multiple S values from different nodes. For example, $m' = S_i \oplus S_{i+2} \oplus S_n \oplus (K_{C,P[i]}$ for $N_{i+1})$. This means that even if two or

more participants collude, they need to gather all relevant S values from other nodes to reconstruct the group key.

- Information distribution. The information necessary to compute the group key is distributed across all participants. Each participant has only partial information, and the full reconstruction requires knowledge of all S and $K_{C,P[i]}$ values, which is highly unlikely to be achieved through collusion alone.

Thus, the complexity and distribution of the S and $K_{C,P[i]}$ values in the protocol ensure its robustness and resilience to such attacks.

6.2. External Attacks

External attacks are carried out by entities that are not part of the network, such as eavesdroppers or hackers attempting to intercept communications. T-MQKA incorporates several mechanisms to safeguard against these threats.

An external attacker might try to intercept the m' messages sent from the root node to other nodes. The protocol protects against this type of attack through the following measures:

- Encrypted messages. Each m' message is encrypted using a unique $K_{C,P[i]}$ key. Intercepting these messages without the corresponding $K_{C,P[i]}$ key provides no useful information. The attacker would only see the result of multiple XOR operations, appearing as random data without the proper keys.
- Integrity checks. Any attempt to modify the intercepted messages would be detected during decryption by the recipient nodes. The XOR operation ensures that any tampering results in the computation of an incorrect group key, which would be immediately noticeable to the participants.

An attacker might attempt to replace the $K_{C,P[i]}$ or S keys during transmission. The protocol is immune to this threat through:

- Quantum security properties. The S keys are distributed using the BB84 protocol, ensuring that any interception or replacement attempt is immediately detectable due to the principles of quantum mechanics. Any eavesdropping will introduce detectable errors in the key.
- Detection mechanisms. Participants can detect any anomalies in the keys through standard BB84 error rate checks. If the error rate exceeds a predefined threshold, the participants know that an interception attempt has occurred.

Half of the transmitted particles are chosen as detection particles to prevent eavesdropping. These detection particles serve as a safeguard using two mechanisms described below:

- Random selection. The selection of detection particles is random, making it difficult for an external attacker to predict which particles are used for detection. This randomness ensures that any eavesdropping attempts are likely to be detected.
- Error rate monitoring. By monitoring the error rates of the detection particles, the protocol may identify and thwart any eavesdropping attempts. High error rates indicate the presence of an eavesdropper, warning the participants.

In conclusion, T-MQKA offers robust security against both internal and external attacks. The use of quantum properties for key distribution, combined with complex operations involving S and $K_{C,P[i]}$ keys, ensures that the group key remains secure and that any attempts to compromise the key are quickly detected. The protocol's design inherently protects it against various threat vectors, maintaining the integrity and confidentiality of the shared keys.

7. Qubit Efficiency Calculation

Qubit efficiency (QE) is a key measure of how effectively quantum resources are used in the protocol. It is defined as the ratio of the total bits in the final group key to the total number of qubits used while executing the protocol, including any classic bits exchanged for decoding the message, as described in [19]. In the proposed protocol, qubit efficiency is determined by the following factors:

- Each BB84 key is divided into two parts: $S_{C,P[i]}$, which helps form the group key and $K_{C,P[i]}$, used for encryption and decryption. For the purpose of our this analysis, $S_{C,P[i]}$ is assumed to be half the length of the BB84 key (n), hence $|S_{C,P[i]}| = \frac{n}{2}$.
- The total length of the group key is equal to $\frac{n}{2}$.
- The generation of a BB84 key between the central node and each child node requires n qubits, and the total number of qubits used in the network is $(N-1) \times n$.

Based on these assumptions, the qubit efficiency for a network with N participants is given by:

$$QE = \frac{c}{q+b}\,, \tag{4}$$

where c represents the length of the final group key, which is $\frac{n}{2}$, q is the total number of qubits used, calculated as $(N-1) \times n$, and b is the total number of classical bits exchanged, which is considered negligible in this analysis.

The qubit efficiency equation simplifies to:

$$QE = \frac{\frac{n}{2}}{(N-1) \times n} = \frac{1}{2\,(N-1)}\,. \tag{5}$$

Equation (5) illustrates that qubit efficiency decreases as the number of nodes in the network increases. It highlights the protocol's ability to use quantum resources effectively, while maintaining security, particularly in large networks.

Tab. 3. Comparative analysis of MQKA protocols in a tree topology.

Ref.	Topology	Quantum efficiency	Security
[20]	Tree	$QE = \frac{1}{11N}$	Secure
[21]	Tree	$QE = \frac{1}{N(2^{N-1})}$	Secure
Proposed	Tree	$\frac{1}{2\,(N-1)}$	Secure

Overall, this analysis demonstrates the effectiveness of the proposed T-MQKA protocol in optimizing quantum resource utilization, while simultaneously ensuring robust security. The balance between resource efficiency and security makes our protocol well-suited for secure communications relying on quantum networks.

8. Comparative Analysis of Different MQKA Protocols

The comparison of several QKA protocols presented in Tab. 3 shows the quantum efficiency of the proposed T-MQKA protocol and that of different existing MQKA protocols, while Fig. 3 contains a graph illustrating the quantum efficiency of different QKA protocols, including the proposed solution, TT-MQKA, and [21]. The x–axis of the graph represents the number of participants N, while the y–axis indicates the quantum efficiency level.

Figure 3 clearly shows that the new protocol offers decent quantum efficiency compared to other solutions, particularly as the number of nodes (participants) increases, highlighting its potential for more robust and scalable quantum key agreement applications.

The heatmap presented in Fig. 4 visualizes the fact that the proposed T-MQKA protocol performs better, in terms of quantum efficiency, than TT-MQKA and [21]. Such a result shows that the new T-MQKA approach is resource-efficient, meaning that it should be taken into account by all parties as the most competent quantum key distribution solution suitable for small and large-scale networks. The results of fault tolerance tests show that the proposed protocol consistently achieves high QE ratings, regardless of the count of nodes.

9. Conclusion

In this paper, we introduced a tree multiparty quantum key agreement protocol (T-MQKA) intended for securing communications. It is based on the principles of the BB84 protocol and facilitates secure key agreement among multiple participants organized in a tree topology. This new protocol has demonstrated decent quantum efficiency compared to other protocols in its category. Moreover, security analysis has confirmed T-MQKA's resilience against a multitude of potential attacks, ensuring the integrity and confidentiality of data transmission. Its robustness covers both external and internal threats, underscoring the protocol's reliability in safeguarding sensitive information.

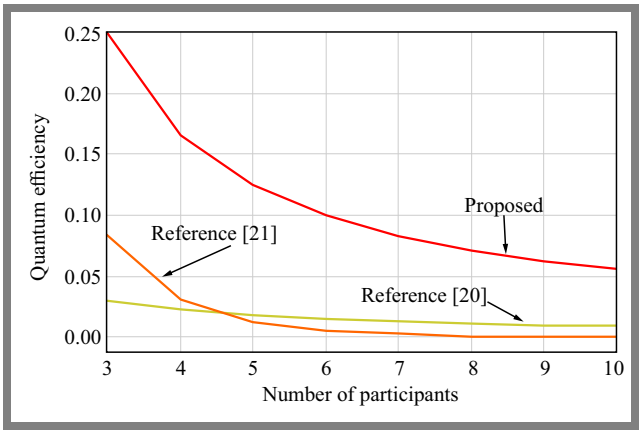

Fig. 3. Quantum efficiency comparison of different T-MKQA protocols.

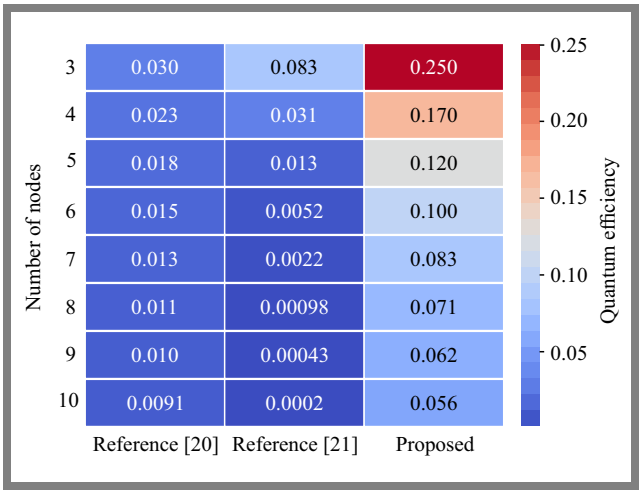

Fig. 4. Heatmap visualization of QE of different tree MKQA protocols for $N = 3 \ldots 10$.

References

[1] Y. Shen, Z. Sun, and T. Zhou, "Survey on Asymmetric Cryptography Algorithms", *2021 International Conference on Electronic Information Engineering and Computer Science (EIECS)*, Changchun, China, 2021 (https://doi.org/10.1109/EIECS53707.2021.9588106).

[2] Y. Cheng, Y. Liu, Z. Zhang, and Y. Li, "An Asymmetric Encryption-based Key Distribution Method for Wireless Sensor Networks", *Sensors*, vol. 23, no. 14, 2023 (https://doi.org/10.3390/s23146460).

[3] V. Martin, J. Martinez-Mateo, and M. Peev, "Introduction to Quantum Key Distribution", in: *Wiley Encyclopedia of Electrical and Electronics Engineering*, 2017 (https://doi.org/10.1002/047134608X.W8354).

[4] B.-X. Liu, R.-C. Huang, Y.-G. Fang, and G.-B. Xu. "Measurement-device-independent Multi-party Quantum Key Agreement", *Frontiers in Quantum Science and Technology*, vol. 2, 2023 (https://doi.org/10.3389/frqst.2023.1182637).

[5] Y. Challal and H. Seba, "Group Key Management Protocols: A Novel Taxonomy", *International Journal of Computer and Information Engineering*, vol. 2, no. 1, 2008 (https://doi.org/10.5281/zenodo.1077968).

[6] N. Zhou, G. Zeng, and J. Xiong, "Quantum Key Agreement Protocol", *Electronics Letters*, vol. 40, no. 18, pp. 1149–1150, 2004 (https://doi.org/10.1049/el:20045183).

[7] B. Liu, D. Xiao, H.-Y. Jia and R.-Z. Liu, "Collusive Attacks to 'Circle-type' Multi-party Quantum Key Agreement Protocols", *Quantum Information Processing*, vol. 15, pp. 2113–2124, 2016 (https://doi.org/10.1007/s11128-016-1264-5).

[8] K.-F. Yu *et al.*, "Design of Quantum Key Agreement Protocols with Fairness Property", arXiv, 2015 (https://doi.org/10.48550/arXiv.1510.02353)

[9] S.-K. Chong and T. Hwang, "Quantum Key Agreement Protocol Based on BB84", *Optics Communications*, vol. 283, no. 6, pp. 1192–1195, 2010 (https://doi.org/10.1016/j.optcom.2009.11.007).

[10] Z. Sun *et al.*, "Improvements on Multiparty Quantum Key Agreement with Single Particles", *Quantum Information Processing*, vol. 12, pp. 3411–3420, 2013 (https://doi.org/10.1007/s11128-013-0608-7).

[11] R.-H. Shi and H. Zhong, "Multi-party Quantum Key Agreement with Bell States and Bell Measurements", *Quantum Information Processing*, vol. 12, pp. 921–932, 2013 (https://doi.org/10.1007/s11128-012-0443-2).

[12] X.-R. Yin, W.-P. Ma, and W.-Y. Liu, "Three-party Quantum Key Agreement with Two-photon Entanglement", *International Journal of Theoretical Physics*, vol. 52, no. 11, pp. 3915–3921, 2013 (https://doi.org/10.1007/s10773-013-1702-4).

[13] G.-B. Xu, Q.-Y. Wen, F. Gao, and S.-J. Qin, "Novel Multiparty Quantum Key Agreement Protocol with GHZ States", *Quantum Information Processing*, vol. 13, p. 2587–2594, 2014 (https://doi.org/10.1007/s11128-014-0816-9).

[14] Y.-F. He and W. Ma, "Quantum Key Agreement Protocols with Four-qubit Cluster States", *Quantum Information Processing*, vol. 14, no. 9, pp. 3483–3498, 2015 (https://doi.org/10.1007/s11128-015-1060-7).

[15] Z. Sun *et al.*, "Multi-party Quantum Key Agreement by an Entangled Six-qubit State", *International Journal of Theoretical Physics*, vol. 55, pp. 1920–1929, 2016 (https://doi.org/10.1007/s10773-015-2831-8).

[16] P. Wang, R. Zhang, and Z. W. Sun, "Practical Quantum Key Agreement Protocol Based on BB84", *Quantum Information and Computation*, vol. 22, pp. 241–250, 2022 (https://doi.org/10.26421/QIC22.3-4-3).

[17] P.W. Shor and J. Preskill, "Simple Proof of Security of the BB84 Quantum Key Distribution Protocol", *Physical Review Letters*, vol. 85, no. 2, p. 441–444, 2000 (https://doi.org/10.1103/PhysRevLett.85.441).

[18] M. Elboukhari, M. Azizi, and A. Azizi, "Verification of Quantum Cryptography Protocols by Model Checking", *International Journal of Network Security and Its Applications*, vol. 2, no. 4, pp. 43–53, 2010 (https://doi.org/10.5121/ijnsa.2010.2404).

[19] A. Cabello, "Quantum Key Distribution in the Holevo Limit", *Physical Review Letters*, vol. 85, pp. 5635–5638, 2001 (https://doi.org/10.1103/PhysRevLett.85.5635).

[20] H. Yang *et al.*, "A Tree-type Multiparty Quantum Key Agreement Protocol Against Collusive Attacks", *International Journal of Theoretical Physics*, vol. 62, art. no. 7, 2023 (https://doi.org/10.1007/s10773-022-05265-w).

[21] J. Gu and T. Hwang, "Improvement of Novel Multiparty Quantum Key Agreement Protocol with GHZ States", *International Journal of Theoretical Physics*, vol. 56, pp. 3108–3116, 2017 (https://doi.org/10.1007/s10773-017-3478-4).

Rima Djellab, Ph.D.
Computer Science Department
https://orcid.org/0000-0001-8072-1868
E-mail: r.djellab@univ-batna2.dz
LAMIE Laboratory, University of Batna 2, Batna, Algeria
http://www.univ-batna2.dz

Youssouf Achouri, Ph.D. Student
Computer Science Department
https://orcid.org/0009-0003-9500-496X
E-mail: y.achouri@univ-batna2.dz
LASTIC Laboratory, University of Batna 2, Batna, Algeria
http://www.univ-batna2.dz

Malak Emziane, Student
Renewable Energies and New Technologies Department
https://orcid.org/0009-0001-1485-8169
E-mail: emziane.malak@hns-re2sd.dz
LEREESI Laboratory, HNS-RE2SD, Batna, Algeria
http://www.hns-re2sd.dz

Lyamine Guezouli, Ph.D.
Renewable Energies and New Technologies Department
https://orcid.org/0000-0002-7406-7633
E-mail: lyamine.guezouli@hns-re2sd.dz
LEREESI Laboratory, HNS-RE2SD, Batna, Algeria
http://www.hns-re2sd.dz

Metamaterial-based Luneburg Lens for RF Applications Using Additive Manufacturing

Emma M. Sadoyan, Mark S. Mnatsakanyan, and Suren G. Eyramjyan

ATG CJSC, Yerevan, Armenia

https://doi.org/10.26636/jtit.2024.4.1786

Abstract — This article takes a detailed look at modeling, simulating, calculating, and fabricating a Luneburg lens using a single material and advanced 3D printing technology. The Luneburg lens is a type of gradient index lens that is spherically symmetrical, which simplifyies its manufacturing process and enhances its structural stability. However, fabrication may be expensive due to the special materials required for manufacturing. Discovering simpler and cost-effective production methods would enable the wider use of Luneburg lenses across various fields. The objective of this study was to use the lens to increase the gain and directivity of antennas at 5.8 GHz while maintaining a compact lens size and using low-cost material, such as ABS-like filament. A single-cell cross-shaped structure was utilized to construct the lens using 3D printing technology.

Keywords — 3D printing, ABS plastic, Luneburg lens, metamaterial

1. Introduction

The Luneburg lens [1] is a type of gradient index lens (GRIN) characterized by the fact that its refractive index n varies gradually from the center outward. The gradual change in the refractive index causes a curved path for the radiation beam [2].

Ideally, the refractive index of the inner layer of the Luneburg lens should be $\sqrt{2}$ and ought to gradually decrease towards the outer layer, until it reaches a value of 1, with the variation complying with the following formula:

$$n(r) = \sqrt{\varepsilon(r)} = \sqrt{2 - \left(\frac{r}{R}\right)^2}, \tag{1}$$

where ε is the effective dielectric permittivity, r is the radius of each layer, and R is the radius of the outer layer [1]–[4]. The Luneburg lens finds various applications, including in acoustics [5]–[8], optics [9]–[12], as well as antenna, communication and radar system designs [13]–[17].

This paper presents a detailed study of the process of designing a Luneburg lens. It analyzes the use of various structures to boost the performance at 5.8 GHz, as well as to increase gain and directivity of antennas in RF and communication systems. This article focuses on using ABS-like filament as a cost-effective material and a cross-shaped structure to simplify the manufacturing process with the use of advanced 3D printing technology.

The goal is to demonstrate how this method is capable of increasing antenna gain and directivity while maintaining a compact lens size.

2. Method

The 5.8 GHz frequency band was selected for this study because it falls within the unlicensed part of the spectrum and is widely used in wireless applications, making it a practical choice for antenna system development. This frequency band also offers the advantage of a shorter wavelength, approximately 5.17 cm, allowing for a more compact lens design. The wavelength is a crucial parameter in determining the physical dimensions of the Luneburg lens, as its geometry must be proportional to the operating wavelength to ensure effective propagation and focusing.

In alignment with the design approach used by Fortify (in collaboration with Rogers Corporation) [18], [19], a 6-layer configuration was adopted for the Luneburg lens, with the radius values of each layer corresponding to those in their model. Although the chosen lens diameter was 6 cm, slightly larger than the desired wavelength of 5.17 cm, this increase in size provides a greater surface area for wave propagation, contributing to improved gain and directivity.

The multilayer design enables the required refractive index gradient to be achieved, which is essential for accurate wave focusing and efficient propagation. Figure 1 illustrates the

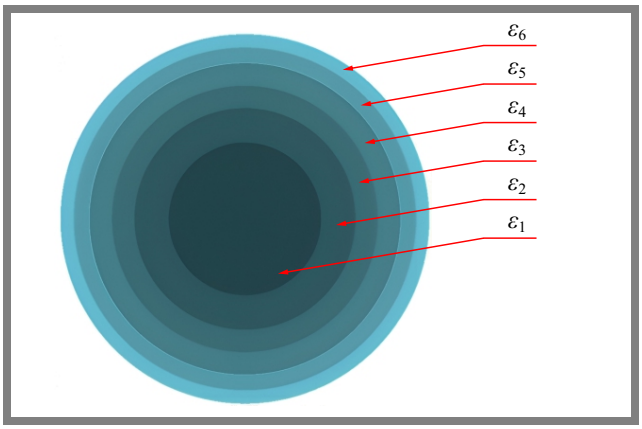

Fig. 1. Luneburg lens layers.

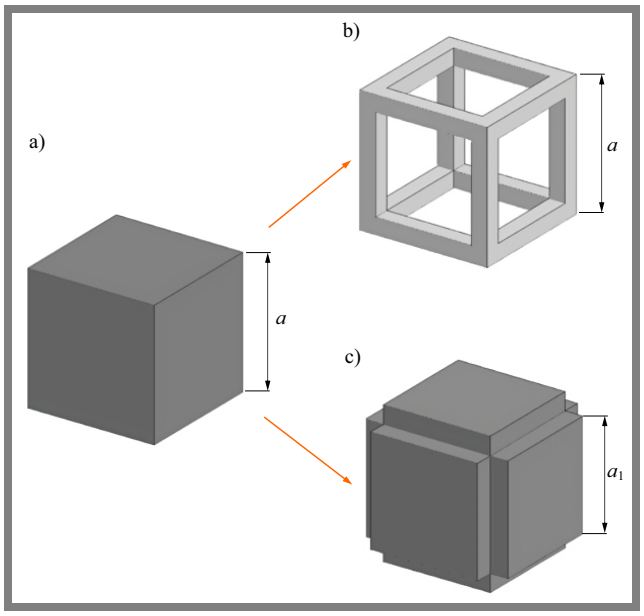

Fig. 2. A cube with a side a), the air part of the cube b), and the solid part of the cube (the unit cell of the lens) c).

layer numbering and the corresponding dielectric permittivities $\varepsilon_1, \varepsilon_2, \ldots, \varepsilon_6$. The permittivity values for each layer were determined through a series of simulations of the lens aimed at identifying appropriate values to achieve gain and directivity at 5.8 GHz. Detailed information on the simulation methodology is provided in Section 4.

To achieve homogeneity in each layer of the lens, a cubic structure, as shown in Fig. 2a, was divided into two parts, with the air part being subtracted to create a cross-shaped single-cell design illustrated in Fig. 2b. This approach allows for a proportional arrangement of unit cells, which is essential to achieve the desired refractive index gradient. Relative permittivity values were adjusted keeping the length of side a constant and varying the length of side a_1 for each layer. A similar method was used for the Luneburg acoustic lens in [7].

3. Lens Design

To determine the value of side a_1 for each layer, it was necessary to establish the relationship between side a_1 (Fig. 2) and the relative permittivity values of each layer. To achieve this, the rule of mixtures [20], [21] was applied. Therefore, the effective permittivity is calculated as follows:

$$\varepsilon_{eff} = \varepsilon_a f_a + \varepsilon_h f_h, \tag{2}$$

where ε_a and f_a are the relative permittivity and the air fill fraction, respectively, while ε_h and f_h are the relative permittivity and the fill fraction of the host material. The relative permittivity of air is $\varepsilon_a = 1$, while the relative permittivity of the host material, represented as ε_h, is that of ABS plastic. Studies referenced in [22]–[25] indicate that the relative dielectric constant of ABS plastic varies between 2.2 and 3.1. Therefore, an average dielectric permittivity value of $\varepsilon_h = 2.75$ and a tangent loss of 0.012 were selected for the calculations.

Tab. 1. Parameters of the Luneburg lens for each layer.

Layer	1	2	3	4	5	6
Radius [mm]	12.4	18	21.7	25.4	27.9	30
a_1 [mm]	1.09	0.97	0.94	0.73	0.58	0.26
ε_{eff}	1.92	1.77	1.74	1.49	1.33	1.07

The filling fraction of the air is:

$$f_a = \frac{Number\ of\ holes \times Volume\ of\ a\ single\ hole}{Total\ volume}, \tag{3}$$

and the filling fraction of the host material is:

$$f_h = \frac{Total\ vol. - No.\ of\ holes \times Vol.\ of\ a\ single\ hole}{Total\ volume}, \tag{4}$$

The number of holes in this work is denoted with N_{hole}, the volume of a single hole with V_{hole}, and the total volume of each layer with V_{total}. The volume of the cube shown in Fig. 2a was also needed in the calculations, denoted by V_{cube}. By substituting the defined variables into Eqs. (3) and (4), the following form is derived:

$$f_a = \frac{N_{hole} \times V_{hole}}{V_{Total}}, \tag{5}$$

$$f_h = 1 - \frac{N_{hole} \times V_{hole}}{V_{Total}}. \tag{6}$$

As previously discussed, each of the cubes consists of two parts: an air hole part and a solid or the unit cell part (Fig. 2). To quantify the volume of holes within the sphere, the total volume of each layer was divided by the volume of a cube, allowing one to determine how many of these cubic structures could fit within the spherical volume and subsequently calculate the number of holes:

$$N_{hole} = \frac{V_{total}}{V_{cube}}. \tag{7}$$

The volume of the hole is:

$$V_{hole} = V_{cube} - V_{unit\_cell}. \tag{8}$$

The volume of the cube is $V_{cube} = a^3$ and the volume of the unit cell is equal to the volume of the cross-shaped structure shown in Fig. 2c:

$$V_{unit\_cell} = 2\,a_1^3 + 3\,a_1^2\,a \tag{9}$$

From Eqs. (8) and (9):

$$V_{hole} = a^3 - (2\,a_1^3 + 3\,a_1^2\,a). \tag{10}$$

After inserting the appropriate variables and constants into Eq. (2) and applying mathematical transformations, the relationship between side a_1 and the effective dielectric permittivity is derived as follows:

$$2\,a_1^3 - 3\,a_1^2\,a + a^3 = V_{cube}\,\frac{\varepsilon_{eff} - \varepsilon_h}{1 - \varepsilon_h}, \tag{11}$$

where a and ε_h are constants mentioned earlier, the side size a was set to 2.1 mm, matching the thickness of the thinnest layer (6th layer). Upon solving Eq. (11), the results presented in Tab. 1 were obtained.

4. Simulation

To evaluate the impact of the approach adopted before performing any manufacturing operations, simulations were conducted using Altair Feko electromagnetic simulator software. First, a baseline radiation pattern was established by simulating a standalone rectangular patch antenna shown in Fig. 3. Next, the lens was positioned in front of the antenna, and the simulation was repeated to assess the lens' influence on the radiation pattern of the patch antenna. Subsequently, the lens was modeled as a continuous structure, consisting of six layers with the corresponding thicknesses, as illustrated in Fig. 1. Each layer was assigned the appropriate dielectric properties, and the final structure with a patch antenna is shown in Fig. 3.

The Luneburg lens was placed 20 mm away from the patch antenna and the resulting radiation pattern, with the lens, was obtained. A comparison between the radiation pattern of the patch antenna solo and that of the antenna with the lens is presented in Fig. 4. The red line represents the far-field radiation of the antenna without the lens, while the blue line shows the radiation pattern after the lens was introduced.

The simulation results showed that antenna performance was significantly improved after the Luneburg lens was introduced. The antenna gain increased by approximately 4.6 dBi, reaching a final value of 8.8 dBi. This increase in gain was due to the lens' ability to focus and concentrate the radiated energy, resulting in a more directional beam. Additionally, the half-power beamwidth (HPBW) was reduced from 92° to approximately 45°. This narrower beamwidth indicates more focused radiation, which can be beneficial in applications requiring precise energy transfer or better directivity.

The simulation was carried out with a continuous structure shown in Fig. 3. To avoid an excessive number of meshes and to shorten the overall simulation and design time, a portion of each layer of the lens was simulated using the proposed structure, rather than simulating the entire lens, to ensure that the desired dielectric properties, particularly dielectric permittivity (Tab. 1), were achieved for each layer. The results closely matched the target values obtained from the continuous lens simulation.

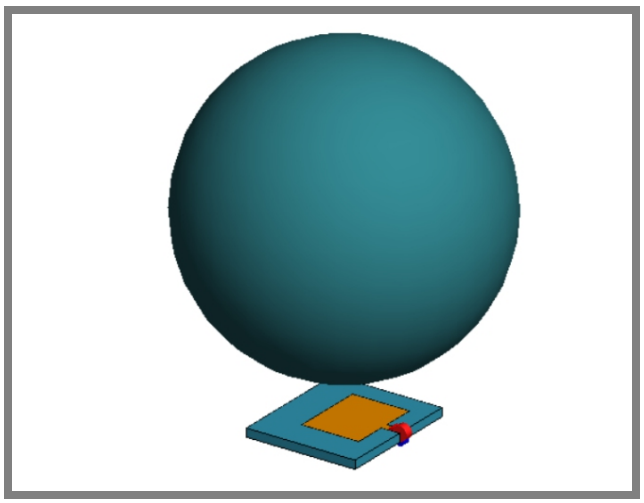

Fig. 3. The lens with the patch antenna.

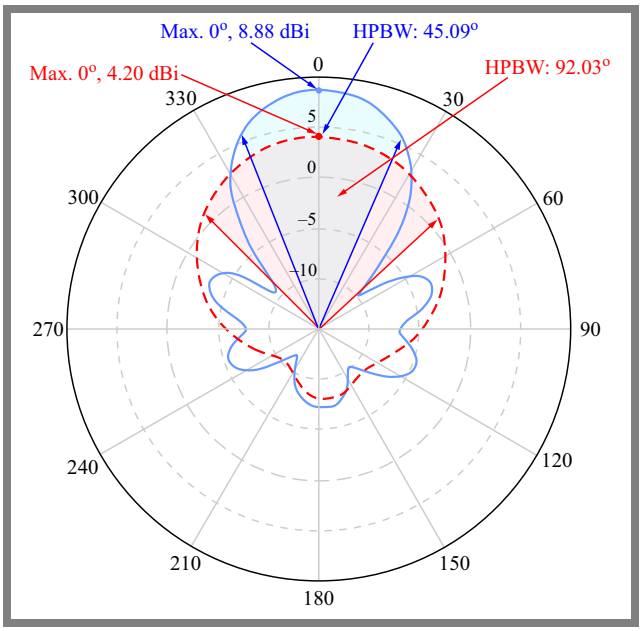

Fig. 4. Comparison between the far fields of the patch antenna only (red line) and the patch antenna with the lens at 5.8 GHz (blue line).

5. Design

Based on the data presented in Tab. 1, the lens was designed using SolidWorks software, with the final model shown in Fig. 5.

Stereolithography (SLA), a high-accuracy 3D printing technique, was used for fabrication. Although the calculations presented in Section 3 were based on parameters for ABS plastic, the lens was constructed using an ABS-like filament, exhibiting similar material properties, due to the requirements of the 3D printing method used. Figure 6 shows the printed lens and provides a closer view of its structure, highlighting the cross-shaped cells within.

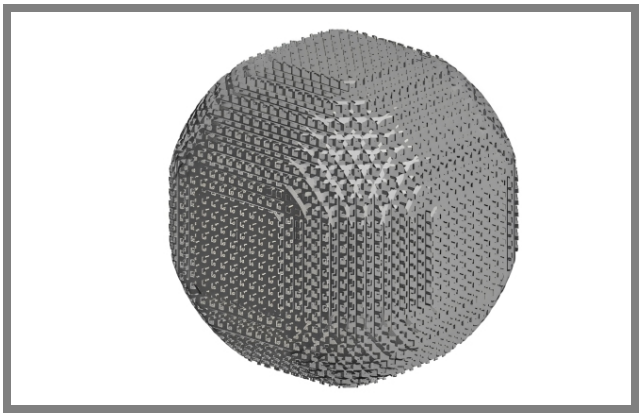

Fig. 5. The 3D model of the lens.

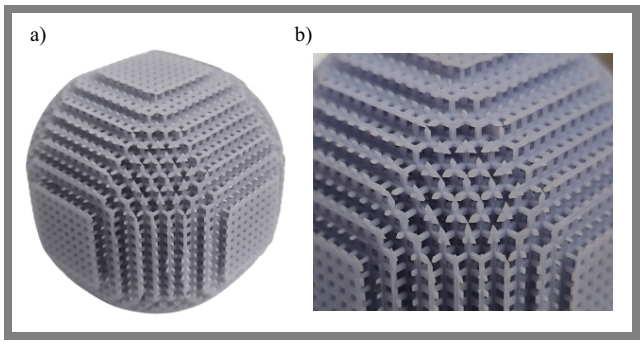

Fig. 6. Printed lens a) and a closer look at its structure b).

6. Testing Results

In the course of the measurements, the receiving and transmitting antennas were placed 28.2 cm apart, with the Luneburg lens positioned 2 cm from the transmitting antenna. The measurement system was enclosed, on all sides, within an anechoic chamber to minimize external interference and ensure accuracy of the data collection process. The results are depicted in Fig. 7, showing a gain improvement of approximately 4.2 dB and a narrowing of the half-power beamwidth (HPBW). These results indicate the focusing effect of the Luneburg lens, which is consistent with expectations based on the simulation data.

Referring to Fig. 4, it is evident that the real measurement results and the simulated ones exhibit a similar overall pattern. In both cases, the addition of the lens has led to an increase in gain and a reduction in HPBW. The simulated results showed a gain increase of approximately 4.6 dB, while the real-world measurements indicated a gain improvement of 4.2 dB. This slight difference may result from fabrication tolerances, material imperfections, or slight misalignments during testing.

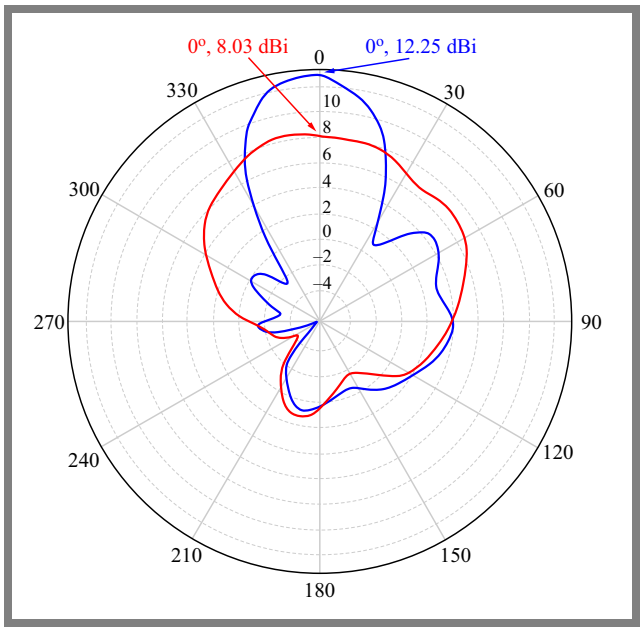

Fig. 7. Radiation patterns of the measured patch antenna (red line) and the patch antenna with the lens (blue line).

Both the simulated and measured results indicated a reduction of approximately two times in HPBW, with slight differences. This reduction demonstrates the effectiveness in focusing the beam. Differences in exact values could be attributed to real-world factors, such as environmental conditions, inaccuracies in the printed lens structure or differences in material properties between the simulated ABS filament and the actual ABS-like filament used in during the fabrication process.

7. Conclusion

This work demonstrated the effectiveness of using the rule of mixtures to determine the appropriate material-air ratio for the lens structure. This method enabled the fabrication of a gradient index (GRIN) Luneburg lens with suitable dielectric properties, achieved without relying on more complex, time-consuming, or costly processes. The results showed a gain improvement of approximately 4.2 dB and a significant narrowing of the half-power beamwidth (HPBW), confirming the enhanced performance of the antenna when the lens was integrated therewith. The successful use of 3D printing for lens construction further highlights the potential of additive manufacturing techniques in producing customized metamaterials.

References

[1] R.K. Luneburg, *Mathematical Theory of Optics*, University of California Press, 448 p., 1964 (https://doi.org/10.1525/9780520328266).

[2] J.E. Gómez-Correa *et al.*, "Generalization of Ray Tracing in Symmetric Gradient-index Media by Fermat's Ray Invariants", *Optics Express*, vol. 29, no. 21, pp. 33009–33026, 2021 (https://doi.org/10.1364/OE.440410).

[3] N. Korotkov and Y.E. Mitelman, "Simulation of Spherical Luneburg Lens Using Numerical Electrodynamic Methods", *Proceedings of Information Technologies, Telecommunications and Control Systems*, 2017 (https://ceur-ws.org/Vol-2035/paper13.pdf).

[4] Q. Cheng, M. Naeem, and Y. Hao, "Composite Luneburg Lens Based on Dielectric or Plasmonic Scatterers", *Optics Express*, vol. 27, no. 8, pp. 10946-10960, 2019 (https://doi.org/10.1364/OE.27.010946).

[5] Y. Xie *et al.*, "Acoustic Imaging with Metamaterial Luneburg Lenses", *Scientific Reports*, vol. 8, art. no. 16188, 2018 (https://doi.org/10.1038/s41598-018-34581-7).

[6] L. Zhao, T. Horiuchi, and M. Yu, "Directional Acoustic Luneburg Lens Waveguide", *ArXiv*, 2022 (https://doi.org/10.48550/arXiv.2201.01876).

[7] L. Zhao, T. Horiuchi, and M. Yu, "Broadband Acoustic Collimation and Focusing Using Reduced Aberration Acoustic Luneburg Lens", *Journal of Applied Physics*, vol. 130, no. 21, art. no. 214901, 2021 (https://doi.org/10.1063/5.0064571).

[8] L. Zhao *et al.*, "A Review of Acoustic Luneburg Lens: Physics and Applications", *Mechanical Systems and Signal Processing*, vol. 199, art. no. 110468, 2023 (https://doi.org/10.1016/j.ymssp.2023.110468).

[9] A. Di Falco, S.C. Kehr, and U. Leonhardt, "Luneburg Lens in Silicon Photonics", *Optics Express*, vol. 19, no. 6, pp. 5156–5162, 2011 (https://doi.org/10.1364/OE.19.005156).

[10] C.E. Garcia-Ortiz *et al.*, "Plasmonic Metasurface Luneburg Lens", *Photonics Research*, vol. 7, no. 10, pp. 1112–1118, 2019 (https://doi.org/10.1364/PRJ.7.001112).

[11] T. Driscoll *et al.*, "Performance of a Three Dimensional Transformation-optical-flattened Luneburg Lens", *Optics Express*, vol. 20, no. 12, pp. 13262–13273, 2012 (https://doi.org/10.1364/OE.20.013262).

[12] W. Dong, Y. Lai, and Jin Hu, "Detecting Spatial Chirp Signals by Luneburg Lens Based Transformation Medium", *Optics Express*, vol. 30, no. 6, pp. 9773–9789, 2022 (https://doi.org/10.1364/OE.453937).

[13] A. Demetriadou and Y. Hao, "Slim Luneburg Lens for Antenna Applications", *Optics Express*, vol. 19, no. 21, pp. 19925–19934, 2011 (https://doi.org/10.1364/OE.19.019925).

[14] H. Saghlatoon, M.M. Honari, S. Aslanzadeh, and R. Mirzavand, "Electrically-small Luneburg Lens for Antenna Gain Enhancement Using New 3D Printing Filling Technique", *AEU - International Journal of Electronics and Communications*, vol. 124, art. no. 153352, 2020 (https://doi.org/10.1016/j.aeue.2020.153352).

[15] Tech-Lightenment, "The Future Satellite Antenna-Luneburg Lens Antenna", (https://tech-lightenment.blogspot.com).

[16] H.-T. Chou *et al.*, "Optimization of Three-Dimensional Multi-Shell Dielectric Lens Antennas to Radiate Multiple Shaped Beams for Cellular Radio Coverage", *IEEE Access*, vol. 7, pp. 182974–182982, 2019 (https://doi.org/10.1109/ACCESS.2019.2959277).

[17] B. Ahn *et al.*, "Wide-angle Scanning Phased Array Antenna Using High Gain Pattern Reconfigurable Antenna Elements", *Scientific Reports*, vol. 9, art. no. 18391, 2019 (https://doi.org/10.1038/s41598-019-54120-2).

[18] Fortify, "Low Loss Dielectric 3D Printing", (https://3dfortify.com/wp-content/uploads/2022/01/RF-One-Pager_RevF.pdf).

[19] Fortify, "3D Printed Dielectric Lenses Increase Antenna Gain and Widen Beam Scanning Angle", (https://3dfortify.com/wp-content/uploads/2021/07/Fortify_3D-Printed-Dielectric-Lenses-White-Paper_RevB.pdf).

[20] University of Cambridge, "Derivation of the Rule of Mixtures and Inverse Rule of Mixtures", (https://www.doitpoms.ac.uk/tlplib/bones/derivation_mixture_rules.php).

[21] University of Cambridge, "Stiffness of Long Fibre Composites", (https://www.doitpoms.ac.uk/tlplib/fibre_composites/stiffness.php).

[22] A. Al Takach *et al.*, "Two-line Technique for Dielectric Material Characterization with Application in 3D-printing Filament Electrical Parameters Extraction", *Progress In Electromagnetics Research M*, vol. 85, pp. 195–207, 2019 (https://doi.org/10.2528/PIERM19071702).

[23] N. Reyns *et al.*, "Complex Dielectric Permittivity of Engineering and 3D-printing Polymers at Q-band", *Journal of Infrared, Millimeter, and Terahertz Waves*, vol. 39, no. 11, pp. 1140–1147, 2018 (https://doi.org/10.1007/s10762-018-0528-9).

[24] B. Behzadnezhad, B.D. Collick, N. Behdad, and A.B. McMillan, "Dielectric Properties of 3D-printed Materials for Anatomy Specific 3D-printed MRI Coils", *Journal of Magnetic Resonance*, vol. 289, pp. 113–121, 2018 (https://doi.org/10.1016/j.jmr.2018.02.013).

[25] T. Hayat, M.U. Afzal, A. Lalbakhsh, and K.P. Esselle, "Additively Manufactured Perforated Superstrate to Improve Directive Radiation Characteristics of Electromagnetic Source", *IEEE Access*, vol. 7, pp. 153445–153452, 2019 (https://doi.org/10.1109/ACCESS.2019.2948735).

Emma M. Sadoyan
https://orcid.org/0009-0006-7824-7507
E-mail: emma.sadoyan@advanced.am
ATG CJSC, Yerevan, Armenia
https://advanced.am

Mark S. Mnatsakanyan
https://orcid.org/0009-0000-9403-6415
E-mail: mark.mnatsakanyan@advanced.am
ATG CJSC, Yerevan, Armenia
https://advanced.am

Suren G. Eyramjyan
https://orcid.org/0009-0001-2694-5059
E-mail: suren.eyramjyan@advanced.am
ATG CJSC, Yerevan, Armenia
https://advanced.am

Development and Optimization of Deep Learning Systems for MRI Analysis in Alzheimer's Disease Monitoring

Jolanta Podolszańska

Jan Długosz University, Częstochowa, Poland

https://doi.org/10.26636/jtit.2024.4.1815

Abstract — Alzheimer's disease is one of the leading causes of dementia worldwide, and its increasing prevalence presents significant diagnostic and therapeutic challenges, particularly in an aging population. Current diagnostic methods, including patient history reviews, neuropsychological tests, and MRI scans, often fail to achieve adequate sensitivity and specificity levels. In response to these challenges, this study introduces an advanced convolutional neural network (CNN) model that combines ResNet-50 and Inception V3 architectures to classify, with a high degree of precision, the stages of Alzheimer's disease based on MRI. The model was developed and evaluated using data from the Alzheimer's Disease Neuroimaging Initiative (ADNI) and classifies MRI scans into four clinical categories representing different stages of disease severity. The evaluation results, based on the precision, sensitivity and F1 score metrics, demonstrate the effectiveness of the model. Additional augmentation techniques and differential class weighting further enhance the accuracy of the model. Visualization of results using the t-SNE method and the confusion matrix underscores the ability to distinguish between disease categories, supporting the model's potential to aid in neurological diagnosis and classification.

Keywords — Alzheimer disease, convolutional neural network, Inception V3, ResNet-50, t-SNE analysis

1. Introduction

Dementia is one of the leading causes of disability and mortality, particularly among the elderly [1]–[5]. It significantly affects cognitive functions, especially memory, making daily activities more difficult. According to the World Health Organization (WHO), approximately 55 million people worldwide suffer from dementia, with this number projected to increase to 139 million by 2050 [6]. Alzheimer's disease, the most common form of dementia, accounts for 60-70% of cases [7]. This paper focuses on developing and validating deep learning models for brain image analysis, specifically designed to assess the severity of Alzheimer's disease.

Recent advances in machine learning and deep learning have contributed significantly to the diagnosis and prognosis of neurodegenerative diseases, such as Alzheimer's. Techniques such as magnetic resonance analysis, deep neural networks, and feature extraction methods have improved the degree of precision achieved in diagnostic processes.

Key studies highlight the effectiveness of various machine learning models in diagnosing Alzheimer's disease. A classification model using ResNet-50 with self-attention layers improved the classification of the stage of Alzheimer's, demonstrating the potential that deep feature extraction techniques combined with Bayesian optimization offer in terms of hyperparameter tuning [8]. The study achieved a high accuracy rate, although concerns about overfitting remain, due to optimized hyperparameters [9].

Another approach from Batangas State University applied principal component analysis (PCA) and the synthetic minority oversampling technique (SMOTE) to address data imbalance, achieving a 99% accuracy rate using the extra tree algorithm [10]. However, the potential for overfitting requires a cautious interpretation of these results.

Other research has focused on more computationally efficient models, such as vision transformers (ViT) which demonstrated a high precision rate of 99.83% in classifying Alzheimer's stages with minimal computational resources [11]. This makes it a promising option for clinical environments with limited resources. Similarly, studies exploring random forest (RF), support vector machine (SVM), and convolutional neural networks (CNN) for dementia classification showed that SVM, especially when combined with advanced feature extraction techniques, could outperform other models [12].

In addition, combining biomarkers, such as amyloid beta and tau proteins, with machine learning classifiers has proven effective in identifying the early stages of Alzheimer's. Ensemble methods, such as boosted trees and logistic regression, have shown strong precision, highlighting the potential of integrating biomarkers into diagnostic models [13]–[18].

These findings suggest that deep learning models, particularly when optimized for data imbalance and computational efficiency, hold promise in improving early diagnosis and classification of Alzheimer's disease. However, more research is needed to validate these models in clinical settings and address potential problems such as overfitting and interpretability.

2. Methods

This section outlines the steps involved in preparing the preprocessed models for application. The project uses the

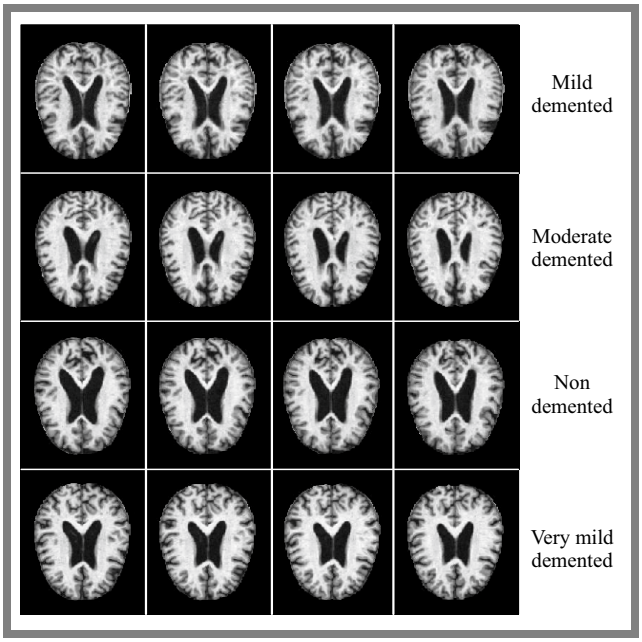

Fig. 1. Sample MRI images representing different stages of Alzheimer's disease classification from the ADNI dataset.

"Alzheimer MRI preprocessed dataset" made available by Kumar and Shastri in 2022 on the Kaggle platform. The dataset consists exclusively of magnetic resonance imaging (MRI) scans of the brains of patients diagnosed with various stages of Alzheimer's disease, as well as healthy control subjects. Data have been preprocessed by applying normalization and other techniques to improve image quality, which is crucial for the effectiveness of deep learning algorithms [19].

The dataset contains images collected from various sources, including websites, hospitals, and public repositories (Fig. 1). They were preprocessed and normalized to a uniform 128×128-pixel format to facilitate data analysis and processing. It contains a total of 6 400 images which have been classified into four classes corresponding to different stages of Alzheimer's disease:

- class 1: mild dementia (896 images),
- class 2: moderate dementia (64 images),
- class 3: non-dementia (3200 images),
- class 4: very mild dementia (2240 images).

The primary objective of using this dataset is to develop and validate advanced predictive models capable of accurately classifying and predicting different stages of Alzheimer's disease through computer analysis. By relying on machine learning and deep learning techniques, the objective is to create models that not only improve medical diagnosis but also contribute to a deeper understanding of the neurodegenerative processes associated with the disease in question.

2.1. Feature Selection and Development of Predictive Models

Two advanced neural network models, ResNet-50 and Inception V3, were used to extract features from the images. Both models were pre-trained on datasets consisting of MRI images. The images were pre-processed and upscaled to a 299×299-pixel format for processing with the use of deep learning algorithms.

The pre-trained network, trained for 50 epochs, utilizes a residual architecture to optimize the training process of the neural networks. In contrast, the model incorporating a multipath data flow concept allows for efficient processing with fewer parameters. The outputs of both models are merged to form a single high-dimensional feature vector. This combined feature vector is passed through a fully connected layer, followed by a dropout layer to regularize the model and prevent overfitting. Finally, the processed features are passed through an output layer which generates predictions for each of the four severity classes.

2.2. Model Validation

A thorough validation was conducted to evaluate the performance of the hybrid CNN model. The data were divided into a training set (approximately 80%) and a validation set (approximately 20%), ensuring that the model was tested on data unseen during training, allowing for the assessment of its generalization capability. The metrics used to evaluate quality included precision, sensitivity, F1 score, and a confusion matrix. The validation process was designed to demonstrate whether the hybrid CNN model, which combines the ResNet-50 and Inception V3 architectures, is capable of effectively classifying different stages of Alzheimer's disease based on MRI images. High precision, sensitivity, and F1 score values should confirm the model's potential to serve as a valuable tool in supporting medical diagnosis and advancing research into Alzheimer's disease.

3. Results

As mentioned earlier, the data were divided into training and validation sets. Cross-validation was used to provide a more comprehensive evaluation of the model, ensuring that the results were not random and adequately represented the entire dataset. The precision metric, which measures the precision of a classifier in predicting the positive class, was used to evaluate the models. Precision is calculated as the ratio of true positives (TP) to the sum of true positives and false positives (FP).

$$Precision = \frac{TP}{TP + FP} \,. \tag{1}$$

Sensitivity is the classifier's ability to provide information about the detection of all true positives and is defined as:

$$Recall = \frac{TP}{TP + FN} \,, \tag{2}$$

where FN stands for false negatives.

The F1 measure involves calculating the harmonic mean of precision and sensitivity, which allows for a balanced model evaluation that considers both accuracy and completeness of predictions:

$$F1 = 2 \times \frac{Precision \times Recall}{Precision + Recall} \,. \tag{3}$$

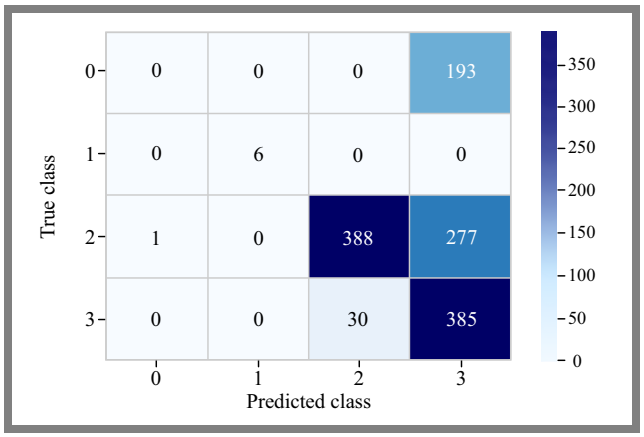

Fig. 2. Confusion matrix showing classification results for four Alzheimer's severity classes, highlighting correct and misclassified samples.

The overall performance of the model was then calculated as the ratio of the sum of true positive and accurate negative results to the total number of samples.

$$ACC = \frac{TP + TN}{TP + TN + FP + FN} . \tag{4}$$

The confusion matrix allowed to assess the classification performance by identifying the numbers of true positive (TP), true negative (TN), false positive (FP), and false negative (FN) outcomes for each class (Fig. 2). This analysis helps determine which classes are most frequently misclassified, indicating potential areas where the model may require improvement. The validation results were presented using graphs and confusion matrices which provide a detailed evaluation of the effectiveness of the classifiers. Despite good overall performance, certain classes, in particular those with smaller sample sizes, may require further optimization, as highlighted in the detailed interpretation of the results.

3.1. Interpretation of Results and Evaluation of Model Effectiveness

This article focuses on developing predictive models that use advanced deep learning techniques to analyze brain magnetic resonance images to assess the severity of Alzheimer's disease. A hybrid neural network architecture, combining the ResNet-50 and Inception V3 models, was used to create a more accurate classification system. Research aimed not only to enhance the accuracy of Alzheimer's disease diagnosis, but also to contribute to a deeper understanding of the neurodegenerative processes associated with the condition. The experiments involved detailed performance analyses of the model, including validation through confusion matrices and visualization of the feature space using t-SNE.

Below is a summary of the evaluation of the convolutional neural network (CNN) model based on precision, recall, F1 score, and accuracy metrics (Tab. 1). The model was evaluated using the test dataset, ensuring its applicability at different stages of Alzheimer's disease.

Tab. 1. Results of the collective evaluation of the convolutional neural network (CNN) model.

Metric	Value
Precision	99.09%
Recall	98.84%
F1 score	98.93%
Accuracy	99.1%

Tab. 2. Results of a collective evaluation the convolutional neural networks (CNN) model's precision, recall, and F1 score, expressed as values between 0 and 1.

Class	Precision	Recall	F1 score
Non-demented	0.995	0.993	0.994
Mild demented	0.987	0.989	0.988
Moderate demented	0.985	0.984	0.985
Very mild demented	0.990	0.988	0.989

Table 2 presents detailed results for each of the four classes, providing a more in-depth analysis of the model's ability to classify different stages of Alzheimer's disease.

The t-distributed stochastic neighbor embedding (t-SNE) projection shown in Fig. 3 illustrates the two-dimensional feature space of the model's output. Each point corresponds to a sample from the dataset. The separation between classes is clear, indicating that the model has learned to effectively distinguish between different stages of Alzheimer's disease. Class 2 (green) and class 3 (red) form distinct clusters, suggesting that these classes are well recognized. Class 0 (orange), represented by a smaller group, is located toward the bottom, indicating potential difficulties in classification or fewer samples. Class 1 (blue) appears to be dispersed across several groups, hinting at challenges in distinguishing this particular category. Most points are tightly clustered, suggesting decent

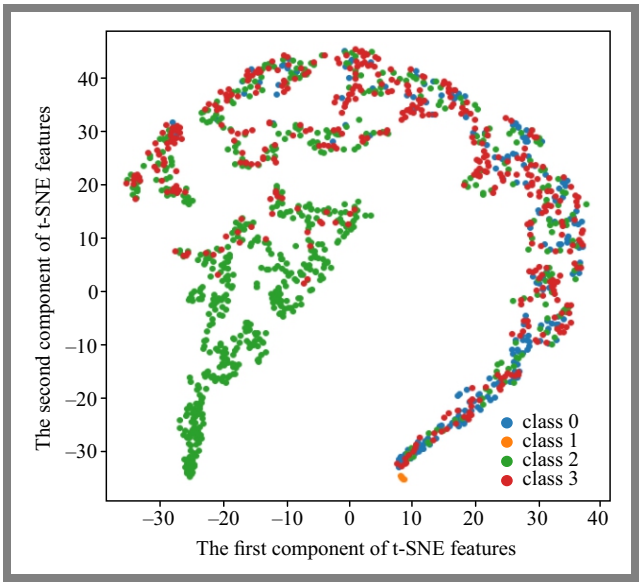

Fig. 3. Projection of t-SNE showing the clustering of Alzheimer's disease severity classes.

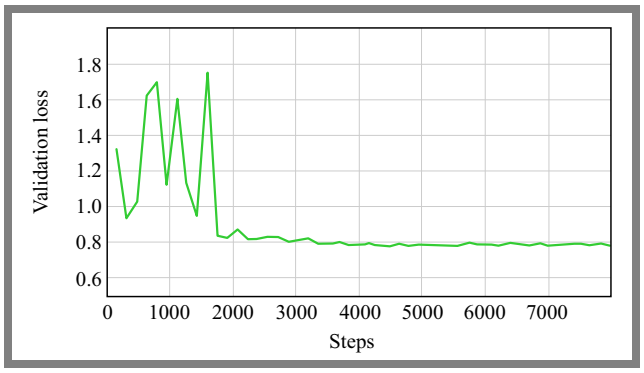

Fig. 4. Validation loss vs. steps, showing stabilization after 2 000 steps and indicating model convergence.

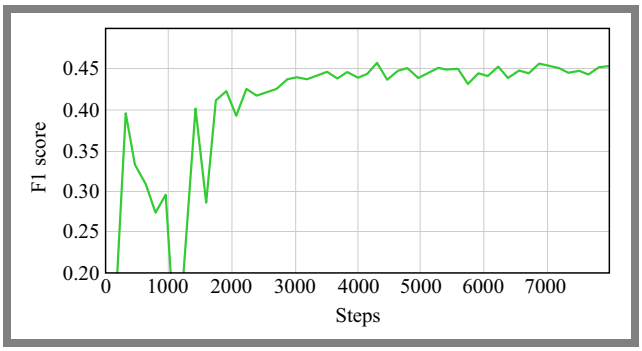

Fig. 5. Graph showing validation of F1 score vs. steps demonstrates a consistent improvement in model's performance after 2 000 steps.

model performance in separating the data, although some dispersion in class 1 and partially in class 0 indicates structural complexity the model struggled with.

The plot shown in Fig. 3 presents the projection of t-SNE onto the two-dimensional feature space of the model's output. Each point on the graph represents one sample of the data set. One may notice a clear separation of classes, suggesting that the model has successfully learned to distinguish between different classes at the level of output characteristics. Class 2 (green) and class 3 (red) form very distinct groups, proving that the model is more efficient at recognizing these particular classes. Class 0 (orange) appears to have the form of a small group and is located at the bottom of the graph, which may suggest that this class has fewer samples or is more difficult for the model to recognize. Class 1 (blue) is present in several groups, which may indicate some problems in distinguishing this class or the complexity of its features. Most of the points in each class are well clustered, which is a positive result.

In the plot, one may notice that the initial changes are large, especially before approximately 2 000 steps, where the value of the loss decreases rapidly (Fig. 4). Once this limit has been exceeded, the graph clearly begins to flatten out, suggesting that further training has a diminishing effect on reducing the loss. This is the point that we call the "elbow", and it indicates the optimal number of epochs after which further training of the model no longer provides significant benefits. The network was trained in 50 epochs.

When analyzing the model training results, one should pay attention to the validation loss function depending on the number of epochs, which can be represented as a function of $L(epoch)$. In the elbow method, we look for a point k for which the change in the value of the loss between epochs k and $k+1$ ceases to be significant and its gradient flattens out. Mathematically, this can be put in the following form:

$$\Delta L = L(k+1) - L(k). \tag{5}$$

In Eq. (5), if

$$|\Delta L| =<< \epsilon \tag{6}$$

for a certain tolerance $\varepsilon > 0$, then k can be considered the optimal number of epochs from the validation loss graphs shown. One may observe that after reaching approximately 30 epochs, ΔL decreases to values close to zero, suggesting that further training of the model does not produce significant improvements.

Formally, we can assume that there is a certain point where $k \geqslant 30$:

$$\frac{\delta L}{\delta\, epoch} \approx 0\,, \tag{7}$$

which indicates that further increases in the number of epochs result in minimal changes in the value of the loss function, and thus in the quality of the model. Calculating the differences between successive epochs using data from the validation loss chart. For epochs in the 1–30 range, the differences in the loss values are significant. From epoch 30 onwards, the loss values begin to stabilize, and the differences between successive epochs are marginal. The values of these differences can be calculated in the form of finite differences in the following way:

$$\Delta L_3 0 = L(31) - L(30)\,. \tag{8}$$

For $\Delta L_3 0$ close to zero, we reach the point where continuing training does not significantly improve performance. The result of the analysis suggests that the number of epochs equaling 30 is the optimal choice for this model, as once this number is reached, the changes in the validation loss value are marginal.

In terms of the F1 validation score vs. steps plot, as shown in Fig. 5, we observe a change in the value of the F1 score for validation data as the model's training process progresses, i.e., the number of steps corresponding to training epochs increases. The F1 score is a measure of the harmonic mean between precision and sensitivity, making it one of the key metrics for classification models, especially when the data are unbalanced.

At first (up to approx. 2 000 steps), the F1 score fluctuates and is subject to irregular changes. This could mean that the model needs more epochs to learn effective data representations and adjust to the classification task. Once this number of steps is exceeded, the F1 score values begin to rise more steadily until approx. 5 000 steps, after which they become flatter, indicating stabilization. The elbow method may be used in this case to identify the point at which the F1 score value stops increasing significantly.

We are looking for the step after which the change in the F1 score value becomes marginal, and further training does not result in any significant improvement. Change $\Delta F1$ between

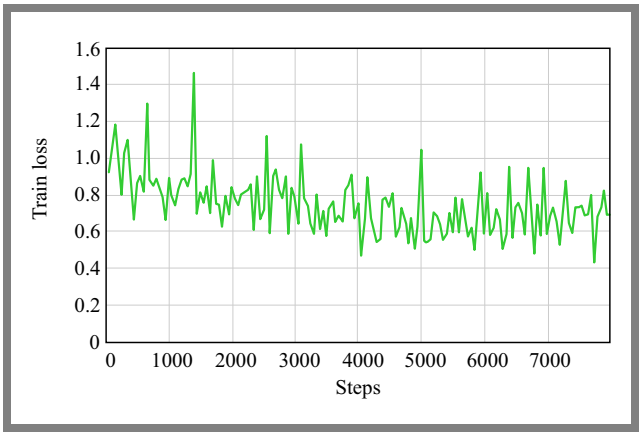

Fig. 6. Changes in the cost function as a function of the number of steps.

steps K and $k+1$ can be described as:

$$\Delta F_1(k) = F_1(k+1) - F_1(k)\,. \tag{9}$$

If $|\Delta F_1|$ becomes close to zero after a certain step k, the model can be considered to have reached optimal performance. In this case, the graph suggests that after approx. 5 000 steps ΔF_1 is declining, suggesting that it is less and less beneficial to continue to train the model. Assuming that we have the corresponding F1 score values for steps 5 000 and 6 000, one may calculate the difference as follows:

$$\Delta F_1(5000) = F_1(6000) - F_1(5000). \tag{10}$$

If $|\Delta F_1(5000)| \approx 0$, it means that further training steps do not bring significant improvement, which would confirm the elbow point at approx. 5 000 steps. According to the elbow method, the number of steps equaling approx. 5 000 may be considered optimal, since after this step changes in the F1 score values are marginal, which means that further training of the model no longer brings significant benefits in improving the quality of classification.

Figure 6 shows the value of the cost function (train loss) for the training data as training progresses, measured in steps. The cost function (loss function) measures how well the model predicts target values (labels) compared to actual performance, and the goal of the optimization process is to minimize this value.

This process can be described using the following iterative equation for gradient descent:

$$\theta_t + 1 = \theta_t - \eta \nabla_\theta L(\theta_t)\,, \tag{11}$$

where: θ_t is the vector of model parameters at step t, η is the learning rate, $\nabla_\theta L(\theta_t)$ is the loss function at point θ_t.

Initially, we observe sharp changes in the loss function, as the gradients $\nabla_\theta L(\theta)$ have high values at the beginning of the training process, leading to large parameter updates $\Delta\theta$ in each step. The early training phase is often unstable, which is reflected in Fig. 6 by large fluctuations, especially in the range of 0–1 000 steps. This can be explained by the fact that at the beginning of the training process, the model is far from the optimal local minimum, so the gradients are steep, causing jumps in the loss function.

As the model approaches the optimal minimum, the gradients decrease, resulting in smaller parameter updates θ. Therefore, we observe a flatter curve for steps $t > 2\,000$, which indicates that the optimization process is slowing down and the model is gradually approaching the minimum of the loss function.

For steps $t > 2\,000$, the curve shows fewer fluctuations, which is typical for the convergence of a gradient algorithm. In particular, the AdamW optimizer further accelerates convergence by using mechanisms that adjust the adaptive step size and regularization weights, thus helping avoid overfitting. This mechanism can be mathematically described by adding regularization to the objective function in the following way:

$$L(\theta) = L_{data}(\theta) + \lambda\|\theta\|^2, \tag{12}$$

where $L_{data}(\theta)$ is the loss function of the data and $\lambda\|\theta\|^2$ is the $L2$ applied by AdamW. In summary, the graph shows the effectiveness of minimizing the loss function as the steps progress. The sharp initial decrease and subsequent stabilization of the loss function indicate that the model is approaching an optimal solution, with a further loss reduction occurring in smaller steps, which is typical for convergence in gradient-based algorithms.

4. Conclusions

The research implemented advanced deep learning techniques using a modified CNN architecture to assess and classify various stages of Alzheimer's disease based on MRI images. The results demonstrate that the model achieves high degrees of precision, sensitivity, and effectiveness in identifying multiple stages of disease progression, highlighting its potential application as a tool supporting medical diagnostic procedures.

Systematic improvements in accuracy showcase its ability to learn complex data patterns, which may contribute to a better understanding of the neurodegenerative processes associated with Alzheimer's disease.

Based on the findings of the study, it is recommended that performance be further evaluated by incorporating more MRI images from diverse populations, which could improve generalizability and contribute to understanding variations between patient groups. This also involves obtaining the appropriate consent to prevent the misuse of patient data. Future research could explore other advanced neural network architectures, such as generative adversarial networks (GANs) and capsule networks, which may offer new perspectives and improved diagnosis accuracy.

Future work should focus on increasing the interpretability of deep learning models, which is critical in a medical context to help physicians better understand the decision-making processes relied upon by the models. Extensive clinical validations are also necessary to confirm the effectiveness in real-world medical environments and constitute a key step in progressing towards practical application.

References

[1] J.H. Shin, "Dementia Epidemiology Fact Sheet 2022", *Annals of Rehabilitation Medicine*, vol. 46, no. 2, pp. 53–59, 2022 (https://doi.org/10.5535/arm.22027).

[2] World Health Organization, *Dementia*, Geneva, Switzerland: World Health Organization, 2024 [Online] (https://www.who.int/news-room/fact-sheets/detail/dementia).

[3] V.A. Ciurea *et al.*, "Alzheimer's Disease: 120 years of Research and Progress", *Journal of Medicine and Life*, vol. 16, no. 2, pp. 173–177, 2023 (https://doi.org/10.25122/jml-2022-0111).

[4] J.A. Soria Lopez, H.M. Gonzalez, and G.C. Leger, "Alzheimer's Disease", in: *Handbook of Clinical Neurology*, pp. 231–255, 2019 (https://doi.org/10.1016/B978-0-12-804766-8.00013-3).

[5] J.S. Snowden, "Changing Perspectives on Frontotemporal Dementia: A Review", *Journal of Neuropsychology*, vol. 17, no. 2, pp. 211–234, 2023 (https://doi.org/10.1111/jnp.12297).

[6] A. Alzheimer, "On Certain Peculiar Diseases of Old Age", in: *History of Psychiatry*, H. Forstl and R. Levy, vol. 2, no. 5, pp. 71–101, 1991 (https://doi.org/10.1177/0957154X9100200505).

[7] A.J. Intorcia *et al.*, "A Modification of the Bielschowsky Silver Stain for Alzheimer Neuritic Plaques: Suppression of Artifactual Staining by Pretreatment with Oxidizing Agents", *BioRxiv*, 2019 (https://doi.org/10.1101/570093).

[8] N. Yaqoob *et al.*, Prediction of Alzheimer's Disease Stages Based on ResNet-Self-attention Architecture with Bayesian Optimization and Best Features Selection", *Frontiers in Computational Neuroscience*, 2024 (https://doi.org/10.3389/fncom.2024.1393849).

[9] H. Habehh and S. Gohel, "Machine Learning in Healthcare", *Current Genomics*, vol. 22, no. 4, pp. 291–300, 2021 (https://doi.org/10.2174/1389202922666210705124359).

[10] R.M. Hernandez *et al.*, "Application of Machine Learning on MRI Scans for Alzheimer's Disease Early Detection", *Proceedings of the 8th International Conference on Sustainable Information Engineering and Technology*, pp. 143–149, 2023 (https://doi.org/10.1145/3626641.3627609).

[11] M.H. Alshayeji, "Alzheimer's Disease Detection and Stage Identification from Magnetic Resonance Brain Images Using Vision Transformer", *Machine Learning: Science and Technology*, vol. 5, no. 3, art. no. 035011, 2024 (https://doi.org/10.1088/2632-2153/ad5fdc).

[12] M.G. Hussain and Y. Shiren, "Identifying Alzheimer Disease Dementia Levels Using Machine Learning Methods", *Medical Research Archives*, vol. 11, no. 7.1, 2023 (https://doi.org/10.18103/mra.v11i7.1.4039).

[13] V.K. Tiwari, P. Indic, and S. Tabassum, "Machine Learning Classification of Alzheimer's Disease Stages Using Cerebrospinal Fluid Biomarkers Alone", *arXiv*, 2024 (https://doi.org/10.48550/arXiv.2401.00981).

[14] S.E. Sorour *et al.*, "Classification of Alzheimer's Disease Using MRI Data Based on Deep Learning Techniques", *Journal of King Saud University-Computer and Information Sciences*, vol. 36, no. 2, art. no. 101940, 2024 (https://doi.org/10.1016/j.jksuci.2024.101940).

[15] D.A. Arafa *et al.*, "A Deep Learning Framework for Early Diagnosis of Alzheimer's Disease on MRI Images", *Multimedia Tools and Applications*, vol. 83, pp. 3767–3799, 2024 (https://doi.org/10.1007/s11042-023-15738-7).

[16] A.M. El-Assy, H.M. Amer, H.M. Ibrahim, and M.A. Mohamed, "A Novel CN Architecture for Accurate Early Detection and Classification of Alzheimer's Disease Using MRI Data", *Scientific Reports*, vol. 14, art. no. 3463, 2024 (https://doi.org/10.1038/s41598-024-53733-6).

[17] Y. Liu *et al.*, "MPC-STANet: Alzheimer's Disease Recognition Method Based on Multiple Phantom Convolution and Spatial Transformation Attention Mechanism", *Frontiers in Aging Neuroscience*, vol. 14, art. no. 918462, 2022 (https://doi.org/10.3389/fnagi.2022.918462).

[18] S. Ha, Y. Yoon, and J. Lee, "Meta-ensemble Learning with a Multi-headed Model for Few-shot Problems", *ICT Express*, vol. 9, no. 5, pp. 909–914, 2023 (https://doi.org/10.1016/j.icte.2022.09.001).

[19] https://www.kaggle.com/datasets

Jolanta Podolszańska, M.Sc.
Department of Mathematics and Computer Science
https://orcid.org/0000-0002-6032-5654
E-mail: j.podolszanska@ujd.edu.pl
Jan Długosz University, Częstochowa, Poland
https://www.ujd.edu.pl

Leveraging Digital Maps to Visualize Data in Doppler Effect-based Localization System Relying on GNSS

Rafał Szczepanik and Paweł Skokowski

Military University of Technology, Warsaw, Poland

https://doi.org/10.26636/jtit.2024.4.1753

Abstract — Abstract – This paper presents a localization solution exploiting the Doppler effect, digital maps and the Global Positioning System (GPS). To deploy such a system, the following steps must be completed: selecting a suitable GPS receiver, developing operating software, creating an app for displaying digital maps offline, choosing a software-defined RF receiver with a stable frequency reference, integrating the GPS receiver with the map and a radio within a software environment, and setting up a transmitter-receiver link. The second part of the research involves comprehensive tests of the integrated localization system and analyzing the empirical results obtained. The novel approach described in this article consists in the use of digital maps and GNSS data for dynamic visualization of transmitter location using the SDF method. The research was carried out in an NLOS environment.

Keywords — localization of radio sources, signal Doppler frequency method, UAV

1. Introduction

One of the key objectives of modern telecommunication systems, civilian rescue operations, and military electromagnetic reconnaissance campaigns is to search for, detect and determine the location of radio signal sources. Localization systems are used, inter alia, in mobile ad hoc networks, aircraft guidance as well as search and rescue (SAR) missions.

Enhancement of the existing localization methods and development of new techniques is of paramount importance for numerous civilian and military applications. Radio frequency (RF) transmitters may be localized based on the features of the received signal.

This work employs an innovative localization method utilizing the Doppler effect, i.e. the signal Doppler frequency (SDF) method, and presents the results obtained with the use of an integrated Doppler localization system. This objective was achieved by selecting a suitable GPS receiver, developing a supporting application and software displaying a digital map.

We also selected a software-defined radio platform with good frequency stability for the receiving path, as well as integrated the GPS receiver, the map, and the SDR into the programming environment. Then, we set up the transmitter-receiver link. In the second part of the research, tests of the integrated localization system were conducted and the results obtained were analyzed.

The novelty of the approach adopted consists in the first practical implementation of SDF method-based algorithms in an integrated measurement system, as well as in the fact that in-field measurements were conducted in non-line of sight (NLOS) conditions.

The structure of the article reflects the research conducted. Section 2 describes the localization method. In Section 3, the general concept of the integrated localization system is presented. Section 4 describes the signal processing steps taken by developed system. The implementation of the GPS receiver and the digital map in the localization system is outlined in Sections 5–6. In Sections 7–9, tests of the integrated system, empirical research, and results of in-field measurements are described. The work concludes with a summary provided in Section 10.

Recent articles related to the localization of radio sources focus on various localization methods, signal processing techniques, and real-world applications under various environmental conditions.

In article [1], received signal strength (RSS) information is explored to improve transmitter localization accuracy. The authors propose a direct position determination (DPD) method using RSS data in distributed receiver arrays with beamforming. The study aims to assess the potential of RSS data in transmitter localization applications and proposes an improved DPD method.

In [2], a single sensor localization method, utilizing time of arrival (TOA) with interpulse modulation, is presented. The presented model uses the nonlinear least squares (NLS) problem from the perspective of maximum likelihood (ML) estimation, achieving high estimation accuracy and surpassing outcomes of conventional methods. Paper [3] discusses various transmitter localization approaches using a single satellite reference, such as difference in received signal strength (DRSS), direction of arrival (DOA), TOA, and frequency of arrival (FOA) methods. The article also addresses challenges associated with passive synthetic aperture (PSA) techniques and proposes solutions to improve localization accuracy.

In article [4], an effective transmitter localization algorithm is proposed that uses frequency difference of arrival (FDOA),

with its application divided into two steps. The authors discuss the limitations of traditional transmitter localization methods and present an innovative approach that enhances accuracy by reducing errors arising from FDOA initialization. Paper [5] describes a technique for localizing a passive transmitter using simultaneous measurements of time difference of arrival (TDOA) and FDOA from unmanned aerial vehicles (UAVs). The article describes numerous numerical experiments, proving the effectiveness of the proposed method.

The research presented in [6] describes a real-time localization testbed based on the TDOA method using software-defined radio (SDR) communication and using GPS-based synchronization. The system aims to achieve high accuracy thanks to updating frequencies for target tracking and employing Kalman filtering to improve the localization results.

Other important works include articles [7] and [8]. These papers focus on the challenge of precise localization and UAV navigation using cooperative localization that exploits inexpensive ultra-wideband (UWB) transmitters. The accuracy of the proposed system is evaluated through simulations and field tests, as well as through comparisons with GNSS data in urban environments. Paper [8] proposes a novel localization and mapping system based on UWB technology that enables real-time motion tracking in an unknown environment. Experiments confirm that the proposed system offers a localization precision level of less than 1 m from the actual trajectory of the object tracked.

The Doppler effect has been widely utilized for the localization of dynamic objects due the simple nature of the process of capturing frequency shifts caused by the relative motion between the transmitter and receiver. This makes the approach in question particularly suitable for scenarios where the tracked objects are in motion, such as in aircraft guidance, SAR operations, and military reconnaissance. However, existing methods often face challenges in complex environments, where multipath propagation and NLOS conditions degrade their accuracy. Many approaches rely on using multiple receivers, precise synchronization, or exploit other techniques, such as RSS, TOA, or FDOA.

Unfortunately, they are susceptible to errors in dynamic and obstructed environment scenarios. The proposed solution, based on the SDF method, fills these gaps by providing localization services with only a single mobile receiver, without requiring external synchronization or relying on received signal strength. This approach offers improved accuracy in NLOS conditions and dynamic environments – an issue which has not been fully addressed in previous research.

Furthermore, by integrating a GPS receiver and digital maps, the proposed solution enhances the ability of Doppler-based methods to provide quasi-real-time accurate localization in challenging scenarios. The comparison with existing methods shows that the proposed approach not only simplifies the hardware, but also improves the accuracy and reliability of the localization process, especially in real-world conditions with signal interference and obstacles affecting the radio link.

2. Proposed Localization Method

The radio source localization system is based on the SDF method [9], [10]. It utilizes the Doppler effect and allows to localize radio transmitters. The Doppler frequency shift (DFS) f_D phenomena are observed in the received signal when at least one of the elements transmitting the signal is in motion. The method is based on the functional relationship between DFS and the location of transmitter and receiver positions and allows to localize multiple radio emitters [11]. It belongs to a narrow group of transmitter position localization methods that rely on a single mobile platform. The advantage of the proposed solution is that external time synchronization of the received signal is not required and received signal strength indicator is not considered.

The SDF method is based on the analytical solution of the wave equation presented in [12], [13]. It refers to a moving signal source that causes the f_D frequency shift that is dependent on time t, velocity v of the moving transmitter or receiver, and their relative positioning x_0, y_0, z_0 [10], [11]:

$$f_D(x_0, y_0, z_0, t) = f_{Dmax} \frac{x_0 - vt}{\sqrt{x_0 - vt^2} + \sqrt{y_0^2 + z_0^2}}, \quad (1)$$

where $f_{Dmax} = \frac{f_0 v}{c}$ is the maximum Doppler frequency, v is the velocity of the moving receiver (or transmitter) along the x axis, c is the velocity of the electromagnetic wave in the given medium, f_0 stands for the carrier frequency of the emitted signal, x_0, y_0, z_0 are the x, y, z coordinates of the position relative to the receiver at time $t = 0$. By some manipulations of Eq. (1), the estimators of the coordinates of the position of the localized signal source are obtained. These coordinates define the SDF method [12], [14]:

$$\begin{aligned} x &\cong v \frac{t_1 A_1 - t_2 A_2}{A(t_1) - A(t_2)} \\ y &\cong \pm \sqrt{\left[\frac{v(t_1 - t_2) A(t_1) A(t_2)}{A(t_1) - A(t_2)} \right]^2 - z_0^2} \end{aligned}, \quad (2)$$

where

$$A(t) = \frac{\sqrt{1 - F^2(t)}}{|F(t)|}, \; F(t) \cong \frac{f_D(t)}{f_{Dmax}}. \quad (3)$$

Equations (2) and (3) describe two-dimensional localization (2D), i.e., they assume that coordinate $z = z_0$ is known.

The three-dimensional version of the SDF method is widely presented in the literature, among others, in [15]. Here, the 2D SDF method was utilized, where RF source localization is possible if the Doppler frequency measurement is performed at two moments in time, namely t_1 and t_2. The concept utilizes a system receiver (Rx) placed in a moving vehicle, allowing to determine stationary coordinates of signal sources, i.e. transmitter (Tx), as shown in Eq. (2).

The SDF method is used in a wide range of applications, such as electronic reconnaissance, navigation, maritime rescue operations, and emergency management scenarios. Moreover, by relying on SDF, one may also determine the positions of signal sources transmitting binary phase shift keying (BPSK) and quadrature phase shift keying (QPSK) modulated signals [15]. To achieve this, the property of phase shift keying

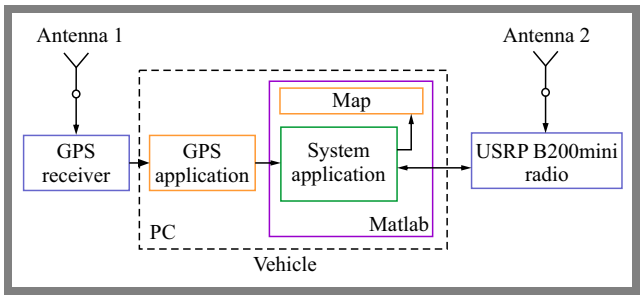

Fig. 1. Diagram of the localization system developed.

(PSK) emission is exploited, resulting in a peak in the signal spectrum raised to a power equal to the modulation depth.

In practice, software and hardware must be integrated into a single system in order to find specific applications of localization methods. The best solution is to utilize software defined radio (SDR) platforms [12] enabling easy and fast implementation of localization algorithms, as well as their testing and further modifications.

3. Integrated Localization System Concept

The localization system developed is made up of several components (Fig. 1). The USRP B200mini radio platform [14] receives the RF signal from the transmitter to be localized. The samples received, in the form of IQ components (in-phase/quadrature-phase), are transmitted via the USB port to a PC computer. The second component of the setup is the GPS receiver. The purpose of this device is to determine the position of the moving receiver, calculate its velocity, and provide time serving as a reference value for the entire system. The GPS receiver is also connected to the PC via a USB port and its operation is ensured by a dedicated application written in the C language.

An offline map is another part of the system, allowing to visualize the position of the moving receiver and the estimated position of the transmitter. The entire system is installed in a vehicle.

A PC-based application that integrates all of the listed components, including radio control, digital map handling, reading of stored data from the GPS receiver, and estimation of the signal source location using the SDF method, has been implemented in the Matlab environment.

4. Signal Processing in the Developed System

In [16], a signal processing method was presented, serving as a foundation for implementing the SDF method. The proposed system extracts the carrier frequency of the target signal from the received spectrum, which appears to change due to the movement of the object. The utilization of SDR radio allows to analyze the selected frequency band, transform it into a digital form, and transmit such data to the PC and the Matlab software. The data buffering and processing diagram is shown in Fig. 2.

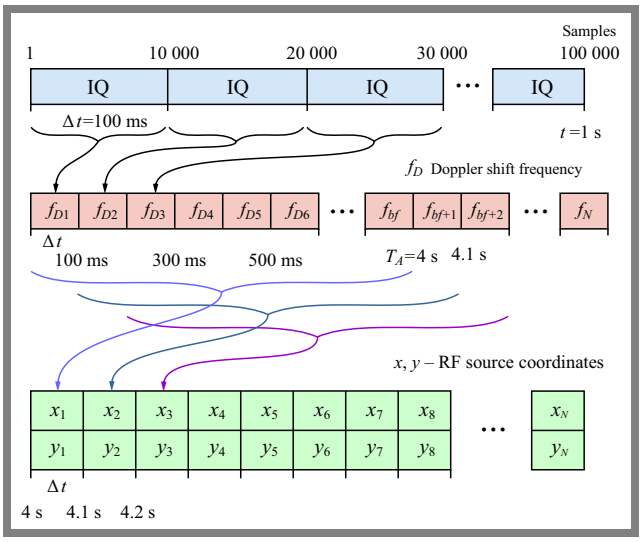

Fig. 2. Processing the received signal and estimating the coordinates of the RF signal source in the system.

The DFS value is determined from each received frame containing 10 000 IQ samples. While one frame lasts for 100 ms and the buffer depth is set to 40 values, the first position of the localized transmitter could be determined after 4 s. Then, after collecting 40 subsequent frames, Tx coordinates x, y are calculated.

Absolute errors x, y and relative errors Δ_r, δ_r of the estimated location may be determined based on the known coordinates x, y [17], as the position calculations are carried out in a local Cartesian coordinate system which is then transformed into a geocentric coordinate system using the Universal Transverse Mercator (UTM) approach. The position of the GPS receiver serves as the reference for mapping the positions onto a geographically projected map.

$$\Delta_r = \sqrt{(\Delta_x)^2 + (\Delta_y)^2} = \sqrt{|x_0 - x|^2 + |y_0 - y|^2}\,, \tag{4}$$

$$\delta_r = \frac{\Delta_r}{\sqrt{x_0^2 + y_0^2}} \times 100\ [\%]\,. \tag{5}$$

5. Implementation of a GPS Receiver

The PhidgetGPS 1040 platform was chosen for the implementation of the GPS receiver in the proposed localization system [18]. This receiver can determine the position, velocity, and the direction of movement with the circular error probable (CEP) specified by the manufacturer at 2.5 m. The percentage probability for this metric, however, is not provided.

In the context of GPS navigation, a 50% probability is most commonly used for CEP, meaning that in 50% of cases, the position measurement should fall within a 2.5-meter radius of the actual position.

Figure 3 shows the PhidgetGPS receiver module used and an antenna adapted for receiving L-band signals.

The application supporting the PhidgetGPS module was developed in the Embarcadero Technologies RAD Studio pro-

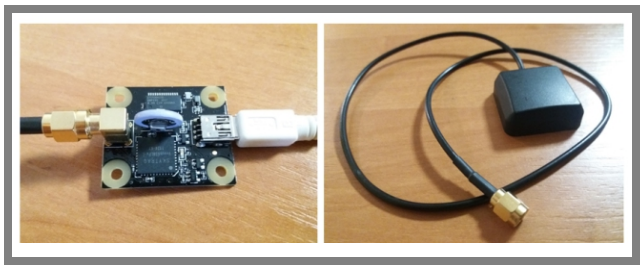

Fig. 3. PhidgetGPS 1040 receiver and external antenna.

gramming environment [19]. The software operates independently in Windows 10, using the latest version of the Phidget22 libraries [20]. The main task of the developed application is to determine and record the current position and velocity of the localization system equipped with a GPS receiver. The application allows data related to coordinates, date, time, altitude above sea level, and velocity of the receiver to be retrieved, and then the information obtained may be saved into a text file.

Alternatively, a second measurement mode may be activated in which a specified number of measurements (e.g., 200) is performed at specified time intervals (minimum 0.1 s). The collected data are also saved into a text file.

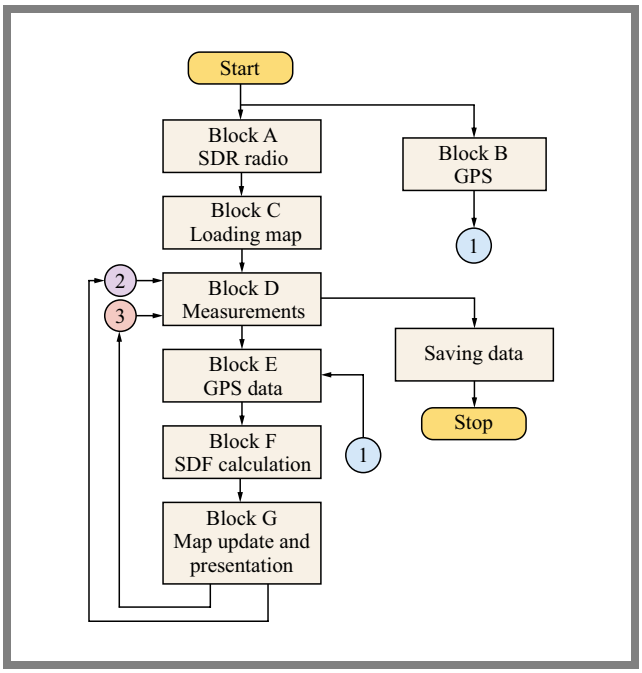

Fig. 4. Block diagram presenting operation of the proposed system and integration of its components.

6. Implementation of a Digital Map in a Location-based System

The current position and the estimated position of the source being localized are visualized on the digital map. Most digital maps are available for use online. Hence, to view them, Internet access is needed. In the project in question, it is assumed that the localization system may operate in areas without cellular network coverage.

To address this issue, an offline digital map was created and uploaded to the application. This map was created using [21], serving as a library of various resources, including topographic maps and aerial photos. A topographic map was chosen to better visualize the positions of the localized transmitters and receivers with metadata that allow the addition of georeferencing information.

Thanks to such an approach, the map created using the software in question contains an image of the designated area along with information about geographic coordinates, reference system parameters, projection details, etc.

7. Testing the Integrated Localization System

A block diagram of the data processing algorithm used in the SDF method is presented in Fig. 4. Block B covers the operation of the GPS receiver and the recording of system positions throughout the measurement campaign. In the next step, Matlab program is run, and data on the number of measurements to be performed are loaded. The present values determine execution time, with one measurement corresponding to one DFS lasting 0.1 s, for a sampling frequency of $F_S = 100$ kHz and the number of samples in a frame $N_S = 10\,000$.

The buffer size indicates how many measured DFS values are to be used to calculate the x, y coordinates of the transmitter being localized.

Upon startup of the application, the program will check if the SDR radio is connected to the PC (block A) and will configure it according to the specified preset values. Block C illustrates the loading of the offline map.

During the measurement loop, the sampled signal is divided into 10 frames. On the basis of spectral analysis, f_d is determined from each frame and stored in the $freq\_Doppler$ buffer. Subsequently, current GPS information containing data on the receiver's position, velocity, and reference time is retrieved. All data are stored in a local database.

The next step is to check if the required number of DFS has already been reached, based on which the transmitter's coordinates could be determined. If not, the software skips the location estimation step and moves on to determine the receiver's position on the map, checking the program termination conditions.

Once the required number of DFS values has been obtained, the program calculates the estimated coordinates of the RF transmitter located using the SDF method. For this purpose, information is used about the current velocity of the moving receiver, the transmitter's carrier frequency and the time at which the DFS were measured. Additionally, the known real coordinates of the located transmitter are introduced as variables, while the difference between the calculated coordinates x_0, y_0, z_0 and the real coordinates x, y, z allows to determine the localization error.

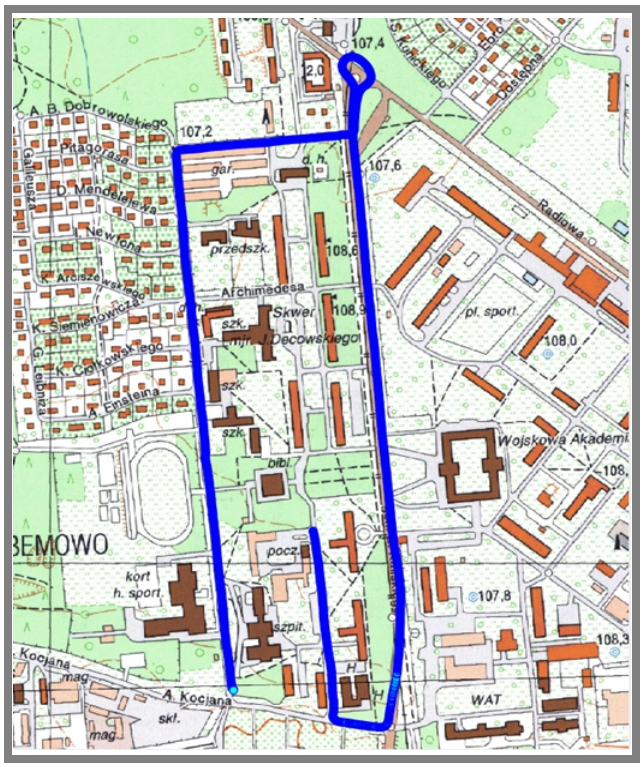

Fig. 5. Route of the vehicle with a GPS receiver on board.

8. Empirical Studies

The GPS system was validated by driving a vehicle in the selected area shown on the map (Fig. 5).

The difference between the coordinates determined by the GPS receiver and its actual position did not exceed 1 m. Position accuracy falls within the manufacturer specified circular error probability of 2.5 m. Figure 6 shows the velocity of the receiver during the measurements, while Fig. 7 depicts the receiving part of the measurement setup. Two antennas were installed on the vehicle's roof: one for GPS and the other for receiving signals from the transmitter. Inside the vehicle, the radio was connected to the antenna by means of a cable, and a laptop with the radio and GPS receiver was connected via a USB port.

The transmission part includes a Rhode & Schwarz SMIQ2 signal generator, an Amplifier Research 5S1G4M4 signal amplifier, a standard source of rubidium frequency (FS725) from Stanford Research Systems, and a Katherin 738449 transmitting antenna. The generator works at 1832 MHz, which, according to Eq. (3), allows to achieve a DFS of up to 100 Hz, while maintaining a vehicle speed of approximately 60 kph. The transmitter setup is shown in Fig. 8.

The generator signal is fed to the RF amplifier and amplified to an output power of 5 W. It is then radiated through the antenna. Such a high power value was selected to make sure that the signal is distinguishable in the spectrum and above the noise level. The rubidium frequency standard at 10 MHz acts as a reference value for the generator.

Empirical studies were conducted based on the selected measurement scenario shown in Fig. 9. The plan was to travel

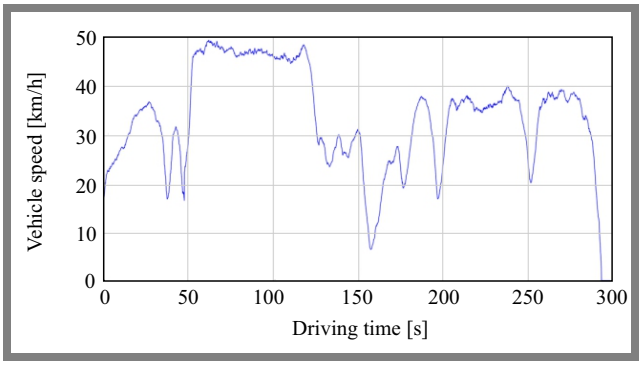

Fig. 6. Speed of the GPS receiver during the measurement campaign.

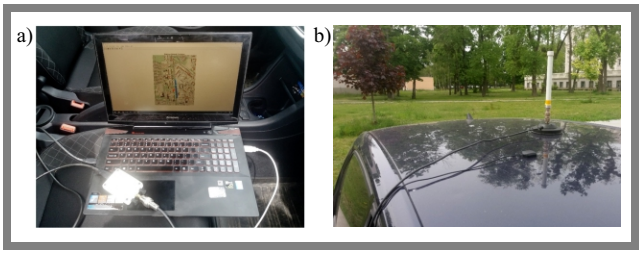

Fig. 7. Diagram of the integrated locator and transmitter system.

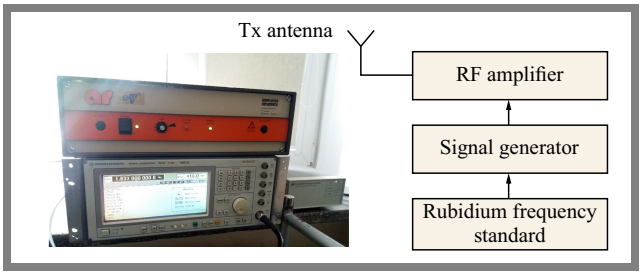

Fig. 8. Transmitter with a generator, amplifier, and rubidium frequency standard a) and diagram of setup b).

along the road between points A–C and C–A. While the car was moving along the selected route, Rx received the signal from Tx. On the basis of the analysis of the received signal and the determination of the position using GPS, the developed localization system estimated the target coordinates. The in-motion test was repeated several times during the night with the vehicle traveling at approximately 60 kph.

9. Results of Empirical Studies

Figure 10 shows the measurement results of the estimated positions of the Tx location, marked in red. Each point was determined based on consecutive sets of 40 DFS. One may notice that the highest density of points is observed near the Tx location.

Using information about the actual position of the localized source, we verified the accuracy of the determined coordinates using Eq. (4). Table 1 presents the determined localization errors, with lowest error value equaling 1.46 m only.

Such results demonstrate that the developed method allows to determine the coordinates of an RF source with accuracy similar to that of other proposals. The best result is achieved when the receiver passes the transmitter at the closest approach

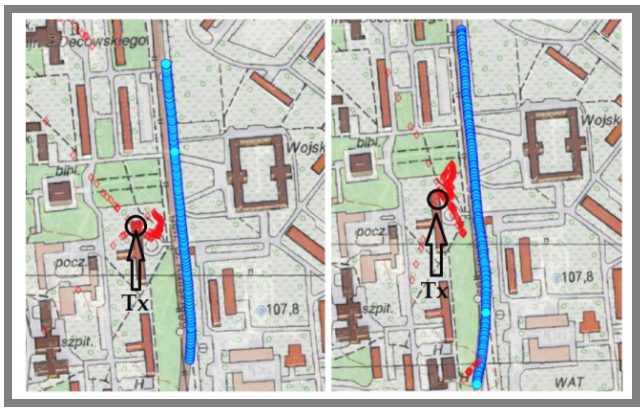

Fig. 9. Route taken by the vehicle during the tests.

(PCA) point. The lowest error is obtained for the section of the route where characteristic rapid changes in DFS occur (Fig. 11). DFS values were determined every 0.1 s, which explains the visible discrete variations. Similarly, the estimated T_x position (values x and y) was also evaluated sequentially, every 0.1 s for consecutive DFS measurements, spaced apart by the signal acquisition time of $T_A = 4$ s. This is why many estimated x_n, y_n values are marked red on the map.

The NLOS environment in which the measurements were performed had the most negative impact on location accuracy. The impact of interference present in the measurement environment is shown in Fig. 11, where a high frequency of rapid changes is visible. The error, defined as the difference between consecutive estimated DFS exceeding $\frac{f_{Dmax}}{2}$, is obtained directly from the complex NLOS environment, with large trees, a building, a tram power line, and other smaller objects affecting the measurements. Such errors were not observed during measurements conducted using UAVs, where a LOS environment was expected between Tx and Rx, hence the transmission was not obstructed.

However, in this experiment, the aim was to test whether the proposed method would succeed in a highly urbanized area. The low-cost SDR used in the system provides short-term frequency stability at a level of 10^{-7} [22], which directly contributed to low error values, appearing as frequency jumps of only 20 Hz, due to atomic frequency standard utilized in Tx.

10. Summary

The aim of this research was to integrate a GPS receiver and a digital map with a Doppler-based RF source localization system. The tests confirmed the functionality of the hardware platform and the dedicated PC-based application.

The tests involving the integrated localization system demonstrated its accuracy and effectiveness. The position of the receiver was determined, on the map, with a very high level of precision, while the error in the estimated coordinates of the localized transmitter amounted to a few meters only. Empirical studies were conducted in an urban environment where obstacles existing between the transmitting and receiving antennas caused multipath propagation. Nevertheless, coordinates showing the location of the RF source were determined successfully.

Tab. 1. Location errors Δ_r obtained during the measurements.

Measurement no.	1	2	3	4	5
Δ_r [m]	3.25	2.99	8.88	1.46	9.50

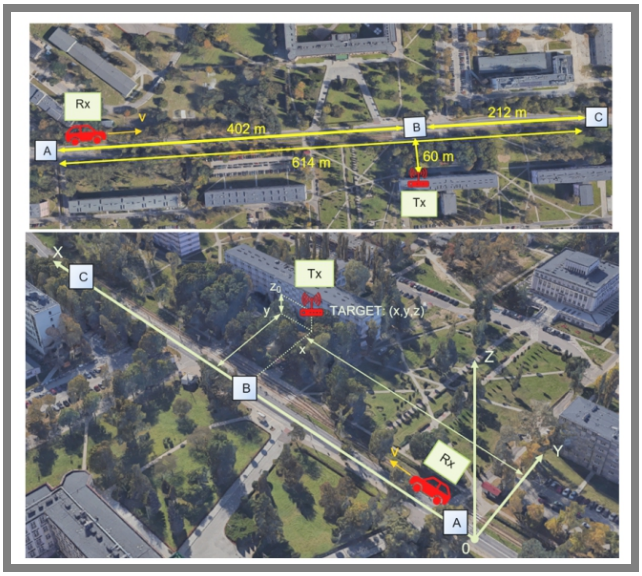

Fig. 10. Map with the path of the receiver (blue) and the estimated coordinates of the transmitter (red).

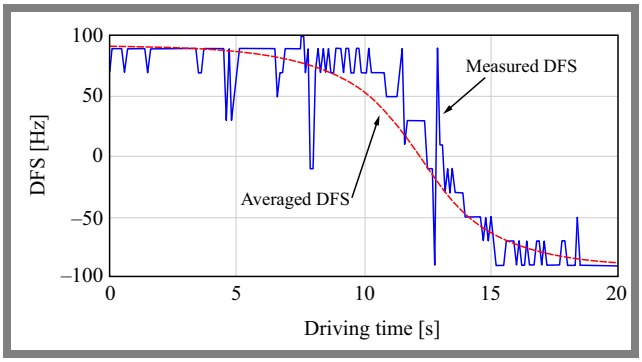

Fig. 11. Measured DFS (blue) and its averaged value (red) for the selected route.

The modular design and compact size of the hardware setup are additional advantages of the proposed solution.

To further improve accuracy, a higher-precision GPS receiver should be utilized and the localization system should be mounted on a flying object, such as a drone. This would help reduce the impact of NLOS environments on the received signals, allowing to extend the research to cover 3D localization methods.

Acknowledgments

This work was financed by the Military University of Technology (WAT) under project no. UGB/22-748/2024/WAT on "Transmission properties of radio wave propagation environments in military applications"

References

[1] F. Williams *et al.*, "Enhancing Emitter Localization Accuracy Through Integration of Received Signal Strength in Direct Position Determination", *2023 IEEE Statistical Signal Processing Workshop (SSP)*, Hanoi, Vietnam, 2023 (https://doi.org/10.1109/SSP53291.2023.10208001).

[2] X. Feng *et al.*, "Single Sensor Emitter Localization Based on TOA Sequence with Inter-pulse Modulation", *2020 IEEE International Radar Conference (RADAR)*, Washington, USA, 2020 (https://doi.org/10.1109/RADAR42522.2020.9114814).

[3] L. Zhang, H. Huan, R. Tao, and Y. Wang, "Emitter Localization Algorithm Based on Passive Synthetic Aperture", *IEEE Transactions on Aerospace and Electronic Systems*, vol. 58, no. 4, pp. 2687–2701, 2022 (https://doi.org/10.1109/TAES.2021.3137090).

[4] H. Xu, Q. Chang, and R. Lang, "A Two-step Algorithm for Locating the Emitter by FDOA", *2023 IEEE International Conference on Consumer Electronics (ICCE)*, Las Vegas, USA, 2023 (https://doi.org/10.1109/ICCE56470.2023.10043390).

[5] S. Agrawal, P. Kumar, and A. Sharma, "Passive Emitter Localization Using TDOA and FDOA Measurements from UAV", *2020 IEEE International Conference for Innovation in Technology (INOCON)*, Bangluru, India, 2020 (https://doi.org/10.1109/INOCON50539.2020.9298328).

[6] J. Schmitz, F. Bartsch, M. Hernandez, and R. Mathar, "Distributed Software Defined Radio Testbed for Real-time Emitter Localization and Tracking", *2017 IEEE International Conference on Communications Workshops (ICC Workshops)*, Paris, France, 2017 (https://doi.org/10.1109/ICCW.2017.7962829).

[7] Y. Xianjia *et al.*, "Cooperative UWB-Based Localization for Outdoors Positioning and Navigation of UAVs Aided by Ground Robots", *2021 IEEE International Conference on Autonomous Systems (ICAS)*, Montreal, Canada, 2021 (https://doi.org/10.1109/ICAS49788.2021.9551177).

[8] K. Li, W. Ni, B. Wei, and M. Guizani, "An Experimental Study of Two-way Ranging Optimization in UWB-based Simultaneous Localization and Wall-Mapping Systems", *2022 International Wireless Communications and Mobile Computing (IWCMC)*, Dubrovnik, Croatia, 2022 (https://doi.org/10.1109/IWCMC55113.2022.9825332).

[9] P. Gajewski, C. Ziółkowski, and J.M. Kelner, "Using SDF method for simultaneous location of multiple radio transmitters", *2012 19th International Conference on Microwaves, Radar & Wireless Communications*, Warsaw, Poland, 2012 (https://doi.org/10.1109/MIKON.2012.6233581).

[10] J. Kelner, C. Ziółkowski, and J. Rafa, "Lokalizacja Źródeł Fal Radiowych na Podstawie Sygnałów Odbieranych przez Ruchomy Odbiornik Pomiarowy", *Biuletyn WAT*, vol. 55, pp. 67–82, 2006 (in Polish).

[11] C. Ziółkowski and J. Rafa, "Influence of Transmitter Motion on Received Signal Parameters – Analysis of the Doppler Effect", *Wave Motion*, vol. 45, no. 3, pp. 178–190, 2008 (https://doi.org/10.1016/j.wavemoti.2007.05.003).

[12] R. Szczepanik and J.M. Kelner, "Software-based Implementation of SDF Method using SDR USRP Platform", *Krajowa Konferencja Radiokomunikacji, Radiofonii i Telewizji*, Wrocław, Poland, 2019 (https://doi.org/10.15199/59.2019.6.18) (in Polish).

[13] R. Szczepanik and J.M. Kelner, "SDF Method Implementation on Software-defined Radio Platform", *Elektronika*, vol. 60, no. 3, pp. 28–33, 2019 (https://doi.org/10.15199/13.2019.3.7) (in Polish).

[14] R. Szczepanik, "Aplikacja Dopplerowskiej Metody Lokalizacji na USRP B200mini", *SECON*, Warsaw, Poland, 2019 (in Polish).

[15] R. Szczepanik and J. M. Kelner, "Localization of Modulated Signal Emitters Using Doppler-based Method Implemented on Single UAV", *2023 Communication and Information Technologies (KIT)*, Vysoké Tatry, Slovakia, 2023 (https://doi.org/10.1109/KIT59097.2023.10297098).

[16] J. Kelner and C. Ziółkowski, "Przestrzenna Lokalizacja Źródła Sygnału Radiowego z Wykorzystaniem Dopplerowskiej Metody Lokalizacji", *Przegląd Telekomunikacyjny – Wiadomości Telekomunikacyjne*, vol. 84, no. 6, pp. 397–400, 2011 (in Polish).

[17] J. Kelner and C. Ziółkowski, "Estymacja położenia źródła sygnału w warunkach wielodrogowej propagacji fal radiowych", *Przegląd Telekomunikacyjny – Wiadomości Telekomunikacyjne*, vol. 85, no. 4, pp. 436–439, 2012 (in Polish).

[18] "Phidget22 – Phidgets Support", [Online]. Available: (https://www.phidgets.com/docs/Phidget22).

[19] "Embarcadero – Środowiska Programistyczne i Narzędzia Bazodanowe", [Online]. Available: (https://www.embarcadero.com.pl).

[20] Ettus Knowledge Base, "B200/B210/B200mini/B205mini", 2021 [Online]. Available: (https://kb.ettus.com/B200/B210/B200mini/B205mini).

[21] "Geoportal.gov.pl", [Online]. Available: (http://geoportal.gov.pl).

[22] K. Bednarz, J. Wojtuń, J.M. Kelner, and K. Różyc, "Frequency Instability Impact of Low-cost SDRS on Doppler-based Localization Accuracy", *Sensors*, vol. 24, no. 4, art. no. 1053, 2024 (https://doi.org/10.3390/s24041053).

[23] R. Szczepanik, J.M. Kelner, and C. Ziółkowski, "Overlapping-based Radio Signal Processing for SDF Location Method", *2021 Signal Processing Symposium (SPSympo)*, Łódź, Poland, 2021 (https://doi.org/10.1109/SPSympo51155.2020.9722573).

Rafał Szczepanik, M.Sc.
Institute of Communications Systems
https://orcid.org/0000-0003-1225-297X
E-mail: rafal.szczepanik@wat.edu.pl
Military University of Technology, Warsaw, Poland
https://wojsko-polskie.pl/wat/

Paweł Skokowski, Ph.D.
Institute of Communications Systems
https://orcid.org/0000-0001-8658-4518
E-mail: pawel.skokowski@wat.edu.pl
Military University of Technology, Warsaw, Poland
https://wojsko-polskie.pl/wat/

Efficient Routing for Delay-energy Tradeoff in Event-based Wireless Sensor Networks

Nadjib Benaouda

University of Mohamed El Bachir El Ibrahimi, Bordj Bou Arreridj, Algeria

https://doi.org/10.26636/jtit.2024.4.1833

Abstract — Wireless sensor networks (WSNs) play a crucial role in the Internet of Things (IoT) by providing a foundation for collecting, transmitting and processing data from the physical world. Beyond the necessity of proposing solutions that are in line with the constrained resources of sensor nodes, particularly their limited energy capacity, the consideration of real-time data collection becomes essential. This is particularly vital due to the fact that many IoT applications require timely data collection. However, the need to establish energy-efficient routes contradicts the requirement to guarantee timely data collection. Hence, achieving an equilibrium and striking, subsequently, a trade-off between these two issued becomes imperative. To answer this question, a localized delay-bounded and energy-efficient routing protocol (abbreviated as LDER) is presented. It is based on another protocol, namely DEDA, aimed at achieving a higher energy conservation degree. To validate the efficacy of LDER, simulations were conducted using the J-sim simulator. The results demonstrate the ability of LDER to achieve the desired equilibrium and prove its superiority over DEDA.

Keywords — delay-bounded path, energy efficiency, LMST, WSN

1. Introduction

Wireless sensor networks constitute a fundamental component of the IoT ecosystem, playing a pivotal role in facilitating data collection [1], [2]. A WSN consists of a group of nodes that offer perception, processing, and communication capabilities, allowing them to collect and share data through a wireless link. These nodes, commonly referred to as sensor nodes, are deployed in a specific geographic area and measure physical parameters that are relevant to our environment (e.g., temperature, humidity, vibrations, etc.). The nodes relay these measurements to each other, until the data reach the sink, i.e. a specific node that acts as a gateway to the host.

Sensor nodes are low-resource embedded systems, meaning they can only transmit at a limited data rate. Moreover, the capacity of these sensors' batteries limits their operational lifetime. Due to these limitations, new algorithms, methods, and protocols must be developed that are suitable for the specific characteristics of these wireless sensor nodes, with a particular emphasis placed on their limited energy resources [3].

Additionally, many IoT applications require real-time data collection. In fact, the process of monitoring various environmental and physical parameters is crucial for such applications as industrial automation, medical monitoring, and environmental detection, where timely information collection is essential [4]–[6].

Protocols that satisfy those two requirements concurrently are not easy to develop. In fact, lower energy consumption of the sensor nodes contradicts the need to ensure timely arrival of collected data. Opting for lower consumption entails accepting greater data latency, as the established routes would involve numerous nodes transmitting over short distances to conserve energy.

On the other hand, prioritizing lower latency comes at the cost of increased energy consumption. Consequently, it is imperative to establish a trade-off between these two key requirements, namely reduction in energy consumption and timely delivery of the sensed data [7].

To address the challenge mentioned above, we present a localized delay-bounded and energy-efficient routing protocol (LDER). It stems from an existing DEDA protocol [8] which we have enhanced to make it more efficient in preserving energy.

Initially, LDER establishes a sparse topology by applying the local minimum spanning tree (LMST) algorithm to the initial configuration. Then, the shortest-path tree that connects the sink with sensor nodes on the top of this sparse topology is established. Specific events trigger adjustments to the initial routes within the pre-established tree. This adaptation entails incorporating shortcuts from the original network topology when the sensed data cannot be delivered in time or when a more energy-efficient path is possible. In fact, DEDA does not account for this alternative. The protocol fails to provide any mechanisms for identifying paths that might be more energy efficient, other than those stemming from the LMST topology.

To validate the proposal, we simulate both LDER and DEDA using the J-sim network simulator [9]. Various experiments were conducted, producing favorable outcomes that underscore LDER's ability to maintain the desired equilibrium and its advantages over DEDA.

The article is structured as follows. Section 2 provides a concise overview of relevant prior research. Section 3 outlines the preliminary aspects of the proposed approach, including the network model, the definition of the problem, and an introduction to the DEDA protocol. Section 4 presents an overview of LDER. Section 5 shows the details of the proposal. The experimental setup and simulation results are presented in Section 6, followed by conclusions drawn in Section 7.

2. Related Work

The existing literature has seen numerous protocols aimed at tackling the challenge of balancing the delay-energy trade-off in WSNs. In this section, we provide an overview of a selection of these propositions.

In [10], the authors introduce a modified version of the firefly algorithm known as firefly with cyclic randomization (FCR). This variant aims to enable energy-efficient and low-latency WSN routing. The primary focus is on selecting an optimal cluster head that is not only in close proximity to the sink, but also strategically positioned relative to the sensor nodes. This spatial proximity significantly reduces time delays, subsequently leading to an improvement in the data packet transmission speed.

Paper [11] presents a novel algorithm called a delay constrained energy-efficient multi-hop routing algorithm for effective routing in WSNs. The method introduces an innovative approach known as the delay-constrained reliable routing algorithm, minimizing energy consumption by creating efficient clusters without increasing end-to-end delay. The sink node initiates the clustering process, which involves three key steps: cluster head selection, cluster formation, and calculation of the trade-off between energy and delay (TED). Once the clusters are established, the route discovery process uses the depth-first search (DFS) algorithm.

The routing process comprises three stages: link and route cost calculation, end-to-end delay calculation, and data communication. The proposed algorithm offers several advantages, including energy efficiency, enhanced link quality, scalability, improved throughput, reliable data delivery, reduced delay, and cost effectiveness in building clusters and routing.

The authors of [12] introduce a routing solution called multi-QoS constraint multipath routing (MQoScMR) in cluster-based WSNs. The design accommodates multiple quality of service (QoS) constraints. The approach consists of three steps: first, the status of the node is estimated – this phase involves assessing the level of residual energy, delay, and congestion of a given node. In the second step, cluster heads (CH) are selected based on such factors as residual energy, estimated delay and congestion observed during the previous data transmission round. The third step involves the construction of multiple pathways. This requires that potential routing paths be established from the source node to the sink, taking into account the estimate of link cost based on energy level, delay, and congestion indices of the intermediate nodes. Following the completion of this final step, diverse routes are delineated to serve different purposes, in alignment with the specific requirements of a given application.

In [13], the authors present a routing protocol aimed at enhancing both delay and energy efficiency within WSNs by using two-hop information. Their contributions encompass three key aspects. Firstly, they introduce potential relay information (PRI) metrics, which are based on residual energy, distance, and delay factors. This parameter evaluates the link quality of neighboring nodes, ensuring that the subsequent forwarder selected for data packet transmission delivers the packets to the destination with the best quality of service ensured. Secondly, they design a preemptive neighborhood state index (NSI) algorithm enabling the nodes to look two hops ahead in their routing trajectory. This foresight helps make informed forwarding decisions, minimize delays, and distribute traffic loads evenly across the system. Finally, they implement a proactive feedback mechanism to streamline the two-hop information update process.

In [14], a data fusion algorithm is presented that relies on a hybrid delay-sensitive clustering approach. This method integrates the strengths of both single-layer and multi-layer cluster structures. Using a decision function, the proposal dynamically selects the appropriate clustering patterns for the clusters. This dynamic selection process aims to strike a balance between network delay and energy consumption.

The authors of [7] introduce a data aggregation routing technique that leverages the ant-colony optimization metaheuristic. This approach aims to design a routing structure that optimizes overlapping routes while minimizing cumulative transmission power. At the same time, the method ensures that the paths adhere to specified delay limits.

Research efforts focusing on wireless sensor and actor networks (WSANs) offer promising solutions to address the delay-energy tradeoff challenge. Paper [15] introduces a routing protocol that aims to deliver good quality of service (QoS) within the context of a WSAN. The protocol emphasizes such factors as delay and energy consumption. The network is organized in clusters supervised by cluster heads that are selected based on key metrics. These metrics comprise energy capability, connectivity richness, and accessibility of all actors. Furthermore, they tackle the intricacies of sensor-actor communication by introducing an on-demand routing-based data communication protocol that provides access to actor nodes with minimal delay and reduced energy consumption.

In [16], the cluster-based coordination protocol (CCR) is proposed, which organizes sensor nodes into clusters. The CH of each of these groups is linked to the actor which is capable of covering a given geographical area. If several actors cover this area, the closest actor node to this CH is selected. CCR takes advantage of data aggregation by allowing each CH to aggregate its members' data. However, this aggregation process must be executed without compromising the timely delivery of sensed data.

The authors of [17] present a reactive protocol that facilitates the segmentation of sensor nodes within the event area into distinct clusters. The authors achieved this partitioning by pairing each event-detecting sensor node with the nearest actor. Each cluster establishes a data aggregation tree, with its root at the respective actor. This tree is then adjusted based on the actor's feedback, defined by the observed reliability value. This value is defined as the ratio between the number of packets received in a given time and the total number of packets generated within a given interval.

Following this feedback, when the observed reliability value falls below a certain threshold, each sensor selects the neighbor that is geographically closest to the final destination. This helps minimize the number of hops leading to the

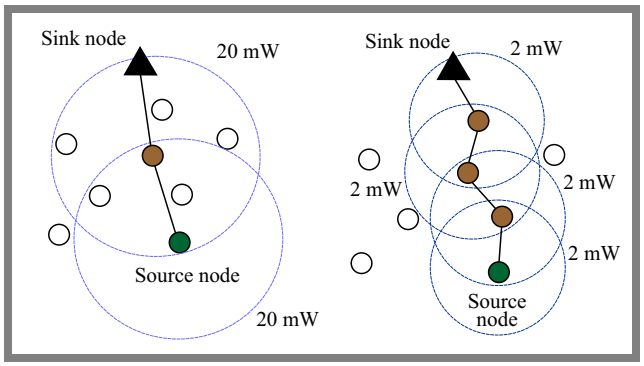

Fig. 1. Two potential routes between the source node and the sink: a) one with a total transmission power of 40 mW and a hop count of 2, and b) one with a power of 8 mW and 4 hops.

destination, thus reducing data latency. However, this minimization comes at the expense of energy consumption. In contrast, when the observed reliability value exceeds the predetermined threshold, indicating excessive reliability, each sensor node forwards its data to its closest neighbor, using a lower transmission power.

3. Preliminaries

This section outlines the preliminary aspects of the proposed approach, elucidates the network model, defines the problem, and presents the DEDA protocol. The network model adopted in this study is outlined as follows:

- all nodes within the network are stationary,
- each sensor i can change its communication range by adjusting its transmission power level,
- any sensor can reach a maximum transmission power of P_{max}, which is equivalent to a maximum range of R_{max}.

The topology of the network is modeled by the $G = (V, E)$ graph, where: $V = (v1, v2, \ldots, v_n)$ comprises a collection of vertices that represent the nodes within the network and E is the set of arcs (links) that interconnect these nodes. The latter set is defined as follows:

$$E = \{(u, v) | u \in V, \quad v \in V, \quad \delta_{u,v} \leqslant R_{max}\} \, . \tag{1}$$

Considering that $\delta_{u,v} = \sqrt{(x_u - x_v)^2 + (y_x - y_v)^2}$ corresponds to the Euclidean distance between the two nodes u and v, where $u = (x_u; y_u)$ and $v = (x_v; y_v)$, the following formula calculates the transmission power required for communication between node i and its neighboring node j [18]:

$$Power_{i,j} = \delta_{i,j}^{\alpha} \, , \tag{2}$$

where $\delta_{i,j}$ represents the distance that separates i from j, which corresponds to the transmission range used by node i to communicate with j, α is the path loss exponent that is typically assigned a value of 2 or 4 [19]. Thus, the power values are expressed as a function of the transmission range (i.e., distance) without providing power levels in a specific energy unit, such as Joules, to allow to compare the protocol with other approaches.

3.1. Problem Definition

In this article, the primary objective is to delve into the intricacies of the routing challenge, specifically with respect to the efficient transmission of the collected data from individual sensor nodes to the designated sink node within the WSN. The limited energy source necessitates energy efficient communication. At the same time, the transmission of collected data must not exceed a specified latency level. Balancing these two objectives poses a challenge: minimizing energy consumption during the routing process necessitates considering paths with short links, thus resulting in a high number of hops and increased data latency.

Figure 1, adapted from [20], depicts two potential routes connecting the source and the sink. Figure 1a shows a two-hop route with a total transmission power of 40 mW, and Fig. 1b shows a second, more energy-efficient route with a total transmission power of 8 mW, but a total number of hops of four.

This illustrates two conflicting objectives: to minimize the total transmission power while simultaneously ensuring that communications adhere to the imposed temporal constraint. This is precisely the challenge that we aim to address in this research.

3.2. DEDA Protocol

In this section, we present the DEDA protocol [8], serving as the foundation of our proposal.

DEDA aims to build aggregation trees with energy-efficient and time-bounded paths. An actor (or sink) serves as the root of each tree, which then connects to its corresponding sensor nodes – Fig. 2. DEDA first establishes a new sparse topology over the original network graph based on the LMST algorithm. On top of this new topology, it builds a tree that connects the actor with its associated sensors, Fig. 2b. This tree is used, without modification, if the given deadline is not exceeded. Otherwise, this tree is adjusted by borrowing other links from the original graph. This adjustment is made on the basis of a certain value of DEP which reflects the desired progress on establishing the sparse topology, ensuring that the deadline is met. This value is calculated as follows:

$$DEP = \left\lceil \frac{LD(w)}{TL - MED} \right\rceil \times l(w) \, , \tag{3}$$

where $LD(w)$ denotes the distance between the current node w and the actor in the sparse topology. The time limit (TL) represents the user-specified deadline. MED is the highest experienced delay specified in all reports received from w children. The value of $l(w)$ is determined based on the traffic load within the network. It assumes the value of 1 when traffic intensity is relatively low. In such scenarios, the distance between two nodes corresponds to the number of hops along the path connecting them.

However, if traffic intensity is high, $l(w)$ corresponds to the degree of node w, and the distance between two nodes becomes the cumulative sum of degrees between all nodes within the connecting path. In the latter scenario, the distance

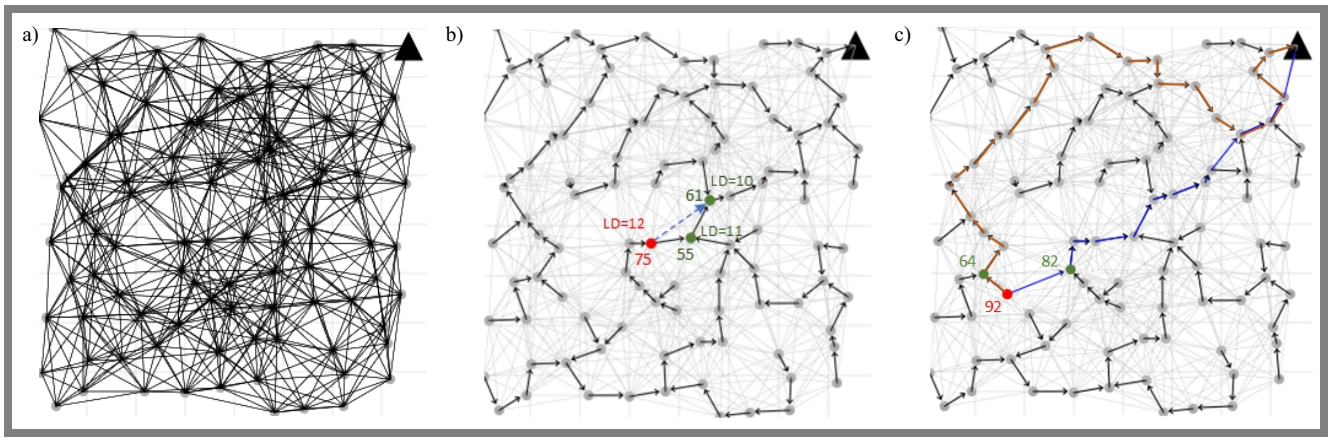

Fig. 2. DEDA principle and the solution addressed in this work: a) the initial topology generated using the maximum transmission power of the network nodes, b) the shortest path tree built on the local minimum spanning tree (LMST) of the initial topology, and c) the route of the source node 92, assuming a time limit equal to ∞. The orange line marks the route built with DEDA, while the blue line represents the outcome of the proposed solution.

is computed using this approach due to the impact of the number of nodes contending for access to the wireless channel on the basis of data latency.

To elaborate on the fundamental concept behind DEDA, let us consider the example shown in Fig. 2b. Suppose we calculate the distance in hops and set TL to 11. Then, node 75 cannot route its data through its parent (node 55) in the pre-established aggregation tree because this last node cannot guarantee the prompt delivery of these data, i.e. $LD(75) = 12$. Consequently, node 75 alters its parent and opts for its neighbor 61 from the original topology. This selection is based on the fact that neighbor 61 facilitates a progress of 2 hops within the sparse topology, that is, $LD(75) - LD(61) = 12 - 10 = 2$, equivalent to the value $DEP = \lceil \frac{12}{11-0} \rceil \times 1 = 2$. Here, MED used in the DEP calculation example equals 0, as we assumed, for illustrative purposes, that node 75 is the source node. Therefore, it does not forward any reports received from its children, but is the one that initiates data transmission.

3.3. Limitations of the DEDA Protocol

DEDA was purposefully designed to gather data from all nodes linked to a particular actor in response to the last query. Here, every node transmits its data which are subsequently aggregated across various paths within the established aggregation tree. These data traverse energy-efficient routes, since these paths were constructed based on the LMST topology.

However, when only the sensor nodes that detect events transmit their data to the actors, DEDA encounters inefficiencies.

Consider the scenario shown in Fig. 2c, where source node 92 (shown in red) aims to transmit its data to its corresponding actor. Assuming an infinite delay bound, node 92 would employ its path within the aggregation tree (indicated by the orange route in Fig. 2c) without any alterations. This final route is notably lengthy, resulting in a considerable energy expenditure, even if it is made exclusively of short links, i.e., nodes utilizing minimal transmission power.

Under these circumstances, opting for alternative paths with reduced energy expenditures is better. For instance, it would be more advantageous for node 92 to route its data through its neighbor 82, utilizing link $e_{92,82}$ from the original topology, as depicted in Fig. 2c.

The question that arises here is how these types of neighbors can be identified and how to efficiently introduce shortcuts from the initial topology to yield paths with reduced energy expenditures. In fact, along this trajectory that our contribution is made, enhancing DEDA's capabilities to find shortcuts by incorporating links from the original topology not only to meet the specified time constraints but also to establish paths with decreased energy expenditures.

4. Overview of the LDER Protocol

In this section, we present an overview of our proposed LDER protocol, designed to enhance DEDA capabilities. LDER operates through a sequence of four steps:

1) Initially, each node in the network gathers data concerning its neighboring nodes, specifically their locations and identifiers. This collection is characterized by the hello messages that each node sends to its vicinity.
2) Based on this information, a new sparse topology is constructed on top of the initial network topology, using the LMST algorithm [21]. The use of such a sparse topology has the benefit of working with an energy-efficient topology from the beginning, as it preserves only the links that require minimal energy consumption.
3) After establishing this new sparse topology, the shortest path tree is derived over this LMST topology, using the sink as the root. We established this tree based on the number of hops along the traversed routes. During this step, each node determines its initial parent and collects information pertinent to all of its neighbors, including those that are not included in the set of neighbors in the sparse topology. Each node specifically obtains information on

the distance and cost of the optimum path connecting each neighbor within the initial topology to the sink. This knowledge enables each node to create shortcuts within the initial topology and choose its new parent.

4) Upon the creation of this tree, the routing of data from the source node to the sink can be performed whenever an event is detected. Each node transmits the messages it receives to its designated parent node, established in the preceding phase if this parent guarantees the prompt delivery of these messages and no other neighbor exists, among all its neighbors in the initial topology, that also ensures timely delivery while simultaneously providing a more energy-efficient route to the sink. Alternatively, a shortcut in the original topology can be added by selecting a new parent node from the neighbors of the current node within this initial topology.

5. Details of LDER

This section highlights the details of LDER protocol by elaborating the specifics of each step outlined in the preceding section. The main data structures employed at every sensor node i are presented in Tab. 1.

Tab. 1. Main data structures employed at each sensor node i.

Data	Description
ID_i	ID of sensor node i
$SinkID_i$	ID of the sink
$Coordinate_i$	Coordinates of node i
$Parent_i$	ID of parent of node i
LD_i	Number of hops along optimal path linking node i with the sink within the LMST topology
TL	Time limit
N_i^{LMST}	Set of nodes neighboring node i within the sparse topology (LMST)
N_i^{MAX}	Denotes the collection of neighboring nodes for node i within the original topology. Every element within this set comprises the neighbor's ID, the path distance (measured in hops) connecting the said neighbor with the sink within the sparse topology, and lastly, the energy expenditure associated with this path

5.1. Collecting Neighboring Node Information

In the initial phase, every sensor node initiates the process of gathering information regarding its neighboring nodes. To do this, each node generates a hello message containing its ID and coordinates, which is then transmitted using its maximum transmission power. This data collection phase continues for a duration of t_{hello}, during which each node transmits its message and awaits acknowledgment from its neighboring nodes.

5.2. Sparse Topology Formation

Once the t_{hello} interval has elapsed, which signifies the end of the phase during which information regarding the neighbors of each sensor node in the initial topology is collected, the LMST algorithm is launched. This phase is essential, as it establishes the network's new topology based on energy-efficient connections between nodes. The entire procedure works as follows [21]:

- Computation of local MST. Each sensor node uses the coordinates of its neighboring nodes to calculate a local minimal spanning tree (MST).
- Selection of new neighbors. Once the MST has been calculated, each node identifies its new neighbors within the new topology. This is achieved by selecting the nodes that are one hop away within the newly established MST.
- Transformation into an undirected graph. The preliminary result of this MST-based neighbor selection procedure has the form of a directed graph. To establish a functional and resilient topology, the directed graph must be converted to an undirected graph. This can be accomplished by relying on one of two methods:
  - LMST$^-$ method. An edge between nodes i and j is established in the new topology only if both directed edges $e_{i,j}$ and $e_{j,i}$ are present in the respective MSTs of nodes i and j. This ensures a mutual agreement for the connection, leading to a sparse but reliable topology. This variant is known as LMST$^-$.
  - LMST$^+$ method. Alternatively, an edge between nodes i and j is created if either of the directed edges $e_{i,j}$ or $e_{j,i}$ is present in the MSTs. This more relaxed criterion results in a denser topology, referred to as LMST$^+$.

Here, sparse topology was formed using Prim's algorithm, while the weights of the links were calculated using Eq. (2). As a variation of LMST, we have adopted LMST$^-$. This was done by allowing each node to share information about its newly computed neighbors using route discovery messages while constructing the shortest path tree.

5.3. Calculation of the Shortest Path Tree Across the Sparse Topology

When the formation of the sparse topology is complete, the process of creating the shortest path tree connecting sensor nodes to the sink may commence. It is initiated, as depicted in line 1 of Algorithm 1, by the sink broadcasting a route discovery (RD) message to its neighboring nodes. This message comprises several fields:

- Sender,
- Sink ID,
- LD denoting the distance (in terms of hops) traveled by the RD message within the sparse topology (LMST) since its dissemination by the sink (initialized to 0),
- TL representing the designated time limit,

Algorithm 1 The process of determining the shortest path tree across the sparse topology.

1: The sink creates and broadcasts a RD message
   ▷ R_{RD} is the set of nodes receiving the RD message
2: **for** each node $i \in R_{RD}$ **do**
3: Node i updates the element that matches $RD.sender$ in N_i^{MAX} with $RD.LD$ and $RD.cost$
4: **if** $ID_i \notin RD.N_{LMST}$ and $RD.sender \in N_i^{LMST}$ **then**
5: Node i deletes $RD.sender$ from its set N_i^{LMST}
6: **end if**
7: **if** $LD_i > RD.LD + 1$ and $RD.sender \in N_i^{LMST}$ **then**
8: $Parent_i \leftarrow RD.sender$
9: $LD_i \leftarrow RD.LD + 1$
10: $SinkID_i \leftarrow RD.sinkID$
11: $TL \leftarrow RD.TL$
12: $RD.cost \leftarrow RD.cost + power_{i,RD.sender}$
13: $RD.sender \leftarrow ID_i$
14: $RD.LD \leftarrow LD_i$
15: Node i re-broadcasts the RD message
16: **end if**
17: **end for**

- Cost signifying the cumulative cost since the initial broadcast (initialized to 0),
- N_{LMST} which indicates the set of neighbors of the sender within the sparse topology.

Upon receiving this message, each node i proceeds to update the entry in its set N_i^{MAX} that corresponds to RD.sender with RD.cost and RD.LD values. Taking into account the use of the LMST$^-$ variation, node i additionally removes RD.sender from its set N_i^{MAX} under the condition that the mentioned sender is part of N_i^{MAX} and ID_i is not included in the $RD.N_{LMST}$ set. Subsequently, node i verifies whether the RD message comes from one of its LMST neighbor with a better path. If this is the case, it proceeds to update its internal data along with the fields of the RD message, as outlined in lines 8–11 and 12–14 of Algorithm 1, respectively. Following this update, the node re-broadcasts the RD message with maximum transmission power.

Concluding this phase, each node i acquires knowledge about the distance and cost of the optimal path that links each neighbor within the N_i^{MAX} set with the sink. This information serves as a foundation for the subsequent phase.

5.4. Determining an Appropriate Route in Response to an Event

Following the creation of the shortest path tree, the sensor nodes await for events to unfold. Upon detection of an event, the source node generates a parent decision message (PDM). The purpose of this message is to determine a route that guarantees a prompt transmission of the sensed data while potentially conserving more energy than the initial path established in the preceding phase. Therefore, each node aiming to determine the next hop for the PDM message evaluates whether its previously designated primary parent remains the optimal choice.

In other words, this parent should guarantee data arrival prior to the set deadline, while no other neighboring node in N_i^{MAX} suggests a path with a superior energy efficiency level. If these criteria cannot be met, exploration of potential shortcuts within the original topology becomes imperative.

In a more detailed explanation, each node i, aiming to identify the next hop for the PDM message, starts by calculating the desired progress value (DEP). The latter is defined as the desired progress, measured in the count of hops, of the PDM message within the sparse LMST topology, so as not to exceed the specified time limit. This DEP value is calculated as follows:

$$DEP = \left\lceil \frac{LD_i}{TL - ED} \right\rceil , \tag{4}$$

In this formula, ED corresponds to the experienced delay of the PDM message from the moment of its dissemination by the source node.

Upon the calculation of DEP, node i proceeds to compute, for every neighbor j within N_i^{MAX}, the proposed progress that j offers, using the following formula:

$$Progress_j = LD_i - LD_j , \tag{5}$$

where LD_j is obtained from the entry corresponding to node j within set N_i^{MAX}.

After calculating these values, node i selects its parent n as:

$$n = \begin{cases} \underset{j \in N_i^{MAX}}{\arg\min}\ Cost_j & , \text{ if } \exists\ j \in N_i^{MAX} \text{ such that } Progress_j \geqslant DEP \\ \underset{j \in N_i^{MAX}}{\arg\max}\ Progress_j & , \text{ otherwise} \end{cases} . \tag{6}$$

In order to ensure a progress rate that exceeds DEP, node i chooses, as its parent node n, from among all of its neighbors, the one which presents the lowest energy cost towards the sink. In cases where no neighbor offers an advancement greater than DEP, node i opts for the neighbor that provides the most substantial advancement.

Once this node n has been selected, node i updates the fields of the message (PDM) and sends it to n. The same process as illustrated in Algorithm 2 is repeated until the PDM message successfully reaches the sink. Subsequent data will then travel an identical route as undertaken by the PDM message.

Tab. 2. Simulation parameters.

Parameter	Value
Number of sensor nodes	500
Sink position	Center of the field
Number of source nodes	4
Density	20
Communication range	80 m
Path loss α	2

Algorithm 2 Routing process of a PDM message.

▷ s is the source node
▷ c is the current node of the PDM message
▷ n corresponds to the selected parent

$c \leftarrow s$
while $c \neq$ SinkID **do**
    Node c computes DEP according to Eq. (4)
    for each node $j \in N_i^{MAX}$ **do**
        Node c computes $Progress_j$ using Eq. (5)
    end for
    Node c selects n according to Eq. (6)
    $c \leftarrow n$
end while

6. Experiments and Results

We conducted the simulation using the J-sim simulator [9], incorporating both our protocol and DEDA, for evaluation purposes. Table 2 presents the primary simulation parameters that were utilized. The area of the deployment field was calculated as follows: network density d is defined by the number of nodes per unit area, meaning that there are d nodes inside the communication region of each node, represented as a circle of radius r and area πr^2.

To equally distribute n nodes across a deployment region with a uniform density d, the total deployment area A must be sufficient to support all n nodes at that density. Consequently, the necessary area is determined by the $\frac{(n\pi r)^2}{d}$ formula. In a square deployment region, side length L is the square root of the area, resulting in:

$$L = \sqrt{\frac{(n\pi r^2)}{d}} \,. \tag{7}$$

Therefore, a square deployment area is adopted in the experiments, with a side length of L calculated with the use of the previous formula.

The primary goal of the experiments conducted is two-fold. Firstly, it aims to demonstrate the ability of LDER to achieve the intended trade-off, and secondly, to show its proficiency in discovering paths with lower energy costs compared to those computed by DEDA. To achieve this goal, a series of various experiments were undertaken, considering various time limits Γ. The results obtained are presented in the form of snapshots that are used to visually depict the routes established by each protocol for various values of Γ. These snapshots distinctly illustrate the introduction of various shortcuts.

The curves show the different costs (i.e., total transmission powers) of the routes built by each protocol according to Γ.

Figure 3 represents the distinct routes obtained following the execution of the proposed LDER protocol with corresponding Γ values of 6, 8, 10, and ∞. Firstly, it is evident that the hop count for each route consistently remains below the specified Γ value. Secondly, there is a noticeable trend – the average hop count for the established routes gradually increases as the Γ value grows.

This phenomenon is logical considering a closer examination of Fig. 3, where a decrease in Γ is associated with an increase in the number of shortcuts. This stems from the necessity to continually locate nodes capable of ensuring progress within the initial topology while adhering to the designated time limit. In fact, this decrease in the average hop count is coupled with a decrease in energy preservation. This stems from the incorporation of shortcuts, which entails the inclusion of less energy-efficient links. This addition becomes more pronounced with each decrease of Γ.

Figure 4 presents a visualization of the various routes obtained after running DEDA using similar Γ values. The same

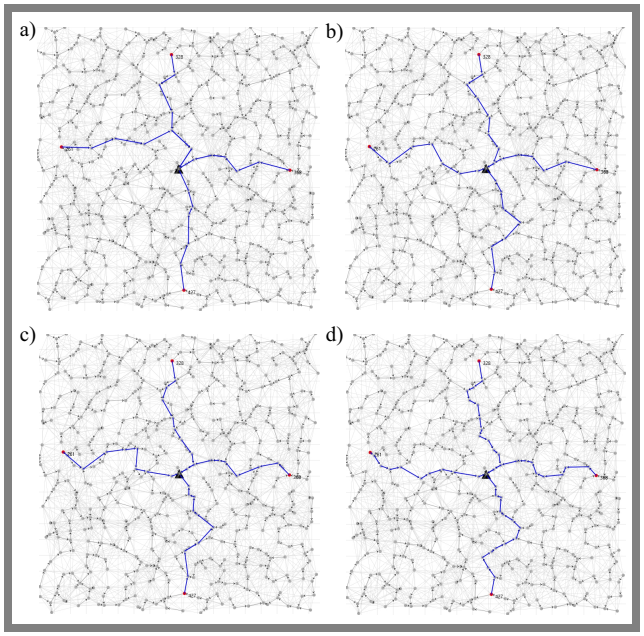

Fig. 3. Snapshots showing the distinct routes constructed by LDER using: a) Γ=6, b) Γ=8, c) Γ=10, and d) Γ=∞ hops.

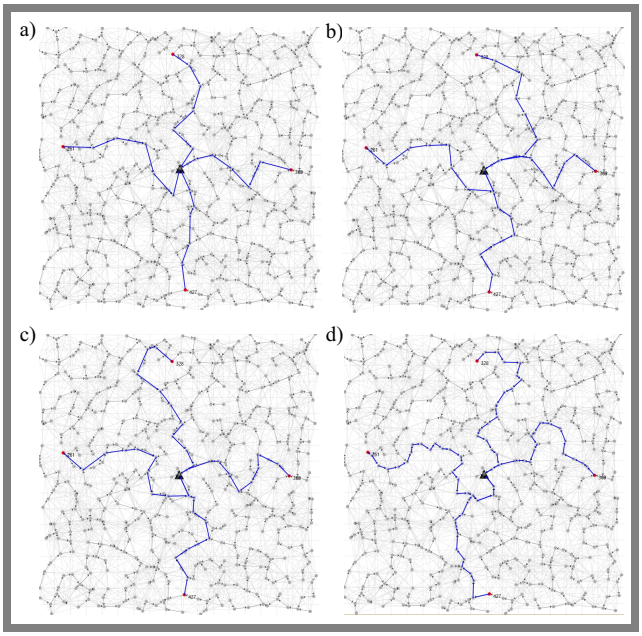

Fig. 4. Snapshots displaying different routes constructed by DEDA using: a) Γ=6, b) Γ=8, c) Γ=10, and d) Γ=∞ hops.

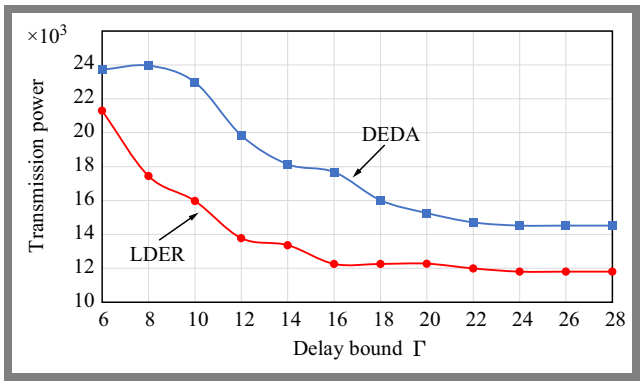

Fig. 5. Average total transmission power of the routes formed by LDER and DEDA with respect to Γ.

observations apply. However, when comparing Fig. 3d with Fig. 4d, it becomes apparent that DEDA does not incorporate any shortcuts. The established routes are entirely restricted to the LMST topology due to the large Γ value, eliminating the need to include shortcuts from the initial topology.

On the contrary, the LDER protocol follows a different approach, where specific shortcuts are introduced. These shortcuts are not primarily aimed at ensuring timely data delivery but are rather aimed at adopting paths that are more energy efficient than those provided by the LMST topology.

Figure 5 shows the ability of LDER to discover routes with lower total transmission power compared to the routes formed by DEDA. In this experiment, we compared the total transmission power of the tree routing structures constructed by DEDA and LDER across varying time limits. The results reveal a decent improvement in power efficiency with the adoption of LDER. For example, at a time limit of 8, LDER demonstrated a 27.13% reduction in transmission power compared to DEDA.

As the time limit increased, the benefits persisted, with LDER consistently outperforming DEDA by significant margins. These findings underscore the effectiveness of LDER in enhancing the energy conservation aspects of the routing process, highlighting its potential impact on the overall performance of wireless sensor networks.

7. Conclusion

This study has focused on energy-efficient and real-time data routing processes within event-based wireless sensor networks, a critical domain within the realm of the IoT. We introduced the LDER protocol which adeptly balances the trade-off between minimizing energy consumption and ensuring prompt delivery of sensed data. The novel approach is based upon the foundation of another protocol, known as DEDA.

To validate the effectiveness of LDER, we conducted comprehensive simulations using the J-sim simulator. We seamlessly integrated both LDER and DEDA into this simulator. Through a series of experiments, we obtained positive outcomes that underscore the performance of the protocol.

References

[1] A.M.K. Abdulzahra, A.K.M. Al-Qurabat, and S.A. Abdulzahra, "Optimizing Energy Consumption in WSN-based IoT Using Unequal Clustering and Sleep Scheduling Methods", *Internet of Things*, vol. 22, art. no. 100765, 2023 (https://doi.org/10.1016/j.iot.2023.100765).

[2] T. Fang and Y. Yang, "Distributed Communication Protocol in Wireless Sensor Network Based on Internet of Things Technology", *Wireless Personal Communications*, vol. 126, no. 3, pp. 2361–2377, 2022 (https://doi.org/10.1007/s11277-021-09203-7).

[3] B. A. Begum and S. V. Nandury, "Data Aggregation Protocols for WSN and IoT Applications – A Comprehensive Survey", *Journal of King Saud University – Computer and Information Sciences*, vol. 35, no. 2, pp. 651–681, 2023 (https://doi.org/10.1016/j.jksuci.2023.01.008).

[4] J. Bian *et al.*, "Machine Learning in Real-time Internet of Things (IoT) Systems: A Survey", *IEEE Internet of Things Journal*, vol. 9, no. 11, pp. 8364–8386, 2022 (https://doi.org/10.1016/10.1109/JIOT.2022.3161050).

[5] R. Kavra, A. Gupta, and S. Kansal, "Optimization of Energy and Delay on Interval Data Based Graph Model of Wireless Sensor Networks", *Wireless Networks*, vol. 29, no. 5, pp. 2293–2311, 2023 (https://doi.org/10.1007/s11276-023-03292-x).

[6] A. Hassan, A. Anter, and M. Kayed, "A Survey on Extending the Lifetime for Wireless Sensor Networks in Real-time Applications", *International Journal of Wireless Information Networks*, vol. 28, no. 1, pp. 77–103, 2021 (https://doi.org/10.1007/s10776-020-00502-7).

[7] N. Benaouda and A. Lahlouhi, "Ant-based Delay-bounded and Power-efficient Data Aggregation in Wireless Sensor Networks", *International Journal of Pervasive Computing and Communications*, vol. 15, no. 2, pp. 97–119, 2019 (https://doi.org/10.1108/IJPCC-04-2019-0037).

[8] X. Li *et al.*, "Localized Delay-bounded and Energy-efficient Data Aggregation in Wireless Sensor and Actor Networks", *Wireless Communications and Mobile Computing*, vol. 11, no. 12, pp. 1603–1617, 2011 (https://doi.org/10.1002/wcm.1222).

[9] A. Sobeih *et al.*, "J-sim: a Simulation and Emulation Environment for Wireless Sensor Networks", *IEEE Wireless Communications*, vol. 13, no. 4, pp. 104–119, 2006 (https://doi.org/10.1109/MWC.2006.1678171).

[10] A. Sarkar and T.S. Murugan, "Cluster Head Selection for Energy Efficient and Delay-less Routing in Wireless Sensor Network", *Wireless Networks*, vol. 25, no. 1, pp. 303–320, 2019 (https://doi.org/10.1007/s11276-017-1558-2).

[11] M. Selvi *et al.*, "A Rule Based Delay Constrained Energy Efficient Routing Technique for Wireless Sensor Networks", *Cluster Computing*, vol. 22, no. 5, pp. 10839–10848, 2019 (https://doi.org/10.1007/s10586-017-1191-y).

[12] J. Agarkhed, P.Y. Dattatraya, and S. Patil, "Multi-QoS Constraint Multipath Routing in Cluster-based Wireless Sensor Network", *International Journal of Information Technology*, vol. 13, no. 3, pp. 865–876, 2021 (https://doi.org/10.1007/s41870-020-00461-5).

[13] E.D. Tita, W.-P. Nwadiugwu, J.M. Lee, and D.-S. Kim, "Real-time Optimizations in Energy Profiles and End-to-end Delay in WSN Using Two-hop Information", *Computer Communications*, vol. 172, pp. 169–182, 2021 (https://doi.org/10.1016/j.comcom.2021.02.007).

[14] X. Liu *et al.*, "Intelligent Data Fusion Algorithm Based on Hybrid Delay-aware Adaptive Clustering in Wireless Sensor Networks", *Future Generation Computer Systems*, vol. 104, pp. 1–14, 2020 (https://doi.org/10.1016/j.future.2019.10.001).

[15] S. Yahiaoui *et al.*, "An Energy Efficient and QoS Aware Routing Protocol for Wireless Sensor and Actuator Networks", *AEU – International Journal of Electronics and Communications*, vol. 83, pp. 193–203, 2018 (https://doi.org/10.1016/j.aeue.2017.08.045).

[16] G. Shah, M. Bozyigit, and F. Hussain, "Cluster-based Coordination and Routing Framework for Wireless Sensor and Actor Networks",

Wireless Communications and Mobile Computing, vol. 11, pp. 1140–1154, 2011 (https://doi.org/10.1002/wcm.885).

[17] T. Melodia, D. Pompili, V.C. Gungor, and I.F. Akyildiz, "Communication and Coordination in Wireless Sensor and Actor Networks", *IEEE Transactions on Mobile Computing*, vol. 6, no. 10, pp. 1116–1129, 2007 (https://doi.org/10.1109/TMC.2007.1009).

[18] H. Bagci, I. Korpeoglu, and A. Yazıcı, "A Distributed Fault-tolerant Topology Control Algorithm for Heterogeneous Wireless Sensor Networks", *IEEE Transactions on Parallel and Distributed Systems*, vol. 26, no. 4, pp. 914–923, 2015 (https://doi.org/10.1109/TPDS.2014.2316142).

[19] A. Mehto, S. Tapaswi, and K.K. Pattanaik, "Virtual Grid-based Rendezvous Point and Sojourn Location Selection for Energy and Delay Efficient Data Acquisition in Wireless Sensor Networks with Mobile Sink", *Wireless Networks*, vol. 26, pp. 3763–3779, 2020 (https://doi.org/10.1007/s11276-020-02293-4).

[20] K. Li and C.-C. Shen, "Balancing Transmission Power and Hop Count in ad hoc Unicast Routing with Swarm Intelligence", *2008 IEEE Swarm Intelligence Symposium, SIS 2008*, St. Louis, USA, 2008, (https://doi.org/10.1109/SIS.2008.4668323).

[21] N. Li, J.C. Hou, and L. Sha, "Design and Analysis of an MST-based Topology Control Algorithm", *IEEE Transactions on Wireless Communications*, vol. 4, no. 3, pp. 1195–1206, 2005 (https://doi.org/10.1109/TWC.2005.846971).

Nadjib Benaouda, M.Sc.
Computer Science Department
https://orcid.org/0000-0002-4361-9597
E-mail: nadjib.benaouda@univ-bba.dz
University of Mohamed El Bachir El Ibrahimi, Bordj Bou Arreridj, Algeria
https://www.univ-bba.dz

Optimizing Cognitive Radio Networks with Deep Learning-Based Semantic Spectrum Sensing

Mahesh Kumar N and Arthi R

SRM IST Ramapuram, Chennai, India

https://doi.org/10.26636/jtit.2024.4.1797

Abstract — Spectrum aggregation in 4G and 5G networks is a technique used to combine multiple frequency bands to boost communication performance. The cognitive radio feature improves the ability to combine spectrum in LTE and 5G environments by enabling dynamic spectrum sensing. Spectrum sensing is a major problem in spectrum aggregation due to the presence of various types of interference, such as noise. Phase noise is an issue due to its 1 MHz frequency offset experienced within 5G's 28 GHz operating band, with the distorted signal generating more spectrum sensing-related errors. To solve this problem, the proposed work suggests an optimized deep learning-based semantic spectrum sensing model using three sets of optimizers (ResNet-50, DeepLab V3 and sand cat) offering a high detection accuracy of 99.7% with the optimized training parameter of a high signal-to-noise ratio equaling 40 dB.

Keywords — cognitive radio, ResNet-50, sand cat optimizer, semantic spectrum sensing, wireless sensor network

1. Introduction

A wireless communication transceiver using the cognitive radio (CR) concept identifies and utilizes unused radio channels to make the best use of the available spectrum. This technique has been used to minimize interference and improve the quality of service. In the United States, the Federal Communications Commission (FCC) and the National Telecommunications and Information Administration (NITA) allocate the limited wireless RF spectrum to licensed users – an approach that results in overcrowding or underutilization of the spectra. Consequently, spectrum inefficiencies are experienced, leading to reduced data transmission rates and lower service quality levels.

CR networks are classified into two types: primary and secondary. A primary network consists of licensed users and radio transmitters, while a secondary network shares the unused spectrum with the primary network. Identification of channel occupancy in CR increases spectrum efficiency and minimizes interference. It is achieved by spectrum sensing – a technique allowing to determine whether specific frequency bands are used or not.

Cognitive radio networks detect the presence of primary users within specific frequency bands, allowing secondary users to access the spectrum without creating any interference [1]. In cognitive radio spectrum sensing, holes are defined as periods in which primary-user signals are not detected, thus allowing secondary users to access a given frequency band.

Two spectrum access modes may be distinguished: overlay and underlay. When principal users are not transmitting, secondary users utilize the spectrum in the overlay mode. Therefore, efficient spectrum access is required in the overlay mode to avoid interference from primary users [2]. In the underlay mode, a secondary user transmits a signal simultaneously with a primary user, and the secondary user must adjust its transmit power accordingly, taking account the interference caused by the primary user [3].

Cognitive radio (CR) is a fundamental element of 4G/5G communication systems. It enables multiple wireless and mobile networks to operate efficiently, improves their performance by utilizing the unlicensed spectrum, provides improved coverage in rural areas by using overlay and underlay spectrum access techniques, and facilitates the use of higher frequency bands, such as millimeter wave bands, in 5G wireless communication [4].

Despite the increasing adoption of 5G seen in many countries, coexistence of 4G and 5G networks is still quite common due to the time required to build new telecommunications infrastructure and the widespread availability of 4G networks. 5G networks are well suited for high data rates and low latency applications. However, many rural areas still lack 5G coverage, necessitating the continued use of both networks during the transition period.

Spectrum aggregation (also known as carrier agreement) allows several frequency bands to be combined into a single channel to boost data rate, network capacity and, hence, network performance. Spectrum aggregation enables network operators to allocate the capacity of radio cells operating at different frequencies, thus enhancing the end-user experience.

Spectrum aggregation, introduced in 3G networks, was limited to a 5 MHz bandwidth per carrier. In 4G LTE, each carrier is aggregated with a 20 MHz bandwidth. However, in 5G networks, carrier aggregation is supported at low- and mid-frequencies (below 7 GHz), as well as at high-band millimeter frequencies (above 24 GHz). In 5G, each carrier operates with a bandwidth of 100 MHz, being five times wider than in 3G [5].

Dynamic spectrum sharing between 4G LTE and 5G radio signals is the main issue with spectrum aggregation. In spectrum sharing, 4G users cannot transfer carriers from LTE to 4G due to spectrum aggregation [6].

Phase noise is another problem that reduces performance. During the spectrum aggregation process, noise reduces sensitivity, thus increasing the noise floor, and lowers the quality of the aggregated spectrum. furthermore, it is challenging to discriminate between distinct frequency channels in a local receiver due to phase noise. Phase noise can also lead to signal degradation and distortion, making it difficult to have a steady and reliable connection during spectrum aggregation. Therefore, reducing phase noise is essential to increase the efficacy and efficiency of communication systems.

The wireless communication industry is currently adopting technology that uses mmWave frequencies, thus making higher data speeds possible. To lower the bit error rate, faster data rates require a higher signal-to-noise ratio. Therefore, the proposed work implements an optimized deep learning semantic spectrum localization approach to estimate the phase noise in order to increase the quality of the aggregated spectrum. By measuring and adjusting phase noise, the proposed deep learning semantic spectrum localization technique facilitates data transmission and reception in 4G LTE and 5G networks.

The rest of the article is structured as follows.
Section 2 offers a review of spectrum aggregation, noise interference and spectrum sensing phenomena associated with CR. Section 3 describes the proposed methodology. The results are presented and discussed in Section 4. Conclusions are given in Section 5.

2. Literature Review

Over the years, researchers have proposed many spectrum aggregation techniques, including the multi-agent long- and short-term (LSTM)-based deep Q-learning architecture (DQN) as a solution to the distributed dynamic spectrum access issue experienced in temporal correlations involving primary and secondary users [7]. For the effective detection of spectrum gaps, the author [8] employed a spectrum detection algorithm based on spiking neural networks (SNN) trained with the modified whale optimization algorithm (MWOA).

Another spectrum aggregation technique was employed in [9] to detect unlicensed users to facilitate the efficient transmission of smart agriculture technologies. Using spectrum aggregation technology, the maximum entropy actor-critic (MEAC) algorithm was presented in [10], allowing secondary users to share the spectrum. It was discovered, with the use of the spectrum aggregation technology, that the MEAC algorithm allowed secondary users to effectively share the spectrum resources. The SNN-based spectrum sensing method trained on MWOA has shown efficacy in identifying spectrum gaps, thus enhancing spectrum accessibility for primary and secondary users.

In the face of noise uncertainty, the authors of [11] detected the unoccupied primary bands using the estimator-correlator-based optimum detectors and the generalized likelihood ratio test (GLRT) paradigm.

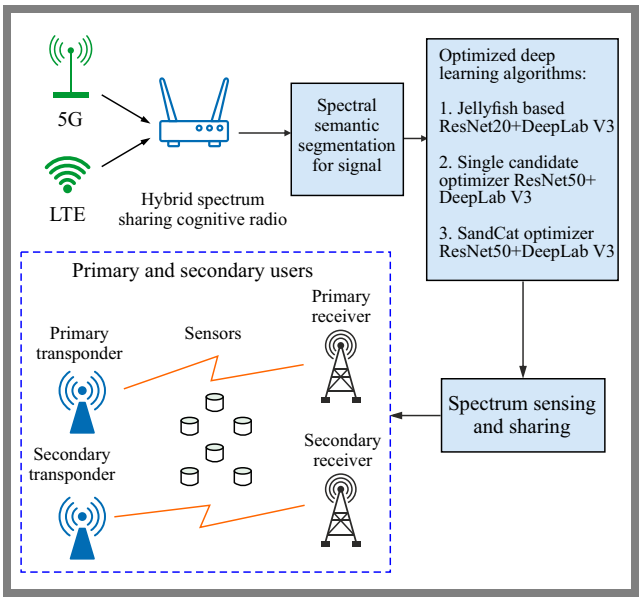

Fig. 1. Proposed architecture for spectrum aggregation in optimized deep learning-based semantic segmentation network.

To identify the principal user, paper [12] relied on a primary key cryptosystem. The secondary user provided the error correction key which was used to eliminate noise while assigning resources to the secondary user. When sensing the spectrum, Kendall's tau detector finds the main signal in the additive non-Gaussian noise that is described by the contaminated Gaussian model (CGM).

In [13], the eigenvalue-based random matrix theory (RMT) is used for multidimensional cognitive radio receivers to find correlation noise caused by oversampling and filtration errors. The bivariate isotropic symmetric α-stable (BISαS) model presented in [14] was used by the author to identify non-Gaussian impulsive noise in spectrum detection. By employing a radial basis function network, article [15] resolved the issue of an increased rate of misclassification in the detection of spectrum, based on time series data.

In [16], a highly efficient spectral network is presented, employing the frequency division multiplexing technique described in the physical layer, while in [17], three unique deep learning models, including convolutional neural networks, recurrent neural networks, and neural networks are employed to determine the spectrum of the secondary user (SU). These models were employed to detect the spectrum in a 5G network. A large data set was used to train these models to precisely determine spectrum occupancy. The results demonstrated that deep learning models outperform conventional spectrum sensing techniques, offering a much higher accuracy rate and generating fewer errors.

3. Proposed Methodology

The proposed architecture of spectrum sensing in spectrum aggregation using the semantic segmentation technique is

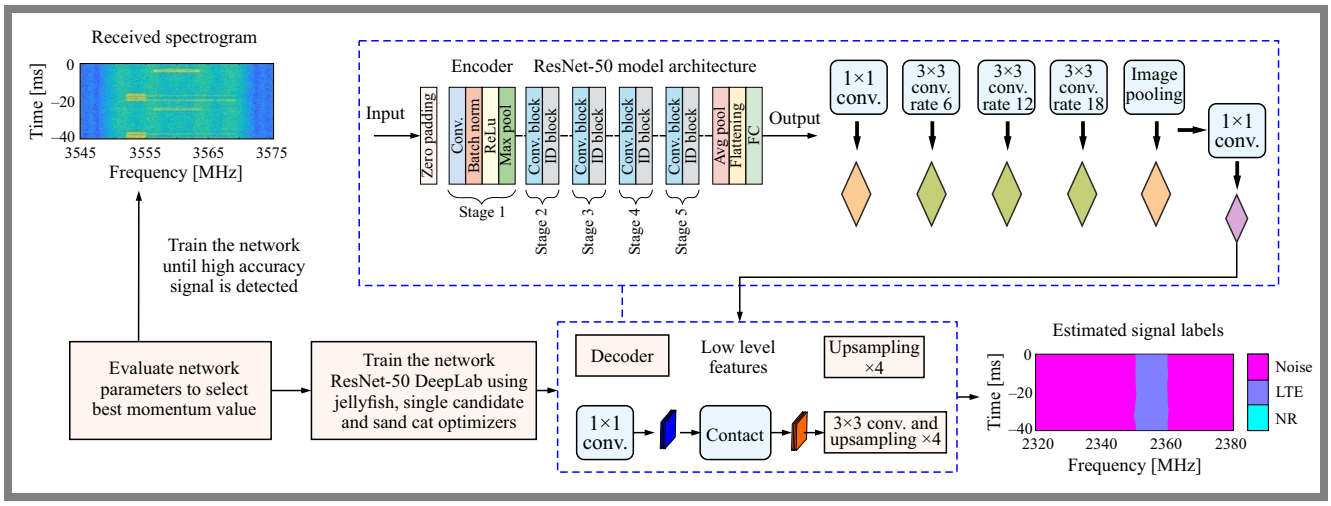

Fig. 2. Block diagram of the proposed ResNet-50 and DeepLab V3 semantic segmentation spectrum network.

shown in Fig. 1. Spectrum sensing is performed in spectrum sharing environments using an optimized deep learning model of a cognitive radio network. 5G and 4G LTE signals are generated with a sampling rate of 61.44 MHz, with an image size of 256 by 256, with each frame lasting 10 ms.

The frequency of each signal is analyzed and segmented into different classes, such as LTE, 5G, and phase noise signals based on spectral characteristics, using an optimized deep learning model. After semantic segmentation, the spectrum signals are allocated to primary and secondary users based on their requirements for the shared spectrum signal. This allocation process ensures efficient utilization of the spectrum resources, allowing primary users to have priority access, with secondary users being allowed to access the remaining part of the spectrum. Additionally, by detecting and decreasing phase noise, the overall quality of the shared spectrum signal is improved for both primary and secondary users.

3.1. Semantic Spectrum Segmentation

Semantic spectrum segmentation is a technique that is used to identify the spectrum based on the high-level features of the signal. Semantic spectrum segmentation in CR (SSS-CR) employs dynamic spectrum access for underutilized spectrum bands and enables context-aware spectrum usage. SSS in CR improves spectrum sharing between primary and secondary users while minimizing interference and optimizing spectrum allocation.

The proposed work employs LTE and 5G NR interfaces that detect the presence of phase noise using the deep learning approach. The presence of phase noise is classified by the semantic segmentation method and optimizes spectrum sensing.

3.2. ResNet-50 Based Deep Semantic Segmentation Network

Semantic segmentation (SS) is used to classify pixels that belong to a particular class. SS is used to combine pixels of the same class and supports multiclass segmentation. The proposed work uses ResNet-50 as a backbone network with DeepLab V3 to segment signals in cognitive radio, such as 5G, LTE and phase noise signals. ResNet-50 comprises 4 stages of layers, such as the initial stage, containing convolution, and the maximum pooling layer, followed by 3 sets of residual blocks. Thanks to the convolutional module, the skip connection feature and accurate pixel detection, ResNet-50 is capable of obtaining information about pixels that are inside a spectrogram signal. Therefore, the model is suitable for extracting such features as frequency content, frequency bands, spectral density, time frequency location, and spectral peaks from the spectrogram.

DeepLab V3 uses an arbitrary convolution network and a spatial feature pyramid to acquire multiscale features without adding more parameters to the proposed architecture. The DeepLab V3 architecture uses an encoder and decoder. The encoder encodes finer details of the spectrogram, while the decoder is used to obtain the desired resolution. In DeepLab V3, dilation rates are used to capture multiscale features which regulate the space between kernel weights and the receptive field.

The training parameters for stochastic gradient descent with a momentum algorithm is optimized using jellyfish, single candidate, and sand cat optimizer algorithms to increase the performance of the proposed ResNet-50 and DeepLab V3 network. Optimization strategies improving speed and accuracy are chosen as well.

Figure 2 shows the proposed architecture of the semantic segmentation network.

3.3. Jellyfish Optimization

Jellyfish is a bio-inspired optimization algorithm implemented based on the food search habits of jellyfish. The algorithm finds the best location where the most food is available. While the lookout for food, jellyfish are carried by the ocean current or move in a swarm. We used the jellyfish optimization algorithm to optimize the momentum training parameter

Algorithm 1 Jellyfish-based semantic spectrum sensing

Initialize parameters and variables, number of population, number of dimensions, lower and upper bound for momentum, and maximum iteration
Initialize population using logistic map initialization technique and set lower bound and upper bound to vectors
Evaluate the initial population using the cost function
Initialize the best solution `BestSol` and its corresponding cost `BestCost`
for each iteration until the maximum iteration is reached **do**
    Calculate the mean of the current population `Meanvl`
    Sort the population based on costs
    for each solution in the population **do**
        Calculate the time control factor A_r
        if $A_r \geqslant 0.5$ **then**
            Update the solution by following the ocean current method and update the new position of jellyfish
        else
            Determine the type of motion (active or passive)
        end if
    end for
end for
Output the optimal momentum value u and its corresponding cost f_{val}

based on the condition of a high mean accuracy value in deep learning semantic spectrum segmentation.

The momentum training parameter is essential to enhance the convergence speed and stability of deep learning models. Using the jellyfish optimization algorithm, we can effectively search for the optimal value of this parameter, leading to enhanced performance in semantic spectrum segmentation tasks. Algorithm 1 illustrates the pseudocode of jellyfish optimization.

3.4. Single Candidate Optimization

The single candidate optimizer (SCO) supports the entire optimization process to find the best solution. The evaluation process depends on the maximum number of function evaluations or iterations involved. The process is divided into two phases, and candidates update their positions in each phase. The Algorithm 2 evaluates the cost function in semantic spectrum sensing to optimize the momentum training parameter and updates the position of a candidate based on the current mean accuracy value. Additionally, by dividing the optimization into two phases, the algorithm can adapt and refine its search strategy based on the results obtained in each phase.

3.5. Sand Cat Optimization

The sand cat swarm optimization method (SCSO) was implemented based on the behavior of sand cats. The SCSO algorithm simulates sand cats' hunting techniques, allowing them to successfully locate and capture prey. Using this

Algorithm 2 SCO-based semantic spectrum sensing

Initialize parameters: lower bound for momentum, upper bound for momentum, number of dimensions, cost function for optimization, number of iterations
Initialize a random candidate solution within the specified limits
Evaluate the best fitness of the initial candidate solution `BF` using the cost function f_{obj}
Set the initial values for counters and parameters
for each iteration t from 1 to T **do**
    Calculate the inertia weight
    Update counters and check if in the second phase
    Generate a new candidate solution and determine the motion strategy based on the current phase
    if $t < \alpha$ **then**
        Determine the motion strategy for the first phase
    else
        Determine the motion strategy for the second phase
    end if
    Enforce boundary constraints on the new candidate solution
    Evaluate the fitness $F(t)$ of the newly generated candidate solution
    if $F(t)$ is better than the current best fitness **then**
        Update the best solution and its fitness
    end if
    Store the `BF` for the current iteration t in $\texttt{BF}(T)$
end for
Output the optimal momentum value $gbest$ and its corresponding cost $\texttt{BF}(T)$

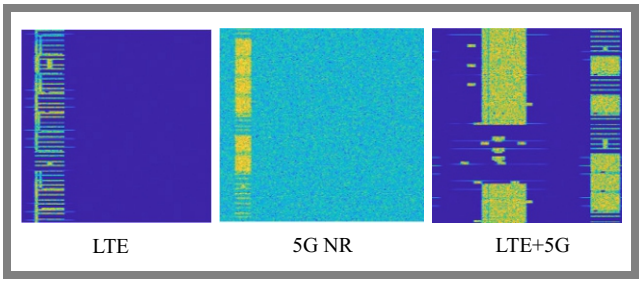

Fig. 3. LTE and 5G NR generated signal samples.

behavior during the optimization process, the SCSO algorithm performs better at detecting and tracking low-frequency noises that could be food sources. As a result, modifying the momentum training parameter with the SCSO technique is an effective method to improve overall performance. Algorithm 3 shows the pseudocode of SCSO.

4. Results and Discussions

The data set for the simulation is generated for 5G and LTE signals with added phase noise of the specified bandwidth. More detailed data from case A relate to urban areas, and less detailed data from case B to rural areas. Sub-carrier spacing between 15 and 30 kHz and synchronization of a single block

Algorithm 3 SCSO pseudocode

Initialize parameters: number of search agents `SearchAgents-no`, maximum iterations `max-iter`, lower bound and upper bound for each dimension, number of dimensions, and cost function for optimization
Initialize the best score `BS` to positive infinity and the best fitness `BF` to an array of zeros with length equal to dim
Initialize the positions of search agents (`positions`) using the initialization function
Initialize the convergence curve array to zeros with length equal to `max-iter`
if number of values = 1 **then**
    assign initial condition
else
    set the iteration counter t to 0
end if
while $t <$ `max-iter` **do**
    for each search agent i from 1 to `SearchAgents-no` **do**
        Evaluate the fitness of the current position using the cost function f_{obj}
        if the current fitness is better than `BS` **then**
            update `BS` and `BF`
        end if
    end for
    Update the maximum sensitivity range S and the guide range r_g
    for each search agent i from 1 to `SearchAgents-no` **do**
        Generate a random value r between 0 and r_g
        Generate a random value R between $-r_g$ and r_g
        for each dimension j from 1 to dim **do**
            Calculate the transition phase angle θ using the `RouletteWheelSelection` function
            if R satisfies the motion strategy condition **then**
                Select a random search agent `cp` and update the position of dimension j
            end if
        end for
        Enforce boundary constraints on the updated position of dimension j
    end for

    Increment the iteration counter t
    Update the convergence curve array with the current `BS`
end while
Output the best score `BS`, the best fitness `BF`, and the convergence curve array (`convergence-curve`)

period of 40 ms are used as well. LTE signals are created using R.2, R.6, R.8 and R.9 reference channels for downlink transmissions in cities or in indoor environments, with low or high interference levels and a frequency division duplex (FDD). Table 1 shows the parameters used in the simulation, whereas Fig. 3 shows the sample signals.

Tab. 1. Parameters used for the generation of the signal data set.

Parameter	Value	Units
5G NR		
Bandwidth	10, 15, 20, 25, 30, 40, 50	MHz
Subcarrier spacing	15, 30	kHz
SSB block pattern	case A, case B	
SSB period	20	ms
LTE		
Reference channel	R.2, R.6, R.8, R.9	
Bandwidth	5, 10, 15, 20	MHz
Duplex mode	FDD	
Phase noise		
SNR	0 40	dB
Carrier frequency	2.5	kHz

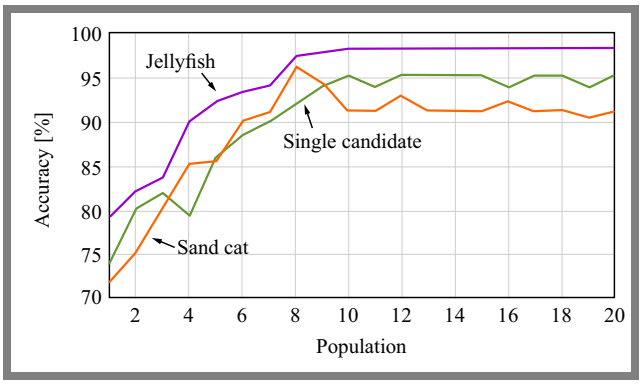

Fig. 4. Accuracy of three considered optimizers.

4.1. Training Parameters Based on Optimized Algorithms

Figure 4 shows the cost values of various spectrum sensing optimization strategies, including jellyfish, single candidate solution, and sand cat. According to the graph, the sand cat algorithm outperforms other optimization strategies in terms of accuracy, and with momentum of 0.9 because the algorithm locates and forecasts accuracy even in low noise environments. As a result, the algorithm classifies the semantic signal with an excellent accuracy level of 98.3%.

Figure 5 shows the degree of precision of the three optimizers under consideration, with respect to 5G, LTE, and phase noise. One may conclude from the figure that the dominance of phase noise is higher than 5G and LTE.

Figure 6 illustrates the sensitivity values of optimizers for 5G, LTE, and phase noise cases, while Fig. 7 provides specific values. One may observe from Fig. 6 that sensitivity to phase noise is lower than in 5G and LTE, and Fig. 7 shows that the sand cat optimizer exhibits faster convergence and greater generalization capabilities, making it an excellent alternative for semantic spectrum deep learning classification problems.

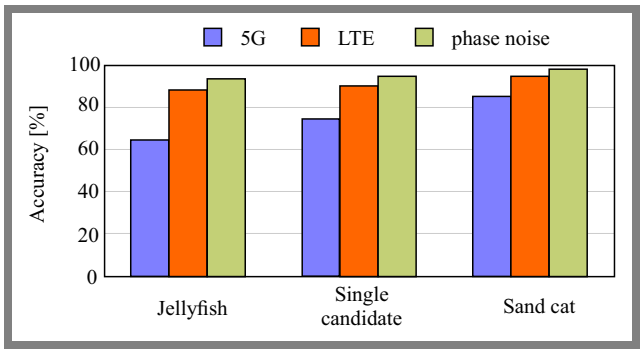

Fig. 5. Accuracy for various classifier models.

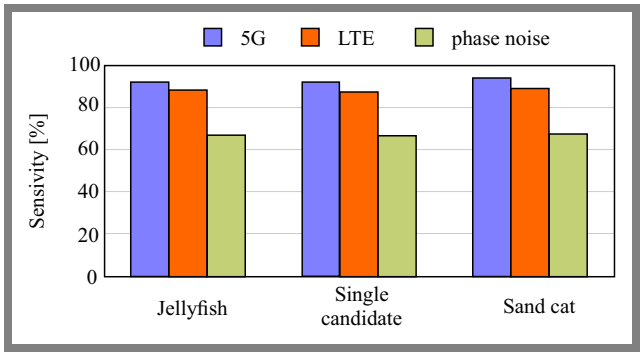

Fig. 6. Sensitivity for three considered classifier models.

These data also demonstrate that the sand cat optimizer outperforms other methods across a wide range of assessment measures.

4.2. Performance Analysis Using ResNet-50 and DeepLab V3

To assess the decrease in the presence of phase noise, all considered optimization classifiers are trained with ResNet-50 and DeepLab V3 (Fig. 8). Figure 9a shows the performance of the optimized ResNet-50 semantic spectrum sensing approach, in terms of global accuracy. It is evident that the captured spectrum sensing for the proposed sand cat optimizer is high when compared with other optimizers. Figure 9b shows the mean captured spectrum sensing accuracy value, with the sand cat optimizer producing a better result compared with other optimizers. Figure 9c proves that the mean spectrum sensing IOU of the sand cat optimizer is high versus the remaining approaches. Fig. 9d shows that the weighted spectrum sensing IOU of the sand cat optimizer is the highest. Figure 9e shows the ResNet-50 BF score that has the highest captured spectrum detection value for the sand cat optimizer, and Fig. 9f presents the F1 score that has a greater captured spectrum detection value for the sand cat optimizer, compared to the ResNet-50 optimizer.

In general, the performance analysis proves that the captured spectrum sensing becomes higher when phase noise is decreased, which enhances the effective utilization of semantic spectrum sensing – see Fig. 10 and Tab. 2.

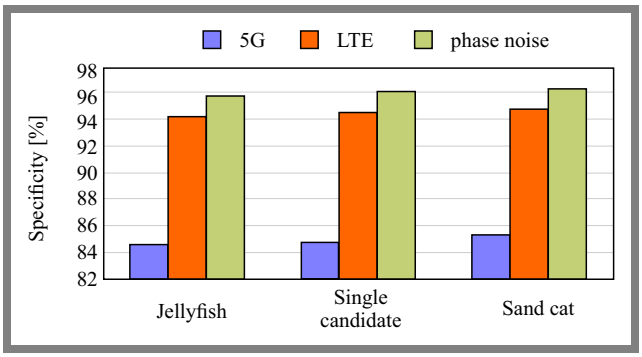

Fig. 7. Specificity for three classifier models.

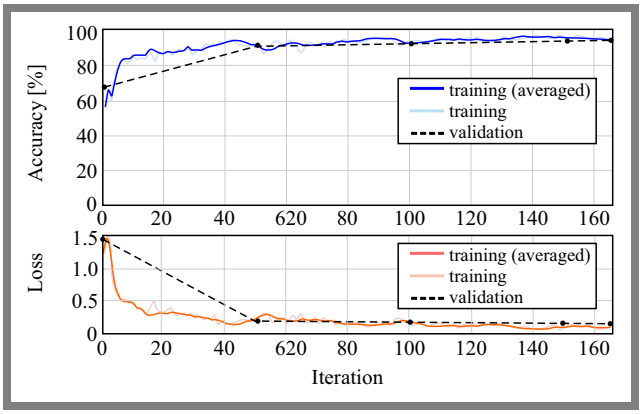

Fig. 8. Training and validation of optimized ResNet-50 and DeepLab V3.

Tab. 2. Comparison of spectrum sensing methods.

Spectrum sensing	Accuracy
ResNet 152 [18]	90.55%
SenseNet [19]	91.25%
DetectNet+SVM [20]	89%
1DCNN+BiLSTM+SA [21]	92%
VGG [22]	95%
Proposed ResNet-50 + DeepLab V3	99.7%

5. Conclusion

The proposed phase noise detection technique minimizes interference, improves signal quality, enhances network capacity and augments spectral efficiency. Unfortunately, the proposed model requires significant amounts of computing power, is sensitive to parameter tuning, and the spectrum characteristics may be subject to change depending on the real-time environment. However, the model provides good results in terms of phase detection and labelling. Therefore, additional research and development work is required to optimize the model for practical deployment in dynamic and unpredictable scenarios. Additionally, the efficacy in changing signal environments will require constant observation and parameter modification.

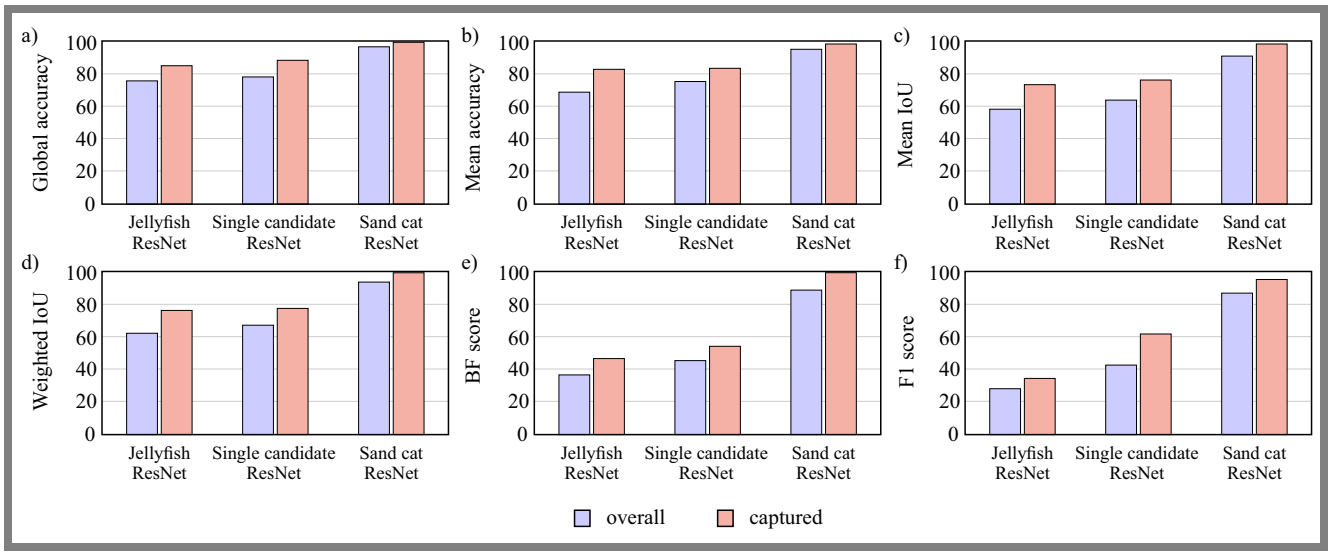

Fig. 9. Performance analysis of optimized ResNet-50 semantic spectrum sensing approach: a) global accuracy, b) mean accuracy, c) mean IoU, d) weighted IoU, e) BF score, and f) F1 score.

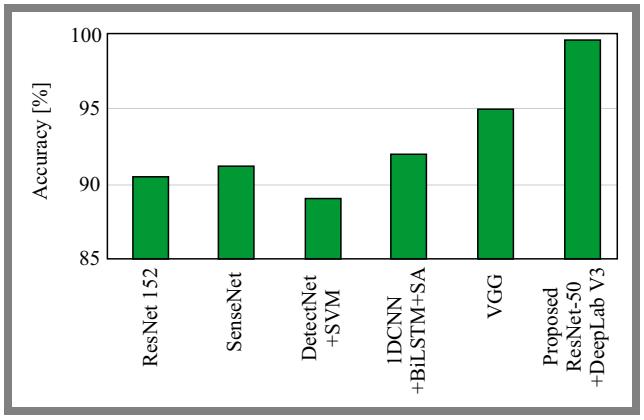

Fig. 10. Comparison of spectrum sensing methods.

References

[1] P.H. Talajiya, A. Gangurde, U. Ragavendran, and H. Murali, "Cognitive Radio Networks and Spectrum Sensing: A Review", *International Journal of Online and Biomedical Engineering*, vol. 16, no. 13, pp. 4–18, 2020 (https://doi.org/10.3991/ijoe.v16i13.18549).

[2] J. Xie, J. Fang, C. Liu, and L. Yang, "Unsupervised Deep Spectrum Sensing: A Variational Auto-encoder Based Approach", *IEEE Transactions on Vehicular Technology*, vol. 69, no. 5, pp. 5307–5319, 2020 (https://doi.org/10.1109/TVT.2020.2982203).

[3] R. Fan, Q. Gu, X. An, and Y. Zhang, "Robust Power Allocation for Cognitive Radio System in Underlay Mode", in: *IoT as a Service*, pp. 426–430, 2018 (https://doi.org/10.1007/978-3-030-14657-3_44).

[4] Z. Zhang, "Research on the Performance of Overlay/Underlay Cognitive Radio Waveforms in Different Channels", *9th Int. Symposium on Next Generation Electronics (ISNE)*, Changsha, China, 2021 (https://doi.org/10.1109/ISNE48910.2021.9493626).

[5] X. Lu *et al.*, "Integrated Use of Licensed- and Unlicensed-Band mmWave Radio Technology in 5G and Beyond", *IEEE Access*, vol. 7, pp. 24376–24391, 2019 (https://doi.org/10.1109/ACCESS.2019.2900195).

[6] G. Eappen, T. Shankar, and R. Nilavalan, "Cooperative Relay Spectrum Sensing for Cognitive Radio Network: Mutated MWOA-SNN Approach", *Applied Soft Computing*, vol. 114, art. no. 108072, 2022 (https://doi.org/10.1016/j.asoc.2021.108072).

[7] Z. Gu *et al.*, "Efficient Distributed Broadcasting Algorithms for Cognitive Radio Networks-enabled Smart Agriculture", *Computers and Electrical Engineering*, vol.108, art. no. 108690, 2023 (https://doi.org/10.1016/j.compeleceng.2023.108690).

[8] T. Sheng *et al.*, "Dynamic Spectrum Sharing and Aggregation Scheme Based on Deep Reinforcement Learning", *International Wireless Communications and Mobile Computing*, Dubrovnik, Croatia, 2022 (https://doi.org/10.1109/IWCMC55113.2022.9825001).

[9] R. Ahmed, Y. Chen, and B. Hassan, "Optimal Spectrum Sensing in MIMO-based Cognitive Radio Wireless Sensor Network (CR-WSN) Using GLRT with Noise Uncertainty at Low SNR", *International Journal of Electronics and Communications*, vol. 136, art. no. 153741, 2021 (https://doi.org/10.1016/j.aeue.2021.153741).

[10] A. Haldorai and A. Ramu, "Security and Channel Noise Management in Cognitive Radio Networks", *Computers & Electrical Engineering*, vol. 87, art. no. 106784, 2020 (https://doi.org/10.1016/j.compeleceng.2020.106784).

[11] W. Xu, H. Lai, J. Dai, and Y. Zhou, "Spectrum Sensing for Cognitive Radio Based on Kendall's Tau in the Presence of Non-Gaussian Impulsive Noise", *Digital Signal Processing*, vol. 123, art. no. 103443, 2022 (https://doi.org/10.1016/j.dsp.2022.103443).

[12] C. Charan and R. Pandey, "Eigenvalue-based Spectrum Sensing under Correlated Noise for Multi-dimensional Cognitive Radio Receiver", *Wireless Personal Communication*, vol. 133, pp. 227–244, 2023 (https://doi.org/10.1007/s11277-023-10765-x).

[13] M. Girmay *et al.*, "Enabling Uncoordinated Dynamic Spectrum Sharing between LTE and NR Networks", *IEEE Transactions on Wireless Communications*, vol. 23, no. 6, pp. 5953–5968, 2024 (https://doi.org/10.1109/TWC.2023.3329385).

[14] S. Kim, "4G/5G Coexistent Dynamic Spectrum Sharing Scheme Based on Dual Bargaining Game Approach", *Computer Communications*, vol. 181, pp. 215–223, 2022 (https://doi.org/10.1016/j.comcom.2021.10.025).

[15] F. Ali and H. Yigang, "Spectrum Sensing-focused Cognitive Radio Network for 5G Revolution", *Frontiers in Environmental Science*, vol. 11, 2023 (https://doi.org/10.3389/fenvs.2023.1113832).

[16] D.S. Sofia and A.S. Edward, "Overlay Dynamic Spectrum Sharing in Cognitive Radio for 4G and 5G Using FBMC", *Materials Today: Proceedings*, vol. 80, pp. 2781–2785, 2023 (https://doi.org/10.1016/j.matpr.2021.07.038).

[17] M. Wasilewska, H. Bogucka, and A. Kliks, "Spectrum Sensing and Prediction for 5G Radio", in: *Big Data Technologies and Application*,

vol. 371, pp. 176–194, 2021 (https://doi.org/10.1007/978-3-030-72802-1_13).

[18] S. Zheng *et al.*, "Spectrum Sensing Based on Deep Learning Classification for Cognitive Radios", *China Communications*, vol. 17, no. 2, pp. 138–148, 2020 (https://doi.org/10.23919/JCC.2020.02.012).

[19] Y. Geng, J. Huang, J. Yang, and S. Zhang, "Spectrum Sensing for Cognitive Radio Based on Feature Extraction and Deep Learning", *Journal of Physics: Conference Series*, vol. 2261, 2022 (https://doi.org/10.1088/1742-6596/2261/1/012016).

[20] Z. Sabrina *et al.*, "Spectrum Sensing Based on an Improved Deep Learning Classification for Cognitive Radio", *International Conference on Electrical, Computer, Communications and Mechatronics Engineering*, Male, Maldives, 2022 (https://doi.org/10.1109/ICECCME55909.2022.9987999).

[21] H. Xing *et al.*, "Spectrum Sensing in Cognitive Radio: A Deep Learning Based Model", *Transactions on Emerging Telecommunications Technologies*, vol. 33, no. 1, 2022 (https://doi.org/10.1002/ett.4388).

[22] Y. Mishra and V.S. Chaudhary, "Spectrum Sensing in Cognitive Radio for Internet of Things using Deep Learning Models", *SAMRIDDHI: A Journal of Physical Sciences, Engineering and Technology*, vol. 15, no. 1, pp. 27–33, 2023 (https://doi.org/10.18090/samriddhi.v15i01.04).

Mahesh Kumar N
Department of ECE, Faculty of Engineering & Technology
https://orcid.org/0000-0001-7224-4512
E-mail: maheshkn@srmist.edu.in
SRM IST Ramapuram, Chennai, India
https://srmrmp.edu.in

Arthi R, Ph.D.
Department of ECE, Faculty of Engineering & Technology
https://orcid.org/0000-0001-9638-1634
E-mail: arthir2@srmist.edu.in
SRM IST Ramapuram, Chennai, India
https://srmrmp.edu.in

Efficiency and Fairness Optimization in Energy Management

Grzegorz Zalewski[1,2], Janusz Granat[1,2], and Marek Makowski[3,4]

[1]*Warsaw University of Technology, Warsaw, Poland,*
[2]*National Institute of Telecommunications, Warsaw, Poland,*
[3]*Systems Research Institute, Polish Academy of Sciences, Warsaw, Poland,*
[4]*International Institute for Applied Systems Analysis, Laxenburg, Austria*

https://doi.org/10.26636/jtit.2024.4.1819

Abstract — The paper proposes a solution to the problem of distributing electricity originating from various sources. In the proposed model, each source has a different cost of acquisition and is characterized by varying energy efficiency factors. Additionally, in the case of renewable sources, the costs of storing energy are taken into consideration as well. This work presents a fair and cost-efficient approach to distributing the demands of energy providers. A model has been developed and verified for the purpose of corroborating the process.

Keywords — fair distribution of limited resources, linear programming, microgrids, renewable energy sources

1. Introduction

One of the most important areas of research currently undertaken in the field of energy is the smart use of renewable energy sources, such as wind, water, and the sun. The first factor that needs to be taken into account is to ensure the highest degree of environmental protection. The use of renewable energy sources is an alternative to fossil fuels which are the primary source of carbon dioxide and thus adversely impact the earth's climate. Furthermore, the extraction of fossil fuels causes environmental degradation, which is another factor to consider.

Recently, new concepts for the production and use of hydrogen have emerged that expand the range of alternatives to fossil fuels. Taking into account the constantly growing demand for energy, new energy generation plants (referred to as agents) will be established. A smaller plant may operate as a standalone unit or may work in cooperation with other suppliers, with the latter solution being more cost-effective in various scenarios.

In such a complicated landscape, the paper presents a method for organizing such cooperation between agents, so that everyone benefits from the relationships established between them. The financial profit generated in the cooperative approach is a finite resource that must be shared fairly too. The paper describes and presents a linear optimization approach allowing for fair distribution of resources to all agents participating in the process, and introduces a relevant energy management system (EMS).

2. Energy Management Approach

The development of a system capable of optimally pricing energy poses a great challenge. Among the different types of management approaches, demand side management (DSM), also known as demand response management, is often considered. In the DSM approach, control is exercise by ensuring an even distribution of energy demand throughout the day.

This involves the use of solutions that are capable of managing temporary energy loads in separate energy sub-networks, usually with their own energy-generating facilities, especially those relying on renewable sources. In modern distribution networks, costs of energy vary over time and are a function of market demand that changes depending on the time of day, day of the week and is different on non-working days as well.

Furthermore, in the case under consideration, rapid changes in demand resulting from incidents, such as natural disasters, may occur. Smart grid (SG) energy management systems are designed to provide energy to consumers in the cheapest possible way. This concept is based on dynamic electricity tariffs and household consumption estimates.

Consequently, energy suppliers are capable of reducing costs by better matching energy supply with current demand levels. Unclaimed energy must be stored, or its surplus must be eliminated in power plants that produce energy, which increases the cost of their operation.

The control mechanism that allows for the handling of energy surpluses, as well as minimizing energy shortages in selected periods, is the key feature that drives consumer demand. Controlling the price over a given period of time is one of the main factors that boost demand. This creates new challenges in decision-making processes that are related to energy distribution and reduces costs for users actively participating in generating energy (prosumers), as well as for those who are only receiving energy, but pay non-flat rates.

The problem of choosing an energy supplier by individual users in a given period of time is researched in [1]. The situation described in the article deals with finding an optimal schedule for assigning the k-th user to the energy supplier in the t-th hour, in a way that minimizes costs.

Nowadays, the development of a market of solutions enabling households to generate their own electricity allows to adopt

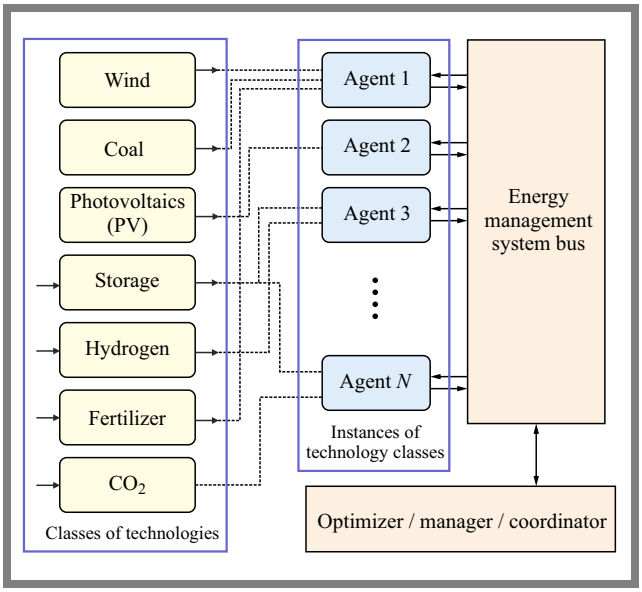

Fig. 1. Concept of the proposed energy management system.

a slightly different approach to decision making. In such a case, the goal is to develop an energy flow management system by defining a time-dependent list of prices at which energy is imported and exported by system agents [2].

Therefore, intermediate solutions have appeared on the market, with their task being to deliver energy to the end user and provide a load for suppliers, such as power plants.

Currently, a large number of power plants operate on fossil fuels and coal, with global demand for energy increasing continuously. Another significant trend is associated with the development of new, renewable energy sources. Many government policies focus on the promotion of privately-operated energy generation installations, usually based on solar energy. Scientific work is closely related to decision-making processes, with this approach often being referred to as micro networks or "power to x".

Various studies verifying the environmental impact of different energy generation technologies have been performed. It is undoubtedly worth considering the main trends on the energy market, placing an ever great emphasis on the negative environmental impact, such as CO_2 emissions, water consumption, acoustic noise level, environmental degradation caused by combustion products or the quantities of toxic residues (e.g. chemical compounds) generated in these processes [3].

The concept of smart grids is often considered to be an effective way of managing the relations between multiple energy suppliers and consumers.

The main goal is to minimize the total cost of energy while maintaining a balance between demand and supply. Prices may depend on the time of day, day of the week, month, and year. The cost is also related to the amount of energy supplied at a given moment in time. For example, when the demand for electricity is low at night, the price of energy is lower. Most energy suppliers have variable tariffs to encourage users to increase their energy consumption when the supply exceeds the demand.

The concept of smart grid addresses this problem by introducing dynamic unit energy costs. As part of this approach, various hardware solutions are proposed to support dynamic demand and supply control processes. To improve the efficiency of energy distribution systems, current technologies allow for the purchase of energy from consumers and producers. Therefore, the energy management system should take into account the equal treatment of each of these agents (consumers, prosumers, energy producers) in order to prevent their discrimination or uneven treatment.

An optimization process that is based solely on a simple criterion of minimizing cost may lead to such a situation. Therefore, the optimization model should be defined in such a manner as to protect against the undesirable case of "starving" some consumers or "ignoring" the supply of energy generated by selected producers.

3. Problem Analysis

A decision management system is based on the exchange of information between agents operating within the energy distribution chain and having the capacity to control the flow of resources. Agents present in the system may either distribute, consume or store energy, simultaneously generating other resources, such as waste.

The proposed approach is presented in Fig. 1, with the general concept intended to create a universal model capable of solving a wide array of problems. Each agent in the model may be described using a vector of incomes (demand) and outcomes (supply). In the example considered, relations between agents are taken into consideration, as an intelligent energy management system should rely on a process of optimizing the energy flow.

To make this possible, it is important to adopt one of two assumptions. The first of them is related to a scenario in which there is no exchange of information between agents, meaning none of the agents has any knowledge about prices, costs, or supply volumes. The second assumption is based on the cooperative approach, in which agents exchange information and jointly implement the process of optimizing the distribution of energy and determining the trade terms. To ensure such a functionality, an energy management system bus has been introduced in the proposed model to enable information to be exchanged between agents.

The main idea behind an energy management system (EMS) is to establish connections between each agent and use such an internal bus to exchange relevant data. Thanks to EMS, agents receive recommendations about the unit costs and expected quantities of energy (or other products) to be generated and resources to be provided to the agent or transferred further. EMS also helps better organize material flows using a cooperation-based approach.

An alternative to this is an individual approach, where each agent works as a standalone operation. The input and output flows influence the profits of the agents.

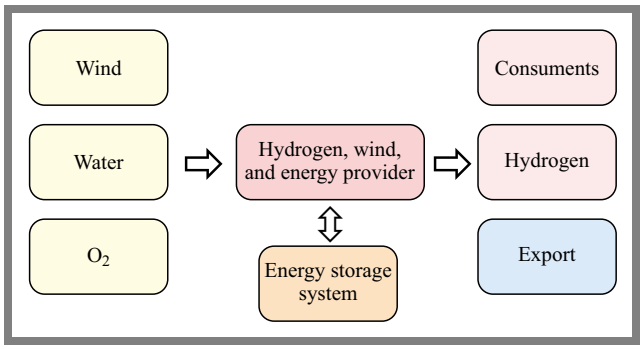

Fig. 2. Relationships between main energy resources, facilities and processes involved in energy transformation processes.

In this work, we focus on comparing these approaches and propose a model that allows for effective and fair distribution of incomes.

4. Flow of Information

Let us consider a scenario aiming to help several agents make decisions based on their mutual cooperation.

Here, the resource that is to be distributed by the system is the amount of energy transferred from sources (i.e., energy generators) to consumers with a specific demand level. We assume that given input and output flow vectors are constant and reflect situations where each operator acts separately, in a manner that is optimal considering their own needs.

In this approach, we treat the EMS bus as a control system that exchanges information between agents and, during the dynamic optimization process, as an output that provides recommendations (Fig. 2).

According to the game theory, a solution in which players cooperate will always be more profitable for the general public than competition. Therefore, additional savings and incomes are expected for each agent. These profits should be distributed so that partners feel treated unfairly. Such an approach is shown in Fig. 3.

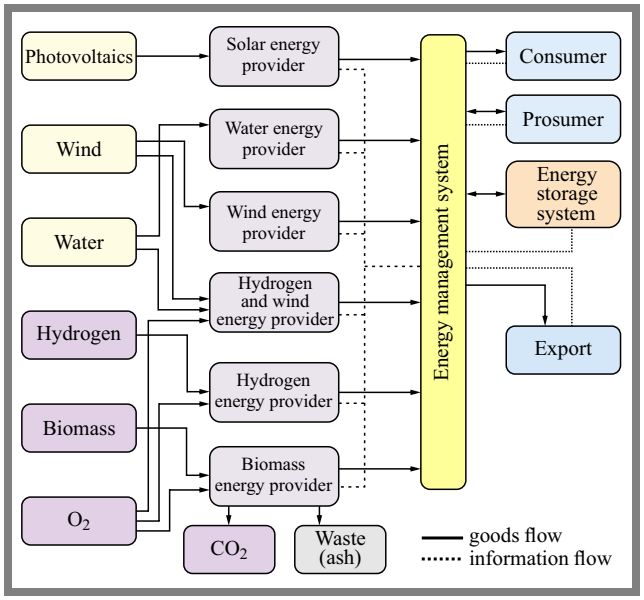

Fig. 3. Processes, information flow, and resource exchange in EMS.

Here, we are dealing with networks where agents often play the role of prosumers and, hence, the relationship between agents within the network is bidirectional.

This leads to the creation of areas where energy exchange between agents, supervised by EMS, occurs and where energy is temporarily stored. The proposed solution is similar to the one presented in [4], where an approach was introduced with a system of cooperating agents. The principle of operation comes down to the fact that when one of them reports a need for increased power consumption, it passes such a request to the system, and each of the remaining participants report their offers. In this way, a decision is made that minimizes energy costs.

5. Case Study

5.1. Individual Agent Approach

The approach of an individual agent does not rely on mutual information exchange and no energy management system bus is present within the solution. The energy prices are obtained directly from the market and each agent covers all decision-making processes (Fig. 4). An agent buys a unit of energy at price c and sells it at price p, where $p > c$ and it is assumed that all material flows have optimal values that satisfy the agent's efficiency requirements. The input and output flow vectors are considered to be optimal and stable values. This means that the revenues, costs, and profits are calculated for each agent.

In such a scheme, the income constraint of i-th agent may be formulated as:

$$I_i = \sum_{n \in i, suppliers} x_{n,i}\, p_n, \quad \forall i \in agents \ , \tag{1}$$

where x is the variable that refers to units of goods traded. Total cost constraint of the i-th agent is defined in the following way:

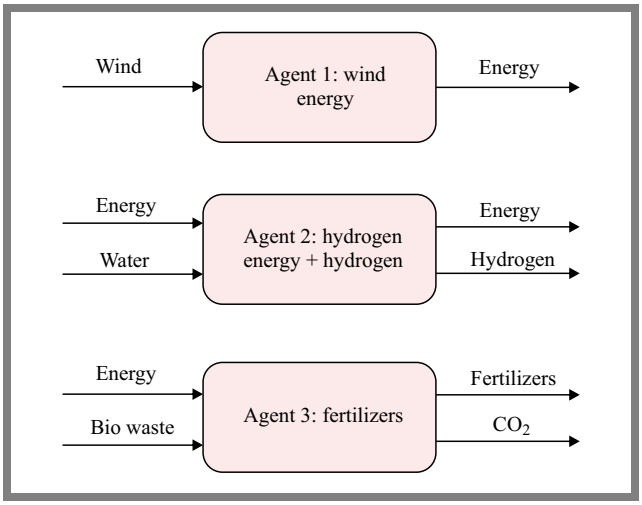

Fig. 4. The concept of an individual approach to energy prosumers.

$$C_i = \sum_{n \in i, demands} y_{n,i}\, c_n, \;\; \forall\, i \in agents \;\; , \tag{2}$$

where y is the variable referring to units whose costs are calculated.
The revenue constraint of i-th agent is:

$$R_i = I_i - C_i, \;\; \forall\, i \in agents \;\; , \tag{3}$$

The system individual total revenue may be defined as:

$$TR_{ind} = \sum_{i \in A} R_i \;\; . \tag{4}$$

5.2. Cooperative Approach

In the cooperative approach, an energy management system bus is used for the optimization process to achieve the highest possible performance – see Fig. 5. Here, each agent declares his capacity demands for materials and supplies. These values are added to a shared pool of requirements, i.e., cooperation demands (CD) and resources, i.e., cooperation supplies (CS).

In the next step, the requirements vector is considered for each agent. If the agent demands a resource located in the CS pool, it gets its requested value without payment.

Then, the values of the agent's supply vector are considered in the same way. Here, the agent is initially obliged to meet the demand for cooperation concerning a given resource and cannot sell at the market price.

The income for the agent at this stage is based solely on the sale of the surplus of goods, i.e., the supply minus the demand of CD. Similarly, the demand for a resource for the agent is not a cost if its resources are in the cooperation pool. In the next phase, the vector is calculated to determine the differences between the cooperative and individual solutions to find maximum values. The weights are computed as percentage losses of agents between the cooperation and individual models.

In this approach, the EMS system is responsible for controlling the energy network load between the seller and the buyer. However, it should be noted that several energy sources can be used to meet the agent's demand. The fairness criterion provided in this case guarantees that no sources are discriminated against or ignored due to price.

In a simple approach based on minimizing costs, while maintaining constraints, an outcome is possible in which the entire energy demand will be met by the cheapest supplier. This may lead to undesired elimination of competition, as energy obtained from fossil fuels is still cheaper than power generated from renewables.

The authors' proposal is based on a linear optimization model that can be tuned to promote those producers who are less competitive price-wise.

In the cooperative scenario, the following equations are used to design the model.
Cooperation demands pool (CD):

$$CD_n = \sum_{i \in agents} y_{n,i}\,, \;\; \forall n \in i.supplies \;\; . \tag{5}$$

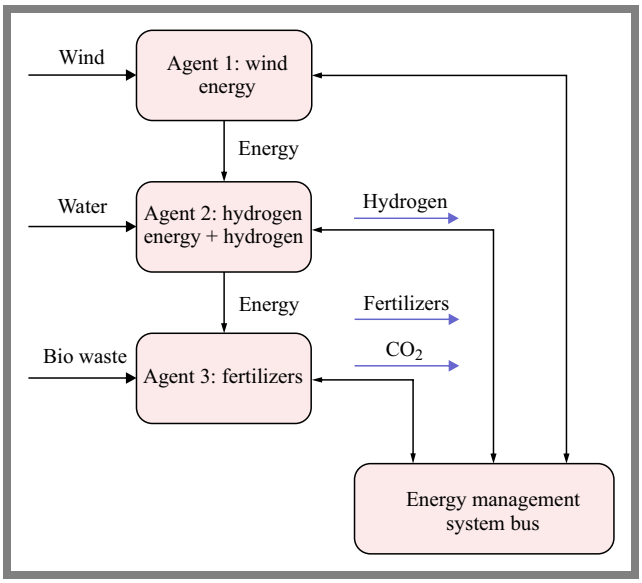

Fig. 5. Cooperative approach to energy prosumers.

Cooperation supplies pool (CS):

$$CS_n = \sum_{i \in agents} x_{n,i}\,, \;\; \forall\, n \in i.demands \;\; . \tag{6}$$

Income constraint of the i-th agent is determined from:

$$I_i = \begin{cases} \sum\limits_{n \in i.sup} x_{n,i}\, p_n, & \text{if } \; CS_n = 0 \\ \sum\limits_{n \in i.sup} (x_{n,i} - CS_n)\, p_n, & \text{if } \; 0 < CS_n < x_{n,i} \\ 0, & \text{otherwise} \end{cases} \;\; . \tag{7}$$

The total cost constraints of the i-th agent are:

$$C_i = \begin{cases} \sum\limits_{n \in i.sup} y_{n,i}\, p_n, & \text{if } CD_n = 0 \\ \sum\limits_{n \in i.sup} (x_{n,i} - CS_n)\, p_n, & \text{if } \; 0 < CS_n < x_{n,i} \\ 0, & \text{otherwise} \end{cases} \;\; . \tag{8}$$

Revenue constraint from the i-th agent is derived as:

$$R_i = I_i - C_i\,, \;\; \forall\, i \in agents \;\; . \tag{9}$$

Total revenues resulting from the system's cooperation may be formulated from:

$$TR_{coop} = \sum_{i \in A} R_i \;\; . \tag{10}$$

The system gain difference is:

$$\Delta coop - ind = TR_{coop} - TR_{ind} \;\; . \tag{11}$$

5.3. Fairness Linear Optimization Model

The multi-criteria optimization process is designed to distribute the profit resulting from the cooperation approach between the specific agents. The fairness criteria in the model are implemented by the appropriate treatment of agents, taking into account the profits gained from a simple individual approach, compared to those earned from the cooperation scheme. During the optimization process, the first assumption is to find a resource allocation scheme in which no one

gains less than the in the individual scenario. This is the model that offers the most equal approach, based on the max-min concept [5].

Unfortunately, this scheme is usually not an efficient solution. Therefore, two multicriteria models have been proposed to increase the efficiency of the solution: the ratio model (RGM) and the ordered weighted averages (OWA). Furthermore, the fairness optimization ratio uses the Gini index as the inequality measure defined by the following set of equations:

$$\min \frac{z_0 + \varepsilon}{z - \tau} \ , \tag{12}$$

$$z_0 = \frac{\sum\limits_{i \in A} \sum\limits_{j \in A} q_{ij}}{2\, m^2}, \ \ q_{ij} \geqslant 0 \ , \tag{13}$$

$$z = \frac{1}{m} \sum_{i \in A} z_i \, W_i \ , \ \ z_i \geqslant 0 \ , \tag{14}$$

$$z \geqslant \tau + \varepsilon \ , \tag{15}$$

$$\sum_{i \in A} z_i \leqslant \Delta_{coop-ind} \ , \tag{16}$$

$$q_{ij} \geqslant z_i, w_i, \ \forall \, i, j \in A \ , \tag{17}$$

$$q_{ij} \geqslant z_j, w_j, \ \forall \, i, j \in A \ , \tag{18}$$

$$\tau = \frac{\Delta_{coop-ind}}{m} \ . \tag{19}$$

where m is the number of agents and ε is the model parameter (0.001 – 0.1).

To linearize the model, a substitution set of equations is used:

$$\begin{gathered} v = \frac{z}{z - \tau}, \ \ v_0 = \frac{1}{z - \tau}, \ \ \widetilde{z_i} = \frac{z_i}{z - \tau} \ , \\ \widetilde{q_i j} = \frac{q_i \, j}{z - \tau}, \ \ \widetilde{z_i \, j} = \frac{z_i \, j}{z - \tau} \ . \end{gathered} \tag{20}$$

Using Eq. (20), the model could be presented in linear form as:

$$\min \frac{\sum\limits_{i \in D} \sum\limits_{j \in D} \widetilde{q_{ij}}}{2\, m^2} + \varepsilon \, v_0 \ , \tag{21}$$

$$v = \frac{1}{m} \sum_{i \in A} \widetilde{z_i} \, W_i \ , \tag{22}$$

$$1 \geqslant v_0 \, \varepsilon \ , \tag{23}$$

$$1 = v - \tau \, v_0 \ , \tag{24}$$

$$\widetilde{q_{ij}} \geqslant \widetilde{z_i} \, w_i - \widetilde{z_j} \, w_j, \ \forall \, i, j \in A \ , \tag{25}$$

$$\widetilde{q_{ij}} \geqslant \widetilde{z_j} \, w_j - \widetilde{z_i} \, w_i, \ \forall \, i, j \in A \ , \tag{26}$$

where w_i stands for weight of i-th agent related to the cost difference between individual and cooperation models, and z_i is value of the amount of energy units transmitted to i-th agent.

The OWA model can be defined as follows:

$$\max \sum_{d=1,\ldots,m} \overline{\omega_d} \, \eta_d \ . \tag{27}$$

In Eq. (27) the following constraints are applied:

$$\eta_d = dt_d - \sum_{i=1}^{m} z_{di} \ , \tag{28}$$

$$t_d - z_{di} \leqslant h_i \, r_i \ , \tag{29}$$

$$z_{di} \geqslant 0 \ , \tag{30}$$

$$\omega_d \geqslant 0 \ . \tag{31}$$

These equations define the typical constraints affecting the process of optimizing an ordered vector of ratings. The OWA model takes into account the weights ω assigned to the next smallest values of the rating vector. The largest weight is the smallest value of the allocation of the resource under consideration, i.e., the energy obtained from the least competitive supplier. The last and smallest weight is assigned to the most attractive energy supplier. Such an approach allows the non-increasingly ordered vectors of weight to control the significance of the model fairness criterion.

The model also includes auxiliary variables t and η, required to enable dynamic determination of possible permutations of the allocation vector within the studied area of feasible solutions.

6. Experiments

The proposed model was developed assuming cooperation-based and individual sales approaches, and is divided into two parts. The first of them predicts the expected total revenue value obtained from the two types of sales mentioned above. The difference between the calculated revenues is treated as a limited resource that must be fairly assigned to agents. This is the second part of the problem solving process.

Fairness models were implemented and compared to perform the allocation between agents. Firstly, the simple max-min model was used to find the most discriminated demand and increase it as much as possible. In other words, the model solver will return the solution where all demands have possible maximum values, with special consideration given to the smallest values of the objective function vector.

The second part is the OWA model which can be controlled by weight parameters. In the proposed model, the number of weights and the number of demands must be equal. The weights have to be sorted in a non-increasing manner and are related to the following objective function vector values (starting from the smallest value).

For example, when there are three demands, the weight vector [5, 1, 1] will return a solution similar to max-min. On the other hand, weights such as [5, 5, 5] will return a solution similar to the simple maximization problem (effmax) which assigns all resources to the demand offering the highest revenue. Revenue is related to the value of the income difference of a given agent between the individual and the cooperation sales models.

Tab. 1. Results achieved with the use of specific optimization methods.

Method	Agent 1	Agent 2	Agent 3	Agent 4	Agent 5	Agent 6	Agent 7	Agent 8	Agent 9
Maxmin	8050	8050	8050	8050	8050	8050	8050	8050	8050
Effmax	0	0	0	0	0	0	0	40250	40250
OWA	14999.77	8107.99	8107.99	7594.82	8450.58	8571.3	0	6451.52	6451.52
RGM 1	0	9964.74	9964.74	9334.06	10385.79	10534.16	0	7928.93	7928.93
RGM 4	0	12146.35	12146.35	11377.6	12659.58	12840.43	0	9664.84	9664.84

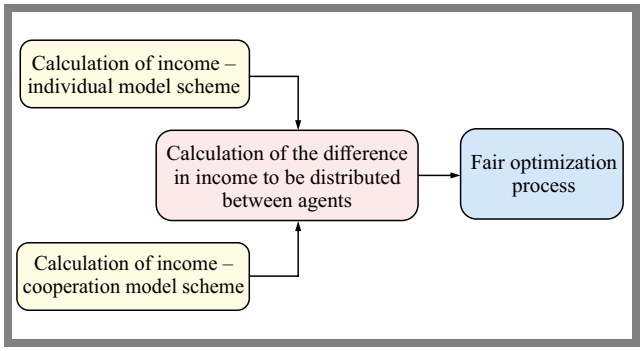

Fig. 6. Initial optimization process in which limits are set and tested.

The last business fairness model is a ration model which considers efficiency maximization and simultaneously uses the Gini index minimization scheme. This model takes only one input parameter and returns the variety of solutions from the fairest to the best (in terms of efficiency). The fairness optimization model may also be developed by relying on other inequality measures used in statistics [6].

7. Results

In the simulation, several instances of the problem were taken into consideration and the number of agents and flows of given materials and goods were varied. The models were optimized in the Python 3.8 environment, with Python Pyomo libraries used for linear optimization.

Table 1 illustrates the results of simulations obtained using the profit vector shown in Tab. 2. The calculations were carried out for the case in which there is cooperation between the system agents and the solution is achieved by means of a central system controlling flows by returning recommendations on energy distribution.

Optimization models were developed to take into account the maximization of the total profit from the sale of energy but also to ensure equal distribution, i.e. taking into account the criterion of fairness. Linear optimization models are characterized by the short lead time required to achieve the result and can be used successfully in real-time decision support systems.

Tab. 2. Revenue vector.

Agent no.	1	2	3	4	5	6	7	8	9	10
Revenue	93	100	78	78	49	44	43	0	58	58

8. Discussion and Conclusions

Table 1 presents the results achieved with the use of the linear optimization methods, where the load vector was assessed for each agent and one unit of the resource allocated to the agent was associated with the unit of profit. For the final assessment, two opposing criteria were taken into account. The first is the total profit (effmax method). It is the simplest solution with no restrictions on the maximum value of resources allocated to the associated agents.

Maximization of the smallest value of the resulting vector (max-min method) is a more complicated approach, but us still simple to implement. Such solutions are the most effective, because they allow for allocating resources to each agent evenly. However, max-min optimization is often characterized by a significant drop in performance due to the even distribution of the result vector.

This work aims to present the results achieved by methods using the model's parameters to control the final solution, i.e. the ordered weighted averages (OWA) method. The parameters controlling the methods include the vector of weights assigned to each agent, making it possible to force the model to assign high priority to the next least efficient allocation (agent), i.e. the one bringing the most negligible revenue.

Another method allows to control the result to achieve a compromise between the uniformity of the solution (fairness) and its efficiency, considered as the allocation of resources to subsequent agents. RGM offers the possibility of returning several solutions which, via one parameter, allow for returning a spectrum of solutions by means of parametrization.

This is a useful feature for decision makers aiming to analyze a range of solutions, from the fairest to the most efficient one, and to choose the one that is good enough for their needs.

The RGM method shows the most desirable features in the optimization process, where two opposing evaluation criteria are considered. In the case under consideration, where the total cost is minimized and the fairness criterion is maximized (no discrimination of less competitive suppliers), the RGM method is much easier to control due to using only one parameter τ in Eq. (12).

In the optimization process, in order to obtain a set of solutions, from the fairest (least cost-effective) to the least fair (most cost-effective), the approach with recursive parameters tuned between the average allocation value from the max-min approach and those from the previous solution is worth considering. This allows to obtain many solutions between the

max-min and the simple minimization of the single-criterion model focused on cost minimization.

Acknowledgments

The authors gratefully acknowledge the financial support of the National Science Centre, Poland [2018/30/Q/HS4/00764].

References

[1] A. Malik *et al.*, "Achieving Cost Minimization and Fairness in Multi-supplier Smart Grid Environment", *Energies*, vol. 11, no. 6, art. no. 1367, 2018 (https://doi.org/10.3390/en11061367).

[2] F. Moret and P. Pinson, "Energy Collectives: A Community and Fairness Based Approach to Future Electricity Markets", *IEEE Transactions on Power Systems*, vol. 34, no. 5, pp. 3994–4004, 2019 (https://doi.org/10.1109/TPWRS.2018.2808961).

[3] A. Milovanoff, I.D. Posen, and H.L. MacLean, "Electrification of Light-duty Vehicle Fleet Alone will not Meet Mitigation Targets", *Nature Climate Changes*, vol. 10, no. 12, pp. 1102–1107, 2020 (https://doi.org/10.1038/s41558-020-00921-7).

[4] P. Palka, W. Radziszewska, and Z. Nahorski, "Balancing Electric Power in a Microgrid via Programmable Agents Auctions", *Control and Cybernetics*, vol. 41, no. 4, pp. 777–797, 2012.

[5] W. Ogryczak, H. Luss, M. Pioro, D. Nace, and A. Tomaszewski, "Fair Optimization and Networks: A Survey", *Journal of Applied Mathematics*, vol. 2014, pp. 1–25, 2014 (https://doi.org/10.1155/2014/612018).

[6] G. Zalewski and W. Ogryczak, "Network Dimensioning with Minimum Unfairness Cost for the Efficiency", *Advances in Intelligent Systems and Computing*, vol. 559, pp. 217–229, 2018 (https://doi.org/10.1007/978-3-319-65545-1_20).

Grzegorz Zalewski, Ph.D.
Institute of Control and Computation Engineering
https://orcid.org/0000-0001-8620-0019
E-mail: g.zalewski@il-pib.pl
Warsaw University of Technology, Warsaw, Poland
https://www.pw.edu.pl
National Institute of Telecommunications, Warsaw, Poland
https://www.gov.pl/web/instytut-lacznosci

Janusz Granat, Ph.D.
Institute of Control and Computation Engineering
https://orcid.org/0000-0003-3130-5555
E-mail: janusz.granat@pw.edu.pl
Warsaw University of Technology, Warsaw, Poland
https://www.pw.edu.pl
National Institute of Telecommunications, Warsaw, Poland
https://www.gov.pl/web/instytut-lacznosci

Marek Makowski, Ph.D.
https://orcid.org/0000-0002-6107-0972
E-mail: marek@iiasa.ac.at
Systems Research Institute, Polish Academy of Sciences, Warsaw, Poland
https://www.ibspan.waw.pl/en/home/
International Institute for Applied Systems Analysis, Laxenburg, Austria
https://iiasa.ac.at

Examination of 5G NR, LTE, and NB-IoT Radio Interfaces and Their Vulnerabilities to Interference

Piotr Rajchowski

Gdansk University of Technology, Gdańsk, Poland

https://doi.org/10.26636/jtit.2024.4.1960

Abstract — Modern cellular wireless communication systems of the fourth (4G) and fifth generation (5G) face a problem of various types of interference or intentional jamming. Consequently, a degradation of the services provided and an incorrect network operation may occur. In this paper, configuration of the networks' physical layer is investigated, with the said investigation preceded by the measurement of parameters of commercial networks operating in two different environments, to assess their vulnerabilities to interference or intentional jamming. Finally, a method for analyzing the radio signal received with the use of 5G New Radio (NR), Long Term Evolution (LTE), and Narrowband Internet of Things (NB-IoT) radio interfaces is proposed, to detect and mitigate the negative impact of unwanted signals. Software-based implementation of the proposed method allows one to detect and mitigate co-channel interference, intentional jamming and maintain compatibility of user equipment (UE) with the 3rd Generation Partnership Project (3GPP) standard, as it does not affect operations performed, for instance, at the time and frequency synchronization or channel parameter estimation phases.

Keywords — 5G NR, interference, jamming, NB-IoT, LTE

1. Introduction

The growing popularity of cellular communication systems, especially those of the fifth generation, stems from a rapid evolution in user habits and demands. The emergence of previous generation solutions (4G LTE [1]) and the new 5G networks addressed the needs of users taking advantage of popular services relying on mobile data transmission. Furthermore, other technologies, such as the Internet of Things (IoT), led to the development of new radio interfaces, e.g. Narrowband IoT (NB-IoT), which relied on a modified version of the LTE radio interface [2].

Regardless of the geographical region considered, an increase in the quantity of user equipment (UE) operating within increasingly dense networks may be observed in highly urbanized areas [3]. In many European countries, frequency range 1 (FR1) bands are reallocated from other systems to 4G and 5G solutions to ensure higher network capacity. Thus, the same radio interfaces, e.g. 5G NR, LTE and NB-IoT, operate together, in the same multiple bands, but with different physical layer configurations. Therefore, one may assume that network planning and optimization tasks have become, mostly in urban areas, more challenging due to co-channel interference (CCI).

It is worth mentioning that interference is not the only problem encountered by commercial and private networks. Intentional jamming is another issue of great importance. Beyond national networks, private companies or government entities create several private 5G/4G networks based on software-defined network cores and radio access networks (RAN) [4]. These networks may be the target of intentional attacks, especially when one considers the ease with which software defined radio (SDR) technology may be accessed, and the open-source nature of the software relied upon.

In this context, the paper addresses the problem of CCI and intentional jamming of signals transmitted in frequency bands that 4G and 5G cellular networks rely on. The proposed method is designed for implementation on the UE receiving path and is supported by measurements aimed at discovering the most common configuration of the network's physical layer.

The main goal of this paper is to present the concept of processing the downlink signal independently of operations performed during frequency and time synchronization, as well as decoding the messages broadcast. Furthermore, the author assumes that interaction between the proposed solution and the regular signal processing algorithms will additionally benefit the process of mitigating interference and jamming.

The key contributions of the paper can be summarized as follows:

- A literature review has been presented, focusing on the methodology of identifying the parameters of interference signals observed in real world networks and on testing vulnerability of 4G/5G networks to jamming.
- A physical layer of 4G/5G networks has been created to gather information on the configuration of time-frequency resources used, thus directly implying the potential sequences of interference and interference signals.
- A method for processing signals in along the 4G/5G UE receiving path is proposed, allowing us to implement interference and jamming detection and mitigation functionalities, while maintaining compliance with 3GPP standards. In addition, operational capabilities may be adjusted suit the computational resources available.

The rest of the paper is organized as follows. The state of the art regarding interference, jamming and jamming mitigation techniques is presented in Section 2. Section 3 describes the measurement campaign during which signals from real 4G and 5G NR commercial networks were analyzed in the context of the physical layer's configuration. Section 4 identifies the proposed method used for processing signals along the UE receiving path, intended to detect and mitigate the impact of interference or jamming. Finally, a summary of the research conducted is presented in Section 5.

2. Related Work on Interference and Jamming

This section addresses the main research problem, i.e. interference observed in 4G/5G networks and methods for mitigating its negative impact on signal reception. Detailed parameters of such interference are given as well.

2.1. Interference Detection and Mitigation

The typical method of jamming a radio system is based on the transmission of a wideband signal, with a frequency range equal or close to that of the affected radio interface [5]. Additive white Gaussian noise (AWGN) or quadrature phase shift keying (QPSK) modulated signals, relying on the orthogonal frequency division multiplexing (OFDM) technique, may be used as examples of such jamming signals.

Such a method is usually effective in disrupting radio communication, but is energy-inefficient and easily detectable [6]. Therefore, some papers present jamming detection solutions based on estimating the received signal's power in the analyzed bandwidth, or the power of reference signals. Such an approach is taken, for instance, in [7], [8].

In contrast, in [9], the authors investigate a smart or adaptive jamming method in which the jamming signal is generated based on the configuration of the radio interface to be affected, i.e. as CCI. The problem of CCI cancelation was also investigated in [10], where the authors proposed the least mean squares-based method to reduce its negative impact in a multipath environment.

In [11], the authors proposed a method for minimizing LTE cell-specific reference signal (CRS) interference in cases in which interference is caused by another 5G network operating in the same area. In that paper, the authors estimated channel state information (CSI) based on zero-power resource elements and the CRS allocated according to pattern omitting 5G NR demodulation reference signal (DMRS). This assumption was made to detect interference.

Furthermore, the authors proposed multiple CRS rate matching patterns to mitigate the negative impact on DMRS interference. Despite the proved effectiveness of the solution, this method is not compatible with the physical layer defined by 3GPP and cannot be currently implemented in UE.

In article [12], the authors proposed an interference detection method based on analyzing a physical broadcast channel block of the synchronization signal (SS/PBCH). The authors assumed that DMRS resource components will be jammed by the attacker after the initial cell search procedure and while determining the DMRS pattern. The proposed detection mechanism is based on analyzing the failures in master information block (MIB) decoding, with adaptive threshold estimation, as not all MIBs are correctly decoded in non-jamming conditions.

The approach presented in [12] may be transferred to scenario involving LTE or NB-IoT radio interfaces, with a change to the signal processing methodology that is required due to the independent transmission of primary synchronization signal narrowband primary synchronization signal (PSS/NPSS) signals and broadcast messages.

Research has also been conducted that is not related to specific radio interfaces, but dealing with radio links relying on the OFDM technique to create the radio signal. In paper [13], the authors proposed a method for estimating narrowband interference using the subspace-based approach [14] and analyzing the cyclic prefix of the received signal. In the presented example, the authors proved that it is possible to reduce the bit error rate (BER) when the OFDM signal interferes with a single-tone sinusoidal waveform.

Furthermore, the simulations presented were performed with the signal-to-interference ratio (SIR) in a range of –25 to 25 dB. Despite significant effectiveness of the method, the research needs to be expanded by analyzing other scenarios, for instance those involving radio channels not modeled by AWGN noise only.

2.2. Parameters of Interference

The literature review revealed a few common approaches and main assumptions concerning the parameters of the simulation model used, regardless of the type of radio interference. During CCI analysis, the interference signal was usually of the same form as the impacted interface [15], [16]. However, in some publications, different numerical parameters, such as physical cell identity (PCI), number of antenna ports, or subcarrier spacing [17], [18], were taken into consideration.

In addition to CCI, in other research papers, interface affected narrowband [19] or wideband signals. In [20], a signal with a bandwidth of one physical resource block of 30 kHz was considered. The waveform was created using the OFDM technique, without complying with the 5G NR standard. Additionally, SNR was in the range of 0 to 6 dB. In another group of studies, interfering signals could be classified based on the synchronization of their frequency with the interface. In [5], the authors used an AWGN noise signal with a bandwidth of 1 MHz that was transmitted in a part of the interfered signal's band or swept over its entire frequency band. In papers [12], [21], initial time and frequency synchronization with next generation NodeB (gNB) was performed and parameters of the interfering signal, e.g. center frequency and transmission time, were adjusted.

Furthermore, in addition to analyzing interference and jamming attacks, there is another branch of research focused on

investigating the influence of the channel on the effectiveness of interference detection. This problem was mentioned, for instance, in papers [13], [22], where the authors assumed no channel impact or where the channel was modeled to comply with the AWGN profile. Such a simplification may be sufficient at the initial stage of research; in practice, the channel has to be modeled using profiles consistent with the environment under analysis. Moreover, it should be defined during the analysis whether channels existing between gNb/eNB (evolved NodeB), UE and the source of interference are correlated.

3. Measurement Studies of 4G/5G Radio Interfaces

In this section, the research methodology and the measurements are presented. Then, an analysis of the parameters of the physical layer of commercial and private networks is performed.

3.1. Test bed and Measurement Methodology

The physical layer is highly dependent on the network provider and on the assumptions made during the network planning and further optimization processes. The 3GPP specification contains detailed information on the potential configurations of the physical layer and on the dependencies between various modes of operation. These parameters are determined and interpreted on the UE platform, but are not reported to high-level user applications.

To reveal a detailed network configuration, the TSME6 SDR receiver (scanner) by Rohde&Schwarz was used for testing and measuring [22]. Moreover, using R&S ROMES software, it was possible to receive and analyze 5G NR, LTE and NB-IoT radio interface signals [23]. The block diagram of the test bed is presented in Fig. 1. The TSME6 scanner was connected to a wideband omnidirectional QRC antenna covering the 350 – 6000 MHz band [24]. It was also connected to a GPS antenna to determine the coordinates of the measurement position and enable synchronization of the scanner. The instrument was taken from the ROMES software.

The downlink (DL) signals of 5G NR, LTE, and NB-IoT radio interfaces were recorded at two fixed locations and in different environmental conditions. The Gdańsk University Campus and the suburbs of Gdańsk City were selected to represent urban and suburban cases, respectively. Such a choice was characterized by large and variable number of pieces of UE with different network traffic characteristics, and by various distances to nearest eNBs/gNBs. Moreover, a large variety of cell sizes, numbers and configurations was expected at those locations [25].

At each measurement location, eNBs and gNBs data were recorded for 15 minutes and measurement reports were generated afterwards. The set of measurement data contained detailed information about the configuration of the physical layer, radio interface operation mode, decoded MIB, and (in selected cases) the system information block no. 1 (SIB-1) broadcast messages. One should notice that for a 5G NR radio interface operating in the non-standalone (NSA) mode, the SIB1 message cannot be decoded receiving signal only in the n77 band.

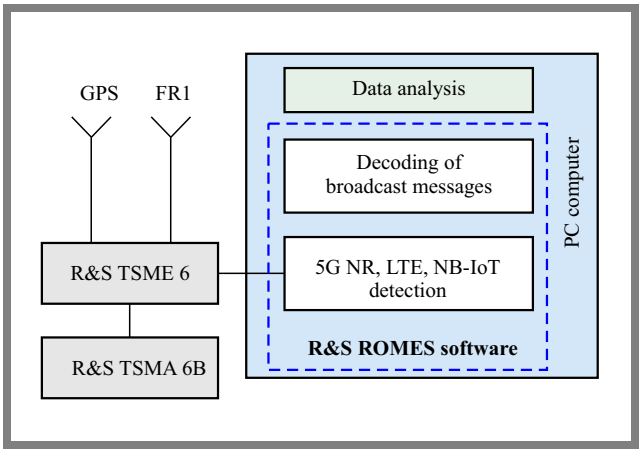

Fig. 1. Block diagram of the test bed used to reveal the parameters of the physical layer and decode messages broadcast using 5G NR, LTE and NB-IoT radio interfaces.

3.2. Analysis of 4G/5G Network Configuration

The radio signals transmitted by gNBs and eNBs were recorded in all frequency bands assigned to network operators in Poland [26]. The data was analyzed statistically and numerically in the Matlab environment. The exported data files were filtered to extract numerical parameters for each radio interface and to determine empirical cumulative distribution functions (CDFs) of the signal-to-interference and noise ratio (SINR) in various frequency bands and environments. For the 5G NR radio interface, DMRS SINR presented as the SS/PBCH block is the only element assumed to be present in the DL, regardless of interface load [25], [27].

The 4G LTE radio interface was deployed in six frequency bands (ranging from 0.8 to 2.7 GHz), with resources for the NB-IoT radio interface assigned in the 800 and 900 MHz bands (n8, n20). A detailed configuration of the radio interfaces under investigation is presented in Tab. 1, where the data are grouped for each radio interface, highlighting the key parameters closely related to detection and mitigation of interference.

The 5G network in the investigated environments was configured to operate in the NSA mode. It was discovered that 5G NR radio signals were transmitted in two basic configurations, as co-existing in the LTE bands: n1, n38, n65 in the frequency division duplex (FDD) mode or in a separated n77 frequency band. The sharing of resources with the LTE interface is explained in the following subsection. For the n77 band, the interface operated in the time division duplex (TDD) mode with a channel bandwidth of 100 MHz. Additionally, gNB transmission was carried out by means of smart radio heads with a multiple input multiple output (MIMO) antenna array – a configuration used by operators to form three radio beams, all having the same cell number, in the sector of a given cell. Bearing in mind the main scope

of the research conducted, such an approach to transmitting signal via the interface increases the number of the receiver's processing operations, as it is necessary to separately distinguish each beam and perform a more extensive analysis of the SSB transmission's configuration (transmission period and repetition). Moreover, in each environment, multipath propagation will result in the reception of numerous reflected signals which may unintentionally result in CCI. To visualize this phenomenon, in Fig. 2, the empirical CDFs of DMRS SINR are plotted for different gNBs, the n77 band, and the suburban scenario. Notice that each color in the figure presents one PCI number.

From Fig. 2, one may observe that despite the long distance to the closest gNB (1.2, 1.7, and 2.6 km) [28], it was possible to receive and identify many sectors (or sector beams) from 3 physical gNBs, each with 3 sectors [28]. During this discovery process, the SINR of the DMRS was far below –10 dB for 50% of the cases in the case of most received DL signals, and the estimated received DMRS reference signal receive power (RSRP) was in a range of –125 to –80 dBm.

In contrast, Fig. 3 presents the empirical CDFs of 5G NR DMRS SINR for the urban scenario. In this case, one may notice that the test bed was located, during the measurements, within the beam of one sector of the closest gNB (line-of-sight conditions and distance of 215 m). Therefore, the determined DMRS SINR is higher than 22 dB for 50% of the cases (as shown on the right, purple curve) and the DMRS RSRP reached –69 dBm. Moreover, in Figs. 2 and 3, few empirical distributions are affected by non-Gaussian, rapid changes in the distribution, i.e. step-shaped SINR change. This phenomenon may be caused by the transmission of data on the DL and the adjustment of the gNB's DMRS power, as the measurements were performed in a stationary environment, with no moving objects in its proximity.

From the analysis of the measurement dataset, we concluded that the configuration of the LTE radio interface is highly dependent on the frequency band used by the network. For n8 and n22 (800, 900 MHz) bands, the radio interface was configured to use 1 (1 eNB, 5 MHz DL bandwidth) or 2 antenna ports (regardless of the network operator) for different DL bandwidths (5, 10, and 20 MHz). For higher frequencies, i.e. n1 – 2.1 GHz, n3 – 1.8 GHz, n7 – 2.7 GHz, eNBs transmitted the DL signal using 4 antenna ports.

Another important aspect of the physical layer's configuration is dynamic spectrum sharing (DSS), a service that is supported by up to 50% of the identified eNBs. This functionality was noticed in the operation of eNBs in the n1 band. From the main scope of the research this implies further analysis of LTE downlink signals to classify multicast-broadcast single frequency network (MBSFN) and non-MBSFN radio frames to minimize the possibility of false interference detection caused by overlapping SSB and CRS resource components [25], [27]. It is also worth pointing out that some eNBs transmitted the LTE-M radio interface signal (four eNBs in the suburban environment) that is not considered in the presented research.

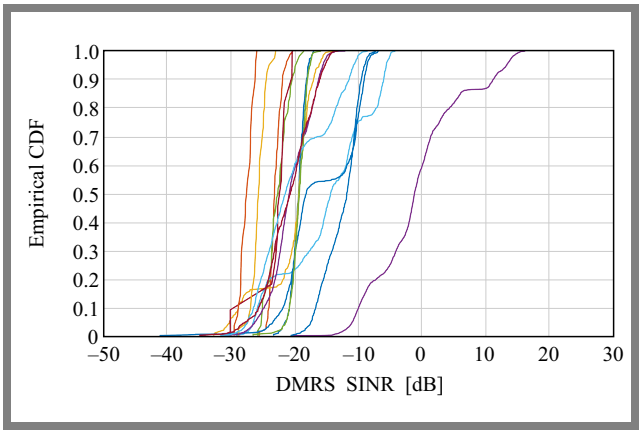

Fig. 2. Empirical CDFs of the DMRS SINR in the 5G NR radio interface for the n77 band in a suburban environment.

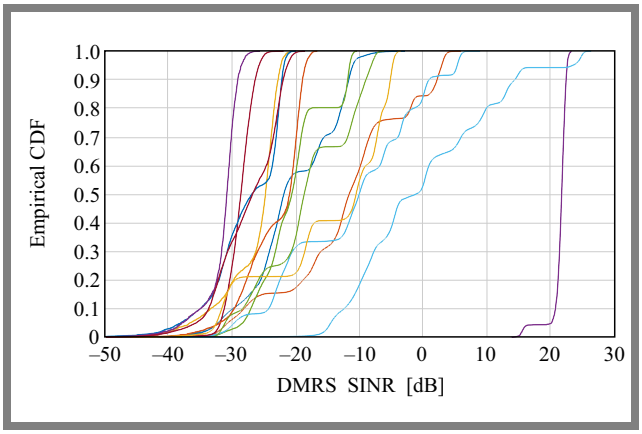

Fig. 3. Empirical CDFs of the DMRS SINR in the 5G NR radio interface for the n77 band in an urban environment.

The CDFs of estimated SINR in the LTE radio interface are presented in Fig. 4. The CDFs shown are representative for measurements performed in the urban environment and eNBs transmitting in the n8 band (900 MHz). In Fig. 4, one may notice that signals were received from four nearby eNB sectors, where SINR was in a range of 6 to 14 dB for more than 50% of cases, with the received signal power equaling up to –41 dBm. Furthermore, 12 other DL signals were received with significantly lower SINR (–19 to –11 dB for 50% of the cases).

In the case of the NB-IoT radio interface, the configuration of the physical layer is not dependent on the type of environment (urban or suburban). For both cases, the radio signal is transmitted by eNBs using one or two antenna ports, both for network operators A and B. The measurement result show a difference in the configuration of the physical layer, as reported in MIB messages. For network operator A, the NB-IoT radio interface is configured to operate in the standalone mode (for both environments). This implies a simplified time-frequency resource grid configuration, without the transmission of LTE CRS symbols. The NB-IoT radio interface of network operator B is configured to operate in the guard band mode, with an additional 2.5 kHz frequency shift. Similarly to previous investigations, the empirical CDFs of SINR for urban environment are presented in Fig. 5.

Tab. 1. Physical parameters of 5G NR, LTE and NB-IoT network interfaces determined during the measurement campaign.

Parameter	Urban	Suburban 1	Suburban 2
5G NR			
Subcarrier spacing [kHz]	15/30		
DMRS mapping	A		
DMRS position	2/3		
Frequency band [GHz]	2.1, 2.6, 3.5, 3.6, 3.7		
Number of PCIs	43	59	86
LTE			
Antenna ports	1, 2, 4	2, 4	
DL bandwidth [MHz]	5, 10, 15, 20		
Frequency band [GHz]	0.8 – 2.7	0.8, 0.9, 1.8, 2.1, 2.6	
Number of PCIs	29	44	71
NB-IoT			
Antenna ports	1, 2		
Frequency band [GHz]	0.8, 0.9	0.8, 0.9, 1.8, 2.2	
Number of PCIs	4	15	20

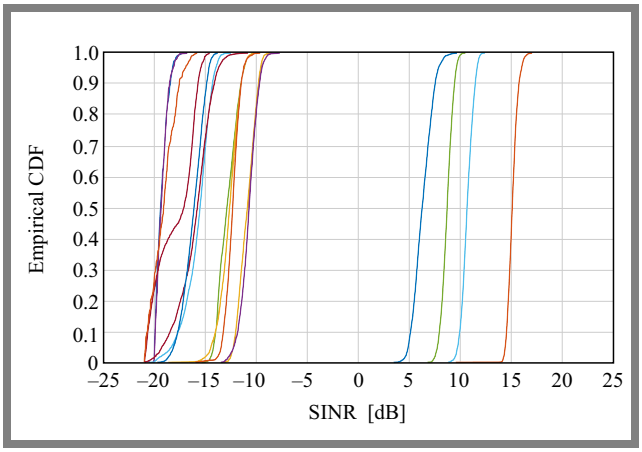

Fig. 4. Empirical SINR CDFs in LTE radio interface for 900 MHz frequency channel (n8 band) in urban environment.

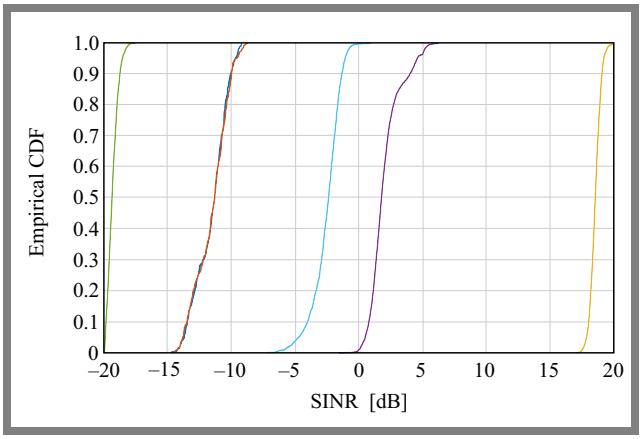

Fig. 5. Empirical SINR CDFs in NB-IoT radio interface for 800 MHz frequency channel (n20 band) in urban environment.

From Fig. 5 one may conclude that while performing the measurements in the urban environment (n20 band), a good quality NB-IoT DL signal (SINR equaling 18.5 dB for 50% of the cases) was received from one nearest eNB. A similar result can be provided for DL in the n8 band (900 MHz). The remaining detected signals come from other sectors, with different azimuths of physical eNBs and eNBs located outside the measurement area.

In Fig. 6, CDFs of SINR for a suburban environment are presented. For this scenario, there are 8 DL NB-IoT signals, with 4 of them potentially causing CCI, as they are identified by the same PCI from the same network operator.

The RSSI of the NB-IoT DL signal in bands n8 and n20 was similar and remained in the range of –71 to –66 dBm.

3.3. Vulnerability of Radio Interfaces to Interference and Jamming

The analysis presented in Subsection 3.2. The physical layer parameters related to 5G NR, LTE, and NB-IoT can be summarized in light of key vulnerabilities to interference, especially with the main scope of this research borne in mind. The first aspect to be mentioned is the simple grid configuration in all radio interfaces analyzed. The interface configuration parameters may be easily disclosed after receiving the synchronization signals and broadcast messages. Afterwards, a jamming signal waveform may be generated to match, e.g., the CRS or DMRS reference symbol allocation in LTE or 5G NR interface.

The NSA operation mode of the 5G NR radio interface can also be classified as a hypothetical vulnerability loophole. UE data transmission in the n77 band is followed by the cell attachment process and by the decoding of control messages

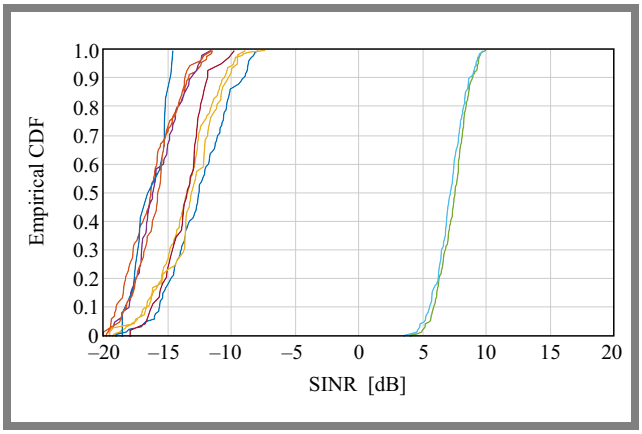

Fig. 6. SINR measured CDFs at NB-IoT radio interface for 800 MHz frequency channel (n20 band) in suburban environment.

that are processed in the lower LTE bands. Thus, one could prepare an attack vector in which only the LTE bands, i.e. the synchronization signals, will be impacted. Therefore, the UE will not be able to connect with the eNB and will further switch to the 5G-NR NSA n77 band. Another threat is linked to the time synchronization of the gNBs and the eNB. In various studies, radio frames of the 4G/5G radio interfaces were synchronized in time [21]. This simplifies the jamming attack, as the jamming signal may be transmitted only at the frequency and time typical of the resource component present in the attacked radio interface. Moreover, it is not necessary to initially synchronize the jammer with gNB/eNB using DL synchronization signals, which simplifies such an attack.

4. Detecting and Mitigating Interference and Jamming

In this section, a concept of a DL signal processing method for 5G NR, LTE, and NB-IoT radio interfaces is introduced for implementation in the receiver in order to detect and mitigate interference. The block diagram of the proposed method is presented in Fig. 7.

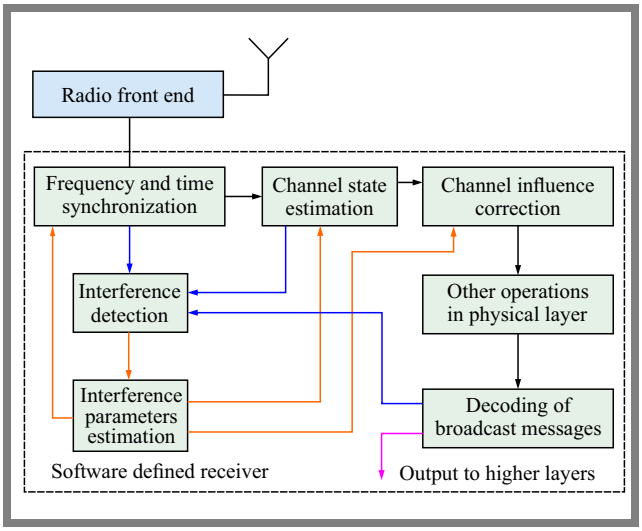

Fig. 7. Block diagram of the proposed DL signal processing method designed to detect and mitigate interference in 5G NR, LTE, NB-IoT radio interfaces.

In general, the concept assumes interception, from the radio transmission, of the investigated radio interface, e.g. using the SDR front end, and initiates an operation performed during the cell attachment process [26]. At this point, it should be mentioned that the methods described in the literature assume complete initial time and frequency synchronization of UE with eNB/gNB or even full UE cell attachment [25], [27]. This assumption may limit the operational abilities of these methods, especially when the networks are highly affected by interfering signals (low value SINR), as described in Subsection 3.2.

On the contrary, the interference detection process should be initiated at the level of physical signal detection, i.e. PSS/SSS for 5G NR, LTE and NPSS/NSSS for NB-IoT. The detection of primary and secondary signals is followed by decoding the broadcast messages, MIB and SIB. Therefore, it implies the second stage of signal analysis in the proposed method. To correctly decode the transmitted messages and transmitted data in other physical channels, it is necessary to estimate channel state parameters and use them to compensate for the negative impact of the channel on the received radio signal.

To make this operation possible, reference symbols are located on the time-frequency resource grid [27]. Their allocation depends on the configuration of the physical layer and on the type of radio interference [27]. There is a possibility that reference signals will be analyzed to detect anomalies, e.g. a phase error characterized by a large degree of variance or constant deviation from the mean over time or over subcarriers.

Moreover, in Fig. 7 the blocks entitled “Interference detection” and “Interference parameters estimation” receive feedback from modules concerned with the estimation of time/frequency synchronization and the once related to channel state parameters. This logical connection between the blocks will allow them to transfer data, e.g. in the form of a resource element grid or OFDM symbols that should be neglected during channel state estimation due to their disruption by interference. This offers the possibility of changing the operating mode of the adaptive receiver, and it will be investigated during future research work. Additionally, the proposed method does not assume the introduction of additional signals to waveforms defined by 3GPP [27] to facilitate the applicability of this method in software-defined UEs.

The main goal of using the proposed method is to shorten the lead time required to obtain the correct time and frequency synchronization of the UE terminal with the eNB/gNB, especially when the radio interfaces are affected by interference signals. Furthermore, increasing the reliability of the cell attachment processes is crucial to minimize computational cost and thus energy consumption, and to ensure the proper operation of all components of the receiving path. Consequently, mitigating the negative influence of the interfering signal may allow to maintain the assumed level of data transmission quality or increase the quality of service (QoS) compared to the scenario in which the proposed approach is not used.

It should also be taken into account that at multiple locations, despite the interference, the NB-IoT terminal will be forced to operate in one frequency channel, due to the lack of alternative communication methods, e.g. other interface operating bands. This situation can also be observed in the case of 5G NR and LTE radio interfaces used in private networks or in suburban areas, where only one eNB/gNB is deployed.

5. Conclusions

It should be mentioned that the presented approach offers only preliminary results of the research and development project pursued.

It clearly identifies a priority configuration which should be investigated further during the development process (Fig. 7) in which a large set of potential physical layer parameters and their combinations will be examined. Additionally, the measurement results serve as reference data for radio channel profile parameters, which will give credibility to further research.

The analysis presented in Subsection 3.2 shows the numerical assessment of DL signal quality, i.e., DMRS SINR and RSSI, which provides information about the state of the interfaces when no intentional jamming signals are transmitted and only signals from other gNBs/eNBs may be classified as CCI. The measurement data, as well as the results presented, will be further investigated during the practical implementation of the proposed DL signal processing method to adjust its sensitivity and minimize the probability of a false alarm.

Acknowledgments

This work was carried out as part of the research and development project entitled "Software-Defined Device for Detecting and Mitigating Inner, Outer System Interference and Hidden Transmissions in 4G-LTE, 5G NR radio interfaces", financed by the National Research and Development Center under the LIDER XIV program, agreement no. LIDER14/0116/2023 signed on 13.02.2024.

References

[1] ETSI, "Evolved Universal Terrestrial Radio Access (E-UTRA) Physical Channels and Modulation", *3GPP 3rd Generation Partnership Project*, 3GPP, TS 36.211, V8.8.0, 2009.

[2] ETSI, "LTE, Evolved Universal Terrestrial Radio Access (E-UTRA) Physical Channels and Modulation", *3GPP 3rd Generation Partnership Project*, 3GPP, TS 36.211, V13.4.0, 2017.

[3] K. Cheon, S. Park, J. Jahng, and J.K. Choi, "Methodology for Network Capacity Assessment of 5G NSA EN-DC Network", *2021 International Conference on Information and Communication Technology Convergence (ICTC)*, Jeju Island, South Korea, 2021 (https://doi.org/10.1109/ICTC52510.2021.9620984).

[4] A. Wulandari, M. Hasan, and A. Hikmaturokhman, "Private 5G Network Capacity and Coverage Deployment for Vertical Industries: Case Study in Indonesia", *2022 IEEE International Conference on Communication, Networks and Satellite (COMNETSAT)*, Solo, Indonesia, 2022 (https://doi.org/10.1109/COMNETSAT56033.2022.9994332).

[5] P.J. Varga, T. Wuhrl, S. Gycnyi, M.T. Baross, and A. Nameth, "Jamming Attacks in 5G NR FR1", *2022 IEEE 5th International Conference and Workshop Obuda on Electrical and Power Engineering (CANDO-EPE)*, Budapest, Hungary, 2022 (https://doi.org/10.1109/CANDO-EPE57516.2022.10046381).

[6] P. Skokowski, K. Malon, M. Kryk, K. Maslanka, J.M. Kelner, P. Rajchowski, and J. Magiera, "Practical Trial for Low-Energy Effective Jamming on Private Networks With 5G-NR and NB-IoT Radio Interfaces", IEEE Access vol. 12, pp. 51523–51535, 2024 (https://doi.org/10.1109/ACCESS.2024.3385630).

[7] J. Ming *et al.*, "A 5G Noise and Interference Power Estimation Method Based on the Fusion of Time-Frequency Acquisition Information", *2023 IEEE 11th Joint International Information Technology and Artificial Intelligence Conference (ITAIC)*, Chongqing, China, 2023 (https://doi.org/10.1109/ITAIC58329.2023.10408885).

[8] A. Usman, B.A. Salihu, and K.P. Dawar, "Interference Mitigation Using Enhanced Active Power Control Technique for 5G Downlink Transmission of Macro-femto Cellular Networks", *2021 International Conference on Electrical, Computer and Energy Technologies (ICECET)*, Cape Town, South Africa, 2021 (https://doi.org/10.1109/ICECET52533.2021.9698634).

[9] H. Li, X. Zhang, L. Cao, X. Hu, and D. Yang, "Performance Evaluation of Interference Coexistence in Dense Urban Scenario for 5G NR System", *2018 IEEE 4th International Conference on Computer and Communications (ICCC)*, Chengdu, China, 2018 (https://doi.org/10.1109/CompComm.2018.8780903).

[10] S. Xu, J. Xin, S. Xiong, and Z. Sun, "Performance Analysis of CRS Interference Mitigation Algorithm in LTE and NR Coexistence Scenario", *2021 2nd Information Communication Technologies Conference (ICTC)*, Nanjing, China, 2021 (https://doi.org/10.1109/ICTC51749.2021.9441653).

[11] S.D. Wang, H.M. Wang, W. Wang, and V.C.M. Leung, "Detecting Intelligent Jamming on Physical Broadcast Channel in 5G NR", IEEE Communications Letters, vol. 27, no. 5, pp. 1292–1296, 2023 (https://doi.org/10.1109/LCOMM.2023.3260194).

[12] C. de Frein, M. Flanagan, and A. Fagan, "OFDM Narrowband Interference Estimation Using Cyclic Prefix Based Algorithm", *University College Dublin*, 2006 [Online].

[13] P. Stoica, *Spectral Analysis of Signals*, Hoboken: Pearson/Prentice Hall, 2005 (ISBN: 9780131139565).

[14] G. Morillo, U. Roedig, and D. Pesch, "Detecting Targeted Interference in NB-IoT", *2023 19th International Conference on Distributed Computing in Smart Systems and the Internet of Things (DCOSS-IoT)*, Pafos, Cyprus, 2023 (https://doi.org/10.1109/DCOSS-IoT58021.2023.00080).

[15] K. Bechta, J.M. Kelner, C. Ziółkowski, and L. Nowosielski, "Inter-beam Co-channel Downlink and Uplink Interference for 5G New Radio in mm-Wave Bands", *Sensors*, vol. 21, no. 3, art. no. 793, 2021 (https://doi.org/10.3390/s21030793).

[16] J. Wu *et al.*, "CRS Interference Handling on NR and LTE Overlapping Spectrum: Analysis on Performance and Standard Impact", *2022 IEEE/CIC International Conference on Communications in China (ICCC Workshops)*, Sanshui, China, 2022 (https://doi.org/10.1109/ICCCWorkshops55477.2022.9896636).

[17] A. Ghiulai, G. Barb, F. Alexa, and M. Otesteanu, "Downlink Interference Measurement in 4G/5G Systems with Dynamic Spectrum Sharing", *2022 14th International Conference on Communications (COMM)*, Bucharest, Romania, 2022 (https://doi.org/10.1109/COMM54429.2022.9817351).

[18] G. Morillo, U. Roedig, and D. Pesch, "Detecting Targeted Interference in NB-IoT", *2023 19th International Conference on Distributed Computing in Smart Systems and the Internet of Things (DCOSS-IoT)*, Pafos, Cyprus, 2023 (https://doi.org/10.1109/DCOSS-IoT58021.2023.00080).

[19] K. Wesołowski, "A Simple Algorithm for Jamming Detection in OFDM Systems", *2023 IEEE 97th Vehicular Technology Conference (VTC2023-Spring)*, Florence, Italy, 2023 (https://doi.org/10.1109/VTC2023-Spring57618.2023.10200416).

[20] J. Magiera and P. Rajchowski, "Intentional Pilot Contamination in 5G NR Uplink", *Przegląd Telekomunikacyjny – Wiadomości Telekomunikacyjne*, vol. 2024, no. 4, 2024 (https://doi.org/10.15199/59.2024.4.43) (in Polish).

[21] C. Shahriar *et al.*, "PHY-layer Resiliency in OFDM Communications: A Tutorial", *IEEE Communications Surveys and Tutorials*, vol. 17, no. 1, pp. 292–314, 2015 (https://doi.org/10.1109/COMST.2014.2349883).

[22] "TSME6 Ultracompact Drive Test Scanner", Rohde & Schwarz, V17.00, 2024.

[23] "ROMES Drive Test Software, Mobile Coverage and QoS Measurements in Mobile Networks", Rohde & Schwarz, v.31.00, 2024.

[24] "Wideband Antenna User Guide", QRC Technologies, v.004, Fredericksburg, VA, USA, 2015.

[25] M. Kottkamp, A. Pandey, A. Roessler, R. Stuhlfauth, and D. Raddino, "5G New Radio Fundamentals, Procedures, Testing Aspects", Munich: Rohde & Schwarz, 450 p., 2019 (ISBN: 9783939837152).

[26] "Information on Spectrum Occupancy in the 420 MHz, 450 MHz, 800 MHz, 900 MHz, 1800 MHz, 2100 MHz, 2600 MHz, 3600 MHz bands", *Office of Electronic Communications*, 2024 (in Polish).

[27] ETSI, "5G, NR, Physical Channels and Modulation", *3GPP 3rd Generation Partnership Project*, 3GPP, TS 38.211, V18.2.0, 2024

[28] "Electromagnetic Field Map", *SI2PEM* [Online] Available: (https://si2pem.gov.pl) (in Polish).

Piotr Rajchowski, Ph.D.
Department of Radio Communication Systems and Networks
https://orcid.org/0000-0002-7736-3526
E-mail: piorajch@pg.edu.pl
Gdansk University of Technology, Gdańsk, Poland
https://pg.edu.pl

Information for Authors

Journal of Telecommunications and Information Technology (JTIT) is published quarterly since 2000. It comprises original contributions, dealing with a wide range of topics related to telecommunications and information technology. **All papers are subject to peer review.** Topics presented in the JTIT report primary and/or experimental research results, which advance the base of scientific and technological knowledge about telecommunications and information technology.

JTIT is dedicated to publishing research results which advance the level of current research or add to the understanding of problems related to modulation and signal design, wireless communications, optical communications and photonic systems, voice communications devices, image and signal processing, transmission systems, network architecture, coding and communication theory, as well as information technology.

We encourage submissions from a diverse range of authors from across all countries and backgrounds.

Manuscript

Latex files are preferred and Editorial Office provides a style to prepare the material along with the documentation. We also accept Microsoft Word and PDF files. A typical article is 10 pages long (approximately 6,000 words) and must include the following contents:

- Authors' names and affiliations in the following format:
  First name and surname (last name), academic title,
  Position held,
  ORCID number,
  E-mail address from the University's domain,
  Faculty and name of the University,
  Link to University website.
- Abstract (150-200 words). The abstract should contain statement of the problem, assumptions and methodology, results and conclusion or discussion on the importance of the results. Abstracts must not include mathematical expressions or bibliographic references.
- Keywords related to the content of the article. About four keywords or phrases in alphabetical order should be used, separated by commas.
- The content of the article in a typical structure, i.e.: introduction, related work, conducted research, conclusions, references.

Figures, Tables and Photos

Together with the article, please send files with graphics with the highest resolution available, 150 dpi or more in bitmap resolution (jpg, png) and vector (cdr, svg, ps, pdf) formats are welcomed.

References

We use four main citation styles for a journal article, for an Internet article, for a conference paper, and for a book. Below are examples of citations. In each item, the DOI number or link to the PDF of the cited article should be provided.

[1] R.K. Meyers and A.H. Desoky, "An implementation of the blowfish cryptosystem", *2008 IEEE International Symposium on Signal Processing and Information Technology*, 2008 ((https://doi.org/10.1109/ISSPIT.2008.4775664).

[2] K. Nowicki and T. Uhl, *Ethernet End-to-End*, 1st ed. Germany, Shaker-Publisher, 2008 (ISBN: 978383832271404).

[3] C. Shorten and T.M. Khoshgoftaar, "A survey on image data augmentation for deep learning", *Journal of Big Data*, vol. 6, no. 1, pp. 1–48, 2019 (https://doi.org/10.1186/s40537-019-0197-0).

[4] S. Wong *et al.*, "Traffic forecasting using vehicle-to-vehicle communication", *3rd Annual Conference on Learning for Dynamics and Control*, pp. 917–929, 2021 (https://arxiv.org/pdf/2104.05528).

Submission

The paper with full PDF version and anonymous PDF version for the blind review process should be submitted on the JTIT website https://www.jtit.pl/jtit/about/submissions.

Reviewing Process

The article is initially approved by the Editor-In-Chief and if the decision is positive, is then sent to the reviewers. Depending on the subject of the article, it takes few weeks. In the next step, reviews are showed to authors who have 2 weeks to correct the article. Finally, the corrected text can be re-presented to the reviewer for reevaluation, which will take another 2 weeks.

As a result, after about 3 months, we are able to send the text for publication in the upcoming issue of JTIT.

When the reviews are inconsistent, additional corrections are necessary, or the reviewer expects additional verification because the corrections ordered by the author are insufficient or additional problems arise, the review of the article may be extended by another month or more.

Editorial Work

Positively reviewed and corrected article is next prepared by the editorial office for publication. At the end of this process the author receives an copyedited version for approval.

Licensing

Manuscript submitted to JTIT should not be published or simultaneously submitted for publication elsewhere. By submitting a manuscript the author grants license to the National Institute of Telecommunications, for the use of the paper in the fields of exploitation: reproducing and fixing the paper, distributing the paper by means of introduction to trade, letting for use or rental of the original or copies, and distributing the paper by means of public exhibition, screening, presentation and broadcast as well as rebroadcast, and making the paper publicly available in such a manner that anyone could access it at a place and time selected thereby, or by making it available in a way not allowing selection of time or place, including by means of Internet or other networks.

Ghostwriting Declaration

We require formal declaration that the process of writing the paper was not influenced by any third party. In the article, all the contributions of other people are clearly indicated. The theories presented, methods used, analysis and research, as well as the copyrights to the drawings, photographs and other figures belong to the authors or are clearly credited in the text. The author must also indicate whether his work has received financial support and if the realization of the whole project was possible thanks to the permission and cooperation with scientific institutions, associations and others.

Other Information

- The JTIT being an Open Access Journal (OAJ) has no article processing charges (APCs). The published articles can be downloaded freely without payment.
- JTIT supports open access and using continuous publishing "publish-as-you-go" scheme. This means that we no longer wait to accumulate several articles into a quarterly issue before publication. Rather, articles are continuously added to current issues after acceptation. Publish-as-you-go reduces publication lag for our authors, and make the newest research available quickly. After completing the review process, an article is published online in the current issue with DOI registration. When the issue period ends, a new issue is activated. So accepted articles are published without waiting for the quarterly issue end.

National Institute of Telecommunications

Editorial Office

National Institute
of Telecommunications
Szachowa st 1
04-894 Warsaw, Poland
https://www.gov.pl/web/instytut-lacznosci

phone +48 22 512 81 83
fax +48 22 512 84 00

e-mail: journal@jtit.pl
www.jtit.pl

JOURNAL OF TELECOMMUNICATIONS AND INFORMATION TECHNOLOGY 4/2024 • vol. 98